GOBIERNO DE ESPAÑA
MINISTERIO DE CIENCIA E INNOVACIÓN
Ciemat
Centro de Investigaciones Energéticas, Medioambientales y Tecnológicas

DUNE
DEEP UNDERGROUND NEUTRINO EXPERIMENT

Scintillation light detection techniques in a 750-ton liquid argon TPC for the Deep Underground Neutrino Experiment

Técnicas de detección de luz de centelleo en una TPC de argón líquido de 750 toneladas para el experimento de neutrinos DUNE

José Alfonso Soto Otón

Supervised by:
Dr. Inés Gil Botella

Doctoral Dissertation in Physics
Madrid, 2022

"la Caixa" Foundation
UAM Universidad Autónoma de Madrid

Acknowledgements

Me gustaría agradecer a mi directora todo el tiempo dedicado y el apoyo durante la realización de la tesis. Gracias Inés, por tu confianza y accesibilidad desde el primer momento. Gracias también a Carmen y Clara por su dedicación y por las enriquecedoras discusiones.

Estoy encantado de haber podido trabajar en el grupo de neutrinos del Ciemat. Gracias a todos sus miembros, presentes y pasados. Habéis creado un ambiente de trabajo fantástico, y siempre habéis estado dispuestos a ayudar y a compartir conocimientos.

Estoy muy agradecido a todos los que han hecho posible esta experiencia. He aprendido mucho durante este tiempo en el Ciemat, y más importante, he disfrutado aprendiendo cosas nuevas.

The project that gave rise to these results received the support of a fellowship from ”la Caixa” Foundation (ID 100010434). The fellowship code is LCF/BQ/DI18/11660043.

This project has received funding from the European Union’s Horizon 2020 research and innovation programme under the Marie Sklodowska-Curie grant agreement No. 713673.

Abstract

The experimental confirmation of the neutrino oscillations, and therefore the non-zero neutrino mass, opened a new era of physics beyond the Standard Model of particle physics. Neutrinos do have mass, and their flavour change when propagating. Thanks to the huge effort of the neutrino physics community, many neutrino properties have been measured in the last decades, including most of the neutrino oscillation parameters. However, other properties remain unknown, such as the absolute scale of the neutrino masses, or the nature itself of their masses.

The Deep Underground Neutrino Experiment (DUNE) will bring neutrino physics to a new era, measuring the oscillation parameters with unprecedented precision that will allow determining the CP violation phase in the leptonic sector and the neutrino mass ordering. It also aims at detecting neutrinos from a core-collapsing supernova within the galaxy if it occurs during the running of the experiment and performing beyond standard model searches. DUNE is a long-baseline neutrino oscillation experiment designed by an international collaboration of around 1,300 scientists. It will consist of the most powerful neutrino beam installed at Fermilab (US), a Near Detector placed downstream the beam, and a Far Detector located 1.5 km underground at the Sandford Underground Research Facility (SURF), around 1,300 km away from the beam. The Far Detector of DUNE will consist of four liquid-argon time projection chambers (LAr-TPCs) of 17 kton each. DUNE will bring the LAr-TPC technology to an unprecedented large scale.

A LAr-TPC is a kind of particle detector that allows the particle-track reconstruction with millimetre precision. In a LAr-TPC, the interacting particles ionize the liquid argon along their tracks. This charge is drifted by a uniform electric field and readout. Additionally, scintillation light is produced, providing a fast signal used as a trigger and also to reconstruct the particle interaction time. The excellent imaging capabilities of the LAr-TPC technology, and the advantages of using liquid argon as a detector medium for neutrino physics, will allow DUNE to fulfil its physics goals.

A full prototyping effort is being carried out by the DUNE collaboration to validate

the LAr-TPC technology at the kiloton scale. In particular, two prototypes have been assembled and operated at the CERN neutrino platform: ProtoDUNE Single-Phase and ProtoDUNE Dual-Phase, of $\sim$300 ton of active mass each, and which took data from 2018 to 2020. While ProtoDUNE Single-Phase is based on a more traditional approach of a LAr-TPC based on wire readout planes, the innovative Dual-Phase approach includes a gas layer at the top, with an extraction layer and Large Electron Multipliers (LEMs) to amplify the signal. The work presented in this thesis has been carried out in the framework of this prototyping work, specifically it has been focused on the operation and performance measurement of the photon detection system of ProtoDUNE Dual-Phase. The obtained results are of interest for any liquid argon experiment.

The first chapters of this thesis introduce the status of neutrino physics, the operating principles of the LAr-TPC technology and the DUNE experiment. Then, ProtoDUNE Dual-Phase and its different systems are explained in chapter 4, with a particular focus on the photon detection system. The photon detection system is a crucial part of any LAr-TPC, since it provides the interaction time, which is needed to reconstruct the event in three dimensions and contributes to the particle calorimetric recontruction. The photon detection system can also provide a trigger for non-beam events. The ProtoDUNE Dual-Phase photon detection system consists of 36 photomultiplier tubes (PMTs) placed below the TPC active volume. Due to the monolithic design of the detector, the photon detection system must detect scintillation light from more than six meters away, being the longest light detection distance in any liquid argon TPC up to date. A good characterization of the photon detection system is crucial in order to demonstrate its capabilities. The ProtoDUNE Dual-Phase photon detection system performance is studied in detail in chapter 5.

Additionally, a good understanding of the light production, propagation and detection processes is key in order to extrapolate the performance of the detector at larger scales. In this sense, the development of a Monte Carlo simulation allows identifying the main parameters affecting the detector performance. A dedicated Monte Carlo simulation of the scintillation light production, propagation and detection has been developed, including the light production from cosmic muons and low energy radiological backgrounds, and compared with data. The understanding of the radiological backgrounds is critical to correctly evaluate the physics performance of DUNE at low energies. The simulation is explained in chapter 6 and the comparison with ProtoDUNE Dual-Phase data can be found in chapter 7.

Since scintillation light in liquid argon is produced at 127 nm, at which most photosensors are not sensitive, fluorescent materials are introduced in order to shift the light wavelength towards the visible range, where PMTs have maximal detection efficiency.

ProtoDUNE Dual-Phase has carried out an innovative photon detection program, by testing several wavelength shifting techniques at the multi-ton scale which are the object of analysis in this thesis. ProtoDUNE Dual-Phase has been the first detector deploying the novel polyethylene naphthalate (PEN) together with the more traditional tetraphenyl butadiene (TPB) as a wavelength-shifter. Although TPB has proven its good performance in many liquid argon experiments, its deployment requires sophisticated coating setups that are difficult to scale to large surfaces. TPB coatings are also very delicate, making its handling difficult. In this sense, PEN appears as a promising alternative, since it is a thermoplastic similar to PET, very stable and easy to handle. However its wavelength-shifting efficiency is not well known, and it has been never studied in real operating conditions in large scale LAr-TPC. The PEN wavelength efficiency is measured and its performance is evaluated and compared with TPB in chapter 8. This study is critical to understand if PEN represents an effective alternative to TPB for DUNE.

Xenon doping is another alternative light detection technique for large scale LAr-TPCs. The presence of xenon at the level of a few ppm (parts-per-million) in the liquid argon acts as a wavelength shifter, shifting part of the scintillation light to longer wavelengths and reducing the light attenuation with the propagation distance. The simplicity of just adding a small quantity of xenon makes it an attractive alternative for large-scale LAr-TPC that is being considered for one of the DUNE Far Detector modules. However, the light production mechanisms in xenon-doped liquid argon have not been characterized yet, and their effects in the detected light in a several-meter-drift LAr-TPC have never been measured. In this sense, a deep study is needed in order to validate the xenon-doping technique for DUNE. ProtoDUNE Dual-Phase took data with xenon-doped liquid argon contaminated with a small amount of nitrogen. The performance of the photon detection system using xenon-doped liquid argon and its comparison with pure liquid argon using ProtoDUNE Dual-Phase data is explained in chapter 9. This analysis represents a unique opportunity to study the performance of a LAr-TPC using xenon-doped liquid argon, as the ProtoDUNE Dual-Phase is the largest monolithic LAr-TPC ever operated.

The observation of the proton decay is a process beyond the Standard Model that it has never been observed. Proton decay is one of the requirements of many Gran Unification Theories (GUT), and it would also help to explain the matter-antimatter asymmetry in the universe. Placed deeply underground to mitigate backgrounds and thanks to the good imaging capabilities that allow to identify the interacting particles, DUNE has a promising potential to perform proton decay searches. However, the imaging capabilities rely strongly on having a good and efficient light detection system providing the interaction time of the event. In chapter 10, the performance of a light detection system based on TPB-coated

PMTs, as in ProtoDUNE Dual-Phase, is studied. The goal is to validate its capability to provide the event time of proton decay events in the presence of background events in a 10 kton Far Detector of DUNE. This is a key study since the capability to perform proton decay searches is one of the primary physics goals of DUNE.

Resumen

La confirmación experimental de la oscilación de los neutrinos, y por lo tanto de que los neutrinos tienen masa, ha abierto una nueva era en la física más allá del Modelo Estándar. Los neutrinos tienen masa, y su sabor cambia cuando se propagan. Gracias al esfuerzo de la comunidad de física de neutrinos, muchas propiedades del neutrino han sido medidas en las últimas décadas, incluyendo la mayor parte de los parámetros de oscilación. Sin embargo, otras propiedades se desconocen, como la escala absoluta de la masa de los neutrinos, o la naturaleza misma de su masa.

El experimento DUNE (Deep Underground Neutrino Experiment) llevará la física de neutrinos a una nueva era, midiendo los parámetros de oscilación con una precisión sin precedentes que permitirá determinar la fase de violación CP en el sector leptónico y el orden de la masa de los neutrinos. DUNE también aspira a detectar neutrinos producidos por el colapso de una supernova de tipo II en la galaxia, de ocurrir durante el funcionamiento del experimento, así como realizar búsquedas de física más allá del Modelo Estándar. DUNE es un experimento de oscilación de neutrinos diseñado por una colaboración de cerca de 1.300 científicos. Consistirá en el haz de neutrinos más potente del mundo instalado en Fermilab (EE.UU.), un detector cercano situado a continuación del haz, y un detector lejano ubicado 1,5 km bajo tierra en la instalación SURF (Sandford Underground Research Facility) y a una distancia de 1.300 km del haz. El detector lejano de DUNE consistirá en cuatro cámaras de proyección temporal de argón líquido (LAr-TPC) de 17 kilotoneladas cada una. DUNE llevará la tecnología de la LAr-TPC a un tamaño sin precentes.

Una LAr-TPC es un detector de partículas que permite la reconstrución de las trazas con precisión milimétrica. En una LAr-TPC, la particulas ionizan el argón líquido a lo largo de su traza. Esta carga es arrastrada por un campo de eléctrico uniforme y digitalizada. Además se produce luz de centelleo, que es detectada como una señal rápida que puede ser usada como señal de disparo y para reconstruir el punto de interación de la partícula. Las detección de trazas de partículas con alta definición, y las ventajas de usar argón

líquido como medio de detección en física de neutrinos, permitirán a DUNE conseguir sus objetivos de física.

La colaboración DUNE está llevando a cabo un gran esfuero de prototipado para validar la tecnología de las LAr-TPC a la escala de las kilotoneladas. En concreto, dos prototipos han sido construidos y puestos en funcionamiento en la plataforma de neutrinos del CERN: ProtoDUNE Single-Phase y ProtoDUNE Dual-Phase, con una masa activa de en torno a 300 toneladas cada uno, y que tomaron datos de 2018 a 2020. Mientras ProtoDUNE Dual-Phase se basa en un diseño más tradicional de una LAr-TPC basada en planos de cables de extracción de la carga, el diseño inovador de ProtoDUNE Dual-Phase incluye una capa de gas argón sobre el líquido, una capa de extracción y LEMs (Large Electron Multipliers) para amplificar la señal. El trabajo presentado en esta tesis se ha llevado a cabo en este marco de trabajo de prototipado, en concreto se ha enfocado en la operación y el estudio del desempeño del sistema de detección de fotones de ProtoDUNE Dual-Phase. Los resultados son de interés para cualquier experimento de argón líquido.

Los primeros capítulos de esta tesis presentan una introducción al estado la física de neutrinos, los principios de funcionamiento de una LAr-TPC y del experimento DUNE. A continuación, ProtoDUNE Dual-Phase y sus diferentes sistemas son explicados en el capítulo 4, prestando especial atención al sistema de detección de fotones. El sistema de detección de fotones es una parte fundamental de una LAr-TPC, ya que proporciona el tiempo de interacción necesario para reconstruir el evento en tres dimensiones, y contribuye a la reconstrucción energética de la particula. El sistema de detección de fotones de ProtoDUNE Dual-Phase consiste en 36 tubos fotomultiplicadores (PMTs) situados bajo el volumen activo de la TPC. Debido al diseño monolítico del detector, el sistema de detección de fotones debe detectar luz producida a una distancia de más de seis metros, siendo la distancia más larga de detección de luz en una LAr-TPC hasta la fecha. Por lo tanto, una buena caracterización del sistema de detección de fotones es vital. El desempeño del sistema de detección de fotones de ProtoDUNE Dual-Phase es estudiado en detalle en el capítulo 5.

Por otra parte, una buena comprensión de la producción, propagación y detección de la luz es esencial para poder extrapolar el rendimiento del detector a escalas mayores. In este sentido, el desarrollo de una simulación de Monte Carlo permite identificar los parametros que afectan al rendimiento del detector. Una simulación Monte Carlo dedicada de la producción, propagación y detección de la luz ha sido desarrollada, incluyendo la luz producida de muones cósmicos y el fondo radiactivo de baja energía, y comparada con los datos. La comprensión del fondo radiactivo es fundamental para valorar correctamente el rendimiento de DUNE a bajas energías. La simulación se explica en el capítulo 6 y la comparación con los datos de ProtoDUNE Dual-Phase se encuentra en el capítulo 5.

Dado que la luz de centelleo en argón líquido se produce a una longitud de onda de 127 nm, a la cual la mayoría de los fotosensores no son sensibles, se utilizan materiales fluorescentes para desplazar la longitud de onda al rango visible, donde los PMTs tienen máxima eficiencia de detección. ProtoDUNE Dual-Phase ha llevado a cabo un innovador proyecto de fotodetección en el que se han probado diversas tecnicas de desplazamiento de la longitud de onda que son analizadas en esta tesis. ProtoDUNE Dual-Phase ha sido el primer detector en utilizar el novedoso naftalato de polietileno (PEN), combinado con el más tradicional tetrafenil-butadieno (TPB), como desplazadores de la longitud de onda. Aunque el TPB ha demostrado su buen comportamiento en numerosos experimentos, su instalación requiere sofisticados montajes de deposición, por lo que su manejo es complicado. En este sentido, el PEN se presenta como una alternativa prometedora, ya que es un termoplástico similar al PET, muy estable y fácil de manejar. Sin embargo su eficiencia de desplazamiento de fotones del rango VUV al visible no está clara, y nunca ha sido estudiado en condiciones reales de funcionamiento en una LAr-TPC a gran escala. La eficiencia de desplazamiento del PEN es medida y su comportamiento estudiado y comparado con el TPB en el capítulo 8. Este estudio es crucial para comprender si el PEN es una alternativa factible al TPB para DUNE.

La introducción de pequeñas cantidades de xenón en el argón líquido (o argón dopado con xenón) es otra técnica alternativa de detección de luz para grandes LAr-TPCs. Efectivamente, la presencia de xenón al nivel de unas partes por millón (ppm) en el argón líquido provoca el desplazamineto de la longitud de onda de la luz de centelleo a longitudes de onda más largas, reduciendo la atenuación de luz con la distancia de propagación. La simplicidad de añadir una pequeña cantidad de xenón lo hace una alternativa muy atractiva para LAr-TPCs de gran tamaño, y está siendo considerado para uno de los módulos del detector lejano de DUNE. Sin embargo, los mecanismos de producción de luz en argón dopado con xenón no han sido bien estudiados, y sus efectos en la detección de luz en una LAr-TPC de gran tamaño (del orden de metros) nunca han sido medidos. Por ello, se necesita un estudio detallado para validar la técnica del argón dopado con xenón para DUNE. ProtoDUNE Dual-Phase tomó datos con argón dopado con xenón y contaminado con una pequeña cantidad de nitrógeno. El estudio del comportamiento del sistema de detección de fotones usando argón dopado con xenón y su comparación con el caso de argón puro usando datos de ProtoDUNE-Dual-Phase está explicado en el capítulo 9. Este análisis supone una oportunidad única para estudiar el comportamiento de una LAr-TPC usando argón dopado con xenón, ya que ProtoDUNE Dual-Phase es la mayor LAr-TPC con un diseño monolítico jamás construida.

La observación del decaimiento del protón es un proceso más allá del Modelo Estándar que nunca ha sido observado. Sin embargo, el decaimiento del protón es un requisito de muchas teorías de gran unificación (GUT), que además ayudaría a explicar la asimetría entre materia y antimateria en el universo. Situado a una gran profundidad para suprimir fondos, y gracias a su capacidad de registar trazas con alta definición que permite identificar las partículas que interaccionan, DUNE tiene un potencial prometedor para realizar búsquedas del decaimiento del protón. Sin embargo, estas capacidades dependen en gran medida de tener un sistema de detección de fotones eficiente y eficaz, que provea el tiempo de interacción del evento. En el capítulo 10 se estudia el rendimiento de un sistema de detección de luz basado en PMTs recubiertos con TPB como los de ProtoDUNE Dual-Phase. El objetivo es validar su capacidad de medir el tiempo de interacción para eventos de decaimiento del protón en presencia de fondos en un detector lejano de DUNE de 10 kilotoneladas. Este estudio es crucial, ya que la capacidad de realizar búsquedas del decaimiento del protón es uno de los principales objetivos de física de DUNE.

Contents

10 Validation of the design of the DUNE Dual-Phase Photon Detection System to perform proton decay searches 199

List of Figures

List of Tables

Chapter 1

Neutrino physics

Neutrinos are the fundamental particles that remain as the great unknown in the Standard Model of particle physics. Although many neutrino properties have been unveiled in recent decades, there are still some open questions that future neutrino detectors aim to address. In this chapter, the current knowledge of neutrino properties is described. First, a historical overview of the neutrino discovery is summarized in Sec. 1.1. Section 1.2 describes the neutrino in the Standard Model of particle physics. Sections 1.3 and 1.4 provide a theoretical and experimental approach to the neutrino mass and the neutrino oscillation phenomenon respectively. Finally, some of the remaining open questions in neutrino physics are introduced in Sec. 1.5.

1.1 Discovery of the neutrino

Neutrino was first postulated by Wolfgang Pauli in 1930, as a solution to the beta decay problem [2]. While the energy spectrum in the alpha and gamma decay of the atomic nuclei is a discrete line, in the beta decay Chadwick discovered a continuous energy spectrum for the out-coming electrons [3]. The postulation of the neutrino was then a solution to explain the missing energy and angular momentum that the non-detected neutrino was carrying out.

Later, Enrico Fermi developed his theory of the beta decay [4], which also provided a way to detect neutrinos: an antineutrino colliding with a proton, would produce a neutron and a positron in the inverse-beta-decay process:

$$\begin{aligned} \beta^{-}\text{decay: } & n \rightarrow p + e^{-} + \bar{\nu}, \\ \beta^{+}\text{decay: } & p \rightarrow n + e^{+} + \nu, \\ \text{Inverse } \beta^{+}\text{ decay: } & \bar{\nu} + p \rightarrow n + e^{+}. \end{aligned} \tag{1.1}$$

The neutrino was finally discovered more than 20 years later, by F. Reines and C. Cowan, using nuclear reactors, the most powerful neutrino sources available. They used a tank filled with a solution of $CdCl_2$ and water surrounded by liquid scintillator counters. They detected the inverse-beta-decay reaction by looking for a coincidence of the photon signal associated with the positron annihilation and the neutron capture reaction a few μs later. A first attempt using 300 l of liquid scintillator led to a small excess of events consistent with the prediction of the neutrino interactions, but with signal-to-background ratio of just 0.2 [5]. They repeated the experiment with a larger detector containing 4200 l of liquid scintillator and improving the shielding against the background. The detector was placed at the Savanah River reactor, and after 900 hours of data taking with the reactor in operation and 250 hours with the reactor off to estimate the backgrounds, they were able to prove the detection of the neutrinos for the first time [6]. They obtained a cross-section measurement for the inverse-beta-decay reaction of $\sigma = (11 \pm 2.6) \times 10^{-44}\,\text{cm}^2$ in agreement with Fermi's calculation.

1.2 Neutrinos in the Standard Model

According to the Standard Model of particle physics, matter is made of a set of elementary particles called fermions that interact through three forces: electromagnetic, strong and weak interactions. Fermions have spin 1/2. They are six quarks and six leptons. Their symbol and their electric charge Q is given in Tab. 1.1. Additionally, each fermion has an associated antiparticle with an opposite electric charge. In quantum field theory, the interactions occur through the exchange of a boson. Standard Model bosons are listed in Tab. 1.2. Gluons are the mediators of the strong interaction, photons of the electromagnetic interaction, and W and Z bosons of the weak interaction. While quarks are sensitive to the three forces, charged leptons interact through the electromagnetic or the weak force, and neutrinos only interact weakly. Additionally, there is the Higgs Boson, the particle responsible for the mass generation.

The Standard Model is a gauge theory [7–9]. Theoretically, it is the result of the direct product of three groups, SU(3)$\otimes$SU(2)$\otimes$U(1), where SU(3) describes the strong

	Flavour			Q[e]
Quarks	u	c	t	+2/3
	d	s	b	-1/3
Leptons	e	μ	τ	-1
	ν_e	ν_μ	ν_τ	0

Table 1.1: Fermions in the Standard Model of particle physics.

Force	Mediator
Strong	gluon, g
Electromagnetic	photon, γ
Weak	$\mathrm{W}^{\pm}$, Z^0

Table 1.2: Bosons in the Standard Model of particle physics.

interaction, SU(2) the weak isospin and U(1) the hypercharge group.

Fermions are grouped as doublets for chiral left-handed fields Ψ_L and singlets for right-handed fields (Ψ_R). In the case of the leptons:

$$\psi_L = \begin{pmatrix} e \\ \nu_e \end{pmatrix}_L, \begin{pmatrix} \mu \\ \nu_\mu \end{pmatrix}_L, \begin{pmatrix} \tau \\ \nu_\tau \end{pmatrix}_L ; \psi_R = e_R, \mu_R, \tau_R \tag{1.2}$$

In the theory, all particles must be mass-less in order to preserve the gauge invariance. However, the Higgs mechanism also known as spontaneous symmetry breaking allows the particles to acquire mass [10]. This is done through a Yukawa coupling: to conserve the isospin invariance, the Higgs has to be combined with the fermion doublet and the singlet. Therefore in the Standard Model neutrinos remain massless because there are no right-handed ν_R singlet states.

In summary, according to the Standard Model of particle physics, there are three types of neutrinos, one for each of the three charged leptons: ν_e, ν_μ and ν_τ, with their corresponding antiparticles: $\bar{\nu}_e$, $\bar{\nu}_\mu$ and $\bar{\nu}_\tau$. Neutrinos are left-handed, and anti-neutrinos are right-handed. Since they do not have colour, electrical charge or mass, they only interact weakly by exchanging a $W^{\pm}$ boson (charge-current interaction, CC), or a Z^0 boson (neutral-current interaction, NC). Also, as mass-less particles, the neutrino flavour is conserved during propagation. However, several experiments have demonstrated neutrino mixing, indicating that the neutrinos do have mass. This is one of the first hints of physics beyond the Standard Model.

1.3 Neutrino mass

The neutrino masses can be introduced in the Standard Model by applying the mass term of the Dirac equation to neutrinos. The Dirac mass term can be written in its chiral components as

$$\mathcal{L} = m_D \bar{\psi}\psi = m_D(\bar{\psi}_L \psi_R + \bar{\psi}_R \psi_L). \tag{1.3}$$

Contrary to the Standard Model, this requires having both left and right-handed neutrinos. This also requires neutrinos being Dirac particles, which means that neutrino and antineutrino are different particles.

A different approach, considering that neutrinos and antineutrinos are the same particle, leads to the Majorana mass terms:

$$\mathcal{L} = \frac{1}{2} m_M \bar{\psi}\psi^C + h.c, \tag{1.4}$$

where m$_M$ is the Majorana mass, ψ^C is the charge conjugated, and h.c is the hermitian conjugate. This can be written also in terms of its chiral components, considering m_L and m_R the real Majorana masses:

$$\begin{aligned} \mathcal{L}^L &= \frac{1}{2} m_L \bar{\psi}_L \psi_R^C + h.c, \\ \mathcal{L}^R &= \frac{1}{2} m_R \bar{\psi}_L^C \psi_R + h.c. \end{aligned} \tag{1.5}$$

Being neutrinos Majorana particles would imply that the lepton number is not conserved.

The most general mass term is combination of 1.3 and 1.4:

$$2\mathcal{L} = (\bar{\psi}_L, \bar{\psi}_L^C) \begin{pmatrix} m_L & m_D \\ m_D & m_R \end{pmatrix} \begin{pmatrix} \psi_R^C \\ \psi_R \end{pmatrix} + h.c., \tag{1.6}$$

where ψ_L and ψ_R^C represent the known neutrino interactions (active neutrinos), and ψ_L^C and ψ_R represent the sterile neutrinos since they do not interact. The mass eigenstates are obtained diagonalizing the mass matrix. The corresponding mass eigenvalues are:

$$m_{1,2} = \frac{1}{2}\left[(m_L + m_R) \pm \sqrt{(m_L - m_R)^2 + 4m_D^2}\,\right]. \tag{1.7}$$

The case with $m_L = m_R = 0$ corresponds to the pure Dirac case. $m_D = 0$ is the pure Majorana case. The seesaw model was proposed in 1979 [11] to explain the small neutrino masses. This model considers $m_R >> m_D$ and $m_L = 0$, which provides two eigenvalues, a light mass of $m_1 = m_D^2/m_R = m_\nu$ that would correspond with the active neutrino mass, and a heavy mass, $m_2 = m_R(1 + m_D^2/m_R^2) \approx m_R$, for the sterile neutrino [12, 13]. A detailed summary of the different models to explain the neutrino masses can be found in [14].

1.3.1 Experimental neutrino mass searches

From the experimental point of view, two different approaches to studying the neutrino mass are described in this section: First, direct mass searches studying beta decays, and second, neutrino-less double-beta decay experiments. For a more comprehensive review, see for example [15].

Beta-decay experiments

If the total energy in a beta decay is well known, and the final state particles are precisely characterized, it is possible to measure directly the neutrino mass. This is the goal of the beta decay experiments that aim to measure the neutrino mass by a precision characterization of the beta decay spectrum. The original drawing from Fermi [4] in Fig. 1.1, shows the impact of the neutrino mass in the electron energy spectrum in a beta decay.

From all isotopes, tritium is the most suitable to perform neutrino mass searches, due to the simplicity of the decay ($^3H \rightarrow^3 He^+ + e^- + \bar{\nu}_e$), and the small amount of energy released in the decay, with and endpoint energy of 18.6 keV. However, due to the extraordinary challenge of such a precise measurement, currently, it is only possible to provide an upper limit. The strongest constraint to the neutrino mass using this approach has been provided by the KArlsruhe TRItium Neutrino (KATRIN) spectrometer, providing an upper limit to the neutrino mass of 1.1 eV at 90% confidence level [16].

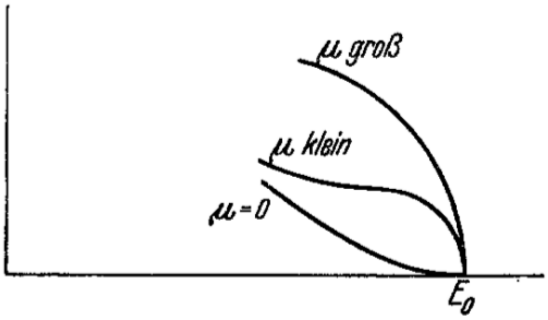

Figure 1.1: Drawing by Fermi showing the impact of the neutrino mass (μ) on the beta energy spectrum, for “large” (groß), “small” (klein) and $\mu = 0$. Large and small are defined relative to the electron mass. Taken from [4]

Neutrino-less double-beta decay experiments

The hypothesis of the neutrinos being Majorana particles, which means the neutrino and the antineutrino are identical, is a key question that concerns the nature of the neutrino mass. If a two-β-decay is observed without mediating a neutrino ($(Z,A) \rightarrow (Z+2,A)+2e^-$), where (Z,A) is a nucleus with atomic number Z and mass number A, the lepton number would be violated and the Majorana nature of the neutrino would be probed. In this way, the neutrino-less-double-beta-decay experiments aim to probe the Majorana nature of the neutrino by detecting a neutrino-less double-beta decay.

Furry [17] proposed in 1939 to perform neutrino-less double-beta decay searches to test the Majorana nature of the neutrino. The half-life time of the decay ($T^{0\nu}_{1/2}$) is given by:

$$T^{0\nu}_{1/2} = \left(G|\mathcal{M}|\langle m_{\beta\beta}\rangle^2\right)^{-1} \simeq 10^{27-28}\left(\frac{0.01eV}{\langle m_{\beta\beta}\rangle}\right)^2 y, \tag{1.8}$$

where G is the phase-space factor, $\mathcal{M}$ is the nuclear matrix element, and $\langle m_{\beta\beta}\rangle$ is the effective Majorana mass. The expected half-life of the decay is in the order of 10^{27-28} years, and therefore experiments containing a large mass are needed. Additionally, not all beta-decay isotopes are good candidates to perform neutrino-less double-beta decay searches. For practical purposes, isotopes with the forbidden or strongly suppressed beta-decay are chosen. Only 36 possible double-beta decay emitters are known. The full list can be found in [18].

Recently published results of the measurement of the half-life and Majorana mass limits using different isotopes are listed in Tab. 1.3. The strongest constraints up to date are set by KamLAND-Zen and EXO-200 using xenon, CUORE using tellurium and GERDA using germanium. For a comprehensive review of neutrino-less double-beta decay experiments, see for example [19]. While the current results stand on detectors in the size of tens to hundreds of kilograms, the next generation of detectors will increase the size of the detector by one order of magnitude, enhancing the sensitivity. A detailed description of the future plans can be found in [20].

Cosmological constraints to the neutrino mass

The Standard Model of cosmology predicts the existence of a thermal relic-neutrino background originated in the Big Bang. Additionally, precision measurements of the Cosmic Microwave Background (CMB) [32] are consistent with the existence of this background. Massive neutrinos are needed in present cosmological models, but since their masses are unknown, they are treated as a free parameter. In this way, the latest cosmological measurements constrain the sum of all neutrino masses, providing an upper

Isotope	$T^{0\nu}_{1/2}(\times 10^{25})$	$\langle m_{\beta\beta}\rangle\,(eV)$	Experiment	Reference
^{48}Ca	$> 5.8\times 10^{-3}$	$< 3.5 - 22$	ELEGANT-IV	[21]
^{76}Ge	> 18	$< 0.079 - 0.180$	GERDA	[22]
	> 2.7	$< 0.200 - 0.433$	MAJORANA DEMONSTRATOR	[23]
^{82}Se	$> 3.6\times 10^{-2}$	$< 0.89 - 2.43$	NEMO-3	[24]
^{96}Zr	$> 9.2\times 10^{-4}$	$< 7.2 - 19.5$	NEMO-3	[25]
^{100}Mo	$> 1.1\times 10^{-1}$	$< 0.33 - 0.62$	NEMO-3	[26]
^{116}Cd	$> 1.0\times 10^{-2}$	$< 1.4 - 2.5$	NEMO-3	[27]
^{130}Te	> 3.2	$< 0.075 - 0.350$	CUORE	[28]
^{136}Xe	> 10.7	$< 0.061 - 0.165$	KamLAND-Zen	[29]
	> 3.5	$< 0.093 - 0.286$	EXO-200	[30]
^{150}Nd	$> 2.0\times 10^{-3}$	$< 1.6 - 5.3$	NEMO-3	[31]

Table 1.3: Recent results for the half-life and Majorana mass limits for several neutrino-less double-beta decay experiments. The table is taken from [15].

limit. A recent analysis by WMAP provides a limit of Σm_i <0.11 eV [33]. Other analyses provide similar bounds of Σm_i <0.12 eV [32] and Σm_i <0.16 eV [34].

In the near future, the next generation of experiments (as CMB-S4 [35]) will be sensitive to $\Sigma m_i > 2\times 10^{-1}$ eV, being able to determine whether Σm_i is non zero at a three-sigma level. This measurement will be a strong confirmation of the measurements neutrino mass measurements performed using neutrino oscillations.

1.4 Neutrino oscillations

The mixing of neutrino flavours is a natural outcome of considering massive neutrinos since the neutrino flavour and mass eigenstates are not the same [36,37]. This phenomenon was first proposed by Pontecorvo in 1957 [38], and it is usually called neutrino oscillations. Neutrino flavour eigenstates (ν_α, with $\alpha = e,\mu,\tau$) can be expressed as a linear combination of the neutrino mass eigenstates (ν_i, with $i = 1,2,3$):

$$|\nu_\alpha\rangle = \sum_i U^*_{\alpha i}|\nu_i\rangle\,, \tag{1.9}$$

where U is the Pontecorvo–Maki–Nakagawa–Sakata (PMNS) matrix, and it is expressed as a 3x3 rotation matrix of angles θ_{ij}:

$$U = \begin{pmatrix} 1 & 0 & 0 \\ 0 & c_{23} & s_{23} \\ 0 & -s_{23} & c_{23} \end{pmatrix} \begin{pmatrix} c_{13} & 0 & s_{13}e^{-i\delta_{CP}} \\ 0 & 1 & 0 \\ -s_{13}e^{-i\delta_{CP}} & 0 & c_{13} \end{pmatrix} \begin{pmatrix} c_{12} & s_{12} & 0 \\ -s_{12} & c_{12} & 0 \\ 0 & 0 & 1 \end{pmatrix} \begin{pmatrix} e^{i\eta_1} & 0 & 0 \\ 0 & e^{i\eta_2} & 0 \\ 0 & 0 & 1 \end{pmatrix}, \tag{1.10}$$

with $c_{ij} = cos\theta_{ij}$ and $s_{ij} = sin\theta_{ij}$. η_1 and η_2 are the Majorana phases. The case of three Dirac neutrinos (see Sec. 1.3) would lead to a unitary PMNS matrix. δ_{CP} is a phase factor that is non-zero only if CP-symmetry is violated in neutrino oscillations.

The propagation of the mass eigenstates can be described by plane wave solutions:

$$|\nu_i(x,t)\rangle = e^{-i(E_it-\vec{p}_i\vec{x})}\,|\nu_i(0,0)\rangle\,, \tag{1.11}$$

that are approximated at the ultra-relativistic limit to:

$$|\nu_i(t)\rangle = e^{-i\frac{m_i^2L}{2E_i}}\,|\nu_i(0)\rangle\,, \tag{1.12}$$

where $L = x = ct$ is the propagation distance and m_i and E_i the mass and energy of the i-th mass eigenstate.

Although neutrinos are generated in the flavour eigenstate (ν_α), during propagation they can be expressed as a linear combination of the mass eigenstates. Therefore, the probability of observing a β-flavour neutrino that was generated in the flavour α is:

$$P(\nu_\alpha \rightarrow \nu_\beta) = |\,\langle\nu_\beta|\nu_\alpha(t)\rangle\,|^2 = \sum_{i,j} e^{-i\frac{\Delta m_{ij}^2L}{2E}}\,U^*_{\beta i}U_{\alpha i}U_{\beta j}U^*_{\alpha j}, \tag{1.13}$$

where $\Delta m_{ij}^2 = m_i^2 - m_j^2$ and the factor $\Delta m_{ij}^2L/2E$ determines the sensitivity of the experiment to the different parameters. The oscillation probability for antineutrinos can be obtained by assuming that the neutrino interaction respects CPT [39,40]. By separating the real and imaginary parts of the mixing matrix, for neutrino (ν_α) and antineutrino ($\bar{\nu}_\alpha$) oscillations, equation 1.13 can be written as:

$$\begin{aligned} P(\overset{(-)}{\nu}_\alpha \rightarrow \overset{(-)}{\nu}_\beta) = \delta_{\alpha\beta} - 4\sum_{j>i}\mathrm{Re}\left[U_{\alpha i}U_{\alpha j}U_{\beta i}U_{\beta j}\sin^2\left(\frac{\Delta m_{ij}^2L}{4E}\right)\right] \\ \overset{+}{(-)}2\sum_{j>i}\mathrm{Im}\left[[U_{\alpha i}U^*_{\alpha j}U^*_{\beta i}U_{\beta j}\sin\left(2\frac{\Delta m_{ij}^2L}{4E}\right)\right]. \end{aligned} \tag{1.14}$$

From equation 1.14 it is clear that if the mixing matrix U is complex,$P(\nu_\alpha \rightarrow \nu_\beta)$ and $P(\bar{\nu}_\alpha \rightarrow \bar{\nu}_\beta)$ would not be identical. As they are CP conjugated processes, measuring a different oscillation probability for neutrinos and antineutrinos would be the evidence of CP violation.

Historically, the results of the neutrino oscillation experiments were interpreted assuming only two neutrino states and no CP violation. This is a valid approximation at the precision level of the measurements due to the large difference between Δm_{21}^2 and Δm_{31}^2. Considering this, Eq. 1.13 can be simplified to the form:

$$P(\nu_\alpha \rightarrow \nu_\beta) = \delta_{\alpha\beta} - (2\delta_{\alpha\beta} - 1)\sin^2 2\theta \sin^2\frac{\Delta m^2L}{4E}. \tag{1.15}$$

Note that in the previous equation, the sinus squared masks the sign of the Δm^2. This is why neutrino oscillation experiments in principle are not sensitive to the sign of Δm^2, and they can only provide the absolute value. In summary, neutrino oscillation happens because the neutrino mass eigenstates are distinct from the flavour eigenstates (non-zero diagonal terms in U), and there is at least one non-zero neutrino mass. Neutrino oscillation is the first sign of physics beyond the standard model.

1.4.1 Matter effects in neutrino oscillations

The propagation of neutrinos usually happens not in vacuum but through matter, either the Sun or the Earth depending on the experiment. During propagation, neutrinos interact with the matter along the path. While the Charged Current (CC) interaction affects only electron neutrinos and antineutrinos (ν_e and $\bar{\nu}_e$), the Neutral Current (NC) interaction affects equally all neutrino flavours. The potential energy for both interactions is given by the equations:

$$V_{CC} = \pm\sqrt{2}\, G_F N_e \text{ and } V_{NC} = \mp\frac{\sqrt{2}}{2} G_F N_n, \tag{1.16}$$

where G_F is the Fermi coupling constant, N_e number of electrons and N_n the number of neutrons per unit volume. The first sign stands for the neutrinos, and the second for the antineutrinos. It is important to remark that according to the Standard Model, the NC and CC interactions do not change the neutrino flavour. Therefore it is still possible to measure neutrino oscillations even when they propagate through matter.

A detailed calculation of the oscillation probabilities through matter can be found in [41,42].

In the case of the two neutrino states, the muon neutrino (ν_μ) appearance probability in an electron neutrino beam (ν_e) propagating through matter is given by:

$$P_M(\nu_e \to \nu_\mu) = \sin^2 2\theta^M \sin^2(\Delta m_M^2 \frac{L}{4E}), \tag{1.17}$$

which is the same as the probability in vacuum given by Eq. 1.15, but considering the effective θ^M and Δ_M^2 defined as:

$$\begin{aligned} \sin^2 2\theta^M &\equiv \frac{\sin^2 2\theta_{12}}{\sin^2 2\theta_{12} + (\cos 2\theta_{12} - A)^2} \\ \Delta m_M^2 &\equiv \Delta m^2 \sqrt{\sin^2 2\theta + (\cos 2\theta - A)^2} \\ A &\equiv \frac{2\sqrt{2}\, G_F N_e E}{\Delta m^2}. \end{aligned} \tag{1.18}$$

Matter plays a critical role in neutrino oscillations: A decreasing density of matter can enhance the neutrino mixing as it was later demonstrated experimentally. This is known as the Mikheyev-Smirnov-Wolfenstein (MSW) [43–46] effect. Also, from the previous equations it is clear that there is a resonance if $\cos 2\theta \simeq A$ that would enhance largely the flavour transition, even if the mixing angle is small [41]. This reveals the importance of the matter effects in neutrino oscillations.

An important consequence of the matter effects is that it allows measuring the sign of Δm^2_{21}. In this way, the matter effects produced by the Sun have allowed solar neutrino oscillation experiments to determine the sign of Δm^2_{21}, while it remains unknown for Δm^2_{32}.

Finally, the case of the muon neutrinos (antineutrinos) propagating through matter is important for accelerator neutrino experiments. The electron neutrino (antineutrino) appearance probability is given by [47]:

$$
\begin{aligned}
P(\overset{(-)}{\nu}_\mu \to \overset{(-)}{\nu}_e) \simeq\, & sin^2\theta_{23} sin^2 2\theta_{13} \frac{sin^2(\Delta_{31} - aL)}{(\Delta_{31} - aL)^2} \Delta_{31}^2 \\
& + sin 2\theta_{23} sin 2\theta_{13} \frac{sin(\Delta_{31} - aL)}{\Delta_{31} - aL} \Delta_{31} \frac{sin(aL)}{aL} \Delta_{21} cos(\Delta_{31} \pm \delta_{CP}) \\
& + cos^2\theta_{23} sin^2\theta_{12} \frac{sin^2(aL)}{(aL)^2} \Delta_{21}^2
\end{aligned}
\tag{1.19}
$$

where $\Delta_{ij} = \Delta m^2_{ij} L/4E_\nu$, $a = \pm G_F N_e/\sqrt{2}$, G_F is the Fermi constant, N_e in the number density of electrons in the Earth, L is the baseline in km, E_ν is the neutrino energy in GeV. Both a and δ_{CP} are positive for $\nu_\mu \to \nu_e$ and negative for $\bar{\nu}_\mu \to \bar{\nu}_e$, *i.e.* the neutrino antineutrino asymmetry in oscillations through matter is introduced by both, the matter effect and δ_{CP}.

1.4.2 Measurement of the neutrino oscillation parameters

The determination of the neutrino oscillation parameters is a huge effort of many experiments during decades involving several detector technologies. These experiments can be classified attending to the neutrino source. Up to date the neutrino sources used in neutrino oscillation experiments are the Sun, the atmosphere, nuclear reactors and accelerators.

The neutrino source energy and the neutrino propagation distance determines the sensitivity to the oscillation parameters, as it is shown in Eq. 1.15, where the oscillation frequency depends on the energy of the neutrino (E), the propagation distance (L) and Δm^2. In the case of the solar and atmospheric neutrinos, the neutrino energy and the range of propagation distances are naturally fixed. However, experiments using reactors or accelerators as neutrino sources can optimize detector placement in order to enhance the experiment sensitivity. Table 1.4 shows the contribution of the different types of experiments to the determination of the oscillation parameters.

Experiment	Dominant	Important
Solar	θ_{12}	$\Delta m^2_{21}, \theta_{13}$
Reactor LBL	$\lvert\Delta m^2_{21}\rvert$	θ_{12}, θ_{13}
Reactor MBL	$\theta_{13}, \lvert\Delta m^2_{31,32}\rvert$	
Atmospherics	$\theta_{23}, \lvert\Delta m^2_{31,32}\rvert, \theta_{13}, \delta_{CP}$	
Accel. LBL $\nu_\mu, \bar{\nu}_\mu$, disappearance	$\lvert\Delta m^2_{31,32}\rvert, \theta_{23}$	
Accel. LBL $\nu_e, \bar{\nu}_e$, appearance	δ_{CP}	θ_{13}, θ_{23}

Table 1.4: Contribution of the different type of experiments to the determination of the oscillation parameters. Taken from [42].

Solar neutrino experiments

The Sun produces electron neutrinos from the thermonuclear reactions in the energy range of $0.1-20$ MeV. Bahcall and his collaborators developed the Standard Solar Model (SSM) [48, 49] which provides the solar neutrino flux on Earth. According to the SSM, four nuclear reactions are the main contributors to the neutrino flux. The flux spectrum of the different reactions is shown in Fig. 1.2.

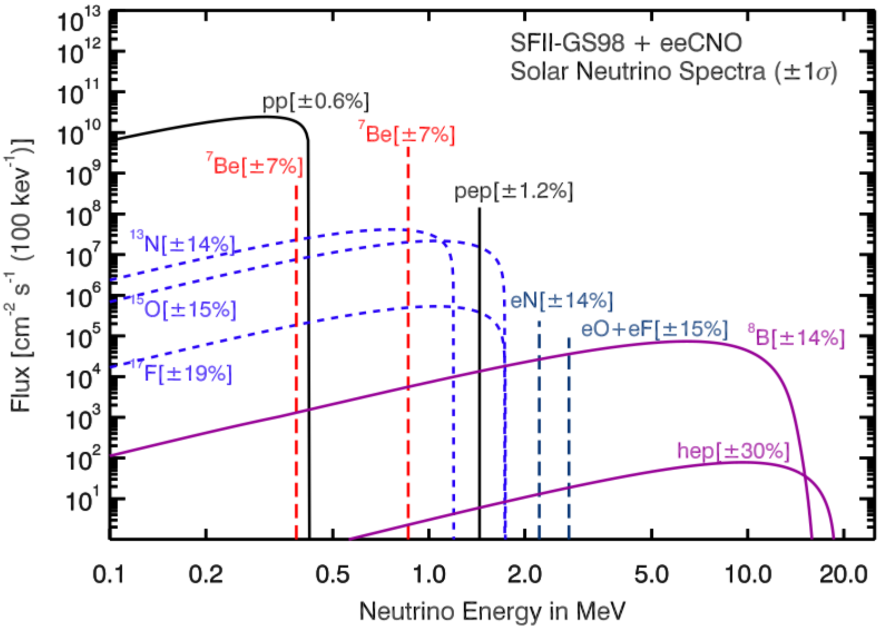

Figure 1.2: Spectrum of solar neutrino fluxes as predicted by SSM [50]. Taken from [51]

The Homestake experiment led by R. Davies, which run from 1970 to 1994, was the first to detect solar neutrinos, receiving the Nobel prize in 2002 for his pioneering work.

Using a tank of dry-cleaning fluid rich in chlorine, they were able to count the number of neutrino capture reactions:

$$\nu_e +^{37} Cl \to e^- +^{37} Ar^+. \tag{1.20}$$

By collecting the argon atoms and detecting their decay, they were able to count the number of interacting neutrinos. With an energy threshold of 814 keV, the most relevant contribution were the ^{7}Be, ^{8}B and pep neutrinos (see Fig. 1.2). However, the number of measured events did not correspond to the predictions. They measured a rate of 2.56 ± 0.16 SNU [52], where SNU (solar neutrino unit) is a unit of event rate, 1 SN $= 10^{-36}$captures/(s atom), in opposition with the prediction of 8.46 SNU based on the SSM [53]. This was the origin of the so-called *solar neutrino problem.* Later on, a new generation of experiments using gallium as the detection technique ($\nu_e +^{71}$ Ga $\to$ $e^- +^{71}$Ge), with a lower energy threshold of 233 keV, was sensitive to the dominant reaction (pp, see Fig. 1.2). GALLEX (and its successor GNO) [54–56] and SAGE [57, 58] confirmed a deficit of around 1/2.

Kamiokande [59], a 3,000-t water-Cherenkov detector placed in Kamioka mine (Japan), achieved an energy threshold of 6.5 MeV, sufficiently low to detect ^{8}B solar neutrinos undergoing elastic scattering ($\nu_x + e^- \to \nu_x + e^-$). As an advantage, this technology is sensitive to the three neutrino flavours, and also the directionality of the Cherenkov radiation allows to separate the background events. However, again a deficit of ∼1/2 was measured by Kamiokande [60, 61] and its successor Super-Kamiokande [62, 63].

The solution to the solar neutrino problem was given by the SNO experiment in Canada [64]. SNO used 1,000 t of heavy water (D_2O) as a target, surrounded by a water (H_2O) shield. An array of PMTs detected the Cherenkov radiation. However, in addition to the elastic scattering, SNO was also sensitive to the charged current interactions by electron neutrinos ($\nu_e + d \to e^- + p + p$) and neutral current interactions ($\nu_x + d \to \nu_x + p + n$) by all active neutrino flavours with equal cross-sections. Finally, SNO had all the pieces to solve the puzzle. Together with the reactor neutrino experiment KamLAND (see Sec. 1.4.2), they determined that the solution to the neutrino problem was a flavour transition with a Large Mixing Angle (MSW-LMA solution) with parameters $\Delta m^2_{21} = 7.5 \times 10^{-5}$eV^2 and $\sin^2\theta_{12} \sim 0.3$. This contribution was recognized with a Nobel prize shared with Super-Kamiokande in 2015.

The Borexino experiment at Gran Sasso, a 300 t ultra-pure liquid scintillator experiment, with a very low energy threshold of 0.19 MeV and a 5% energy resolution, was able to measure the fluxes of ^{7}Be [65], pep [66], pp [67] together with ^{8}B [68] neutrinos. The fluxes measured were consistent with the SSM and the MSW-LMA solution.

Atmospheric neutrino experiments

Cosmic rays interact with the nucleons in the atmosphere, producing kaons and pions that decay producing atmospheric neutrinos (through $\pi^+ \rightarrow \mu^+ + \nu_\mu$ and $\mu + \rightarrow e^+ \nu_e \bar{\nu}_\mu$). They have a large energy range, from 0.1 GeV to several TeV, and the travel distance is in the range of $\sim$10 km (if they are detected from above) to 1.3×10^4m (as the zenit angle increases if they traverse the Earth). The ratio $(\nu_\mu + \bar{\nu}_\mu)/(\nu_e + \bar{\nu}_e)$ is expected to be around 2 at low energies ($\sim$ 1 GeV).

The experiments detecting atmospheric neutrinos are Kamiokande [69], its successor Super-Kamiokande [70] and IMB [71] using water Cherenkov detectors and Frejus [72] and NUSEX [73] using iron tracking calorimeters. Kamiokande and IMB first reported a deficit in the $\nu_\mu + \bar{\nu}_\mu$ flux, which was not seen by Frejus and NUSEX. Later Kamiokande showed that the deficit depends on the zenith angle, and thus the travel distance, pointing to neutrino oscillations of ν_μ to a third flavour, ν_τ. Super-Kamiokande confirmed this, providing the oscillation parameters of $\Delta m_{32} \sim 2.5 \times 10^{-3}\text{eV}^2$ and $\theta_{23} \sim 45^\circ$. This contribution was recognized with a Nobel prize shared with SNO in 2015. Later on, Super-Kamiokande [74] and IceCube [75] reported also ν_τ appearance using atmospheric neutrinos.

Accelerator neutrino experiments

Neutrinos can be produced in accelerators by colliding high energy protons into a target. Colliding protons produce pions and kaons that then decay into neutrinos. The most abundant flavour in a neutrino beam is ν_μ or $\bar{\nu}_\mu$, although there is always a contamination of ν_e and $\bar{\nu}_e$. More details about neutrino beams can be found in [76].

Accelerator experiments must tune the ratio of the propagation distance and the neutrino energy (L/E), in order to increase the sensitivity to the studied oscillation. In general, there are Long Baseline (LBL) and Short Baseline (SBL) experiments. While LBL experiments use $\sim$ GeV neutrino beams and a baseline of 10^{3-4} m, SBL experiments, with a baseline of $\sim$ 1 km, are able to study neutrino oscillations at the 1 eV scale.

A list of the past and present LBL experiments is shown in Tab. 1.5. K2K experiment was the first LBL experiment, sending a 1.3 GeV neutrino beam towards Super-Kamiokande at a baseline of 250 km [77]. K2K confirmed for the first time using a neutrino beam, the muon neutrino disappearance initially reported by Super-Kamiokande [78]. Using iron-scintillator tracking calorimeters as detection technology, and combining accelerator and atmospheric neutrino data, MINOS measured the oscillation parameters in both appearance and disappearance modes [79, 80], by detecting the neutrinos from the NuMI beamline at Fermilab [81]. MINOS+ reported the dependence of the ν_μ disappearance with the energy. ICARUS [82] and OPERA [83] detected a high energy neutrino beam from CERN with a baseline of 732 km. OPERA reported the ν_τ appearance and confirmed the $\nu_\mu \to \nu_\tau$ oscillation [83].

Name	Beamline	Far Detector	L (km)	E_ν (GeV)
K2K	KEK-PS	Water Cherenkov	250	1.3
MINOS	NuMI	Iron-scintillator	735	3
MINOS+	NuMI	Iron-scintillator	735	7
OPERA	CNGS	Emulsion	730	17
ICARUS	CNGS	Liquid argon TPC	730	17
T2K	J-PARC	Water Cherenkov	295	0.6
NOνA	NuMI	Liquid scintillator tracking carlorimeter	810	2

Table 1.5: List of long-baseline (LBL) neutrino oscillation experiments. Taken from [42].

T2K started its operation in 2010, using a high-intensity beam at J-PARC and Super-Kamiokande as far detector. The detector is 2.5° offline, to set the maximum of the neutrino energy beam at 0.6 GeV, matching the first maximum of oscillation at the baseline of 295 km. T2K measured the ν_e appearance for the first time, confirming the $\nu_\mu \to \nu_e$ oscillations [84, 85]. The NOνA experiment, which is also placed off-axis, confirmed the ν_e appearance [86, 87], reported for the first time the $\bar{\nu}_e$ appearance from a $\bar{\nu}_\mu$ beam [88], and measured δm^2_{32} and θ_{23}.

In the near future, two new long-baseline oscillation experiments are expected to operate. DUNE (that will be detailed in chapter 3), and Hyper-Kamiokande as the successor of Super-Kamiokande, a water Cherenkov detector of 260 kt of total mass.

In the SBL experiments, the detector is placed near the neutrino source. LSND used 167 t of diluted liquid scintillator to perform $\bar{\nu}_\mu \to \bar{\nu}_e$ appearance searches. They reported an excess of events [89] while KARMEN 2, a segmented liquid scintillation calorimeter found no signal of $\bar{\nu}_\mu \to \bar{\nu}_e$ oscillations [90]. Later, the MiniBooNE experiment reported an excess in the ν_e and $\bar{\nu}_e$ appearance in the same region of LSND [91].

In the future, the JSNS [92] at J-PARC and the short-baseline neutrino (SBN) program at Fermilab will investigate the excess reported by LSND and MiniBooNE [93]. The SBN program will consist of three liquid argon time projection chambers at different baselines: SBND at 110 m, MicroBooNE at 470 m and ICARUS (after being transported from Europe) at 600 m.

Reactor antineutrino experiments

Nuclear reactors are powerful sources of antineutrinos and they played a key role in the neutrino experiments, starting by the discovery of the neutrino by Reines and Cowan (see Sec. 1.1). The flux of neutrinos produced by the fission reactions can be estimated considering the thermal power of the reactor and the fuel composition. Tipically, a 1 GW reactor emits around 2×10^{20} $\bar{\nu}_e$'s per second.

Reactor experiments search for $\bar{\nu}_e$ disappearance through the inverse-beta-decay reaction ($\bar{\nu}_e + p \rightarrow e^+ + n$). The events are identified by correlating the fast signal of the e^+ with the γ rays emitted by the neutron capture. They typically use liquid scintillator that is usually doped with gadolinium in order to increase the neutron capture cross-section and the energy of the γ released (8 MeV for the neutron capture by gadolinium versus 2.2 MeV by hydrogen).

In the 1900's CHOOZ [94] and Palo Verde [95] set a first limit on θ_{13}. KamLAND, with a detector of 1,000 t of ultra-pure liquid scintillator [96], and an average baseline of 180 km, reported the evidence of reactor $\bar{\nu}_e$ disappearance, confirming the mixing angle provided by solar neutrino experiments. However, while the mixing angle is consistent, there is a tension between the solar data and KamLAND concerning the value of Δm^2_{21}.

Later, a new generation of reactor experiments, Double Chooz [97], Daya Bay [98] and RENO [99] were proposed in order to measure the last angle, θ_{13}. They all reported the $\bar{\nu}_e$ disappearance in 2012, providing a precise measurement of θ_{13} [100–102].

Finally, a last generation of reactor experiments at very short baselines (6-24 m) are searching for oscillations at the $\delta m^2 \sim 1$ eV^2 range: NEOSS [103], PROSPECT [104], DANSS [105], STEREO [106], NEUTRINO-4 [107] and SoLid [108].

Current knowledge of neutrino oscillation parameters

Although most neutrino oscillation experiment results can be explained with the two flavour paradigm individually, a three-flavour model is needed to explain all results. Table 1.6 shows the current knowledge of the neutrino oscillation parameters obtained from a global analysis of data from different experiments. Since the sign of Δm^2_{32} remains unknown, two orderings are possible: Normal Ordering, being m_1 the lightest neutrino mass ($m_1 < m_2 < m_3$), and Inverted Ordering ($m_3 < m_1 < m_2$), being m_3 the lightest neutrino mass eigenstate. For this reason, two sets of values are given in Tab. 1.6, for both possible orderings.

The better known parameters are θ_{12}, θ_{13}, Δm^2_{21} and $|\Delta m^2_{32}|$. As detailed in the previous section, θ_{12} and Δm^2_{21} are well-characterized with a precission of 2% and 3% thanks to the study of solar (SNO [109]) and reactor neutrinos (KamLAND [29]). θ_{23} and $|\Delta m^2_{32}|$ are measured in accelerator experiments with a precision of 3% and 1%, by measuring the disappearance of ν_μ and $\bar{\nu}_\mu$ (T2K [110], MINOS [80], NOνA [86]), or in atmospheric neutrino experiments (SuperKamiokande [74]). θ_{13} has been measured with a precision of

	Normal ordering		Inverted ordering	
	best fit$\pm1\sigma$	3σ range	best fit$\pm1\sigma$	3σ range
$\theta_{12}/^\circ$	$33.82^{+0.78}_{-0.76}$	$31.61 \to 36.27$	$33.82^{+0.78}_{-0.76}$	$31.61 \to 36.27$
$\theta_{23}/^\circ$	$48.3^{+1.2}_{-1.9}$	$40.8 \to 51.3$	$48.6^{+1.1}_{-1.5}$	$41.0 \to 51.5$
$\theta_{13}/^\circ$	$8.61^{+0.13}_{-0.13}$	$8.22 \to 8.99$	$8.65^{+0.13}_{0.12}$	$8.26 \to 9.02$
$\delta_{CP}/^\circ$	222^{+38}_{-28}	$141 \to 370$	285^{+24}_{-26}	$205 \to 354$
$\frac{\Delta m^2_{21}}{10^{-5}\text{eV}^2}$	$7.39^{+0.21}_{-0.20}$	$6.79 \to 8.01$	$7.39^{+0.21}_{-0.2}$	$6.79 \to 8.01$
$\frac{\Delta m^2_{32}}{10^{-3}\text{eV}^2}$	$+2.449^{+0.032}_{-0.030}$	$+2.358 \to +2.544$	$-2.509^{+0.032}_{-0.032}$	$-2.603 \to -2.416$

Table 1.6: Current knowledge of the 3ν neutrino oscillation parameters. Taken from [42].

1.5% in reactor (DoubleCHOOZ [100], RENO [102], Daya Bay [101]) and accelerator experiments (T2K [111]).

However, as well as the mass ordering, the octant of the θ_{23} has not been determined yet (whether it is greater or smaller than 45°), and the CP violation phase has been poorly constrained [112, 113]. This will be detailed in Sec. 1.5.

1.5 Open questions in neutrino oscillations

Neutrino mass ordering

Neutrino oscillations are only sensitive to the sign of Δm^2_{ij} through matter effects (see Sec. 1.4.1). In this way, while the matter effects in the Sun have provided the sign for Δm^2_{21}, the sign Δm^2_{32} remains unknown, since it has been only measured via neutrino oscillations in vacuum. Therefore, there are two possibilities for the ordering of the neutrino masses: either it is normal ($m_1 < m_2 < m_3$) or inverted ($m_3 < m_1 < m_2$). Both situations are illustrated in Fig. 1.3. Unveiling the neutrino mass ordering is crucial for a deep understanding of the flavour physics.

Long-baseline oscillation experiments have the potential to determine the neutrino mass ordering thanks to the matter effects, as the beam is sent underground through the Earth. As it can be appreciated in Eq. 1.19, the oscillation probability is sensitive to the sign of Δm^2_{32}. Indeed, the next generation of neutrino oscillation experiments aim to determine the order of the neutrino masses, and specially, HyperKamiokande [115] and DUNE [116–119], have among their goals to determine the neutrino mass ordering. Since the baseline of 300 km of HyperKamiokande is too short to be sensitive to matter effects they will use the atmospheric neutrinos instead. DUNE, with a longer baseline of 1,300 km will determine the mass ordering regardless δ_{CP} with a precision of 5σ after two years of operation with the nominal design [120] (see Sec. 3.1). Finally, the future neutrino

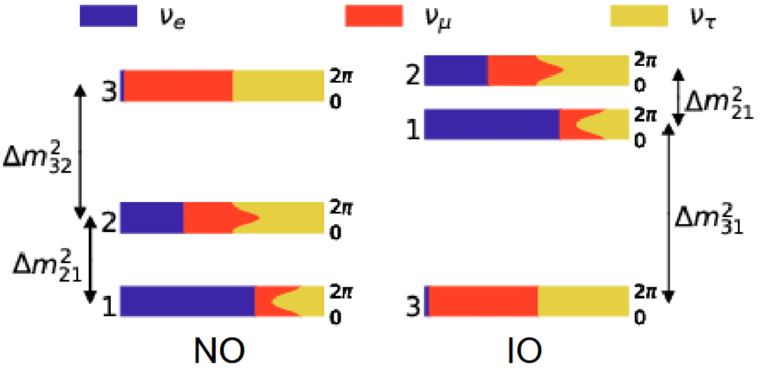

Figure 1.3: Normal (left) and inverted (right) neutrino mass orderings. The bar colour indicates the flavour content of the *i*-th mass eigen-state as the δ_{CP} phase varies from 0 (bottom of the bar) to 2π (top of the bar). Taken from [114].

telescopes KM3NET-ORCA [121] and ICECUBE-PINGU [122] also have among their goals to determine the neutrino mass ordering.

Additionally, both beta decay and neutrino-less double-beta decay experiments (see Sec. 1.3.1) have the potential to determine the neutrino mass ordering, as they are sensitive to the absolute scale of the neutrino masses. Figure 1.4 shows the dependence of the neutrino mass observable for both, beta decay (left) and neutrino-less double-beta decay (right) experiments with the lightest neutrino mass. Sensitivities of 10^{-2} eV are needed in order to resolve the mass ordering, which have not been reached yet (See Sec. 1.3.1).

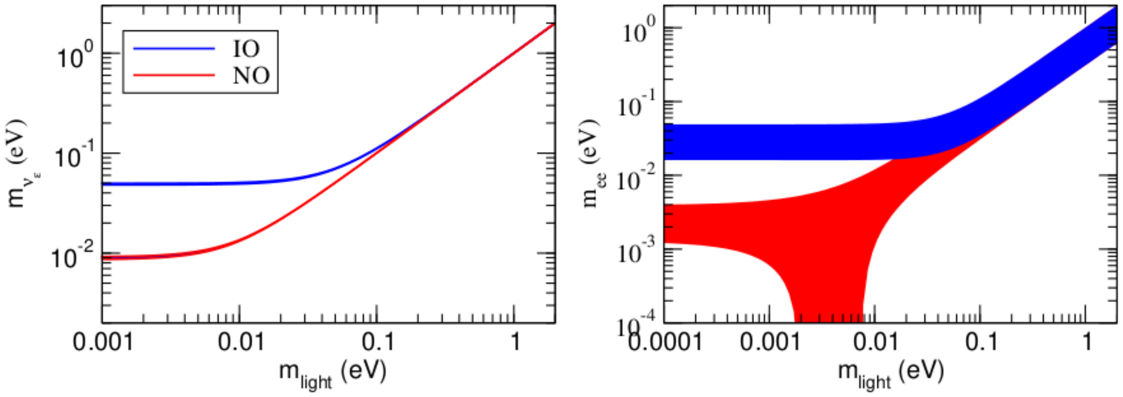

Figure 1.4: Allowed regions at 95% CL ranges for the neutrino mass observable determined in tritium beta decay (left panel) and in neutrino-less double-beta decay (right panel) as a function of the lightest neutrino mass. Taken from [42].

CP violation

CP violation implies that the charge (C) and parity (P) conjugation symmetry is not respected. CP violation has been already observed in the quark sector (in kaons and B mesons), but not in leptons. The observation of CP violation in neutrinos would be an important step in understanding the origin of the baryon asymmetry of the universe.

The possibility of CP violation is introduced in the neutrino oscillation formalism through the δ_{CP} phase (see Sec. 1.4). If $\delta_{CP} \neq 0, \pi$, then $P(\nu_\alpha \to \nu_\beta) \neq P(\bar{\nu}_\alpha \to \bar{\nu}_\beta)$. In this way, by measuring the oscillation differences between neutrinos and antineutrinos, the CP violation phase can be determined. However, as it is seen in Eq. 1.19, not only δ_{CP} introduces an asymmetry between neutrinos and antineutrinos, but also the matter effect determined by the parameter a, which is positive for neutrinos and negative for antineutrinos. Therefore, the matter effect reduces the sensitivity to δ_{CP}.

T2K and NOνA are the current long-baseline experiments pursuing to measure δ_{CP}, being T2K the first experiment constraining the CP violation phase in a range at three-sigma confidence level interval of [-3.41,-0.03] for the normal mass ordering case and [-2.54,-0.32] for the inverse ordering case [112]. In comparison, NOνA constrains the CP-violating phase excluding the region around $\delta_{CP} = \pi/2$ for the inverted mass ordering, in agreement with T2K, and excluding the region around $\delta_{CP} = -\pi/2$ in the normal ordering, in tension with T2K data [123]. This tension is due to the more pronounced asymmetry of ν_e versus $\bar{\nu}_e$ oscillations measured by T2K in comparison with NOνA [123].

DUNE and HyperKamiokande have among their primary goals the measurement of δ_{CP}. In this case, as the matter effect reduces δ_{CP} sensitivity, HyperKamiokande, with a shorter baseline would be in principle more sensitive to the δ_{CP}. However, thanks to the broad energy range of the beam that will cover two oscillation maxima, DUNE will be still competitive in the measurement of the CP-violation phase (see Sec. 3.1).

Neutrino oscillation anomalies

Regardless the success of the three-flavour oscillation paradigm to explain the plethora of neutrino experiment results, some anomalies cannot be explained with the present model.

First LSND experiment [89], reported an excess of $\bar{\nu}_e$ in $\bar{\nu}_\mu \to \bar{\nu}_e$ oscillations at 3.8σ. This was later confirmed by MiniBooNE [124] with ν_e (3.4σ) and $\bar{\nu}_e$ (2.8σ), although no excess was observed by MicroBooNE [125].

Additionally, a deficit of $\bar{\nu}_e$ was reported by radioactive source experiments, such as SAGE and GALLEX/GNO (the "gallium anomaly") [126,127], that would be confirmed by reactor neutrino experiments after new calculations of the reactor neutrino flux [128, 129] (the "reactor anomaly") [130]. However, this deficit is not consistent in all the reactor experiments (Daya Bay remains consistent with the old flux predictions), and this deficit is still under study by the community.

Nevertheless, these effects could be explained by the introduction of an oscillation to a fourth neutrino with $\Delta m^2 \sim 1\mathrm{eV}^2$, a sterile neutrino. This anomaly at short baselines has motivated the new generation of reactor (see Sec. 1.4.2) and accelerator experiments (see Sec. 1.4.2) to search oscillations in the eV^2 range.

Chapter 2

The Liquid-Argon TPC technology

A Time Projection Chamber (TPC) is a type of particle detector that allows reconstructing the trajectory of a particle in 3D. First proposed by David Nygren in the 1970s [131], it uses an active volume filled with a material to be ionized by a crossing charged particle. Ionization electrons and primary scintillation photons are produced along the track. Electrons are drifted by a uniform electric field towards an anode segmented in several channels (cables, strips or pixels) that provides a 2D picture of the interaction. If the electric field is uniform, the electron-drift velocity is constant, and the electron arrival time can be used to reconstruct the distance from the anode to the point of interaction. Additionally, the collected charge at the anode is proportional to the particle energy loss (dE/dx), which allows identifying the crossing particle and measuring its energy. Since the scintillation photons propagate much faster than the drifted electrons, the light signal is used to reconstruct the initial time of the interaction, and it also contributes to the calorimentric reconstruction. A schematic view is shown in Fig. 2.1.

Carlo Rubbia proposed scaling the TPC technology towards the multi-kiloton scale for neutrino physics using pure liquid argon as the active volume [133]. Indeed, the combination of high 3D imaging resolution and a large active volume, makes the LAr-TPC an excellent technology for neutrino physics, dark matter and proton decay searches. The advantages of using noble elements are that they do not capture electrons enabling long drift distances, and also they are transparent to their own scintillation light. The main reason for using argon and not other noble elements is that it is very abundant in nature (being the third most abundant gas in the atmosphere with a concentration of 1%), and thus, it is affordable for building large detectors.

Additionally, liquid argon has other advantages for neutrino detection: it is a dense material where the crossing particles deposit significant energy. Since the ionization

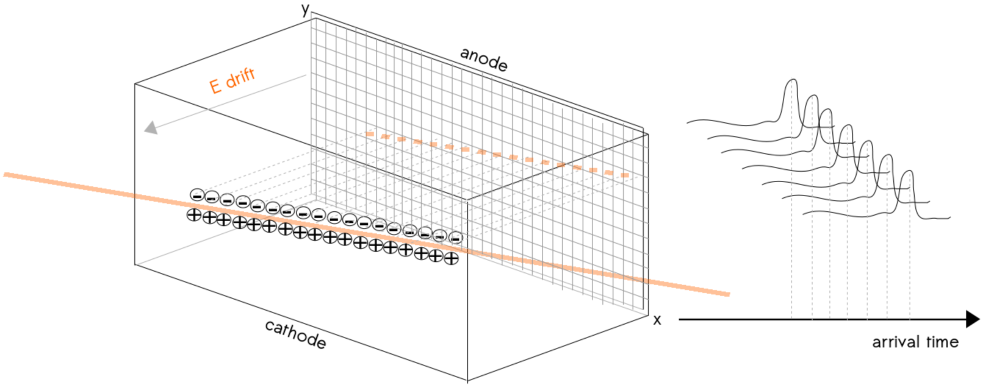

Figure 2.1: Schematic view of the working principle of a Time Projection Chamber. Figure is taken from [132]. The ionizing particle is drawn in orange, the electrons are drifted by the drift field and produce signals in the segmented anode.

electrons suffer a small diffusion, the ionization tracks can be drifted by an uniform electric field and extracted practically undistorted over long drift distances, providing excellent imaging capabilities. Ionization electrons are not attached to argon atoms but to electronegative impurities, however, with the present purification technology, it is feasible to reach high purity levels which enable reaching drift distances of the order of meters [134]. Also, the large dielectric strength of argon allows using high voltages to drift the electrons. Finally, in contrast with other techniques such as Cherenkov detectors, the energy threshold is very small since the average energy needed to create an electron-ion pair is just $\sim$24 eV [135].

2.1 Single-phase and dual-phase designs

There are two approaches to the LAr-TPC technology, the single-phase and the dual-phase designs. A schematic view of both technologies is shown in Fig. 2.2.

In the single-phase design, the electrons are drifted horizontally towards the anode, which is composed of three planes of parallel wires immersed in the liquid argon. Electrons produce a bipolar signal in the first two planes, called induction planes, and a monopolar signal in the last collection plane. While bipolar signals must be deconvoluted in order to be reconstructed, the monopolar signals are easier to reconstruct. This technology has been successfully used in many experiments. The first LAr-TPC using the single-phase design at the ton scale was ICARUS-T600 [136], and it is also the approach followed by ArgoNeuT [137], LArIAT [138], SBND [139] and MicroBoone [93].

The dual-phase design includes an argon gas layer above the liquid argon volume. In this configuration, the ionization electrons are drifted vertically towards the liquid-gas interphase. They are extracted to the gas phase and multiplied through a Townsend avalanche thanks to a large electric field. The electrons are then read out by an anode placed at the top. Then, apart from the primary scintillation light which is common in both technologies, the amplification of the electric signal produces a secondary electroluminescence light signal in the gas phase which is specific from the dual-phase configuration.

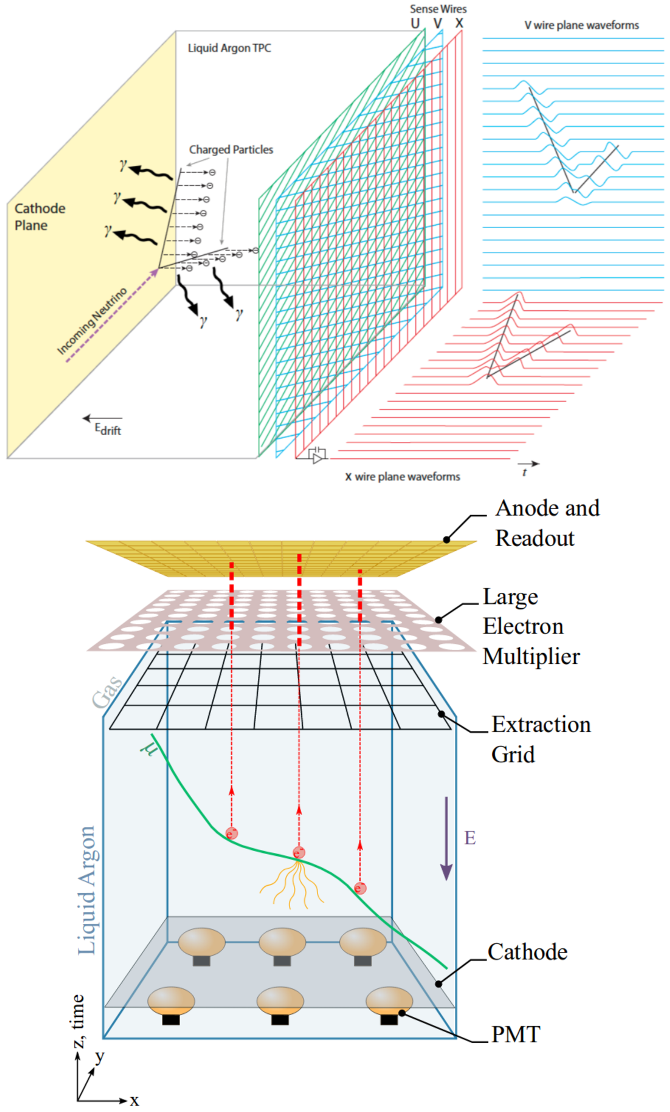

Figure 2.2: Schematic view of a single-phase (above) and a dual-phase (below) liquid-argon TPC. Taken from [116].

Since the signal readout is performed in the gas phase, the dual-phase configuration allows using large monolithic volumes without segmentation, as it is needed in a single-phase TPC. However, the electrons must drift over the full vertical length of the detector. The idea of amplifying the signal in the gas phase allows recovering the signal attenuation due to the longer drift path required in this approach. The amplification is done using special devices called Large Electron Multipliers (LEMs) [140–142]. The readout of the signal is based on two sets of electrode strips printed in a PCB. This approach allows a small strip pitch of $\sim$3 mm. In this case, both are collection views providing monopolar signals which are easier to reconstruct. The WA105 collaboration constructed a dual-phase LAr-TPC of 25 ton, the largest ever operated [143, 144]. The dual-phase approach is also used by the dark matter community as for ArDM [145] using argon, and XENON100 [146] and LUX [147] using xenon.

The amplification in the gas phase should allow the dual-phase design to reach a lower energy threshold and a better signal-to-noise ratio than the single-phase approach, making the dual-phase design a better candidate for neutrino physics, especially when a high energy resolution is desirable at low energies (in the range of a few MeV). Additionally, the monolithic design without segmentation reduces the number of channels and the overall cost of the detector. It also helps the reconstruction of large tracks that are divided into several pieces in a segmented TPC. Nevertheless, the extraction of the charge in the gas phase introduces other challenges that need to be addressed when scaling the technology towards the kiloton scale. These challenges will be explained in detail in chapter 4.

2.2 Energy deposit and electron transport in a LAr-TPC

A charged particle crossing a LAr-TPC deposits energy in the liquid argon through several mechanisms. If the particle is a Minimum Ionizing Particle (MIP) the dominant process is ionization. At higher energies, other processes become dominant such as pair-production, bremsstrahlung and photonuclear interactions. The energy deposited by a MIP, such as a cosmic muon, is 2.11 MeV/cm in liquid argon. A detailed discussion on the energy deposition mechanisms can be found in [42].

The work function W_{e^-} =23.6 eV provides the average deposited energy needed to create an electron-ion pair in liquid-argon [148]. Therefore a MIP produces an average ionization charge of $\sim$10 fC/cm in a LAr-TPC.

In absence of an electric field, the ionization electrons would recombine again with the argon ions. However, in a LAr-TPC, the drift field allows the electrons to overcome the Coulomb attraction by the argon ions, mitigating the recombination. A drift field of 0.5 kV/cm effectively suppresses the electron-ion recombination. Some models that describe the recombination process are the Onsager [149] and Box models [150]. A comprehensive study of the recombination in liquid argon can be found in [151], and will be described in more detail in Sec. 2.3.1 in the context of the light production.

Then, the ionization electrons must be drifted by an electric field towards the anode. The average drift velocity depends on the liquid argon temperature and the drift field, and it has been well characterized in several experiments [152–155]. The electron drift velocity at the nominal drift field of 0.5 kV/cm and a temperature of 87 K is v=1.6 m/ms [156]. This results in a drift time of 3.75 ms for 6 m of drift.

During the drift, electrons can scatter with the argon atoms, resulting in a diffusion of the drifted electron cloud. This diffusion is well described by the kinetic model of gasses [157]. The drift field mitigates the diffusion along the drift direction. As a result, the diffusion is larger for the direction perpendicular to the drift direction. On average the displacement of an electron due to diffusion along the drift (λ_L) and in the transverse direction (λ_T) is given by the equation:

$$\lambda_{L,T} = \sqrt{2 \times D_{L,T} \times t}\,, \tag{2.1}$$

where D_L is the diffusion constant along the drift direction, D_T in the transverse direction, and t the drift time. The values for $D_T \sim 1.4\,\mathrm{mm}^2/\mathrm{ms}$ [158, 159] and $D_L \sim 0.4 - 0.7\,\mathrm{mm}^2/\mathrm{ms}$ [156, 160] are determined experimentally. This results in a transverse diffusion of just ~3 mm in 6 m of drift.

Finally, the electron signal can be suppressed by the presence of electronegative impurities. Contaminants such as oxygen capture the electrons attenuating the charge signal. As a stochastic process, the signal attenuation responds to an exponential law:

$$R_Q = e^{-t/\tau}, \tag{2.2}$$

where R_Q is the ratio of surviving charge after a time t, and τ is the electron lifetime, which depends on the contaminants concentration. The dependence of τ with the concentration of water ($[H_2O]$) and oxygen ($[O_2]$) has been measured [155, 161] and is given by:

$$\tau \sim \frac{307}{[O_2](\mathrm{ppb})}\ \mu\mathrm{s} \ \text{ and } \tau \sim \frac{17}{[H_2O](\mathrm{ppb})}\ \mu\mathrm{s}\ . \tag{2.3}$$

.

As an example, a small amount of 100 ppb (parts-per-billion) of oxygen would reduce the electron lifetime to just 3 μs, making it impossible to extract any charge signal over a drift length in the range of meters. This makes necessary the introduction of filtration systems to maintain a high purity by removing oxygen and water contaminants from liquid argon.

2.3 Scintillation light production

Not all the energy deposited by ionizing particles goes to the production of electron-ion pairs ($\mathrm{Ar}^+ + e$). It also produces argon excitons (Ar^*) when the energy is not enough to release the electron from the Coulomb potential produced by the argon atom. Then, both argon excitons and argon ions couple with other argon atoms producing the molecular states of Ar_2^* and Ar_2^+ respectively (see Eq. 2.4).

In absence of an electric field, the Ar_2^+ molecules eventually recombine with the free electrons, producing more molecular argon excimers (Ar_2^*). However, in the presence of a drift field, like in a LAr-TPC, the ionization electrons are drifted towards the anode, suppressing most of the recombination.

$$\begin{aligned} \text{Recombination} : \mathrm{Ar}^+ + \mathrm{Ar} \rightarrow \mathrm{Ar}_2^+ + \mathrm{e}^- \rightarrow \mathrm{Ar}_2^*, \\ \text{Excitation} : \mathrm{Ar}^* + \mathrm{Ar} \rightarrow \mathrm{Ar}_2^*. \end{aligned} \tag{2.4}$$

These molecular argon excimers then decay producing scintillation light. Therefore, there are two light production paths in liquid argon: excitation and recombination. The excimers (Ar_2^*) are initially in two excited states, singlet and triplet (${}^{1,3}\Sigma_u^+$). Scintillation light in pure liquid argon is produced by radiative decay of the molecular argon excimers from the two excited states to the ground state (see Eq. 2.5). This is called, the primary scintillation light, or S1, to differentiate it from the secondary electroluminescence light, or S2, produced in the gas phase in a dual-phase TPC.

$$Ar_2^*({}^{1,3}\Sigma_u^+) \rightarrow 2Ar + \gamma_{127} \tag{2.5}$$

This radiative decay occurs with two characteristic times, a fast decay of $\tau_{\text{fast}} = 7$ ns for the singlet state (${}^1\Sigma_u^+$), and a slow decay of around $\tau_{\text{slow}} = 1.5$ µs for the triplet state (${}^3\Sigma_u^+$) [162]. Therefore, the photon production rate can be described by the sum of two exponential functions, as shown in equation. 2.6.

$$f(t) = \frac{A_{\text{fast}}}{\tau_{\text{fast}}} e^{-t/\tau_{\text{fast}}} + \frac{A_{\text{slow}}}{\tau_{\text{slow}}} e^{-t/\tau_{\text{slow}}}, \tag{2.6}$$

where A_{fast} (A_{slow}) are the total number of photons produced from the decay of excimers in the singlet (triplet) state. The ratio $\mathrm{A}_{\text{fast}}/\mathrm{A}_{\text{slow}}$ depends on the particle, and has been measured to be 0.3 for electrons and 1.3 for alpha particles [148, 162].

The production of scintillation photons is proportional to the energy deposited by the ionizing particle. The typical light yield in liquid argon is 40k photons per MeV of deposited energy in absence of a drift field [163]. At the nominal drift field of 0.5 kV/cm, this amount decreases to about 24k photons per MeV as the recombination process is reduced.

Scintillation photons in pure liquid argon have a wavelength peaking at 126.8 nm with a full width at half-maximum of 7.8 nm [164]. Scintillation photons are difficult to detect, since most photonsensors are not sensitive at this wavelength and they are easily absorbed during propagation. For this reason, wavelength-shifting techniques are employed, such as the use of fluorescence materials or xenon-doped liquid argon.

2.3.1 Dependence of the scintillation light with the electric field

As introduced in Sec. 2.2 and 2.3, the drift field allows the ionization electrons to overcome the Coulomb potential produced by the argon ions, reducing the recombination and therefore the light production. The so-called Birks' law describes the light production as a function of the drift field. It is given by the equation:

$$L(\varepsilon) = L_0 \left((1 - \frac{A}{1 + \frac{k}{\varepsilon} dE/dx} \right) \tag{2.7}$$

where L is the number of photons produced at a drift field ε, L_0 is the number of photons produced without drift field (*i.e.* full recombination of electron-ion pairs) and dE/dx the deposited energy (2.11 MeV/cm for a MIP in liquid argon). A and k are parameters obtained experimentally. The ICARUS collaboration reported a value of A=0.8 and k=0.0486 kV g MeV^{-1} cm^{-3} [151]. Since the recombination of the electrons enhances the light production but mitigate the charge signal, both are anti-correlated. The variation of the relative light production, L, and collected charge Q, with the drift field is shown in Fig. 2.3. At 6 kV, a decrease of 64% in the light production is observed [165].

2.3.2 Scintillation light quenching by impurities

The presence of contaminants in liquid argon leads to the reduction of the scintillation light production due to a quenching process driven by the two-body collision of excited argon excimers with the impurities. Nitrogen or oxygen are examples of molecules that drive this type of quenching. However, since the presence of oxygen can be mitigated with the present purification systems, the case of nitrogen is taken as a reference in this section:

$$Ar_2^*(^3\Sigma_u^+) + N_2 \to 2Ar + N_2 \tag{2.8}$$

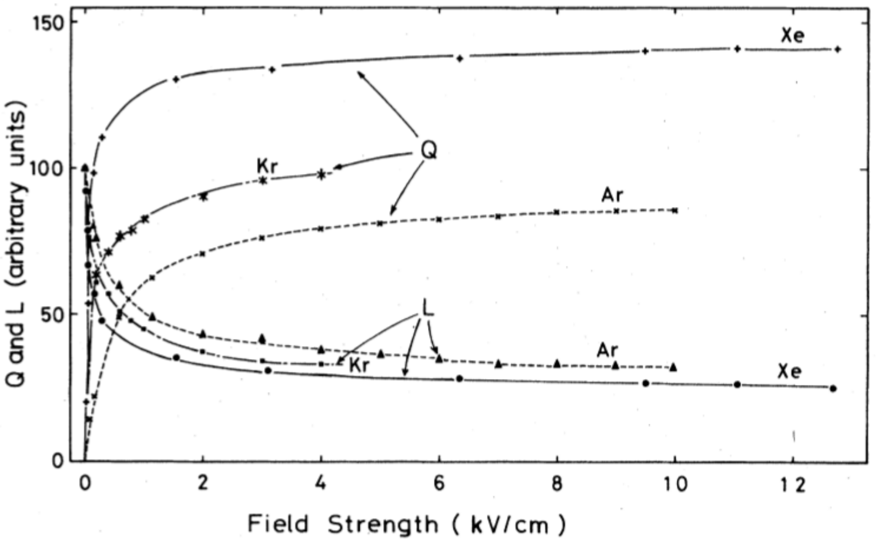

Figure 2.3: Dependence of the light production (L) and collected charge (Q) in liquid argon, krypton, and xenon with the electric field for 0.976-1.05 MeV electrons. Taken from [165].

This process reduces mainly the excimers in the triplet state since the singlet ones decay too fast to be affected at the typical impurities concentrations of a few ppm. The photon production rate, as in pure liquid argon, can be described by the sum of two exponential functions, as it is shown in equation 2.9, where the prime symbol in the number of photons produced (A'_i) and the time decays (τ'_i) indicates that they are affected by the presence of nitrogen. The dependence of these variables with the nitrogen concentration is shown in equation 2.10 for τ_i and in equation 2.11 for A_i, with $i = \{\text{Fast}, \text{Slow}\}$. k_Q is the rate constant of the quenching process and [N$_2$] is the concentration of nitrogen in ppm. The value $k_Q = 0.11 \pm 0.01$ µs $^{-1}$ppm^{-1} is provided in the literature [166]. As an example, the presence of 1 ppm of nitrogen results in a decrease of 14% in the production of scintillation photons.

$$f(x) = \frac{A'_{\text{fast}}}{\tau'_{\text{fast}}} e^{-t/\tau'_{\text{fast}}} + \frac{A'_{\text{slow}}}{\tau'_{\text{slow}}} e^{-t/\tau'_{\text{slow}}} \tag{2.9}$$

$$\frac{1}{\tau'_i} = \frac{1}{\tau_i} + k_Q[N_2] \tag{2.10}$$

$$A'_i = \frac{A_i}{1 + \tau_i k_Q [N_2]} \tag{2.11}$$

2.4 Electroluminescence light signal

The electroluminescence light signal is specific for the dual-phase LAr-TPCs. When the drifted electrons reach the liquid-gas interface, they are extracted towards the gas phase with a high electric field. This electric field is created by an extraction grid placed 5 mm below the liquid-gas interface, inside the liquid, and the LEMs placed 5 mm above the liquid-gas interface, in the gas. The extracted charge is amplified inside the LEMs by producing Townsend avalanches. Therefore the amount of photons produced is proportional to the extracted charge.

Contrary to the primary scintillation light signal, which is anti-correlated with the drifted charge, the S2 charge is proportional to the charge. The photon production mechanisms are similar as those described in liquid argon, and the wavelength is also 127 nm. The production of S2 photons per extracted electron depends on the electric field in the amplification phase [167, 168]:

$$\frac{1}{n}\frac{N_{ph}}{dx} = a\frac{E}{n} - b(\text{photons} \times cm^2/e^-) \tag{2.12}$$

where a and b are empirical constants, E is the electric field and n is the atomic density of the gas. The number of produced photons per primary electron is ∼3000 at an amplification field of 3.5 kV [169].

2.5 Scintillation light propagation

Low energy photons propagating through matter interact mainly via two mechanisms: First, photo-electric effect, in which the photon is absorbed. And second, elastic scattering (also known as Rayleigh scattering), which only changes the direction and the phase of the photon. At higher energies, there is also Compton scattering, in which part of the photon energy is transferred to the recoiling electron, or photo-nuclear interactions (see [42]).

Since the first ionization potential of argon is 15.7 eV, which is smaller than 9.7 eV of energy of a scintillation photon, there is no photo-electric effect and the dominant process is the Rayleigh scattering, being argon transparent to its own scintillation light. However, impurities in liquid argon, such as nitrogen, do contribute to photo-absorption. Also, the TPC elements, such as the field cage or the cathode absorb or reflect photons.

Therefore, scintillation photons undergo two different processes during propagation in argon: They can either elastically scatter with the argon atoms (the so-called Rayleigh scattering) or be absorbed by impurities or the TPC elements.

2.5.1 Rayleigh scattering

The Rayleigh scattering describes the interaction of a photon with a particle when the photon wavelength is much longer than the particle size [170]. As the Rayleigh scattering only changes the direction and the polarization of the photon, it does not contribute to the light attenuation *per se*, but indirectly: It increases the average photon propagation length, and this enhances the probability of the photon to be absorbed.

The Rayleigh scattering is characterized by the Rayleigh scattering length λ_{RS}, which is defined as the mean free path length of the photon before it scatters:

$$\frac{1}{\lambda_{RS}} = \frac{16\pi^3}{6\lambda^4}\left[k_B T k_T \frac{(n^2-1)(n^2+2)}{3}\right], \tag{2.13}$$

where λ is the photon wavelength, k_B is the Boltzmann's constant, T is the temperature, k_T is the isothermal compressibility, and n the refractive index at the given wavelength.

Table 2.1 summarizes some values for λ_{RS} that are found in the literature. Some measurements point to a short $\lambda_{RS} \sim 0.5\,\text{m}$ [171, 172]. However, the latest experimental measurements at CERN, estimating the group velocity of the scintillation light of cosmic muons in liquid argon, results in an estimation of $\lambda_{RS} = 99.1 \pm 2.3\,\text{cm}$ [173]. This is the value used as a reference in the studies presented in this thesis.

Source	λ_{RS}	Reference
Measurement	**99.1 ± 2.3**	[173]
	66 ± 3	[171]
	52.1 ± 10.4	[172]
Calculation	55 ± 5	[174]
	90	[175]

Table 2.1: Summary of Rayleigh scattering length values that are found in the literature

2.5.2 Absorption

The presence of impurities, like nitrogen, affect photon propagation. The nitrogen molecules absorb the photons, suppressing the light signal. The absorption is characterized by the absorption length, λ_{Abs}, which is defined as the distance at which the intensity of the signal beam has dropped to $1/e$.

The absorption length (λ_{Abs}) can be computed from the absorption cross-section, σ, from the following relation:

$$\frac{1}{\lambda_{Abs}} = \sigma * \frac{\rho N_A}{2m_a}, \tag{2.14}$$

being ρ mass density of the contaminant in g/cm^3, m_a its atomic mass and N_A the Avogadro number.

A detailed study in the photo-absorption by nitrogen on the scintillation light in liquid argon is presented in [176]. They measured a cross section of 7.1×10^{-21} which results in a dependence of the absorption length with the concentration of nitrogen contaminants ([N$_2$]) as follows:

$$\lambda_{Abs} = \frac{66.4}{[\mathrm{N_2}](\mathrm{ppmv})}\,\mathrm{m}, \tag{2.15}$$

where [N$_2$] is measured in parts-per-million in volume (ppmv). An absorption length of λ_{Abs} =20 m, which is taken as a reference in this studies corresponds to an equivalent concentration of [N$_2$]$\sim$3 ppmv.

2.6 The importance of the light signal

The primary scintillation light (S1) provides a fast signal since the scintillation photons travel at the speed of light. In comparison, the charge signal arrives at the anode several milliseconds after the particle crosses, since the electron drift time is around 1.6 m/ms. In this way, the S1 provides the initial time of the event (t_0) that can be used as a trigger for the detector to take data. Also, the t_0 allows computing the distance from the anode at which the electrons are produced, allowing a full 3D reconstruction of the event.

The scintillation light also contributes to the calorimetric reconstruction of the events in two ways. First, the number of scintillation photons is proportional to the deposited energy and thus the integral of the light signal provides a direct measurement of the energy deposited in the TPC. Second, the t_0 provided by the light signal allows improving the calorimetric measurement given by the charge signal. Since some degradation is expected in the charge signal with the drift length (due to the diffusion of the electrons and its recombination with impurities, see Sec. 2.2), by knowing the drift distance a correction can be applied, improving the energy resolution of the detector.

Finally, the light signal also helps identify the interacting particle (PID), by looking at the relation of fast and slow photons, since this depends on the nature of the particle (see Sec. 2.3).

For all these reasons, having an efficient and reliable photon detection system becomes crucial in a LAr-TPC.

2.7 Challenges of the light detection in a multi-ton LAr-TPC

Three main challenges arise when designing a photon detection system for a large liquid argon TPC. First, the scintillation light in liquid argon (for both signals S1 and S2) is produced at a wavelength of 127 nm, at which most photosensors are not sensitive. Additionally, the light must travel from the energy deposition point towards the photon detector. In the case of multi-ton detectors, this distance reaches several meters, leading to a large signal attenuation with the distance. Finally, the photon detectors must deal with the strong electric fields that are present in the detector.

A summary of some approaches to deal with these challenges is presented below. Some of them are studied in detail in the next chapters.

2.7.1 Photon detection

Large surface photo-multiplier tubes (PMTs) are reliable and well-known devices for detecting photons. However, PMTs are not efficient in detecting 127 nm photons, and they are affected by the presence of electric fields, such as the drift field in a LAr-TPC.

In order to deal with the electric field, PMTs can be placed outside the active volume. In a dual-phase LAr-TPC, they are typically placed at the bottom of the detector, below a grounded grid as a Faraday cage in order to protect them from the high voltages at the cathode.

To maximize the PMT detection efficiency wavelength shifters are introduced. A wavelength-shifter is a fluorescent material that absorbs the incident VUV photons at 127 nm and re-emit them with a longer wavelength (in the visible range). A typical detection efficiency of around 20% of the visible photons is reached by a bialkali photocathode at a wavelength of ∼400 nm. Several materials can be used, and in particular two are tested in this work, tetraphenyl butadiene (TPB) and polyethylene naphthalate (PEN) in chapter 8.

TPB has been widely used in several detectors, such as ICARUS [177], μBooNE [178] or SBND [179], and it is very efficient in converting photons, with reported efficiency values above unity (i.e. emitting more than one visible photon per incident VUV photon) [180]. TPB comes as a dust that has to be deposited with a dedicated setup [181]. This fact complicates the installation and becomes a big challenge when dealing with hundreds of PMTs for kiloton scale detectors. TPB can be deposited on a plate to be placed in front of the photo-cathode, or directly over the PMT glass. There are also proposals for diluting the TPB in the liquid argon [182].

PEN is a thermoplastic, similar to PET, whose fluorescence has been known since long time ago [183], but only on the recent time has been proposed as an alternative for liquid argon detectors [184]. Since it is a plastic, it is very easy to handle and install. This becomes a huge advantage over TPB for large detectors. However, its efficiency is not well known. The performance of PMTs with PEN foil on top is presented in this work, and compared to PMTs with TPB directly coated on the PMT glass.

A different approach has been proposed by the DUNE collaboration, designing special devices called *X-ARAPUCA*s [185–187]. They are large surface detectors, that using a dichroic filter, trap the photons and re-direct them towards silicon photo-multipliers (SiPMs). They can cover large surfaces at an affordable cost, and also they can work within electric fields in contrast to the PMTs. This is a promising approach that will tested by ProtoDUNE Single-Phase. They have reported a detection efficiency of ~3% [186] for VUV photons.

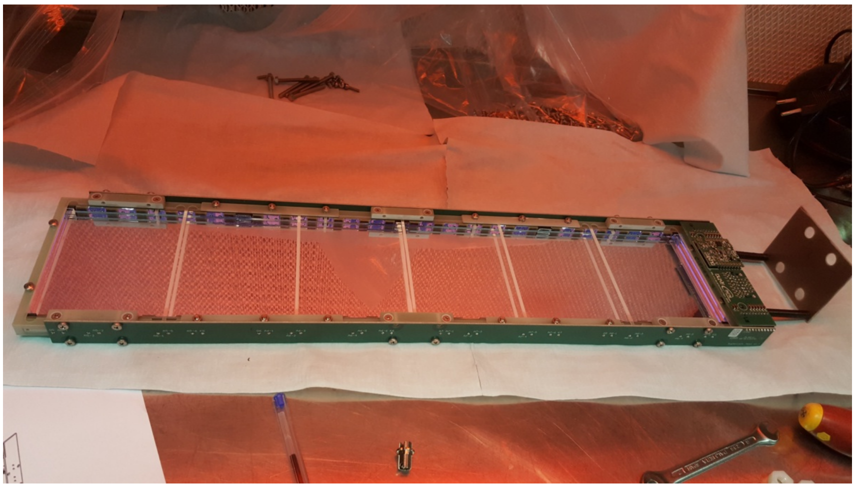

Figure 2.4: Picture of an X-ARAPUCA.

2.7.2 Non-uniformity

Since photons and ionization electrons can be absorbed by impurities during propagation, highly pure argon is required. Typically in pure liquid argon the absorption is small, with a reported value of $\lambda_{Abs} = 30\,\mathrm{m}$ at 2 ppm of N_2, and in the order of kilometres when operating with a purity below 1 ppm (see Sec. 2.5.2) [176]. Additionally, photons can elastically scatter with the argon atoms, changing the photon direction and increasing the mean propagation length, and thus, the probability to be absorbed by an impurity. This is the Rayleigh scattering (see Sec. 2.5.1) that enhances the absorption of photons by impurities.

Indeed, the measured value of $\lambda_{RS} \sim 1$ m [173] leads to a strong non-uniformity of the detected light with the distance. This means that if the photon-detectors are placed at the bottom, like typically the PMTs are in a dual-phase LAr-TPC, the particles crossing the top part of the active volume would provide a signal much smaller than those crossing below.

An approach to compensate for the non-uniformity that will be explored in this work is to place large-surface TPB-coated reflective foils in the top part of the detector, as proposed also by the SBND collaboration. These high efficient reflective foils first convert the VUV photons into the visible range and then reflect them. Apart from avoiding the absorption of the light from the rest elements inside the detector, the new photons at a longer wavelength have a much longer λ_{RS} of $\sim$ km. This improves strongly the uniformity of the detected light with the distance.

A second approach is the use of xenon-doped liquid argon instead of pure liquid argon. A small amount of xenon, in the order of 10 ppm, shifts the wavelength of the scintillation light towards a slightly longer wavelength of 175 nm. At 175 nm, the Rayleigh scattering is much smaller than for 127 nm photons, with a value of $\lambda_{RS} \sim 8$ m. In this way, the uniformity is naturally increased. The advantage of this technique over the TPB-coated reflective foils is that the wavelength shifting is done right after the light is produced and uniformly in all the active volume. A detailed study of this technique is presented in chapter 9.

Finally, another approach is segmenting the detector in smaller TPCs, and placing the *X-ARAPUCA*s within the active volume. In this way, the detection uniformity naturally improves, since the photon propagation distance is smaller due to the segmentation and the *X-ARAPUCA*s can be distributed uniformly. However, segmenting the detector brings other disadvantages, like splitting large events in several parts or the introduction of border effects that a monolithic detector would not have.

Chapter 3

The Deep Underground Neutrino Experiment

The Deep Underground Neutrino Experiment (DUNE) will be one of the most promising long-baseline neutrino experiments in the next decade. It aims to answer some of the fundamental open questions about neutrino physics. DUNE will bring the liquid-argon time projection chamber (LAr-TPC) technology to an unprecedented scale of tens of kilotons. In order to demonstrate the feasibility of the DUNE technology, the collaboration has carried out a full R&D programme at the CERN Neutrino Platform, including the assembly and operation of two LAr-TPC prototypes (ProtoDUNEs). The work presented in this thesis has been developed within the framework of the ProtoDUNE programme.

In this chapter, the DUNE experimental design is described in Sec. 3.1. The DUNE science program is introduced in Sec. 3.2. Finally, the efforts scaling the LAr-TPC technology towards the kiloton scale are summarised in Sec. 3.3

3.1 Experimental design

The Deep Underground Neutrino Experiment (DUNE) [116–119] will be a precision long-baseline neutrino oscillation experiment. It will consist of a neutrino beam and two particle detectors: A Near Detector placed downstream the neutrino source and a Far Detector placed 1.5 km underground, at 1,300 km from the beam (see Fig. 3.1).

With a power of 2.4 MW, the beam will be the most intense neutrino beam ever operated, and it will be placed at Fermilab. The Far Detector will be placed at the Sandford Underground Research Facility (SURF) in South Dakota (US). The chosen baseline of 1,300 km will ensure the sensitivity to the oscillation parameters as it will be detailed in

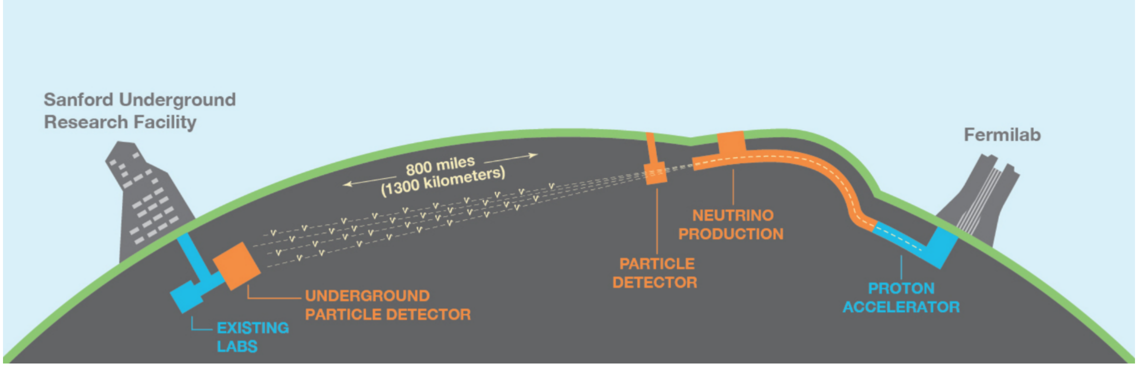

Figure 3.1: Overview of the DUNE experimental setup.

the following sections. Both Near and Far detectors will be placed on-axis the neutrino beam-line.

The Far Detector will be composed of four modules. Each module will have a total mass of 17 kton of liquid argon, and a fiducial mass of at least 10 kton, and they will be deployed gradually. The first module will be a Single-Phase LAr-TPC and the second a Vertical-Drift LAr-TPC. The design of the third and fourth modules remains open in order to profit from the lessons learnt during the construction of the first two modules.

After a prototyping phase, the excavation of the main cavern accommodating the Far Detector is ongoing now. The installation of the first module is expected to start in 2024, following a staged deployment of the rest of the modules and an upgrade of the beam intensity. Although the deployment calendar is still preliminary, the sensitivity studies presented in this section assume that the data-taking starts with two far detector modules and a beam of 1.2 MW. Third and fourth modules are added after one and three years of operation respectively. Finally, the beam is upgraded to 2.4 MW after six years of data-taking.

3.1.1 Neutrino Beam

The Long Baseline Neutrino Facilitiy (LBNF) will provide a powerful beam of neutrinos to the Near and Far Detectors. It will start operating at 1.2 MW and will be upgraded to 2.4 MW after 6 years. A linear proton accelerator will deliver 10^{21} Protons-on-target/year with an energy range from 60 to 120 GeV to a graphite target. The hadronic showers produced as a result contain mainly pions, that are focused by magnetic hornes into a decay pipe of 200 m long. Pions decay into muons and muon neutrinos in the decay pipe:

$$\pi^+ \to \mu^+ \nu_\mu \tag{3.1}$$

$$\pi^- \to \mu^- \bar{\nu}_\mu \tag{3.2}$$

By selecting positive or negative pions in the magnetic hornes, the beam will be able to run in neutrino or antineutrino mode. Muons are stopped in a shielding after the decay pipe, but some of them would decay contributing to the neutrino beam introducing other neutrino flavours and contaminating the beam. The neutrino beam will show a wide energy spectrum from 0.5 GeV to 8 GeV which will be crucial to perform precision oscillation measurements. Figure 3.2 shows the expected neutrino energy spectrum as well as the flavour composition.

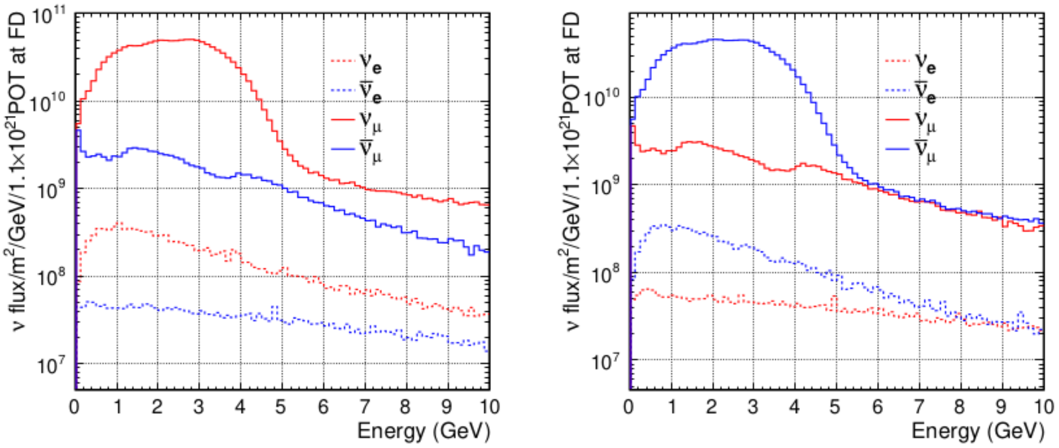

Figure 3.2: Neutrino fluxes at the Far Detector for the beam operating in neutrino mode (left) and in antineutrino mode (right). The figure is taken from [117].

3.1.2 Near Detector complex

The DUNE Near Detector measures the neutrino beam rate and spectrum near the production point, providing the initial state of the neutrinos before oscillating. The Near Detector serves as a control to constrain systematic uncertainties and provides essential input for the neutrino interaction model. The Near Detector will be located at 600 m from the neutrino beam source and will be composed in its final configuration of three detectors as shown in Fig. 3.3:

- ND-LAr is a liquid argon TPC of 67 t fiducial mass, with an active volume of 5 m x 7 m x 3 m and a pixelated readout. It measures the unoscillated neutrinos energy spectra. Since it uses the same technology as the Far Detectors, it is crucial to measure the oscillations reducing systematic uncertainties. ND-LAr will provide

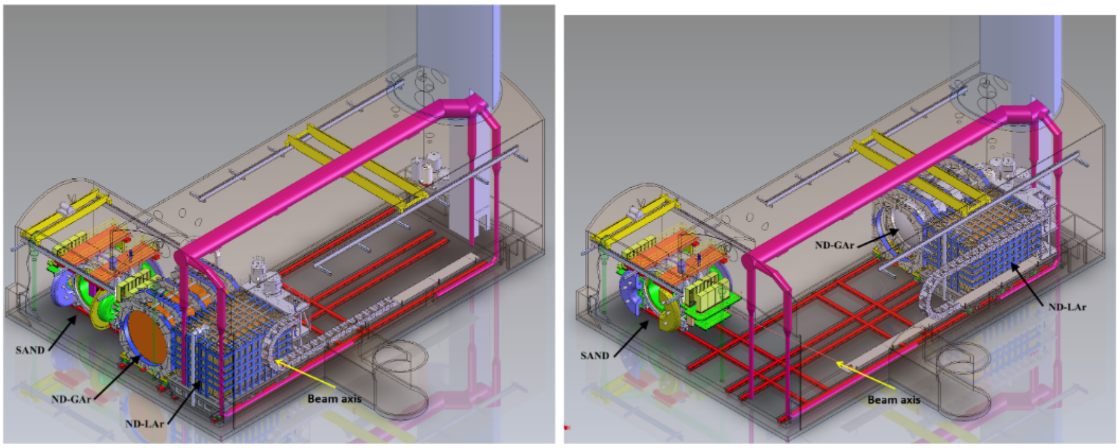

Figure 3.3: View of the DUNE Near Detector composed of three elements: SAND will be placed on-axis, and ND-GAr and ND-LAr will be movable off-axis (left to right).

high statistics ($1 \times 10^8 \nu$CC events/year) and a large volume to contain the hadronic interactions.

- ND-GAr is a high-pressure gaseous argon TPC (HPgTPC) surrounded by an electronic calorimeter in a 0.5 T magnetic field. It provides the momentum and charge of the high energy muons that are not contained within the ND-LAr volume since this measurement is critical to characterize the neutrino energy. It also has a lower energy threshold than ND-LAr and superior identification capabilities of charged pions and protons. However, in a first stage, a Temporary Muon Spectrometer (TMS) will be installed in replacement of ND-GAr, which design is based in MINOS [188] using iron interspersed with scintillator. TMS will be replaced ND-GAr in the phase II.

  ND-LAr and ND-GAr will be movable off-axis up to 33 m thanks to a rail system. This capability is referred as DUNE PRISM. Measuring the neutrino flux at different angles will allow the deconvolution of the neutrino flux and the interaction cross-section.

- The System for On-Axis Beam Monitor (SAND) is composed of 3D scintillators trackers inside a superconducting magnet at 0.6 T and an electronic calorimeter. SAND monitors the flux of neutrinos on-axis when ND-LAr and ND-GAr have moved off-axis. Since it uses a different detector technology and target than the Far Detector, it is useful for comparison and for a systematic cross-check with the neutrino flux determined by ND-LAr. Finally, the different mass numbers of the hydrocarbon target with respect to argon is useful to develop interaction models and to understand the nuclear effects. Additionally, the tracker may introduce neutrons in the event reconstruction, which would help to improve the nuclear model.

The Near Detector will have a rich physics program on its own, such as neutrino cross sections measurements, the study of nuclear effects and beyond standard model searches. A detailed description can be found in the Near Detector Conceptual Design Report [189].

3.1.3 Far Detectors

DUNE Far Detector will consist of four LAr-TPC detector modules with a fiducial mass of at least 10 kton of liquid argon each. Each detector will be placed inside a cryostat of dimensions 15 m x 14 m x 62 m containing a total mass of 17.5 kton. They will be placed 1.5 km underground at Sanford Underground Research Facility (South Dakota, US), at a distance of 13,00 km from the neutrino source (Fig 3.4).

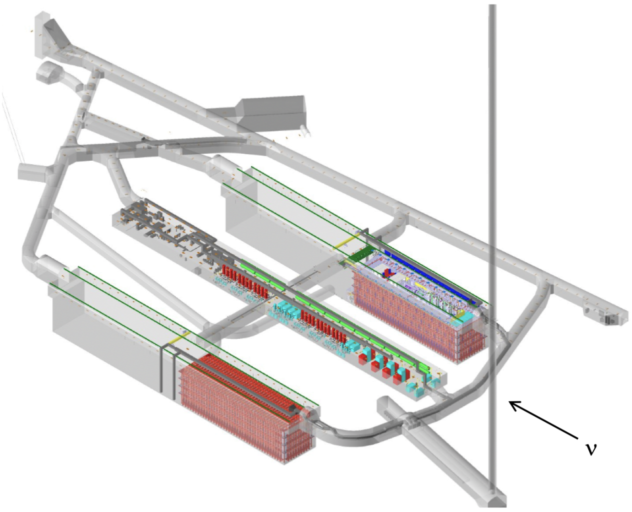

Figure 3.4: View of the Far Detector cavern excavated 1.5 km underground at SURF (South Dakota, US). The two red cubes are the cryostats of the first two Far Detector modules of dimensions 15 m x 14 m x 62 m each.

Several technologies have been considered for the four modules, and there is a full R&D program towards the validation of the different technologies within the ProtoDUNE programme at the CERN neutrino platform (see Sec. 3.3). The first module will be a single-phase horizontal-drift module (DUNE Single-Phase), since the design was validated during the successful operation of ProtoDUNE Single-Phase (see Sec. 3.3.1). The second module was initially proposed as a dual-phase design, however, the results from the prototyping phase have modified the strategy, and the dual-phase technology, at its current state of development, has been discarded for the second module of the DUNE Far Detector. An alternative proposal of a single-phase module with a vertical drift is being considered for the second module, as an evolution of the dual-phase design but renouncing to the gas phase. This is known as the Vertical-Drift design. This approach is being tested to demonstrate its viability and there is a dedicated effort at CERN to build a prototype and validate the design.

The three options mentioned above: Single-Phase, Dual-Phase and Vertical-Drift are described in the following sections.

1^{st} FD module: Single Phase

The design of the Single-Phase Far Detector module [118] is shown in Fig. 3.5. The detector will have a total mass of 17 kton liquid argon and an active volume of 12 m x 14 m x 58.2 m, containing 10 kton of argon. The volume is divided in four drift volumes, with a maximum drift-length of 3.5 m. Two cathode and three anode walls divide the volume as it is shown in Fig. 3.5. The cathodes will be biased at -180 kV, to provide an electric field of 0.5 kV/cm. A field cage around the active volume composed of aluminium rings ensures a uniform electric field.

In this configuration, the electrons are drifted horizontally towards the anodes, where they are read out using three meshes of wires.

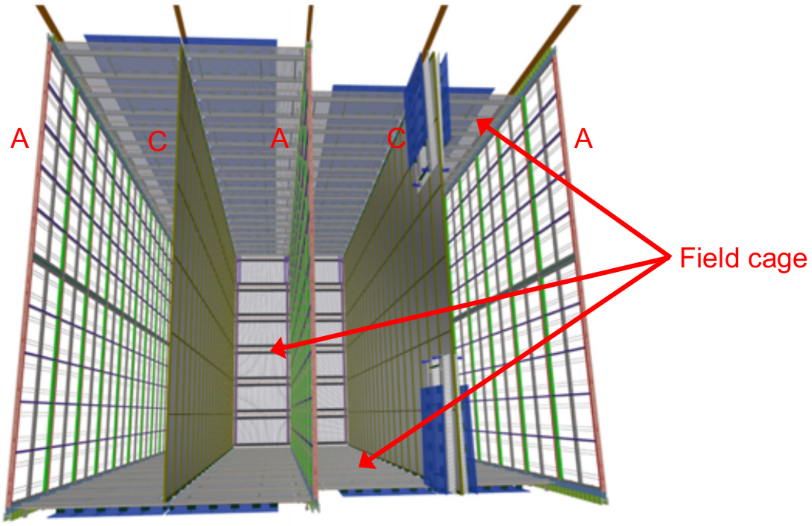

Figure 3.5: View of the DUNE SP FD module. A and C stand for Anode and Cathode respectively. The TPC is segmented in four drift volumes.

The scintillation light detection is performed by special devices developed by the collaboration called *X-ARAPUCAs* [185–187] (see Sec. 2.7.1).The X-ARAPUCAs are placed behind the anode wire-planes. There will be 1500 X-ARAPUCA modules in total.

A picture of an assembled X-ARAPUCA is shown in Fig. 2.4. Each module contains four X-ARAPUCAs.

Proposal for a Dual-Phase module

In contrast to the Single-Phase design, the Dual-Phase module [190] is proposed as a monolithic volume of 12 m x 12 m x 60 m (see Fig. 3.6). In this configuration, the cathode is placed below the active volume and the anode at the top. The cathode is biased at -600 kV and the anode is grounded, providing a vertical electric field of 0.5 kV/cm. As in the Single-Phase design, a field cage around the active volume ensures a uniform electric field in all the volume. The ionization electrons are drifted vertically towards the anode plane, made of 80 independent modules of 3 m x 3 m called Charge Readout Planes (CRPs). Each CRP is placed in the interface liquid-gas. Inside the CRP, the extraction grid placed in the liquid argon, 5 mm below the interface, accelerates the electrons towards the gas phase, where a Large Electron Multiplier (LEM), placed 5 mm above, amplifies the signal producing a Townsend avalanche. A PCB printed anode finally collect the electrons in two views with a pitch of 3.1 mm.

On the one hand, it is remarkable the simplicity of the design, with a smaller number of readout channels and components to be installed with respect to the Single-Phase design. On the other hand, the Dual-Phase design faces many challenges, such as the cathode operation at 600 kV, almost four times the Single-Phase voltage, or placing the 60 m x 12 m anode plane in the liquid-gas interface, with tolerance at the level of the millimetre.

The proposed photon detection system would be composed of 720 PMTs. They are placed at the cryostat floor, as an array of 12 x 60 PMTs with one meter pitch. The proposed PMT model is Hamamatsu R5912-20Mod, with 14 dynodes and a diameter of 8 inches (20 cm). It has a maximum quantum efficiency of $\sim$20% at 430 nm. Each PMT has tetraphenyl butadiene (TPB) deposited on its surface to convert the VUV scintillation light into visible photons. This model has been successfully used in WA105 [143], ProtoDUNE Dual-Phase [191], MicroBoone [192] and ICARUS [177].

Finally, a system of TPB-coated reflector panels is integrated into the top half of the field cage (see Fig. 3.6). The TPB would convert the incident VUV photons into visible light before being reflected. This design is based on the reflector foils used for SBND [193], which provide a reflectivity of 90% at 430 nm, which is the emission peak of the TPB.

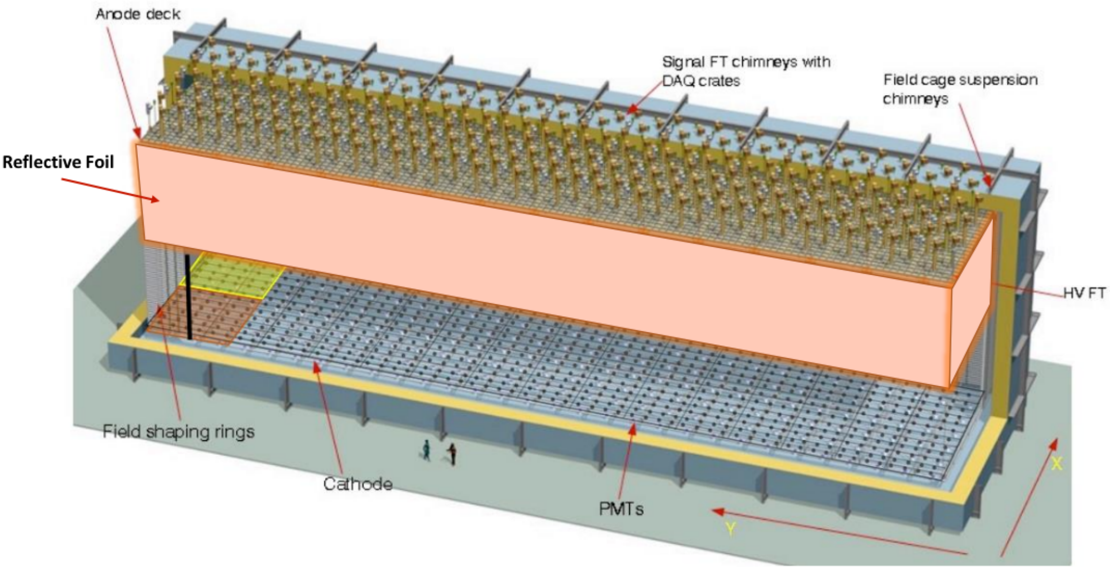

Figure 3.6: View of the proposed Dual-Phase design for a DUNE Far Detector module. It holds a monolithic volume of 60 m x 12 m x 12 m with anode at the top and cathode at the bottom.

2$^{\text{nd}}$ FD module: Vertical Drift

The Vertical Drift design is shown in Fig. 3.7, and it arises as an evolution of the Dual-Phase design. It will have an active volume of 13 m x 13.5 m x 60 m, corresponding to 14.7 kt of the total 17 kt liquid-argon mass. The active volume is divided by the cathode placed in the middle, separating two volumes with a maximum drift length of 6.5 m. Two 60 m x 13.5 m anode planes are placed at the top and the bottom of the detector. The cathode is biased at -325 kV and the anode planes are grounded.

In this configuration, the electrons are drifted vertically towards the top (in the top-half) and the bottom (in the bottom-half) where they are read-out. Since the gas phase is removed, the anode planes are simplified by removing the extraction grid and the LEMs. The anode is based on a perforated PCB system. The cathode will be a thin structure to reduce the loss of active volume and roughly 60% transparent to allow the free flow of the argon.

The photon detection system is based in X-ARAPUCAs, as in the Single-Phase module. They are positioned on the cathode and on the cryostat walls behind a transparent field cage. The field cage transparency is larger near the position of the X-ARAPUCAS placed in the walls, to improve the light collection. The X-ARAPUCAs placed in the cathode, which is biased at -325 kV, will be both powered and read out by optical fibres. The use of liquid argon doped with 10 ppm of xenon is also under consideration. The technical

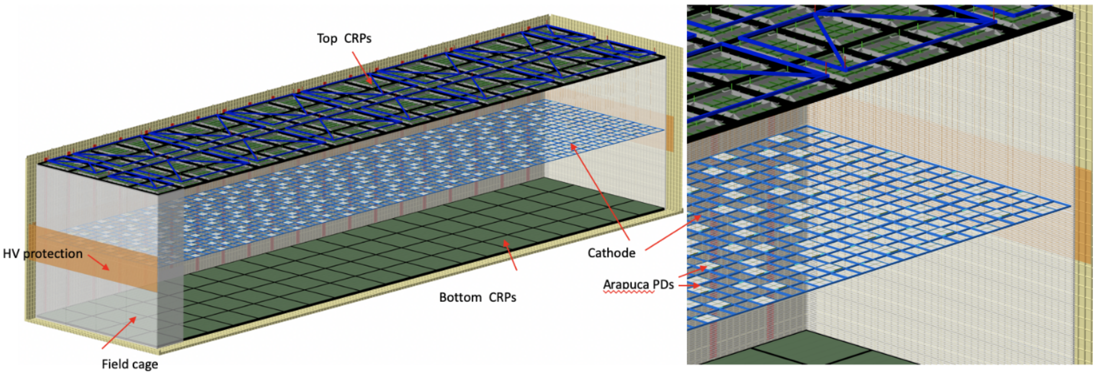

Figure 3.7: Configuration of the Vertical Drift concept [194]. The drift volume is segmented by the cathode placed in the middle.

design report for a Vertical-Drift based Far Detector module is under preparation.

3.2 Science program

The primary goals of DUNE are to determine unambiguously the neutrino mass ordering and discover CP violation in the leptonic sector through the precision measurements of the neutrino oscillations parameters and test the three flavour paradigm. Other primary goals of DUNE are to perform astrophysics and particle physics measurements with supernova burst neutrinos and other low-energy neutrinos, and the search for physics beyond the Standard Model, such as proton decay searches.

Additionally, DUNE science program includes other accelerator-based neutrino oscillation measurements with sensitivity to beyond standard model physics, such as non-standard interactions (NSIs), charge, parity, and time reversal symmetry (CPT) violation, sterile neutrinos, heavy neutral leptons, and measurements of tau neutrino appearance. It will also includes neutrino oscillation measurements using atmospheric and solar neutrinos, dark matter searches and non-accelerator searches for BSM physics such as neutron-antineutron oscillations. Finally, the Near Detector will have a rich physics program, including neutrino cross sections measurements and nuclear effects studies [195].

The primary goals of DUNE are detailed in the following sections. A detailed review of the full physics program of DUNE is available in [117].

3.2.1 Long-baseline oscillations physics

In an accelerator-based long baseline experiment like DUNE, neutrinos are generated in the muon flavour eigenstate (ν_μ or $\bar{\nu}_\mu$). The propagation of a muon neutrino through the

Earth leads to a non-zero electron appearance probability. As it was shown in Sec. 1.4.1, the appearance probability is given by Eq. 1.19. At a baseline of 1,300 km, as it will happen in DUNE, the neutrino appearance probability has a strong dependence on the δ_{CP} values and the neutrino mass ordering in the energy range of the DUNE neutrino beam, as it is shown in Fig. 3.8. Additionally, the unprecedented energy range of the DUNE neutrino beam (from 0.5 to 5 GeV) will allow covering the first two oscillation maxima. This feature is unique among other long-baseline experiments. Also, the high energy resolution and the 3D imaging capabilities of LAr-TPCs allow increasing the detector sensitivity by removing backgrounds.

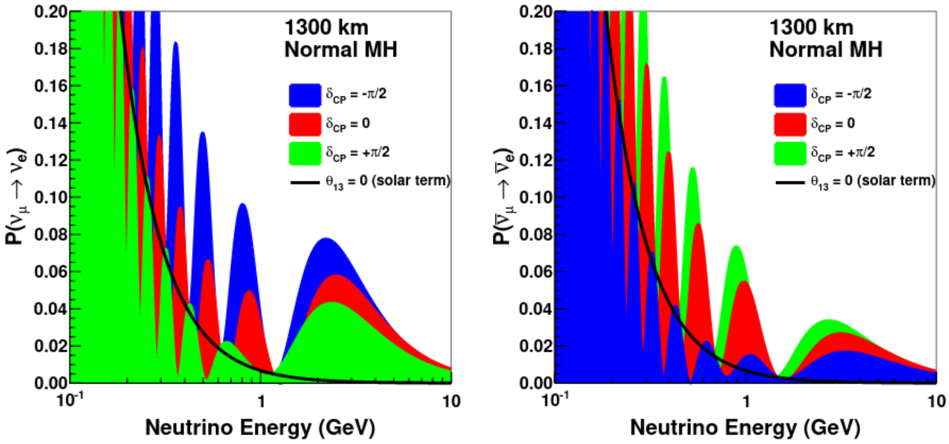

Figure 3.8: Electron neutrino appearance probability at a baseline of 1300 km assuming the normal neutrino mass ordering, as a function of the energy (neutrino left, antineutrino right). The black line indicates the oscillation probability if θ_{13} were equal to zero. Figure is taken from [120]

Figure 3.9 shows the sensitivity of DUNE to the CP-violation phase. The left panel shows the expected CP violation significance as a function of the true value assuming a normal neutrino mass ordering, for exposures of seven and ten years of data and considering the staged deployment of the Far Detector modules (as detailed in Sec. 3.1). Sensitivity is maximal at $\delta_{CP} = \pm\pi/2$, and decreases around CP-conserving values of δ_{CP}. The median CP violation sensitivity reaches 5σ for a small range of values after an exposure of seven years in normal ordering. The right panel shows the significance of the CP violation determination in normal mass ordering for 75% and 50% of the δ_{CP} values, and when $\delta_{CP} = -\pi/2$, as a function of exposure in kt-MW-years. The width of the bands in the right panel shows the impact of applying an external constraint on θ_{13}. CP violation can be observed at 5σ after about seven years (which corresponds with 336 kt-MW-years) if $\delta_{CP} = -\pi/2$ and about 10 years for 50% of δ_{CP} values. CP violation can be observed at

3σ after about 13 years of running for 75% of the δ_{CP} values.

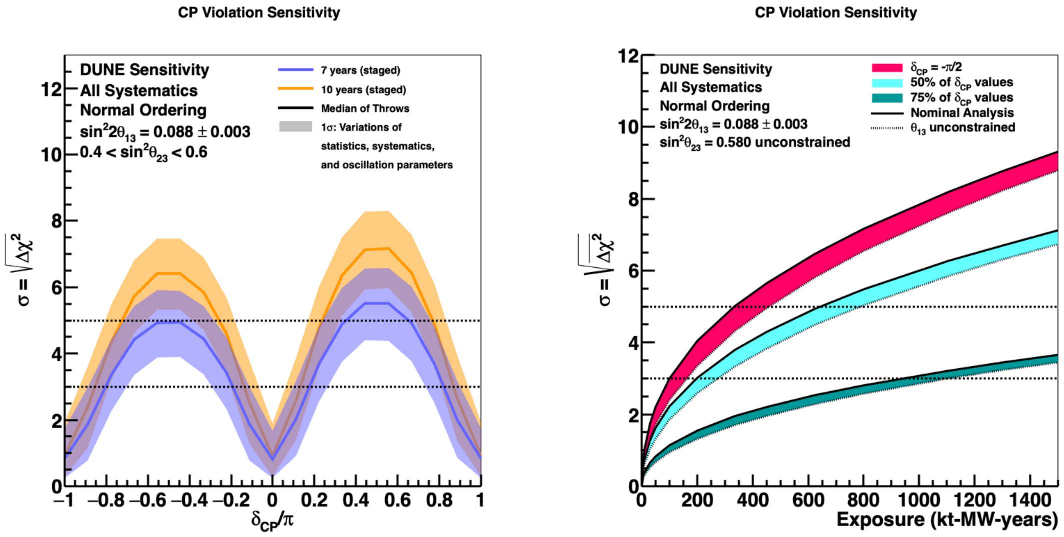

Figure 3.9: Left: Significance of the CP violation discovery by DUNE as a function of the true δ_{CP} value, for seven and ten years of exposure, assuming normal neutrino mass ordering. Right: Significance for $\delta_{CP} = -\pi/2$, and for 50% and 75% of possible true δ_{CP} values as a function of the exposure in kt-MW-years. Taken from [120].

Figure 3.10 shows the significance of the neutrino mass ordering determination by DUNE assuming normal neutrino mass ordering. The left panel shows the significance as a function of the true value of δ_{CP}, for seven and ten years of exposure (assuming the staged scenario). DUNE would achieve a significance above 5σ regardless the value of δ_{CP}. The right panel shows the significance as a function of exposure for the case when $\delta_{CP} = -\pi/2$ and for 100% of possible δ_{CP} values. The width of the bands in the right panel shows the impact of applying an external constraint on the value of θ_{13}. After just 66 kt-MW-years, which corresponds to ~ 2 years of data taking, the neutrino mass ordering will be determined at 5σ regardless the value of δ_{CP}.

Finally, Fig. 3.11 shows the DUNE sensitivity to the determination of the octant of θ_{23} as a function of the true value of $\sin^2\theta_{23}$ for ten and fifteen years of exposure assuming the staged scenario. The width of the bands cover variations of 1 σ considering statistic and systematic uncertainties, as well as the dependence with the true value of other oscillation parameters.

A detailed study of the DUNE contributions to neutrino oscillations measurement is presented in [120].

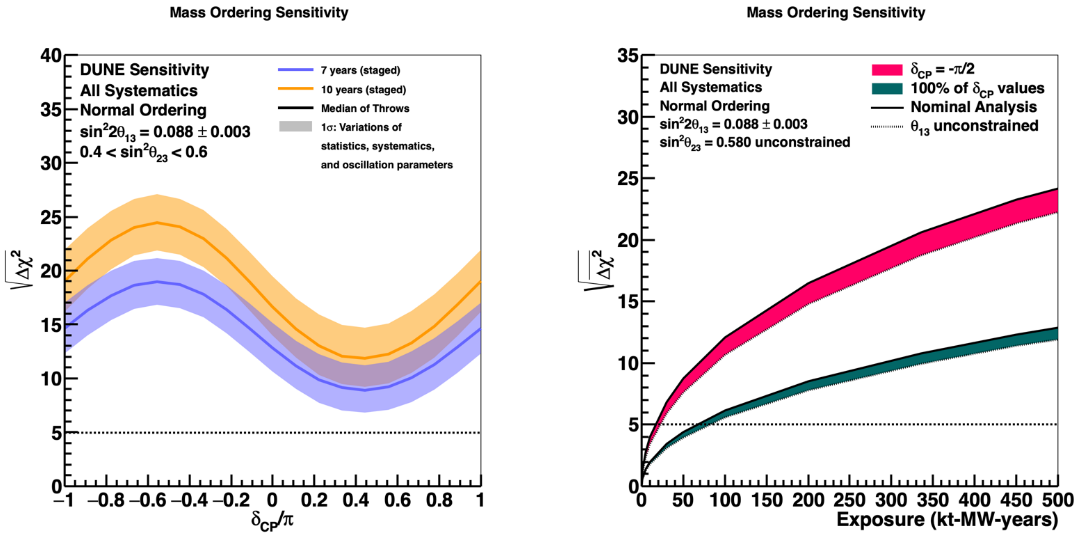

Figure 3.10: Left: Significance of the DUNE determination of the neutrino mass ordering, as a function of the true value of δ_{CP}, for seven and ten years of exposure. Right: Significance the neutrino mass ordering determination for the case when $\delta_{CP} = -\pi/2$, and for 100% of possible true δ_{CP}, as a function of exposure in kt-MW-years. Taken from [120].

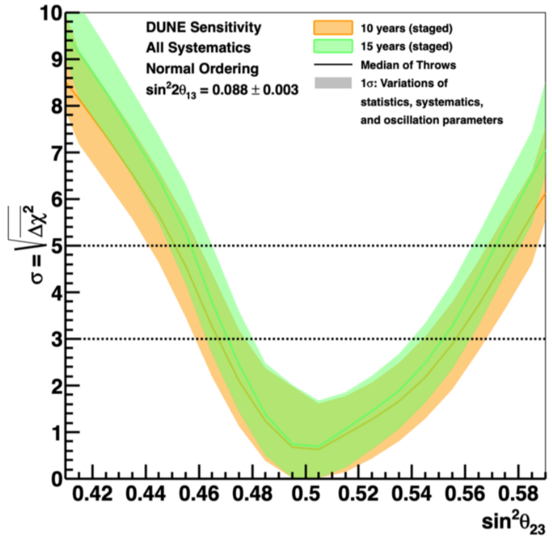

Figure 3.11: DUNE sensitivity to the determination of the θ_{23} octant as a function of the true value of $\sin^2\theta_{23}$, for ten and fifteen years of exposure, assuming normal neutrino mass ordering [120].

3.2.2 Low energy physics

The DUNE Far Detector is sensitive to neutrinos in the energy range of ~5-100 MeV, as those produced in the sun or in core-collapse supernovae.

Stars of masses between eight and ~ 40 solar masses develop into a type II supernova: when it reaches the end of its life it develops an onion layered structure, with a heavy iron core and the lighter elements in the outer layers. Once the mass of the core reaches the Chandrasekah limit, the gravity force exceeds the electron degeneracy pressure, and the nucleus is compressed increasing the temperature inside. When the temperature is high enough to break the iron atoms, the collapse of the core of the star starts. The iron atoms are decomposed into alpha particles, protons and neutrons. The free protons recombine with the electrons producing neutrons and electron neutrinos. These electron neutrinos can escape releasing the energy of the star, and decreasing the electron degeneracy pressure, accelerating the collapse. This is the so-called neutronization burst of electron neutrinos and lasts a few tens of ms [196]. This intense burst of electron neutrinos is followed by the accretion phase which lasts from few tens to few hundreds of ms, depending on the star mass, as matter falls into the core. Once the density of the core reaches $\sim 10^{11}$ g cm^{-1}, the neutrinos are trapped inside the star core, and only those that reach the outer layers can escape. Finally, the cooling phase last over 10 s and represents the main part of the neutrino signal. At the end, 99% of the gravitational binding energy is released in form of neutrinos.

The flavour composition and energy spectra of the emitted neutrinos evolve during these phases. While the electron neutrino flavour dominates during the burst and accretion, the three flavours are equalized during the cooling (see Fig. 3.12). The ability of a detector to measure the different neutrino flavours would provide valuable information of the stellar evolution.

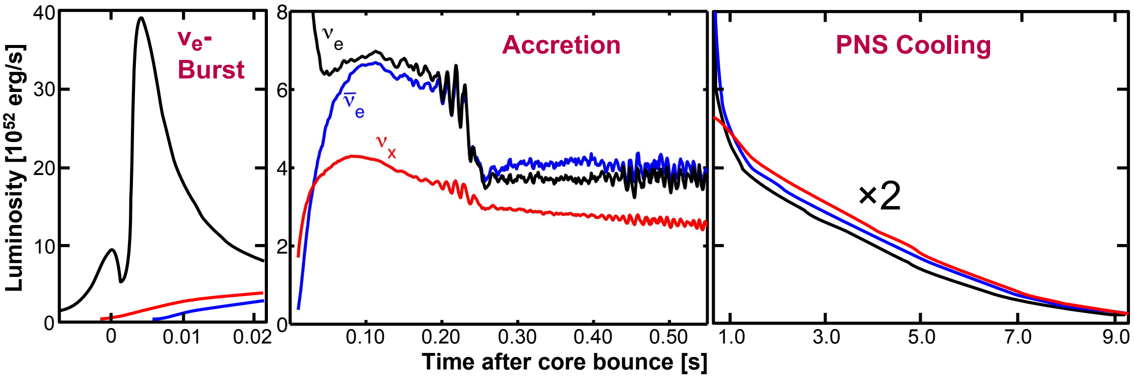

Figure 3.12: Neutrino luminosities during the main neutrino-emission phases: Burst (left), accretion (center) and cooling (right).

Kamiokande [197] and IMB [198] detected 11 and 8 neutrinos respectively emitted by SN1987A, starting the neutrino astronomy era. If a supernova burst happens during the DUNE data-taking, the Far Detector would be sensitive to electron-flavour neutrinos and antineutrinos by the charged current (CC) interaction with the argon nuclei ($\nu_e CC$ and

$\bar{\nu}_e CC$).

$$\nu_e +^{40}\mathrm{Ar} \to e^- +^{40}\mathrm{K}^* \tag{3.3}$$

$$\bar{\nu}_e +^{40}\mathrm{Ar} \to e^+ +^{40}\mathrm{Cl}^* \tag{3.4}$$

This capability of detecting the $\nu_e CC$ by DUNE is unique among other supernova neutrino detectors. For example, HyperKamiokande and JUNO are primarily sensitive to $\bar{\nu}_e$. This fact places DUNE in an advantageous position given the primacy of the ν_e production.

DUNE is able to detect thousands of neutrino events from the neutrino burst of a core-collapse supernova at 10 kiloparsecs, measuring the neutrino energy spectrum and its arrival time with unprecedented sensitivity. These data would allow to validate or discard some of the present models about stellar evolution. Also, the detection of the neutrino burst would be a prompt alert to the astronomers, since the supernova neutrino burst precede the electromagnetic signal. DUNE will be even capable of promptly point to the region of the sky where the supernova is originated, by reconstructing the direction of electrons. Additionally, the measurement of the neutrino flux during the neutronization burst by DUNE would be a signature of the mass ordering, since it is strongly suppressed in the normal ordering case in comparison with the inverted ordering. A detailed study of the DUNE contributions to supernova neutrino detection is available in [199].

Solar neutrinos and diffuse background supernova neutrinos are also potentially detectable. However, due to the presence of low energy backgrounds such as radioactive decays, the detection of this neutrino sources is very challenging. Nevertheless, initial studies suggest that DUNE will be capable to improve the measurement of Δm^2_{21} through the detection of solar neutrinos, as well as observation of hep and ^8B solar neutrino flux.

3.2.3 Physics beyond the Standard Model

The location of the DUNE Far Detector 1.5 km underground as well as the broad energy beam, enhance the capabilities of DUNE to perform searches of physics beyond the Standard Model. The main DUNE capabilities to perform beyond Standard Model physics searches are briefly described below, a detailed description is available in [200].

The three flavour neutrino paradigm is in tension with some experimental results (see Sec. 1.5). To explain this tension, most models include the presence of sterile neutrino states beyond the three light states of the Standard Model, implying that PNMS matrix is not unitary. By looking at the disappearance of charge-current and neutral current neutrino interactions between the Near and the Far Detectors, DUNE is sensitive to potential sterile neutrino mass splitting. DUNE will constrain the parameters describing the non-unitarity of the PNMS matrix.

Additionally, neutrinos propagating through the Earth can be affected by non-standard interactions (NSI). Thanks to its long baseline and broad-energy beam, DUNE can improve the bounds of the NSI parameters.

Also, by using beam neutrinos and, specially, atmospheric neutrinos, DUNE can improve the present limits on Lorentz and CPT violation. Since atmospheric neutrinos cover a wide range of L/E and are very sensitive to matter effects, as they propagate through the Earth, studying atmospheric neutrinos in DUNE is a promising approach to search for physics beyond the Standard Model.

Another test to the Standard Model can be performed by looking for neutrino tridents in the Near Detector. Neutrino trident production is a weak process that generates a pair of charged leptons. The high intensity neutrino flux at the Near Detector will produce a measurable rate of tridents. A deviation of the rate predicted by the SM would point to a new gauge boson interaction.

DUNE will perform dark matter searches at the Near Detector, including axion-like particles and low-mass dark matter (LDM) produced in the beam. Due to the boosted nature of the LDM produced in the beam, DUNE will be able to reach a mass range of low-mass dark matter searches not achieved by the present experiments. Additionally, the ND-GAr detector will have unique sensitivity to heavy neutral leptons (HNL) and heavy axions, due to the low density of the gas argon that reduces the neutrino background.

DUNE will perform also boosted dark matter (BDM) searches in the Far Detector. It is expected to have a competitive sensitivity to possible BDM sources such as the galactic halo, the sun and dwarf spheroidal galaxies. In particular, DUNE will be very sensitive in a particular channel: a low-mass BDM particle interacting inelastically, and upscattering to a higher-mass state, which then decays to a low mass dark matter. This would produce two leptons in the initial interaction, and either an additional lepton or a nucleon recoil, that would be a clear signature in the Far Detector.

The DUNE Far Detector will also search for baryon number violating processes, such as nucleon decay or free neutron oscillations. DUNE will provide a lower limit on the proton lifetime of 1.3×10^{34} in the $p \to K^+ \bar{\nu}$ channel, and of 1.1×10^{34} in the $n \to e^- K^+$ channel at 90% confident level of 1.3×10^{34}, assuming no signal is detected and an exposure of 400 kt-year. The expected limit for the oscillation time of free neutrons is 5.5×10^8. The DUNE capabilities to perform proton decay searches are explained in detail in chapter 10.

3.3 ProtoDUNE programme at CERN Neutrino Platform

The DUNE collaboration has performed a full R&D program in order to validate the LAr-TPC technology at the kiloton scale. Two configurations were first considered, the Single-Phase and the Dual-Phase approach, and two prototypes following these configurations were installed at the CERN Neutrino Platform (ProtoDUNEs, see Fig. 3.13). They have been taking data from 2018 to 2020.

Figure 3.13: View of the Neutrino Platform at CERN. The two red cryostats that contain ProtoDUNE Single-Phase and Dual-Phase are in a beam-line from the SPS.

ProtoDUNE Single-Phase and ProtoDUNE Dual-Phase, with a total mass of 750 ton of liquid argon and an active volume of around 6 m x 6 m x 6 m each, are the largest LAr-TPC ever built. However, they are one step more in the path towards scaling the LAr-TPC technology at the kiloton scale.

The largest LAr-TPCs successfully operated before the construction of the Proto-DUNEs are ICARUS [136], for the Single-Phase technology, and WA105 [143], for the dual-phase approach. The ICARUS collaboration successfully operated a single-phase LAr-TPC of 230 ton. The WA105 collaboration constructed a 25 ton dual-phase TPC that took data during 2017. While ProtoDUNE Single-Phase involves an increase of a factor of two in the mass with respect to previous detectors (ICARUS), for ProtoDUNE Dual-Phase, this increase is of a factor of 30. These numbers emphasize the different nature of the challenges addressed by both detectors. While the Single-Phase technology is on a more mature status of development, the Dual-Phase technology is on an earlier stage.

The operation of ProtoDUNE Single-Phase is addressed in the following section, while the operation of ProtoDUNE Dual-Phase will be explained in chapter 4. The operation of the WA105 detector is summarized in Sec. 3.3.2.

3.3.1 ProtoDUNE Single-Phase

ProtoDUNE Single-Phase (SP) [201] is a prototype to validate the Single-Phase Far Detector components at a real scale. With a total mass of 770 t of liquid argon, it is the largest LAr-TPC detector ever built. ProtoDUNE Single-Phase is placed in the EHN1 hall at the CERN's North Area, where it was exposed to a dedicated test beamline of pions, kaons, protons, muons and electrons with momenta in the range of 0.3 GeV/c to 7 GeV/c.

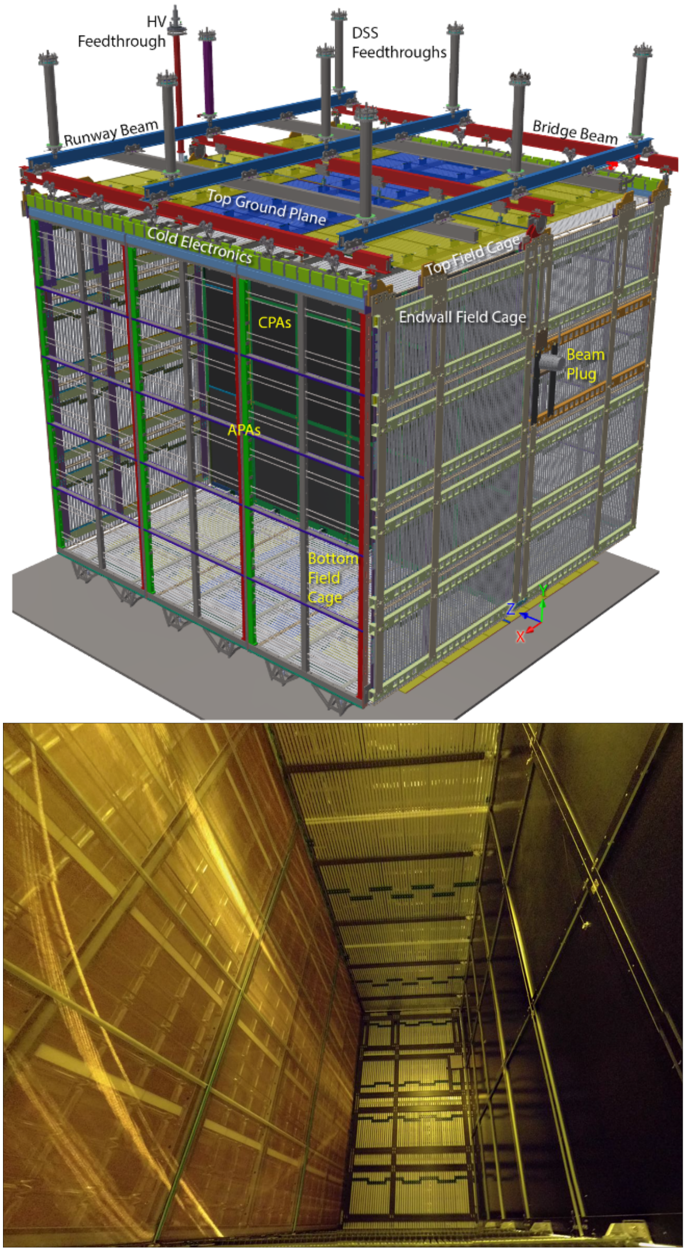

Figure 3.14: Top: Detail of ProtoDUNE Single-Phase geometry; bottom: Photo from the inside of one of the drif volumes from ProtoDUNE Single-Phase. Anode planes are on the left, cathode is on the right [202].

ProtoDUNE Single-Phase has an active volume is 7.2 m x 6.0 m x 6.9 m (see Fig. 3.14). The volume is segmented in two parts, with two anode planes in the sides and a central cathode, to have a maximum drift length of 3.6 m. The cathode is set at -180 kV by the HV feedthrough, and the field-cage surrounds the volume ensuring a uniform drift field of 0.5 kV/cm. The photon detection system modules are embedded in the anode planes. Three different designs are used, all based in wavelength-shifted guide bars and silicon photomultipliers.

The construction and installation was completed in July 2018. The filling and commissioning took place in July and August 2018. The data-taking with the beamline lasted from August 29th to November 11th. From that date, the detector continued taking data with cosmic muons until July 2020, demonstrating the operational stability of the technology. Finally, xenon doping tests were performed at the end of the operation. The construction, installation, and operation of the ProtoDUNE Single-Phase detector is described in [203].

The collected beam and cosmic-ray data allowed a detailed characterization of the detector, and also to perform argon-hadron cross-section measurements at the relevant energies for DUNE. For example, the measurement of the absorption and charge exchange cross-section on argon of positive pions from the beam [204] and from the cosmic muons [205]. Also the measurement of the inelastic cross-section on argon of positive kaons from the beam with average momentum of 6 GeV/c [206]. First results are presented in [202].

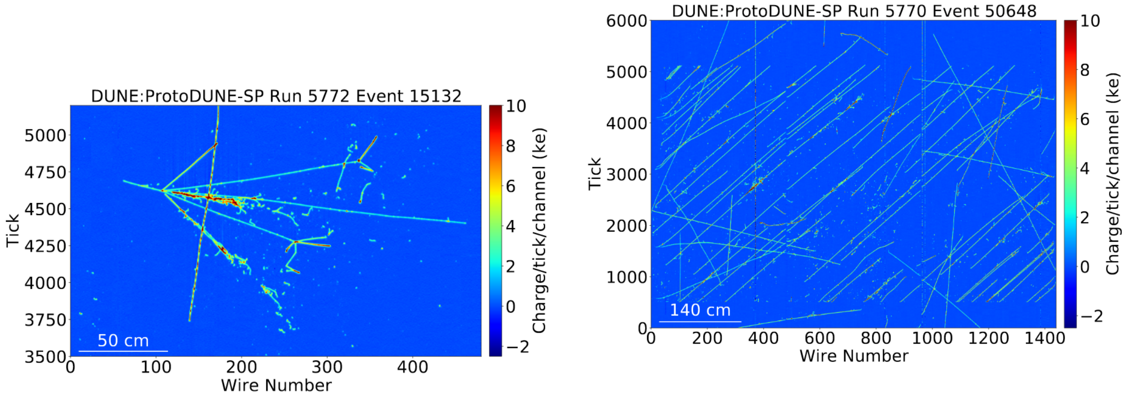

(a) 6 GeV/c pion candidate.

(b) Large cosmic air shower candidate producing many parallel muons.

Figure 3.15: Event candidates from ProtoDUNE Single-Phase data, with beam particles entering from the left. The x-axis shows the wire number. The y-axis shows the time tick in units of 0.5 μs. The colour scale represents the charge deposition [202].

A signal processing chain has been developed in order to fully reconstruct the events, including noise removal techniques, the deconvolution of the TPC waveforms, and patter recognition. The pattern recognition is performed using Pandora [207], which has been successfully used in other experiments such as MicroBooNE [208]. Figure 3.15 shows two example events after applying noise mitigation techniques.

The TPC response has been characterized in detail, which is essential to do calorimetry and to perform particle identification techniques based on the energy loss measurement (dE/dx). In this sense, the space charge effect (SCE) caused by the ion accumulation in the TPC has been characterized, measuring an average uncertainty of 5% with respect to the nominal drift. Figure 3.16 shows the dependence of the dE/dx with the residual range for protons and muons, after SCE corrections. It is remarkable the high purity achieved, with a measured electron lifetime close to 100 ms at the end of the beam data-taking. The clear separation between both bands allows an efficient particle identification.

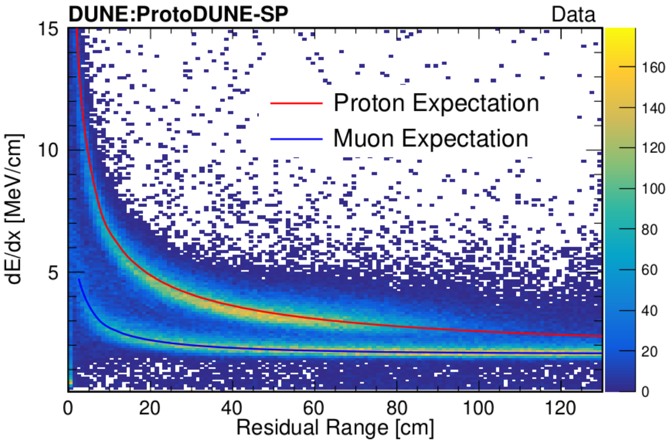

Figure 3.16: dE/dx versus residual range after the SCE corrections for the stopping protons (upper band) and the muons (lower band) in ProtoDUNE Single-Phase [202].

The successful performance of ProtoDUNE Single-Phase paved the way towards the construction of the first module of the DUNE Far Detector. A second run of ProtoDUNE is scheduled for 2022-2024, in order to do a final test of the final components that will be assembled in the Far Detector.

3.3.2 WA105 3x1x1 Dual-Phase LAr-TPC demonstrator

The WA105 Dual-Phase demonstrator was installed and successfully operated at CERN in 2017, as the previous step to ProtoDUNE Dual-Phase. With a total mass of 4.2 t and an active volume of 3 x 1 x 1 m^3, the operation of this detector validated the dual-phase technology at the ton scale.

The cathode was placed below the active volume and was operated at -50 kV. The charge readout planes, dedicated to the extraction, amplification and readout of the charge signal, had a surface of 3 m^2, placed at the liquid-gas interface. Five PMTs were installed below the cathode to detect the scintillation light. Two Cosmic Ray Tagger (CRT) were placed at the sides of the cryostat, in order to trigger on diagonally crossing muons. Some pictures of the detector setup are shown in Fig. 3.17.

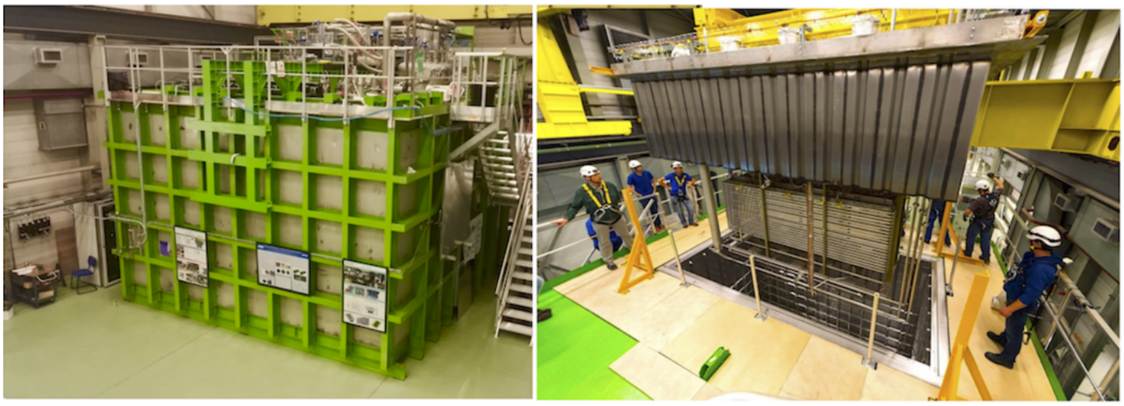

Figure 3.17: Pictures of WA105 3x1x1 m^3 Dual-Phase LAr-TPC demonstrator. Left: Outer view of the cryostat. Right: the TPC is suspended under the top cap during its insertion in the cryostat [143].

The demonstrator recorded cosmic-ray data in 2017, collecting more than 5×10^6 events in different detector conditions. Some of the milestones achieved by the WA105 Dual-Phase demonstrator are the operation of the cryogenic system and the membrane cryostat at the largest scale up to that date, the extraction and amplification of the charge in a surface of $3\,\mathrm{m}^2$, and the validation of the analog TPC front-end electronics and signal readout.

Although the amplification of the charge in the LEMs did not reach the effective gain of $\sim$20 that was proposed for the Dual-Phase DUNE Far Detector, the basic capabilities of the technology were demonstrated [143, 144, 209]. An example raw event recorded in the demonstrator is shown in Fig. 3.18. It is remarkable the low noise achieved. The operation and performance of the WA105 Dual-Phase demonstrator is described in [143, 144].

A detailed Monte Carlo simulation of the Dual-Phase technology was developed, including the amplification in the gas-phase, and the simulation of the CRT and PMT based triggers. Dedicated reconstruction algorithms and an algorithm of track-shower separation were also implemented. The drift field uniformity was characterized, finding a small average distortion of less than 1 cm due to space charge effects. An electron lifetime of 7 ms and an effective gain in the gas phase of 1.9 was measured based on the study of straight muon-like tracks.

Finally, dedicated studies focused on the scintillation light detection were carried out, validating the dual-phase photon detection design at the ton scale. The dependence of the

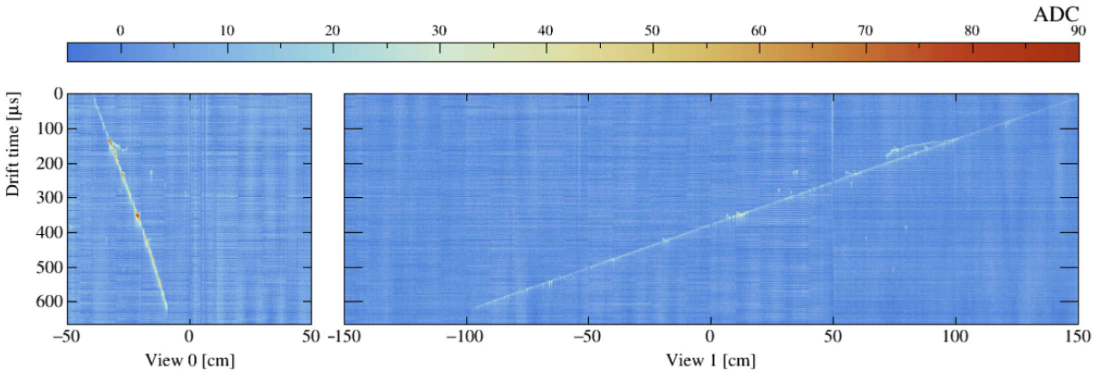

Figure 3.18: Event display of a cosmic-muon track candidate in the WA105 3x1x1 m^3 Dual-Phase demonstrator. Raw waveforms are displayed without applying any noise removal.

scintillation light with the drift field was studied, and an unexpected decrease of the slow decay time with the drift field was observed [132, 209].

Detailed studies of the dual-phase-specific electroluminescence S2 signal were carried out. Top panel of Fig. 3.19 shows the correlation of the S2 light with the charge collected in the TPC anode. Bottom panel of Fig. 3.19 shows a CRT-triggered event with the information provided by the three detector subsystems: CRT and TPC track information on the left, and three PMT waveforms recorded for the same event on the right. The PMT position relative to the track is marked with an arrow on the left. The PMT waveforms show the fast S1 signal centered in the same position (around 0.25 ms) on the three PMTs, and the S2 signal depending on the PMT position. The distance from the S1 signal to the S2 provides the average electron drift time at the PMT position. In this way, the S2 provides information about the track topology complementary to the TPC and using just PMT information. The drift velocity was measured to be $1.58{\pm}0.02$mm/μs, in agreement with the parametrisations that are found in the literature.

The detailed studies of the scintillation light detection in the WA105 3x1x1 Dual-Phase LAr-TPC demonstrator can be found in [132, 209]. The general performance of the detector is presented in [143], and the charge based studies in [144].

In summary, the operation of the WA105 3x1x1 Dual-Phase LAr-TPC demonstrator validated the dual-phase LAr-TPC technology at the ton scale paving the way towards a larger detector, ProtoDUNE Dual-Phase, which is described in chapter 4.

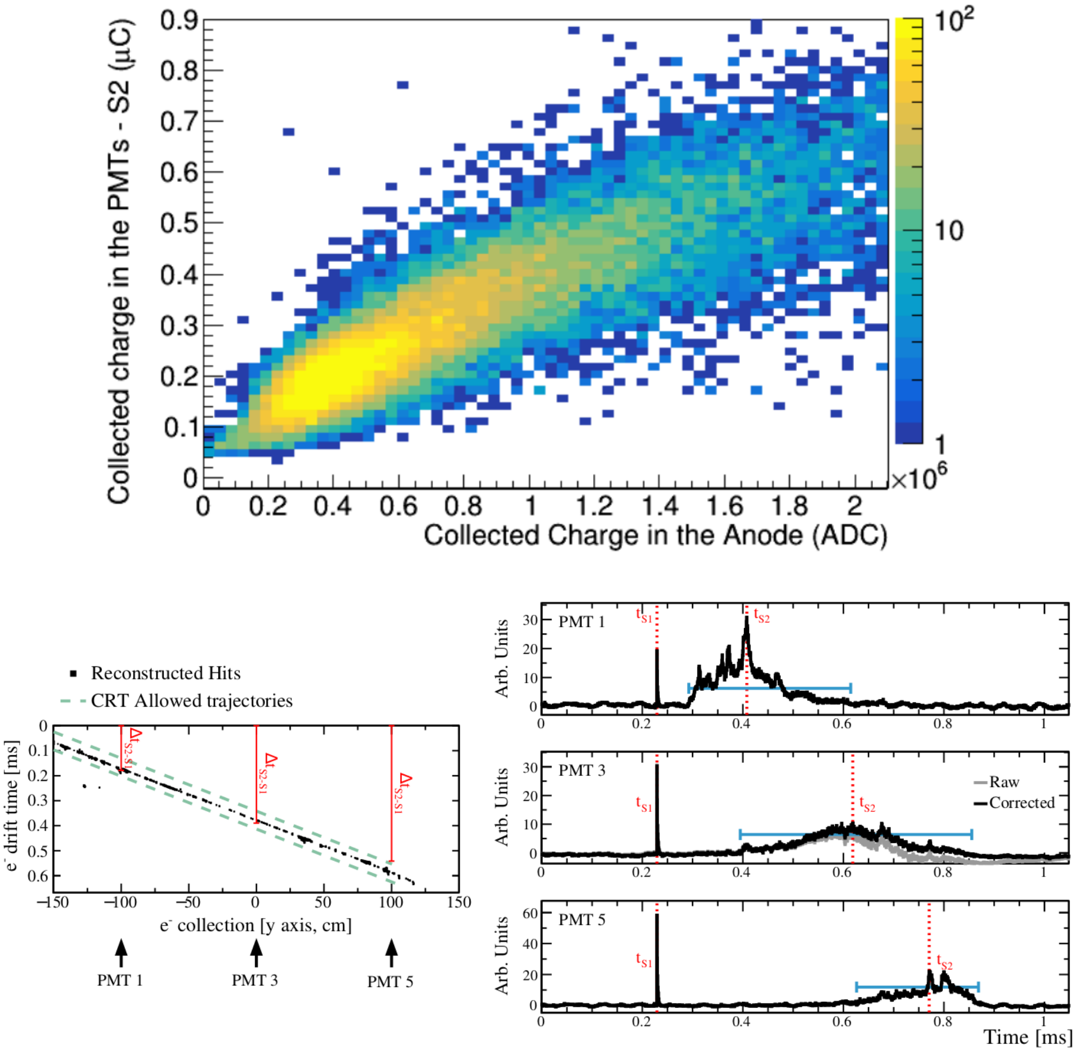

Figure 3.19: Top: Positive correlation of the collected charge in the anode (in x axis) and the detected light in the PMTs (in y axis). Bottom: Example of a cosmic-muon track candidate in the WA105 3x1x1 m^3 Dual-Phase demonstrator. The TPC event is shown on the left, as well as the CRT reconstructed track. The PMT waveforms for three PMTs are shown on the right. S1 and S2 times are shown in red.

Chapter 4

ProtoDUNE Dual-Phase, a 750-ton Dual-Phase LAr-TPC

ProtoDUNE Dual-Phase is the largest dual-phase liquid argon TPC ever operated. With a total mass of 750 tons of liquid argon, it aims at validating the dual-phase LAr-TPC technology at the multi-ton scale. ProtoDUNE Dual-Phase is located at the CERN Neutrino Platform. After its installation and commisioning, ProtoDUNE Dual-Phase took data during one year, from September 2019 to September 2020. After a partial update, a second run started in September 2021 and concluded in March 2022. Figure 4.1 shows a schematic view of the detector with the main elements inside the cryostat.

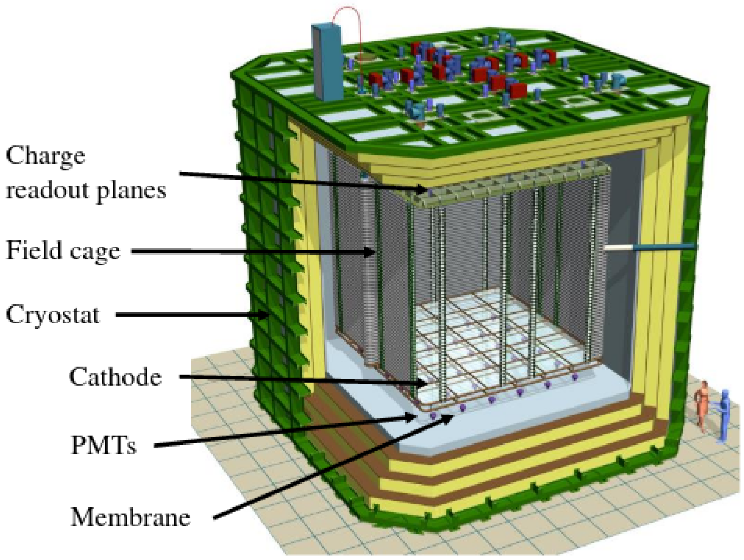

Figure 4.1: Schematic view of ProtoDUNE Dual-Phase.

In this chapter, ProtoDUNE Dual-Phase and its main components are described in

Sec. 4.1. A particular focus is placed on the description of the Photon Detection System in Sec. 4.2. Finally, the installation, commissioning and operation of the detector is detailed in Sec. 4.3.

4.1 Description of the detector

ProtoDUNE Dual-Phase has an active volume of 6 m x 6 m x 6 m, corresponding to 300 ton of liquid argon. The drift of the electrons is performed on the vertical axis, with a total drift length of 6 m. The High Voltage System provides a nominal drift field of 0.5 kV/cm, and ensures the field uniformity. The ionization electrons are extracted to the gas phase, where they are multiplied and read out by the Charge Readout Planes (CRPs). The PMTs placed below the active volume detect the scintillation light produced by the ionizing particles.

4.1.1 Cryostat and purification system

ProtoDUNE Dual-Phase is assembled inside a cubic cryostat of 12-m side, containing 750 tons of liquid argon. The cryostat consists of a steel structure, an insulation foam and a corrugated steel membrane. The inner dimensions of the cryostat are 8.5 m x 8.5 m x 8 m. Pictures of the outside (left) and the inside (right) of the cryostat are shown in Fig. 4.2. A dedicated cryogenic system ensures the operation with a stable level of liquid argon, by compensating the boiling-off gas, and a high level of purity, by purifying the liquid and gas argon to a level below 0.1 ppb (parts per billion) of oxygen equivalent [210]. This level of purity is needed in order to achieve an electron lifetime better than 3 ms.

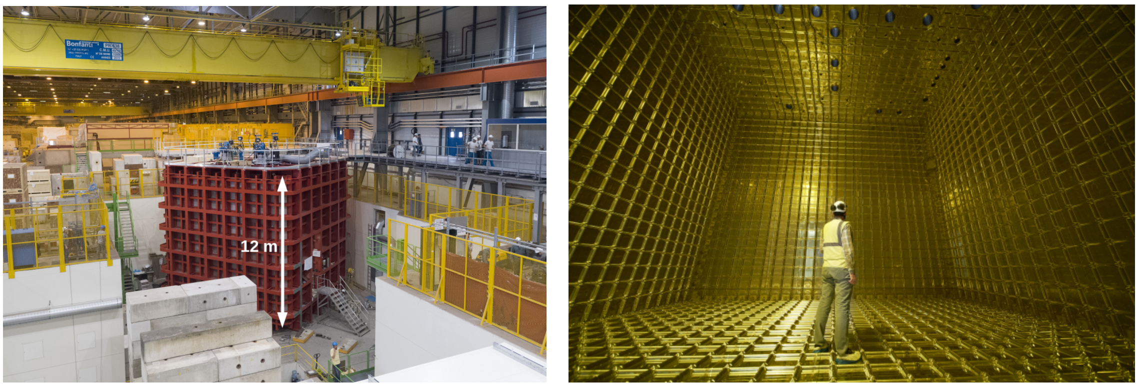

Figure 4.2: Left: Picture from outside ProtoDUNE Dual-Phase cryostat during installation. Right: Picture from inside the corrugated membrane.

4.1.2 High Voltage System

In absence of an electric field, the ionization electrons tend to recombine with the argon ions, suppressing the charge signal. Therefore, a stable, uniform and high electric field is required in the full active volume in order to avoid the recombination and to drift the ionization electrons towards the anode. A minimum electric field of 0.5 kV/cm is needed in order to suppress the recombination.

The High Voltage System provides the uniform vertical drift field at a nominal value of 500V/cm, in the full active volume of 6 m x 6 m x 6 m. It consists of:

- A stainless steel cathode placed at the bottom of the active volume. It is a metal structure made of four 3 x 3 m^2 modules of around 90 kg each. It is biased at 300 kV by a Heinzinger High Precision High Voltage Power Supply, with a negative polarity [134].

- The field cage ensures the uniformity of the electric field along the drift length. It consists of 98 aluminium rings, called field-shapers, equally spaced with a vertical pitch of 6 cm, and held by fibre-reinforced plastic frames. The voltage to each ring is applied by resistive voltage dividers.

- A very high voltage (VHV) feedthrough, and a 6 m long extender connects the cathode to the power supply. The extender consists of a metal conductor enclosed in a cylindrical insulator. Around the insulator, a set of 41 metallic rings connected to the field cage rings mitigate the electric field around the extender.

- A stainless-steel ground grid is installed between the cathode and the PMTs in order to protect them from the high electric field.

Figure 4.3 shows the high voltage system after the assembly inside the cryostat.

4.1.3 Charge Readout Planes

In a dual-phase TPC, the ionization electrons are extracted to the gas phase, where they are amplified and read out. In ProtoDUNE Dual-Phase these tasks are performed by four Charge Readout Planes (CRPs), with a surface of 3 m x 3 m each. They are assembled together at the top of the active volume as shown in Fig. 4.4. Each CRP consists of three elements assembled as it is shown in Fig. 4.5:

- The extraction grid consists of 100 μm diameter stainless steel wires, that are welded with a wire pitch of 3.125 mm. It is placed 5 mm below the liquid-gas inter-phase.

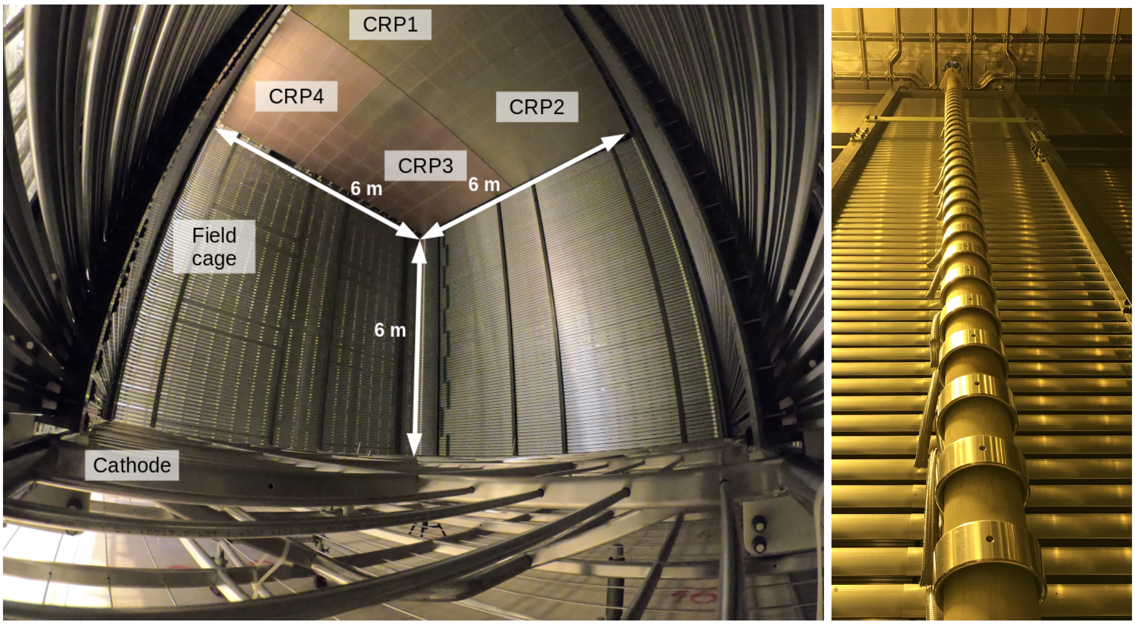

Figure 4.3: Left: Wide view of the ProtoDUNE Dual-Phase high voltage system from the inside of the active volume. The field cage is fully assembled and the cathode is shown below. The CRPs are at the top of the detector. Right: VHV feedthrough extender installed inside the cryostat.

- The Large Electron Multipliers (LEMs) are printed circuit board (PCB) plates pierced with holes of 500 μm in a honeycomb pattern, coated with a layer of 60 μm of copper. The dimensions of each LEM module are 50 cm x 50 cm x 1.12 mm. They are placed 5 mm above the liquid gas inter-phase. There are 36 LEMs per CRP. A picture of a LEM is shown in Fig. 4.4.
- The anode is a PCB with two sets of perpendicular readout strips that collect the charge signal after the amplification. The strip pitch is 3.125 mm, providing a very good resolution.

Only two out of four CRPs are fully instrumented (CRP1 and CRP2). CRP3 and CRP4 do not have LEMs installed, meaning that there is no amplification in half of the active volume. The instrumented CRPs are indicated in Fig. 4.4.

	Voltage (kV)
Anode	0
LEM up	-1
LEM down	-4.3
Extraction grid	-6.8
Cathode	-300kV

Table 4.1: Nominal ProtoDUNE Dual-Phase high voltage settings.

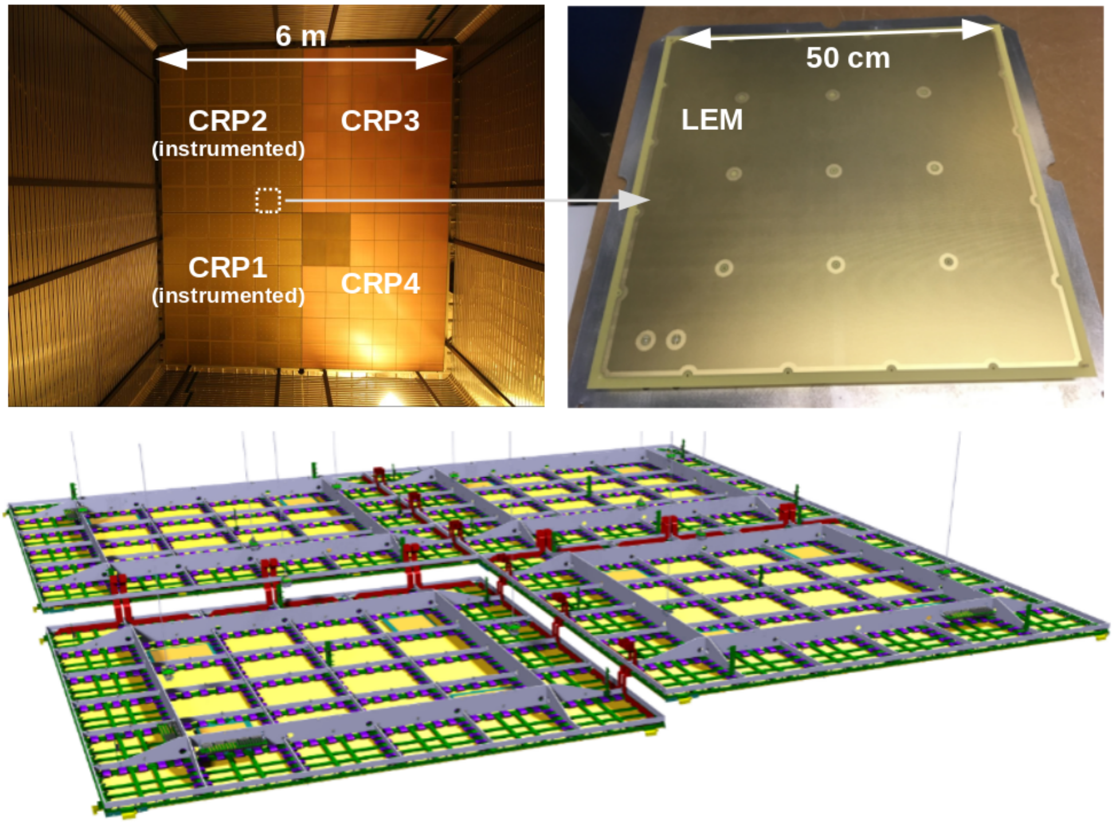

Figure 4.4: Design of the ProtoDUNE Dual-Phase CRPs. Top left: Picture of the assembled CRPs from the inside of the active volume. Top right: Picture of an individual LEM. Bottom: Design of the assembly of the four CRPs from the top.

The nominal voltages of each element are summarized in Tab. 4.1. The electric field in each region is shown in Fig. 4.5. This configuration provides an electric field high enough to extract the electrons towards the gas phase and amplify the signal in the LEMs, by triggering a Townsend avalanche.

4.1.4 Cryogenic instrumentation

The proper operation of the detector is assisted by a complex system of instrumentation, which consists of (see Fig. 4.6):

- Temperature sensors: Fifty eight temperature sensors were installed at two vertical corners of the cryostat at a well-known position, at the level of mm (see left panel of Fig. 4.6). They are used to monitor the fill progress, and variations of the liquid argon temperature during the operation. Twenty four were deployed above the CRPs to monitor the argon gas temperature. Twenty eight are within the CRP structure to estimate the deformation due the thermal gradient. Six are near the liquid argon pipes to monitor the temperature differences due to the recirculation. Twenty one

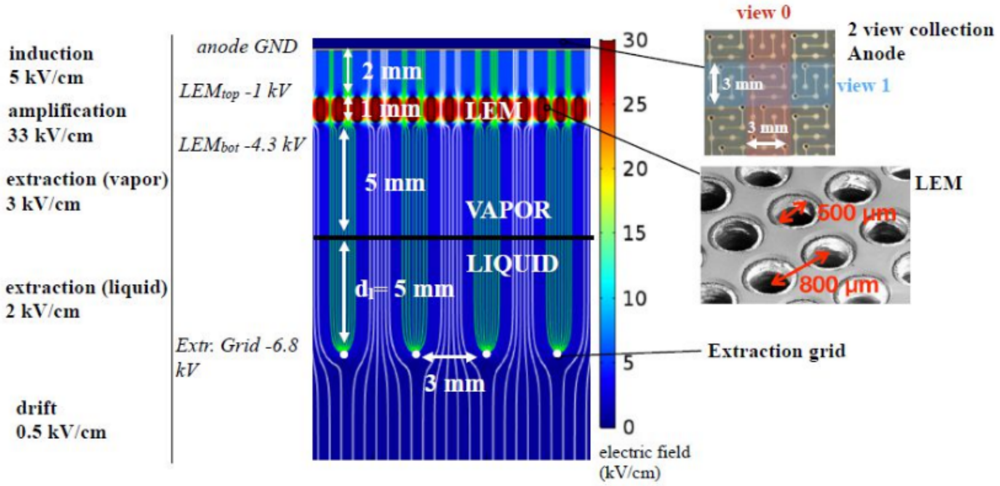

Figure 4.5: Sketch of the nominal voltages and electric fields within the CRPs.

are in the insulation space, and nine underneath the cryostat. They allow to monitor the insulation performance. They have a precision of 10 mK.

- Level meters: They are capacitive sensors that allow to monitor the liquid argon level with a sub-mm precision. Two 4 m-long level meters were installed in a vertical corner. Fourteen 25 mm-long level meters were installed on the CRPs, to adjust the position of the CRPs with respect to the liquid-gas interface. Two 60 mm-long level meters were installed on the cryostat wall to measure precisely the liquid argon level.

- Purity monitors: They are special devices that allow to measure the electron lifetime. The working principle is based in measuring the attenuation of a known charge signal in a well-characterized drift length. Two short purity monitors (17 cm) were installed on the floor (see center panel of Fig. 4.6) and at about 2.5 m height. One long purity monitor (48 cm) was installed on the cryostat floor.

- Camera system: Eleven cryogenic cameras (see right panel of Fig. 4.6) and a LED-based lighting system were developed to monitor the cryostat inside. Six cameras are in the gas, pointing to the CRPs, the liquid argon surface and the liquid argon sprayers. Five cameras are in the liquid monitoring the cathode, the HV extender, the HV feedthrough and the PMTs.

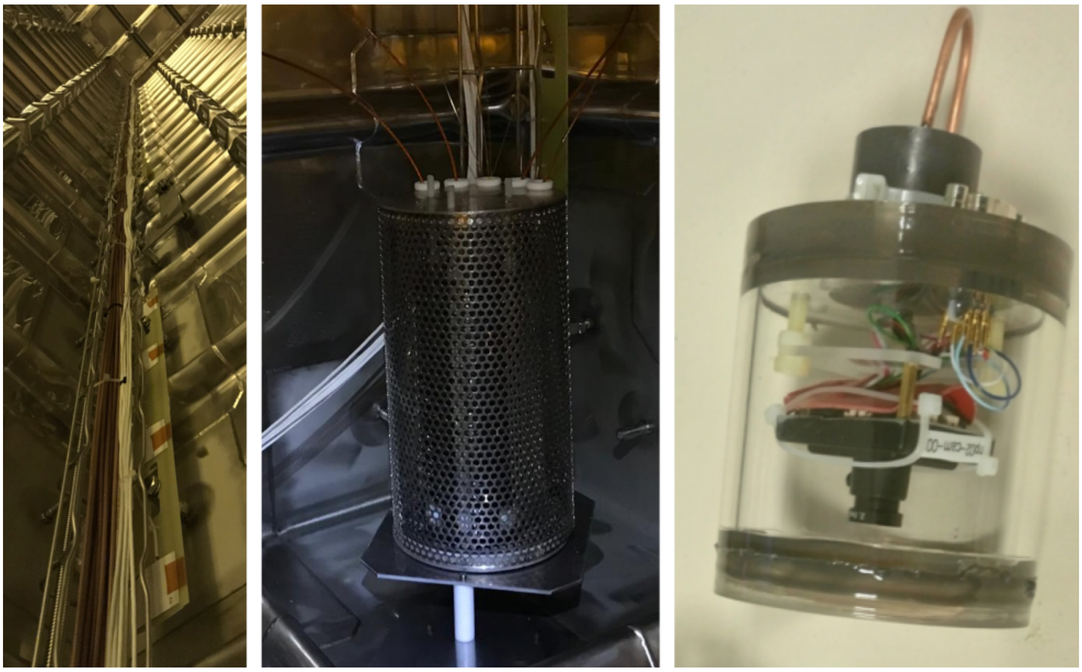

Figure 4.6: Pictures of the temperature sensors (left), the short purity monitor (center), and a cryogenic camera (right).

4.1.5 Cosmic Ray Taggers

Two Cosmic Ray Taggers (CRTs) are placed at the external walls of the cryostat. The CRTs provide a trigger to the rest of the detector for cosmic muons crossing the active volume. They are placed next to the instrumented CRPs, selecting diagonally crossing muons. A picture of one of the CRTs is shown on the right panel of Fig. 4.7. The positioning of the CRT panels is shown on Fig. 4.8.

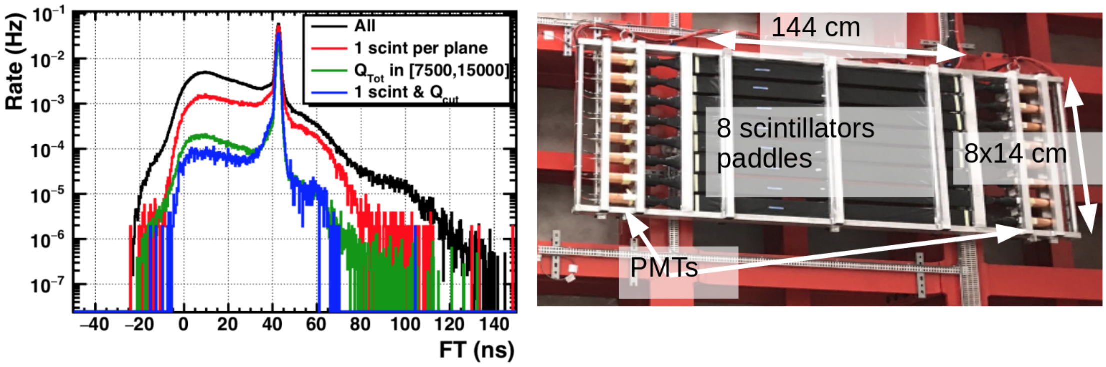

Figure 4.7: Left: Time of flight between the two CRT planes. The raw trigger rate is 0.3 Hz (black), the rate of clean coincidences is 0.11 Hz (blue) [211]. Right: View of the top CRT panel installed on the cryostat wall.

Each CRT is composed by eight scintillator bars with dimensions 1.44 m x 0.12 cm. Each bar has two photomultiplier tubes at the borders, to detect crossing particles. The 32

PMTs are read out by a uTCA system. The trigger logic is also implemented in the uTCA. An intermediate trigger is defined as the analog sum of both PMTs for each scintillator bar. The final trigger is built if two scintillator bars, one from each CRT plane, trigger at the same time.

While the system provides a trigger rate of 0.3 Hz, the final rate of muon-like events after applying a selection is 0.11 Hz. Left panel of Fig. 4.7 shows the event rate versus the time of flight between the two CRTs. The selection of muon-like events is based on the triggering scintillator bar multiplicity and the deposited charge (blue curve in the left panel of Fig. 4.7). The maximum in the time of flight of ~ 42 ns represents the expected travel time between both CRTs by a particle travelling at nearly the speed of light.

The crossing-muon track geometry can be reconstructed by looking at the position of triggering scintillator bars and the time difference between the two PMT signals at each border. This information is time-stamped, in order to match it with the charge and light readout data.

4.2 Photon Detection System

The Photon Detection System of ProtoDUNE Dual-Phase consists of 36 Hamamatsu R5912-20Mod photo-multiplier tubes (PMTs) that have been fully characterized both at room and at cryogenic temperature [191]. A picture of the 36 PMTs placed inside the detector is shown on Fig. 4.9. A diagram with the detailed positioning of the PMTs with respect to the rest of elements inside the detector is shown in Fig. 4.8.

PMTs are biased applying a positive high voltage (HV) at the anode while the photocathode is grounded. In this way only one coaxial cable is needed. A splitter circuit is placed outside the cryostat in order to decouple the HV and PMT signal. Three CAEN A7030 modules [212] are used to bias the PMTs with twelve channels each. They are controlled using WinCC, a control and data acquisition interface from Siemens [213].

The PMTs have maximal photon-detection efficiency of 20% at a wavelength of 400 nm. The photocathode quantum efficiency (i.e. the number of electrons emitted by the photocathode per incident photon, QE) versus the wavelength is shown in Fig. 4.10, as provided by the manufacturer for three of the PMTs at room temperature. Additionally, it has been shown that the QE remains stable when going to liquid argon temperature [214]. The main properties of the PMTs are summarized in Tab. 4.2.

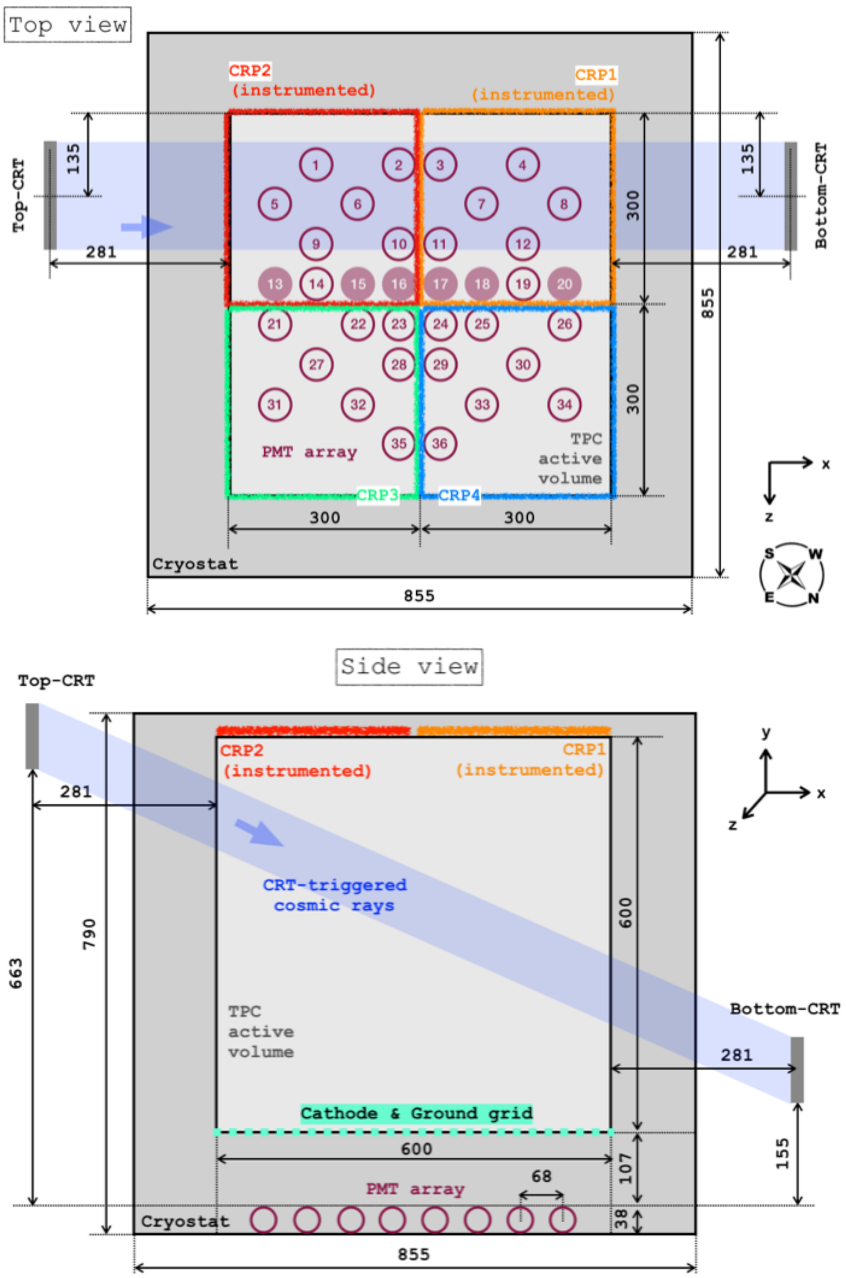

Figure 4.8: Dimension and position of the main elements in ProtoDUNE Dual-Phase (units are cm). The drift direction corresponds to the Y-axis. The PMTs are represented with circles and, on the top view, the empty ones correspond to PEN PMTs and the filled circles to TPB PMTs.

4.2.1 Wavelength shifting in ProtoDUNE Dual-Phase

Scintillation light in liquid argon has an emission peak at 127 nm where most photo-sensors are not sensitive. To efficiently detect this light, fluorescent materials are introduced to shift the wavelength of the scintillation photons towards the visible range where the PMTs have maximal detection efficiency. In this sense, ProtoDUNE Dual-Phase uses 30 PMTs

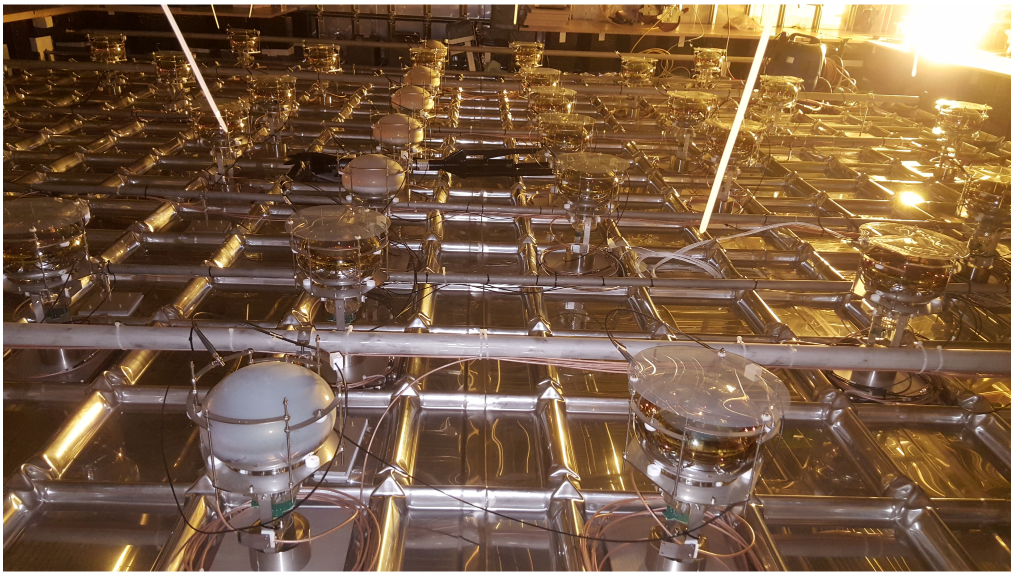

Figure 4.9: Picture of the 36 PMTs placed on the cryostat floor.

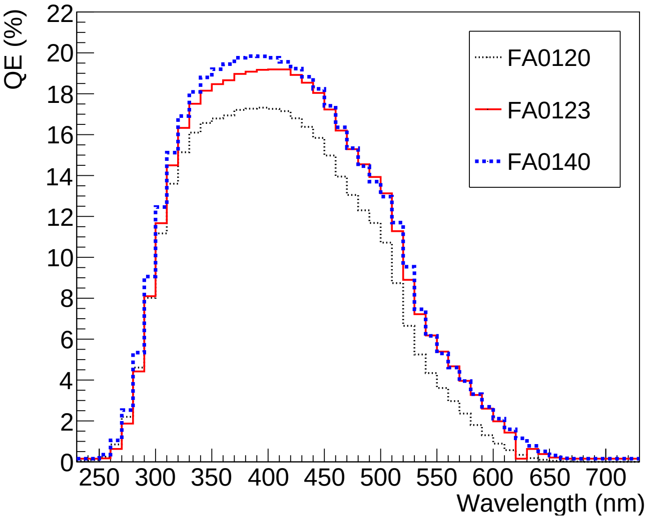

Figure 4.10: Quantum efficiency spectrum for 3 Hamamatsu R5912-20Mod PMTs provided by the manufacturer. The maximal value is obtained around 400 nm.

with polyethylene naphthalate (PEN) foils on top, and 6 with tetraphenyl butadiene (TPB) directly coated over the PMT glass, as shown in Fig. 4.11.

The PEN sample used in ProtoDUNE Dual-Phase is transparent and biaxially oriented, manufactured by GoodFellow [215], with reference ES361090/6. It has been installed as circle foils of 240 mm diameter and 0.125 mm thickness placed tangent to the PMT glass surface. It has a similar re-emission spectrum to TPB, with a maximum around 430 nm.

TPB was deposited over the PMT polished surface, using a dedicated evaporation system developed for ICARUS experiment [181]. The coating density is 0.2 mg/cm^2, which

PMT model	Hamamatsu R5912-20Mod
Number of dynode stages	14
Photocathode diameter	8 inch
Number of PMTs	36
Number of of PEN-foil PMTs	30
Number of TPB-coated PMTs	6
Quantum efficiency at 430 nm	0.183±0.013
Dark current rate at $G=10^7$	1.7±0.3 kHz
HV for $G=10^7$	1324±103 V

Table 4.2: Main properties of the ProtoDUNE Dual-Phase PMTs.

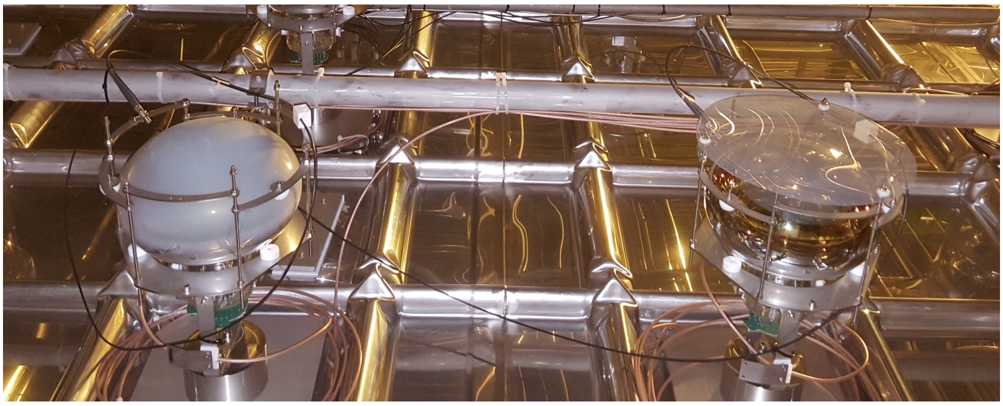

Figure 4.11: Detail of two PMTs inside the detector. TPB coated PMT is on the left, PEN foiled PMT is on the right.

corresponds to a coating thickness around 0.2 µm . As PEN, TPB also has a maximum of re-emitted photons around 430 nm [216]. Additionally, the detection efficiency of the TPB-coated PMTs has been measured at the University of Pavia by comparing the current given by the PMT under test and by a reference calibrated photodiode in a dedicated setup. Four PMTs were tested, obtaining an average detection efficiency of 0.14±0.2 [217]. The individual values are shown in Tab. 4.3. This means that 14% of 127-nm photons arriving at the coated photocathode will produce a photo-electron.

PMT	QE (430 nm)	DE (127 nm)
FA0120	0.168	0.115
FA0123	0.189	0.14
FA0140	0.192	0.145
FA0143	-	0.165
Average	0.183±0.013	0.14±0.02

Table 4.3: PMT quantum efficiency (QE) at 430 nm provided by the manufacturer and TPB-coated PMT effective detection efficiency (DE) for 127 nm photons measured in the laboratory.

A comparison of the performance of both wavelength-shifting systems is presented in Sec. 8.

4.2.2 Light Calibration System

ProtoDUNE Dual-Phase was equipped with a dedicated light calibration system in order to measure and monitor the gain of the PMTs. Having a well-defined gain is important for equalizing the PMT response to provide a uniform trigger, and to perform calorimetric studies.

The calibration system consists of six blue LEDs of 465 nm located outside the detector that are driven using a Kapustinsky circuit [218]. The Kapustinsky circuit provides fast nanosecond pulses with variable amplitude. The LEDs illuminate six fibres and a SiPM used a reference sensor. Each fibre is then connected to a 1-to-7 fibre bundle so that one fibre is installed pointing to each PMT. The response of the different components has been fully characterized [219]. The LEDs are pulsed at 1kHz with a 30 ns pulse width . The Kapustinsky circuit is controlled by a BeagleBone Black board, an open-hardware mini-computer that runs a Linux distribution. A diagram of the light calibration system set-up is shown in Fig. 4.12.

The design of the Light Calibration System has been described in detail in a dedicated publication [219].

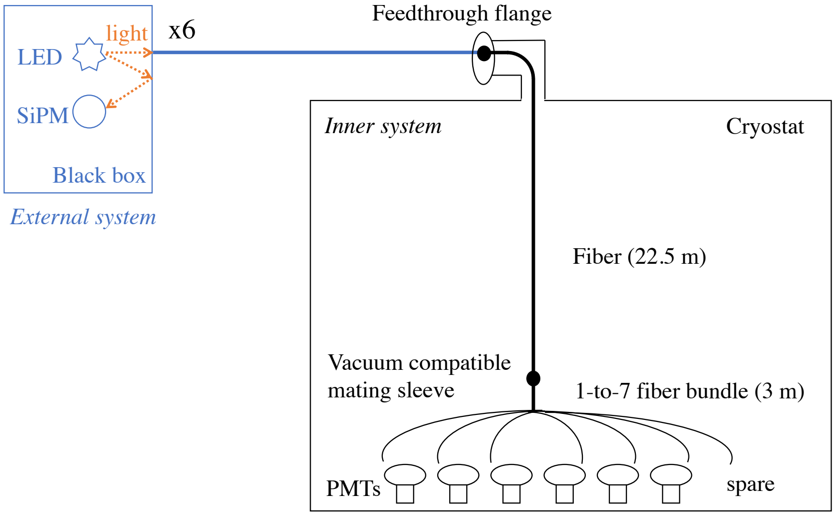

Figure 4.12: Diagram of the ProtoDUNE Dual-Phase light calibration system. The system shown in blue stays at room temperature and the inner system in black is at cryogenic temperature.

4.2.3 Light Readout System

The Light Read-Out (LRO) system digitizes the PMT signals. It is based on the commercial ADC v1740 supplied by CAEN. This digitizer has 64 analog input channels with 2Vpp dynamic range, and a maximum sampling rate of 62.5MS/s. The main specifications are summarized in Tab. 4.4. The ADC is connected to a PC by a 80MB/s optical link, and driven by a DAQ system based on MIDAS [220], a DAQ framework developed by PSI and TRIUMF.

ADC Model	CAEN v1740
Sampling Frequency	62.5 MS/s
Dynamic range	2 Vpp
Resolution	12 bits
Channels	64

Table 4.4: Main properties of the ProtoDUNE Dual-Phase light readout system.

4.2.4 Data Acquisition and Calibration Software

The data taking is performed using a dedicated software [221] which allows four acquisition modes by driving three different systems: the PMT high voltage, the light calibration system, and the light readout.

Four acquisition modes are allowed by the system:

- PMT self-trigger: The trigger is defined by looking at the PMT signals. It allows to define a threshold during a time window, and ask for coincidences among PMTs.
- External trigger: The trigger signal is received by an external system, either the CRT panels (see Sec. 4.1.5) or the DAQ global computer.
- Calibration mode: An external trigger signal is received from the light calibration system at a tunable frequency synchronized with the calibration light pulse sent to the PMTs.
- Random trigger: An external trigger signal is received from the light calibration system at a tunable frequency but keeping the LEDs off.

The software communicates with MIDAS to control the light readout, with WinCC to control the PMT voltages, and with the Beaglebone to control the calibration system. The user can control the full system using an graphical user-friendly interface. Figure 4.13 shows a screenshot of the acquisition software. On the *PMT High Voltage Settings* panel, the voltage and status can be chosen for each PMT. The *Channels in Trigger* panel allows selecting which PMT will take part in the PMT self-trigger. The *Front End Configuration* panel allows to select the acquisition window configuration, the trigger source and the PMT groups to acquire.

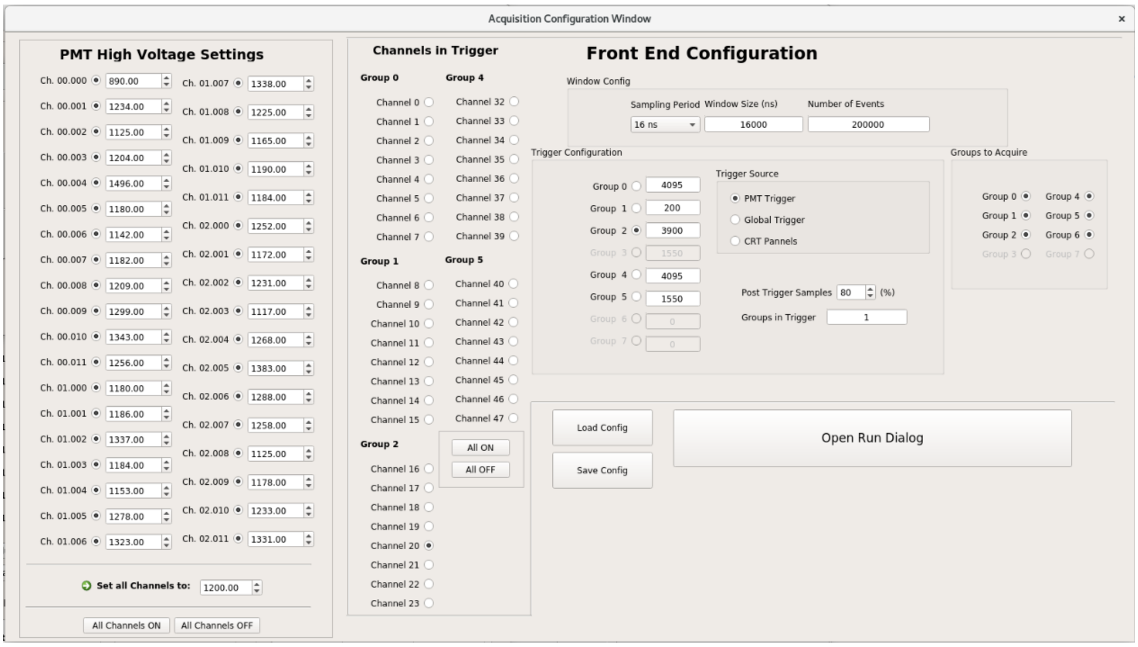

PMT High Voltage Settings

Ch. 00.000 ● 890.00
Ch. 00.001 ● 1234.00
Ch. 00.002 ● 1125.00
Ch. 00.003 ● 1204.00
Ch. 00.004 ● 1496.00
Ch. 00.005 ● 1180.00
Ch. 00.006 ● 1142.00
Ch. 00.007 ● 1182.00
Ch. 00.008 ● 1209.00
Ch. 00.009 ● 1299.00
Ch. 00.010 ● 1343.00
Ch. 00.011 ● 1256.00
Ch. 01.000 ● 1180.00
Ch. 01.001 ● 1186.00
Ch. 01.002 ● 1337.00
Ch. 01.003 ● 1184.00
Ch. 01.004 ● 1153.00
Ch. 01.005 ● 1278.00
Ch. 01.006 ● 1323.00
Ch. 01.007 ● 1338.00
Ch. 01.008 ● 1225.00
Ch. 01.009 ● 1165.00
Ch. 01.010 ● 1190.00
Ch. 01.011 ● 1184.00
Ch. 02.000 ● 1252.00
Ch. 02.001 ● 1172.00
Ch. 02.002 ● 1231.00
Ch. 02.003 ● 1117.00
Ch. 02.004 ● 1268.00
Ch. 02.005 ● 1383.00
Ch. 02.006 ● 1288.00
Ch. 02.007 ● 1258.00
Ch. 02.008 ● 1125.00
Ch. 02.009 ● 1178.00
Ch. 02.010 ● 1233.00
Ch. 02.011 ● 1331.00

Set all Channels to: 1200.00

Channels in Trigger

Group 0
Channel 0 ○
Channel 1 ○
Channel 2 ○
Channel 3 ○
Channel 4 ○
Channel 5 ○
Channel 6 ○
Channel 7 ○

Group 1
Channel 8 ○
Channel 9 ○
Channel 10 ○
Channel 11 ○
Channel 12 ○
Channel 13 ○
Channel 14 ○
Channel 15 ○

Group 2
Channel 16 ○
Channel 17 ○
Channel 18 ○
Channel 19 ○
Channel 20 ●
Channel 21 ○
Channel 22 ○
Channel 23 ○

Group 4
Channel 32 ○
Channel 33 ○
Channel 34 ○
Channel 35 ○
Channel 36 ○
Channel 37 ○
Channel 38 ○
Channel 39 ○

Group 5
Channel 40 ○
Channel 41 ○
Channel 42 ○
Channel 43 ○
Channel 44 ○
Channel 45 ○
Channel 46 ○
Channel 47 ○

Front End Configuration

Window Config
Sampling Period: 16 ns
Window Size (ns): 16000
Number of Events: 200000

Trigger Configuration
Group 0 ○ 4095
Group 1 ○ 200
Group 2 ● 3900
Group 3 ○ 1550
Group 4 ○ 4095
Group 5 ○ 1550
Group 6 ○ 0
Group 7 ○ 0

Trigger Source
● PMT Trigger
○ Global Trigger
○ CRT Pannels

Post Trigger Samples 80 (%)
Groups in Trigger 1

Groups to Acquire
Group 0 ● Group 4 ●
Group 1 ● Group 5 ●
Group 2 ● Group 6 ●
Group 3 ○ Group 7 ○

Figure 4.13: Graphical interface of the ProtoDUNE Dual-Phase acquisition software.

In order to monitor the data-taking, an event display has been developed. It is based on the ROOTANA package [222], and it has been adapted to the used ADC model. It runs online as the data is taken showing the individual waveforms of each PMT. A screenshot of the event display is shown in Fig. 4.14.

The collected data is first stored in the DAQ computer during the data taking. At the end of the day, a dedicated script saves the data in the backup servers and converts the binary files into ROOT format, that are easier to analyze.

The design of this acquisition software has been published in a dedicated article [221].

4.3 Installation, commissioning and operation

The installation of ProtoDUNE Dual-Phase started in 2017 with the installation of the cryostat vessel. The full assembly of the detector took around two years, concluding in June 2019 when the man-hole access was closed. Then, the detector was purged and filled with liquid argon and the different detector systems were commissioned. The first run of operation and data-taking started in September 2019, and concluded a year later, in September 2020. Then, the detector was emptied and several R&D activities took place. A

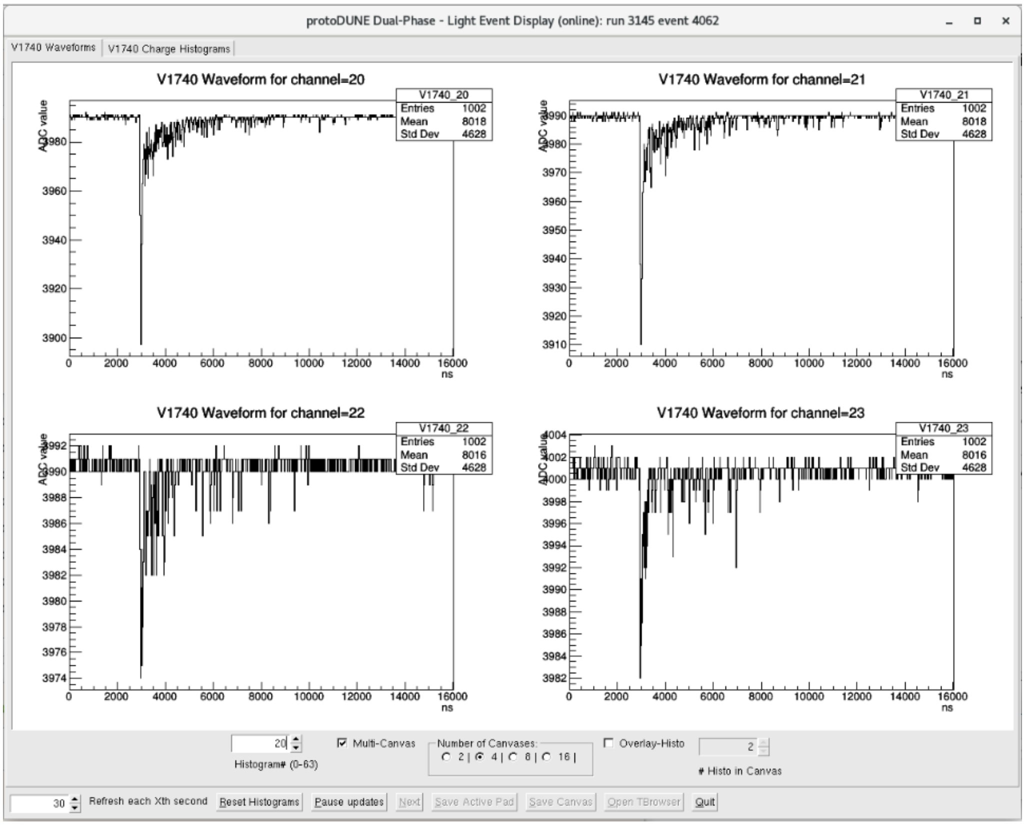

Histogram# (0-63): 20

☑ Multi-Canvas

Number of Canvases: ○ 2 | ● 4 | ○ 8 | ○ 16 |

☐ Overlay-Histo

Histo in Canvas: 2

Refresh each Xth second: 30

Figure 4.14: Event display with four selected PMT channels showing a ProtoDUNE Dual-Phase light event with an S1 signal. The ADC value is shown in the y-axis and the acquisition time in the x-axis with a 16 ns sampling time.

year later, in August 2021, the detector was filled again in order to perform new tests on an improved HV system. Figure 4.15 summarizes the timeline of the main phases since the installation began.

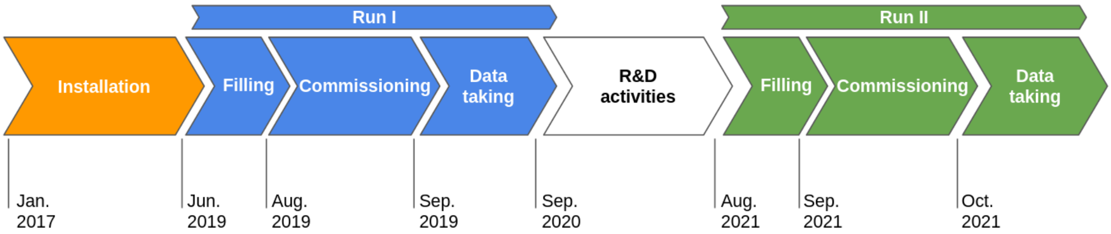

Figure 4.15: Timeline of the ProtoDUNE Dual-Phase installation, commissioning and operation.

4.3.1 Detector installation

The installation the ProtoDUNE Dual-Phase cryostat started in 2016 with the assembly of the outer steel structure and concluded in November 2017 with the installation of the inner membrane and a cleanroom next to the cryostat. Then, the main elements inside the cryostat were assembled. First, the field cage modules were assembled individually in the cleanroom, installed on the cryostat roof and connected. The cathode and the ground grid were constructed outside the detector and assembled inside the cryostat. The full High Voltage system was tested several times at nominal HV in air, with satisfactory results. Due to time constraints, the HV extender was never tested in liquid argon before its installation.

The CRPs were constructed in a cleanroom. Due to time constraints, it was decided to instrument only two of the four CRP modules. Their mechanical behaviour was validated in a cold box and also HV stability tests were performed. After the tests, they were transported and installed inside the cryostat. Finally, a metrology survey was performed to adjust the vertical positioning of the four CRP frames at the same height. This was done using a laser tracker with a positioning precision of 0.1 mm.

The photon detection system was installed in February 2019 on the cryostat membrane floor. The PMTs were oriented with the first dynode perpendicular to the Earth magnetic field, to avoid disturbance on the amplification process in the dynode chain. PMTs were previously characterized with dedicated measurements at CIEMAT to verify their response [191], also at high pressure [223]. The PMT support was designed to stand the PMT in opposition to the buoyancy force in the liquid argon. This was also verified in a dedicated flotation test in the laboratory.

Six PMTs were coated at the CERN Thin Film Facility in the summer 2018. The coating density was 0.2 mg/cm^2 in the middle, with a uniformity tolerance from the edge of 20% [217]. The coating setup is shown in Fig. 4.16. A PEN sheet was placed on top of the other 30 PMTs.

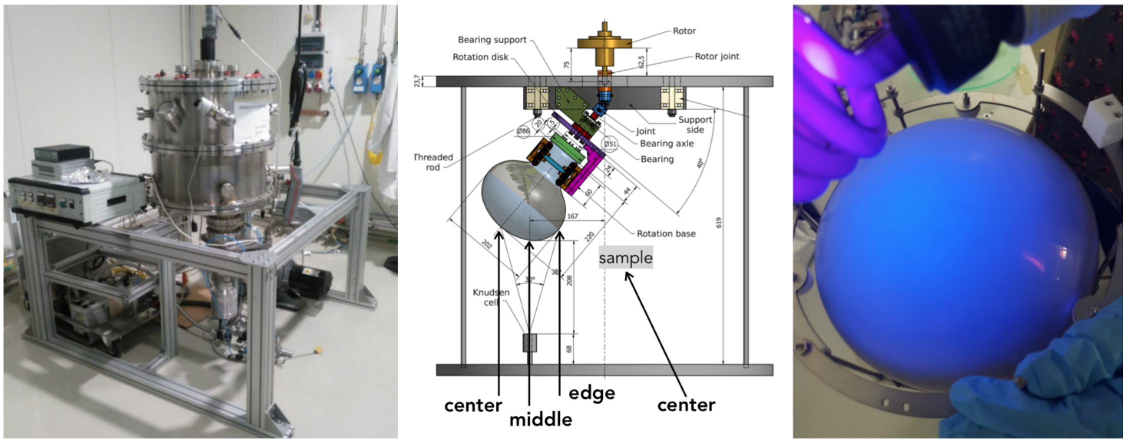

Figure 4.16: Left: Picture of the TPB coating setup. Center: Diagram of the coating setup inside the vessel. Right: Coated PMT illuminated with UV light.

The installation concluded with the sealing of the Temporary Construction Opening

(TCO) in May 2019 and the man-hole access.

4.3.2 Detector filling and commissioning

The cryostat internal volume was purged from June 14th 2019 with purified gas argon injected to the bottom part of the detector, pushing the air upwards, since the argon is denser. After two weeks of purging, the nitrogen and oxygen level went below a few ppm, and the cooling started. A timeline with the main dates of the filling and purification process is shown in Fig. 4.17. The cool-down was performed by spraying droplets of argon, and introducing liquid argon at the bottom of the cryostat. After one month, on August 9th 2019 the nominal temperature of 77 K was reached.

In total 900 tons of argon were used. 750 tons is the stable amount of liquid inside the cryostat, while the rest was evaporated during the cooling phase. Once the filling was completed, the recirculation system was activated, to slowly improve the argon purity.

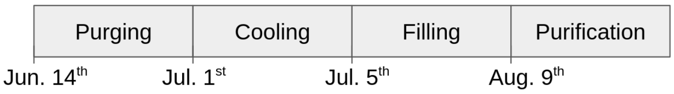

Figure 4.17: Timeline of the purging, filling and purification process during 2019 in ProtoDUNE Dual-Phase.

HV system commissioning

Once the detector was filled, the ramp-up of the high voltage started. However, a fault on the HV extender did not allow it to reach the nominal voltage of -300 kV in the cathode. The cause of the fault was a short circuit in the inner conductor of the extender with the outer ring, around 1 m below the anode plane. As a consequence, the drift field was not uniform and only present in approximately the first meter of drift. Due to this short, the cathode was most of the time at -50 kV. The resulting drift field is simulated using a finite element method model. According to this simulation, the drift field is quite uniform on the top part of the detector, with an average value of 0.15-0.20 kV/cm. The map of the resulting drift field is presented in Fig. 4.18 with the cathode at -50 kV.

Liquid argon surface instability

Additionally, the cameras inside the detector recorded bubbles emerging in the vicinity of the CRPs. The bubble formation was attributed to the argon gas accumulating in the field-shaper corners. Since the presence of the bubbles causes instabilities in the CRP

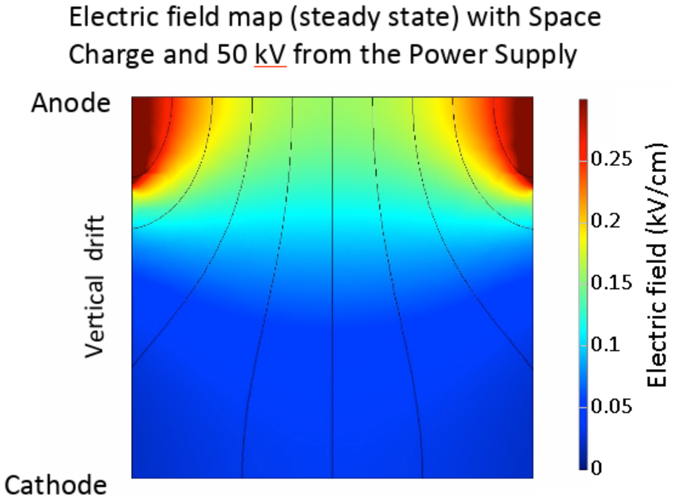

Figure 4.18: Drift field in ProtoDUNE Dual-Phase with the cathode at 50 kV. The drift direction is along the vertical axis and the colour scale represents the electric field strength [211].

operation, they were mitigated by scheduling high-pressure cycles. The pressure inside the cryostat was increased by 10 mbar for 2-3 hours, allowing to stop the bubbling for around one week. Every Monday morning, a high-pressure cycle of two hours was scheduled in order to allow the normal operation. Figure 4.19 shows the liquid argon surface during the bubbling in the left panel, and during a high pressure cycle in the right panel.

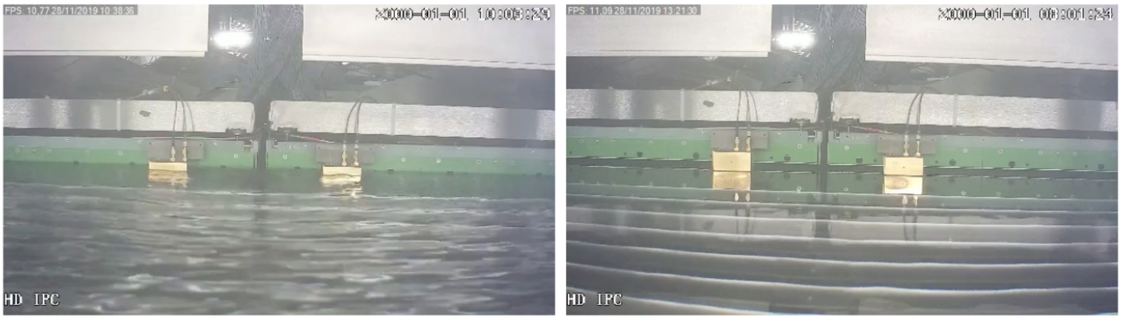

Figure 4.19: Left: Bubbles from the field cage perturbing the liquid surface. Right: Bubbles disappeared during a high pressure cycle [211].

These instabilities in the liquid gas inter-phase impacted the operation of the CRP high voltage, triggering sparks and discharges that could damage the DAQ system, and also the CRPs themselves.

Given these limitations, the detector did not operate at its nominal configuration. The acquired data were affected by the non-uniform drift field and the low CRP gains. Therefore, the work presented in this thesis is based mainly in the data taken in absence of electric fields. This instability did not compromise the operation of the photon detection system, that was stable during all the data-taking (see chapter 5).

4.3.3 Detector operation

Initially, the operation plan of ProtoDUNE Dual-Phase included the data-taking with a beam-line from the SPS for several months in 2018 before the starting of the second long shutdown (LS2) in 2019. However, since the detector installation concluded in 2019 this was not possible. Despite the limitations in the HV and CRP operation (see Sec. 4.3.2) the detector was able to take data from cosmic rays from June 2019 to September 2020.

The first tracks were recorded in August 29th. Figure 4.20 shows some example events taken during the operation.

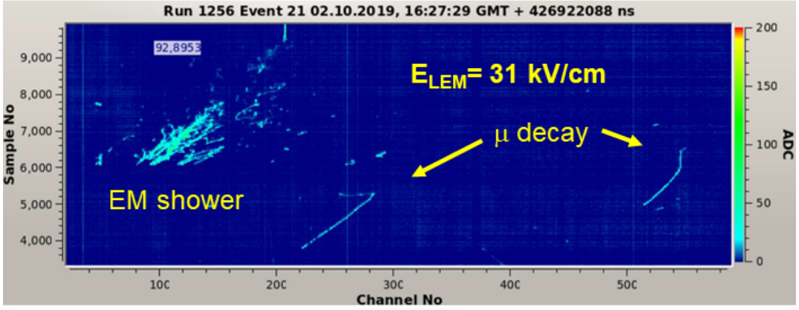

(a) Electromagnetic shower and two muon decay candidates.

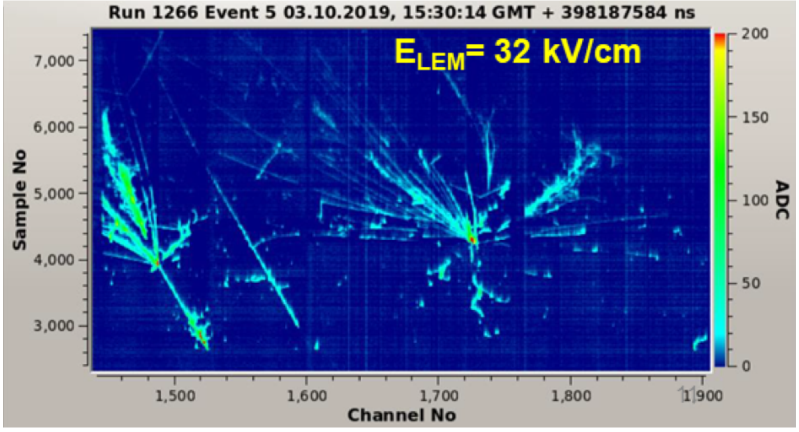

(b) Multiple hadronic interactions in a shower.

Figure 4.20: Example of raw-data tracks from cosmic muons in ProtoDUNE Dual-Phase.

The CRT panels were installed in December 2020, providing an external trigger to the photon detection system.

The CRPs were operated from August 2019 until March 2020. During this time the performance of the CRPs was studied with several dedicated data-taking campaigns, in particular, to study the gain and the charging-up of the LEMs. After 8 months of operation, around 22% of the LEMs had to be kept below the nominal voltage, to mitigate the risk of carbonization due to the frequent discharges. Finally, the charging-up effect on the LEMs reduced the gain in a factor of two after some months of operation. The detailed study on the LEM operation can be found in [211].

The recirculation of the liquid argon increased the purity providing an electron lifetime greater than 9 ms as measured by the long purity monitor (see bottom panel of Fig. 4.21). The measurement provided by the short purity monitors (see top panel of Fig. 4.21) became soon saturated as they are too short to provide reliable measurement for lifetimes greater than 2 ms.

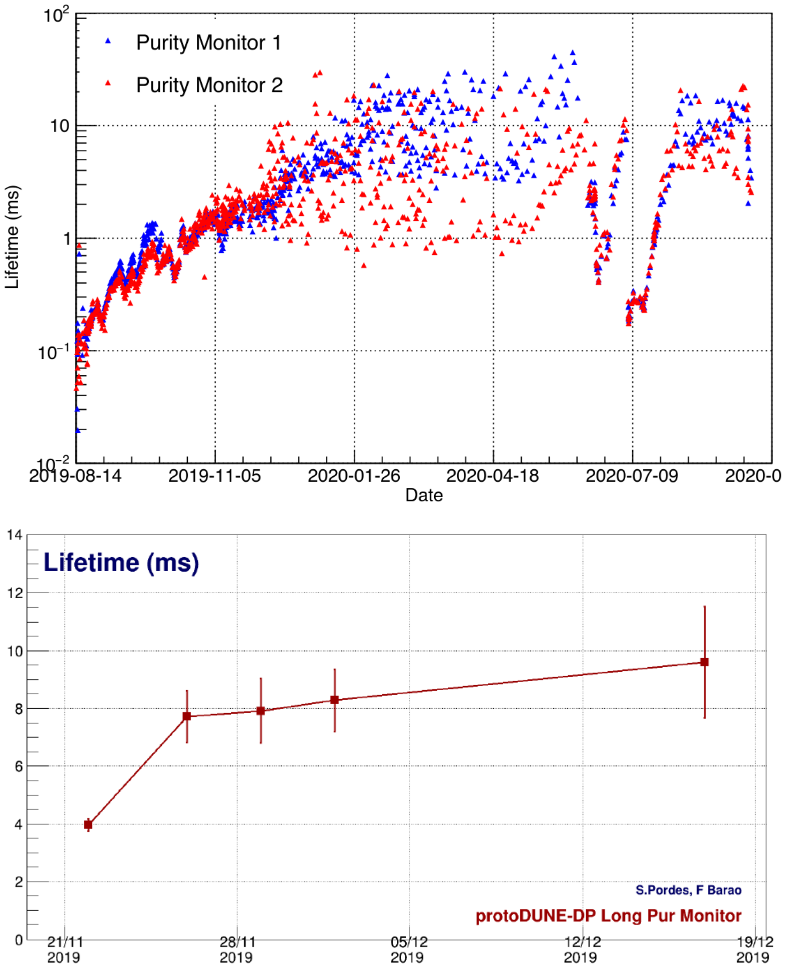

Figure 4.21: Electron lifetime measured by the short (top panel) and long (bottom panel) purity monitors in ProtoDUNE Dual-Phase.

HV intervention

In order to fix the short in the HV extender, an intervention was planned for summer 2020. The goal was to repair the short connection, in order to reach the nominal drift field in the full volume. In May 2020, the recirculation system was stopped, and the liquid argon started to evaporate. The liquid level dropped 2.3 m, exposing the part of the extender to be repaired. In June 17th, the intervention took place. A second intervention took place on July 15th to replace the full HV feedthrough. Although the short was initially solved, current discharges appeared from the HV extender to the field cage connection due to an open circuit. As a result, the operation of the HV system at its nominal value was not accomplished.

Operation with xenon-doped liquid argon

In July 2020, after the HV intervention, the detector was refilled using 230 ton of xenon-doped liquid argon contaminated with nitrogen from ProtoDUNE-SP. The liquid argon from ProtoDUNE Single-Phase was contaminated with nitrogen due to its exposure to air. The concentration of nitrogen was estimated in 7.7 ppmv (ppm in volume or per specie) by analyzing the impact in the slow component of the scintillation light (see Sec. 2.3.2). Afterwards, xenon injections were performed in ProtoDUNE-SP to study its impact on the recovery of light detection. As a result, the liquid argon transferred from ProtoDUNE-SP was contaminated with 7.7 ppmv of nitrogen, and doped with 18.8 ppmm (ppm in mass) of xenon, resulting in a concentration of 5.8 ppmm of xenon and 2.4 ppmv of nitrogen in the ProtoDUNE Dual-Phase volume after the refilling.

Finally, in August 2020 two injections of nitrogen were performed to measure its effect on the light attenuation. Table 4.5 summarizes the liquid conditions in ProtoDUNE Dual-Phase during the full operation time.

Time period	Liquid conditions
Aug. 10th 2019 - May. 4th 2020	pure LAr at nominal level
May. 4th 2020 - Jul. 22nd 2020	LAr evaporation
Jul. 24th 2020 - Aug. 14nd 2020	LAr + Xe (5.8 ppmm) + N_2 (2.4 ppmv)
Aug. 14th 2020 - Aug. 28nd 2020	LAr + Xe (5.8 ppmm) + N_2 (3.4 ppmv)
Aug. 28th 2020 - Sep. 4nd 2020	LAr + Xe (5.8 ppmm) + N_2 (5.3 ppmv)

Table 4.5: Summary of the liquid conditions in ProtoDUNE Dual-Phase during the different data-taking periods. Concentrations are given in ppmm (ppm in mass) for xenon, and in ppmv (ppm in volume or per specie) for nitrogen.

4.3.4 The second run of ProtoDUNE Dual-Phase in 2021

Given the limitations in the HV system during the first run of operation of ProtoDUNE Dual-Phase, a new run of operation was scheduled to test a redesigned HV feedthrough and extender (see the left panel of Fig. 4.22). The complexity of the extender has been reduced to a metallic pipe of 20 cm diameter and highly electro-polished outer surface, using the liquid argon as the insulator. This activity was done in the framework of the R&D activities to validate the new Vertical Drift design (see Sec.3.1.3). The most critical components of the HV feedthrough were tested at Fermilab in April 2021. This second run was a full-scale test of the HV distribution system for the VD design.

The HV feedthrough and extender were replaced, and in August 4th 2021 the cryostat started a new purging cycle with pure gas argon. The filling with liquid argon started on August 16th 2021. In September 15th 2021 the liquid reached the nominal level, and the re-circulation started to slowly improve the purity.

In September 2021, the testing of the HV system started, successfully reaching the nominal voltage of -300 kV without problems. Stability tests were performed, showing that the system is able to maintain the nominal electric field for long time periods. Some current discharges producing a large amount of visible light inside the detector were identified. This light was detected by the cameras inside the detector (see right panel of Fig. 4.22) and by the photon detection system. The discharge rate was around one per hour. This is caused by the accumulation of the ionization electrons right below the gas-liquid interface, since the detector was operating with the CRPs out of the liquid and without collecting charge.

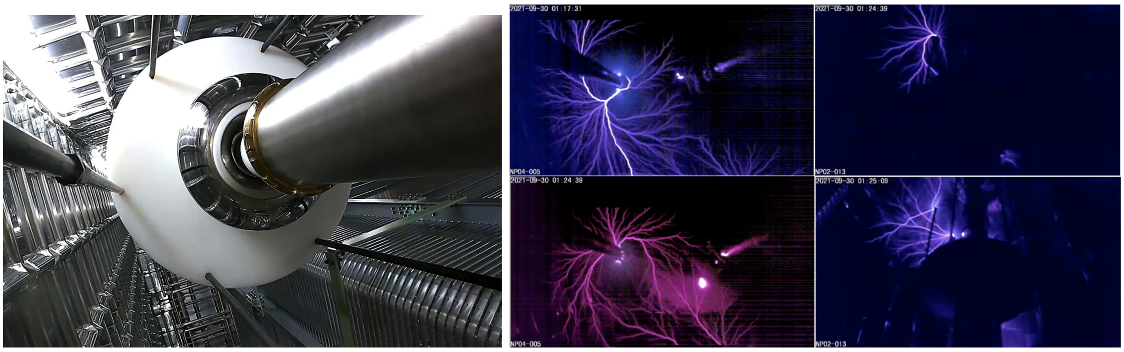

Figure 4.22: Left: Picture of the re-designed HV-Feedthrough tested during the second run. Right: Pictures of discharges at the top end of the rods (in gas) during the second run.

The cathode voltage was maintained at -300 kV from September 14th 2021 to November 4th 2021. In November 2021 the feedthrough was replaced due to a failure in a cable connection, and the cryostat was exposed to open-air. As a consequence the purity dropped. After the replacement, the stability high voltage tests were resumed, and the cathode was maintained at -300 kV from December 22th until March 2^{nd} 2022.

At the end of the run, in February 23^{rd}, the charge readout was reactivated to acquire some events with the TPC in single phase mode. In this configuration, the CRP planes were immersed in the liquid argon, and the anodes collected the drifted electrons without amplifying the signal. Despite the limited purity, long tracks were acquired with the full 6-m drift, validating the design of the HV system for the Vertical Drift module.

Chapter 5

Performance of the ProtoDUNE Dual-Phase Photon Detection System

The operation of the ProtoDUNE Dual-Phase photon detection system lasted from June 2019 until November 2020, taking cosmic-ray data with pure liquid argon and xenon-doped liquid argon contaminated with nitrogen.

In contrast to the charge system, the photon detection system was able to take data without inconvenience during the full detector operation. The data-taking started as soon as the detector was purged with argon gas in June 2019. The data-taking with the detector filled with liquid argon started in August 2019 until November 2020, when the detector was finally emptied (see Sec. 4.3 and Fig. 4.15).

It must be noted that the PMTs could not take data normally: In order to monitor the instabilities in the liquid argon surface, it was required to have the lights and cameras inside the detector activated almost full time. Therefore the PMTs had to be switched on and off every day. Despite this, the system was stable and all the PMTs detected scintillation light from the very first moment. An example of a typical S1 scintillation light signal in pure liquid argon is shown in Fig. 5.1. The prompt signal in the first nanoseconds corresponds to the fast component of the scintillation light, and the long tail corresponds to the slow component (see Sec. 2.3). Figure 5.2 shows an example event in which all the PMTs are detecting an S1 signal. The position of each PMT in the figure represents its position in the detector layout.

An important milestone for the ProtoDUNE Dual-Phase photon detection system is the detection of secondary electroluminescence light signals (S2) by all 36 PMTs. This light is produced by the electrons extracted in the gas phase at 7 m from the PMTs, and it provides information about the track geometry. An example S2 signal produced by a

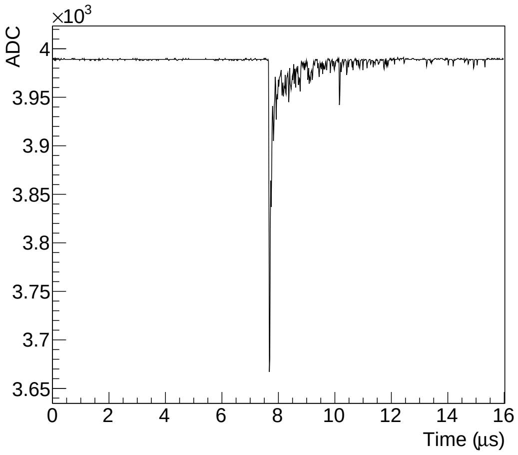

Figure 5.1: Example of a typical scintillation signal detected by a PMT in ProtoDUNE Dual-Phase.

high energy vertical shower is shown in Fig. 5.3. In this waveform, the S2 appears as a continuum of light starting right after the S1 and lasting around 1 ms, meaning that the track crossed the liquid-gas interface.

The integrity of the photon detection after more than one year of operation was verified by a physical inspection once the operation concluded and the detector was emptied and warmed up. This inspection happened in February 2021, and it was found that one PMT had a PEN-foil detached. This was already noticed during the data taking since one PMT suddenly started to detect much less light. The detachment of the foil happened during the partial evaporation of the liquid before the HV intervention (see Sec. 4.3.3), in July 2020, and it is attributed to the argon flow that loosened the supporting washers. This fact does not affect the results shown in this thesis since it happened at the end of the data taking. Concerning the TPB-coated PMTs, despite some dust deposited on them, the integrity of the TPB coating after one year of operation was verified.

Additionally, the photon detection system acquired data in autumn 2021 when the detector was re-filled to test the new high voltage system design (see Sec. 4.3.4). In this time, data was taken with the cathode at the nominal voltage of 300 kV. However, as the CRPs were not operated, the data-taking conditions were not totally under control, and also the level of purity reached was limited. Therefore only a selection of results from this period are included in this chapter.

The performance of the ProtoDUNE Dual-Phase photon detection system is widely described in a dedicated publication [224]. In this chapter, the performance of ProtoDUNE Dual-Phase photon detection system is summarized. First, the collected data is described in Sec. 5.1. Sections 5.3 and 5.4 describe the achieved signal-to-noise ratio and the gain

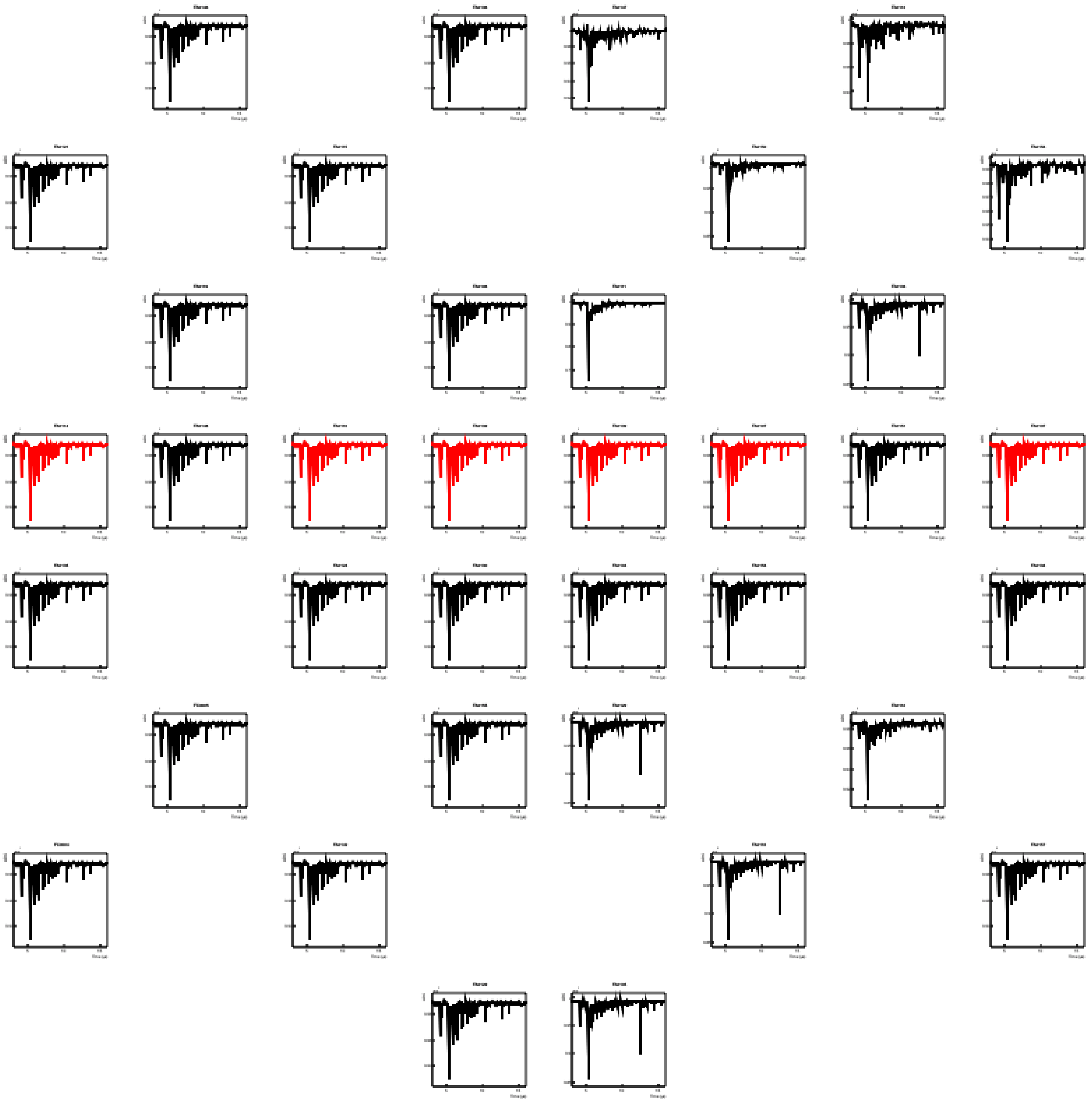

Figure 5.2: Example of a scintillation light event detected by the 36 PMTs in ProtoDUNE Dual-Phase. The position of the histogram represents the PMT position in the detector. TPB PMTs are drawn in red while PEN PMTs are indicated in black. The x-axis range is fixed in 16 μs for all PMTs while the y-axis range (in ADC counts) is customized for each PMT to observe the fast light signal.

stability of the system respectively. The analysis framework and typical data selection criteria applied are explained in Sec. 5.2. The characterization of the scintillation time profile in absence of the drift field is explained in Sec. 5.5. The monitoring of the slow component of the scintillation light as an indicator of the liquid argon purity is shown in Sec. 5.6. The scintillation light attenuation in liquid argon is measured in Sec. 5.7. Finally, the dependence of the scintillation light with the drift field is described in Sec. 5.8.

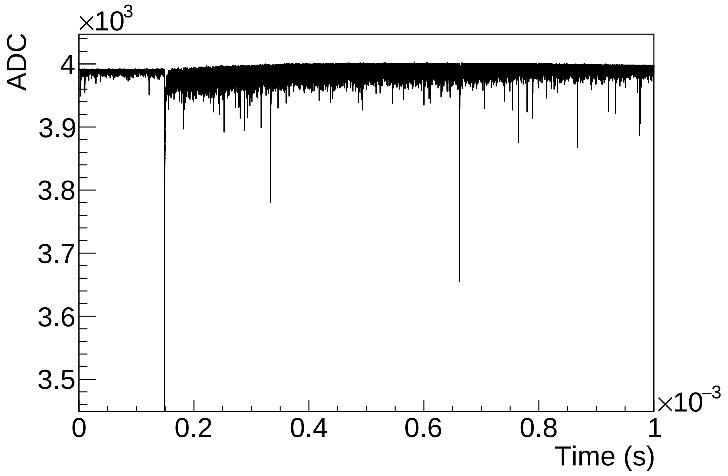

Figure 5.3: Example of a PMT event showing an S1 primary scintillation (at 0.15 ms) and a secondary electroluminescence S2 light signal right after the S1 in ProtoDUNE Dual-Phase lasting around 1 ms. The drift, extraction and amplification fields were active.

5.1 Summary of collected data

The ProtoDUNE Dual-Phase photon detection system took data in four trigger modes (see Sec. 4.2.4): PMT self-trigger, CRT trigger, random trigger and calibration trigger modes. A summary of the taken data by trigger mode is presented in Tab. 5.1. A total time of 675 hours was recorded during the operation of the detector, representing more than 120 million events. Most of the data have been taken in PMT self-trigger mode, although most of the operation time was dedicated to the CRT trigger mode. This is due to the slow rate provided by the CRT panels (see Sec. 4.1.5). It must be noted that the PMTs had to be switched off every day to monitor the instabilities in the liquid argon surface as explained before. This prevented us from taking data continuously. However, the stability of the system was also successfully tested during long runs of $\sim$24 hours duration.

Due to the high voltage limitations (see Sec. 4.3.2), most of the light data were acquired without drift field, containing only primary scintillation signals. Also, events containing secondary light signals were collected at different drift and amplification fields, as it is summarized in Tab. 5.2. Test mode data correspond to data taken with unstable detector conditions.

5.2 Analysis framework and selection criteria

Photon detection system data are divided in runs. A run is a group of events taken with the same trigger and with the detector in stable conditions. Each event is composed by 36

Trigger	# of events (M)	Time (h)
PMT	85.3	96
CRT Panels	0.6	515
Calibration	30	42
Random	14.7	21
Total	130.7	675

Table 5.1: Summary of the trigger conditions indicating the number of events and the total time of data taken during the operation of ProtoDUNE Dual-Phase.

Drift field	LEMs voltage	# of events (M)	Time (h)
OFF	-	85.1	342
ON	0 kV	13.6	72
	2.5-3.6 kV	7.7	212
Test	-	23.2	48
Total	-	130.7	675

Table 5.2: Summary of the detector configurations indicating the number of events and the total time of data taken with different voltage across LEMs during the operation of ProtoDUNE Dual-Phase in 2019-2020.

waveforms, one per PMT. There is one event per trigger signal arriving to the DAQ. An example waveform is shown in Fig. 5.1, and an example event in Fig. 5.2.

The baseline is computed for each waveform by doing the average of 30 consecutive samples in a clean interval without signal. If there is a signal in the first 30 samples, the next 30 samples are considered. The standard deviation (STD) of the baseline is computed (with a typical value of 0.6 ADC, see Sec. 5.3).

The distance from the baseline to the minimum of the signal is called the S1 amplitude ($\sim$300 ADC in Fig. 5.1), the peak time is the time bin when the signal reaches the maximum amplitude and the S1 charge is defined as the integral over 3 μs after the peak time. Since the decay time of the slow component of the scintillation light is typically $\sim$1.5 μs, this range allows integrating most of the S1 charge avoiding the pile up of signals. The S1 charge is converted in PE units dividing by the average charge of an SPE signal.

Additionally, a data selection is required in order to avoid noise and backgrounds distortions. The selection criteria are applied on a per-waveform basis. They are:

- PedestalStatus: Events for which it is not possible to compute a reliable baseline are removed. These are waveforms with the full time window filled with signal from a high energy showers.
- PedSTD: To avoid noisy events, those events with a baseline standard deviation

above 2 ADC are removed. The typical value is around 0.6 ADC.

- PreTriggerSTD: The standard deviation of the 30 samples before the peak time is computed. Events with a standard deviation above 2 ADC are removed. This cut ensures that we are not detecting photons from the slow component of other muons that crossed before. 30 samples correspond to around 0.5 μs.
- PeakTimeRange: Events with the peak time far from the trigger time are removed, with a tolerance of 2 μs. Since the trigger time is always fixed at around 3 μs, the peak time is expected at the same time. This is the most significant cut, removing around 10% of the events. It removes the distortion introduced by the pile-up of signals.

The typical efficiency for a selection of runs is shown in Fig. 5.4.

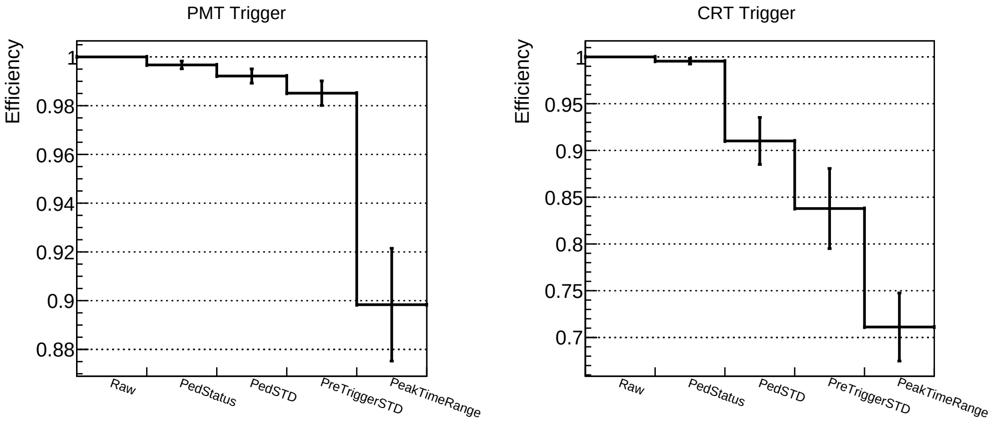

Figure 5.4: Efficiency of the selection criteria. Error bars show the standard deviation for all the PMTs and runs. Selection names are defined in the text.

5.3 Signal-to-noise ratio

The remarkable low level of noise achieved int he detector can be appreciated in the time region before the scintillation light signal in Fig. 5.1. The fluctuation of the baseline was measured as the STD of the ADC counts in the first 480 ns of each waveform (30 samples), obtaining an average of 0.6±0.1 ADC ($\sim$ 0.2 mV). Figure 5.5 shows the excellent noise stability during almost one year of operation. The amplitude of a single photo-electron at the nominal gain of 10^7 is $\sim$7 ADC counts and therefore a signal-to-noise ratio greater than 11 is obtained, which is important to measure low energy signals at the level of the SPE.

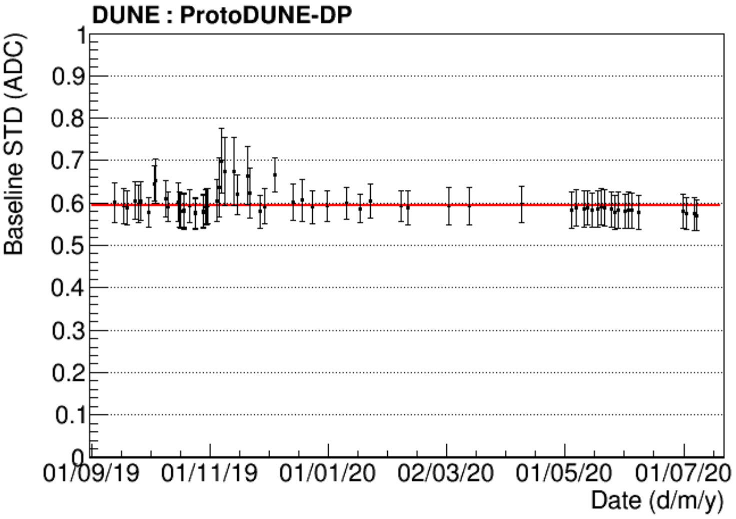

Figure 5.5: Average of the baseline STD during the operation of ProtoDUNE Dual-Phase. The mean value of 0.6±0.1 ADC counts is shown in red. The error bars represent the STD of the value for the 36 PMTs.

5.4 PMT gain stability

The calibration of the PMTs is an important step to perform calorimetry studies and to effectively monitor the production of the light in the detector. This is accomplished by weekly calibration runs, in which the light calibration system illuminates the PMT photocathode at the SPE level (see Sec. 4.2.2). The SPE signal is then integrated in order to measure the SPE charge at a given voltage. An example of the SPE charge spectrum is shown in Fig 5.6 in units of the electron charge ($|e|$). The distance between the first and the second maximum corresponds to the PMT gain. The center of the maxima are determined by Gaussian fits.

Figure 5.7 shows the variation of the PMT gains at a fixed voltage of 1500V during the operation of ProtoDUNE Dual-Phase. The plotted value is the ratio of the individual PMT gain at 1500V over the average gain for all the PMTs. Even though the PMTs were switched on and off every day, the PMT gains are stable with time. The STD of the gain at 1500V on average for all the 36 PMTs during one year of operation is 9%.

5.5 Scintillation time profile in absence of drift field

The scintillation light emission in liquid argon has a characteristic time dependence as mentioned in Sec. 2.3. To get the scintillation time profile from the PMT waveforms, signals from cosmic muons are selected by triggering on a TPB-coated PMT with a minimum amplitude of 25 PEs. PMT gain is set at $5{\cdot}10^6$ and events saturating the ADC

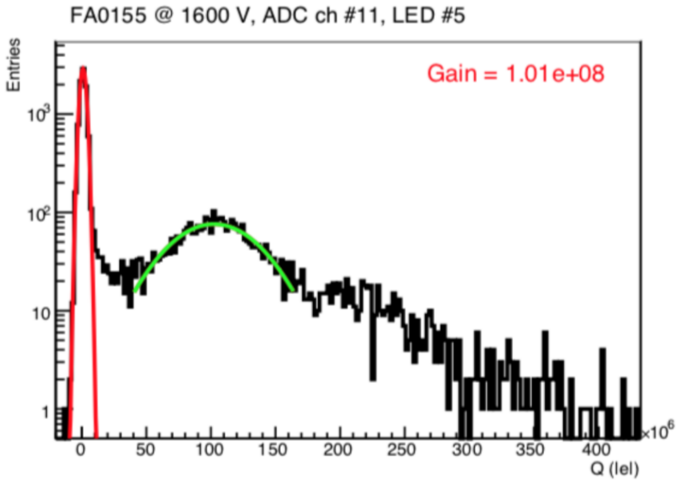

Figure 5.6: Typical PMT SPE spectrum [191] obtained with the light calibration system. Two Gaussian functions are fitted around the two maxima to determine the gain.

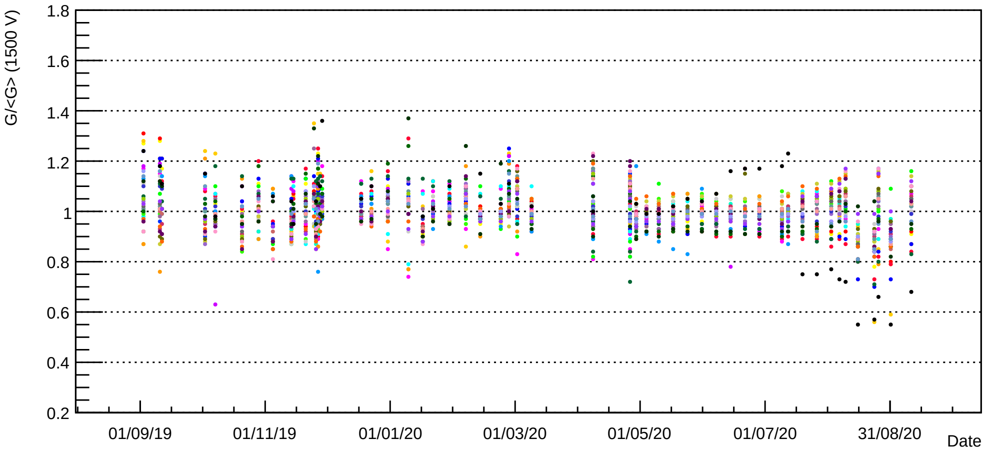

Figure 5.7: Stability of the ProtoDUNE Dual-Phase PMT gains during one year of detector operation. Every point represents one PMT.

dynamic range and the PMT are excluded. On average, a total S1 charge of 500 PEs and an S1 amplitude of 40 PEs is measured on a TPB PMT per cosmic muon event in the selected sample.

To ensure that the events are not saturating the PMTs, the correlation of the S1 charge integrated over the first 80 ns and in the range from 1 to 4 μs is verified for each PMT. If the PMT is not saturating, a linear correlation is expected, as it is shown for an example PMT on the left panel of Fig. 5.8. The right and central panels of Fig. 5.8 show the correlation for two early saturating PMTs. 11 out of the 36 PMTs show this behaviour, and they are excluded from the time profile analysis. This saturation has been extensively described in [132], and it is attributed to the energetic signals in which the high level of pulses due to the slow component limits the recovery of the discharging rate on the capacitor of the last PMT dynode.

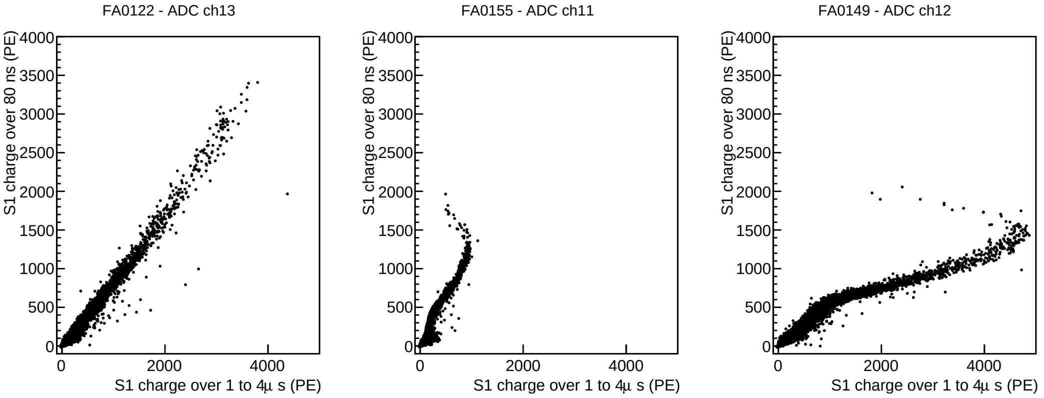

Figure 5.8: Correlation of the S1 charge over 80 ns and in the range from 1 to 4 μs for three example PMTs. Left panel shows a non-saturating PMT, center and right panels show the correlation for two early saturating PMTs that are excluded from this analysis.

The selected waveforms are added, creating an average time profile for each PMT. The average waveform in absence of drift field for one PMT is shown in Fig. 5.9. Waveforms are well described by sum of three exponential functions for the characteristic scintillation times (with time decays τ_{fast}, τ_{int} and τ_{slow}) convoluted with a Gaussian function of width σ to represent the PMT response:

$$f(t) = \sum_{j=\text{fast,slow,int}} \frac{2A_j}{\tau_j} exp\left[\frac{\sigma^2}{2\tau_j^2} - \frac{t-t_0}{\tau_j}\right] \left(1 - \text{Erf}\left[\frac{\sigma^2 - \tau_j(t-t_0)}{\sqrt{2}\,\sigma\tau_j}\right]\right), \tag{5.1}$$

where a A$_i$ is the number of photons produced at each component, and t$_0$ is the initial time (see Sec. 2.3). Although the scintillation time profile should have in principle only two components, from the decay to ground state of singlet (τ_{fast}) and triplet (τ_{slow}) argon excimers, an intermediate component (τ_{int}) is added in order to improve the convergence of the fit as reported also by other experiments [209]. This intermediate component is attributed to a delayed light emission by the wavelength-shifter, as it is shown in [225]. Given the 16-ns digitization sampling, the fit has a limited sensitivity to τ_{fast} and this parameter is fixed to 6 ns [162]. An example of the fit parameters is shown in Fig. 5.9. Additionally it is worth noting that a signal reflection at the flange feed-through appears at ~200 ns limiting the sensitivity to the τ_{int} measurement. To mitigate this, the bins of the reflection are excluded from the fit.

The wiggles appearing at the end of the profile (see Fig. 5.9) are attributed to the voltage divider used to decouple the signal from the high voltage. This voltage divider is an RC circuit that acts as a high pass filter, removing the low frequencies of the signal. This results in the waves starting at 8 μs. This effect has been already observed in other experiments (see [132]), and it does not affect the sensitivity to the τ_{slow}.

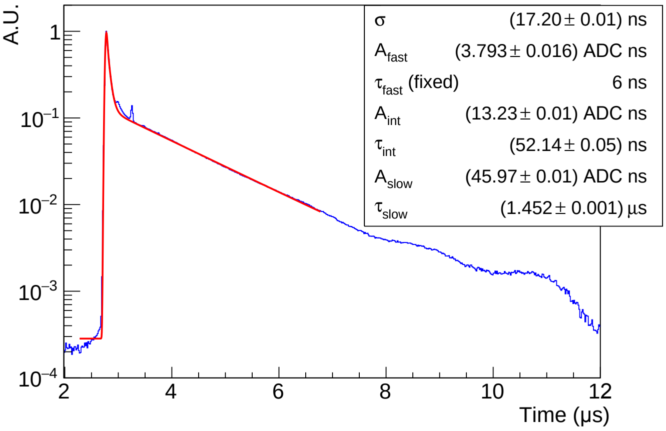

Figure 5.9: Example of the average scintillation waveform of a PMT (blue). The fit to Eq. 5.1 is shown in red. The corresponding fitted parameters are shown on the legend.

The resulting time parameters obtained from the fit to the data taken in absence of drift field during the operation of ProtoDUNE Dual-Phase are summarized in Tab. 5.3. No significant difference is observed on the τ_{slow} between PEN and TPB PMTs. On average, τ_{slow} is $1.45 \pm 0.02\,\mu$s for PEN PMTs and $1.46 \pm 0.02\,\mu$s for TPB PMTs, being the error the STD among the PMT waveforms. This absolute value indicates a high liquid argon purity. Considering nitrogen as the dominant contaminant in the liquid argon, the concentration of nitrogen would be <0.2 ppm, which is compatible with the value provided by supplier. Despite the limited sensitivity of the fit to the τ_{int} parameter due to the reflections at 200 ns, a slightly faster response of 44 ns is measured for TPB, while 50 ns is obtained for PEN. This difference confirms that the intermediate component is due to the wavelength-shifter, as anticipated in [225]. The obtained relative amplitude of fast over slow photons ((A_{fast}+A_{int})/A_{slow}) is 0.36 ± 0.01 for PEN and 0.34 ± 0.01 for TPB PMTs. These values are not far from the measurements reported in the literature for electrons: 0.5±0.2 in [226] and 0.3 in [162]. However, they are slightly above the precise measurement of 0.27±0.01 performed in the 3x1x1 WA105 demonstrator [132] for muons. It must be taken into account that the analysis of the 3x1x1 data was performed using PMTs without signal dividers, to avoid the signal distortion introduced by the capacitor. This distortion explains the small discrepancy with the 3x1x1 data, as the signal divider acts as a high pass filter, stretching the signal, and thus, overestimating the contribution of the fast component. This could be mitigated in the future by deconvoluting the PMT response including the effect of the signal divider as it is being developed for SiPM-based photon detection systems.

Measured parameter	PEN	TPB
τ_{fast} (ns)	6 [fixed]	6 [fixed]
τ_{int} (ns)	50.3±1.7	43.6±0.7
τ_{slow} (ns)	1.45±0.02	1.46±0.02
$(A_{fast}+A_{int})/A_{slow}$	0.36±0.01	0.34±0.01

Table 5.3: Scintillation time parameters obtained from the fit to the data collected in absence of drift field.

5.6 Monitoring τ_{slow} as an indicator of the liquid argon purity

Purity is critical in LArTPCs, since impurities can reduce the signal by trapping the ionization electrons. As explained in Sec. 2.3, the liquid argon purity can be monitored using the photon detection system by measuring the lifetime of the triplet molecular argon excimers, τ_{slow}. Figure 5.10 shows the evolution of the average τ_{slow} during the operation of ProtoDUNE Dual-Phase. The purity increased in September 2019 when the liquid argon purification system was turned on, and remained stable. The value of the τ_{slow} is $1.46 \pm 0.02\,\mu$s, being the error the STD among the PMT waveforms. This average value has a small dispersion over time of just $0.004\,\mu$s. This absolute value indicates a high liquid argon purity at the ppb level.

5.7 Scintillation light attenuation with the distance

In order to evaluate the attenuation of the detected scintillation light, the dependence of the collected light per PMT with the track-PMT distance for muon tracks crossing the CRT panels is studied.

Figure 5.11 shows the detected S1 amplitude and S1 charge versus the track-PMT distance for the TPB and PEN PMTs in pure liquid argon. The colour axis represents the number of entries. There is one entry per event per PMT. The track-PMT distance is computed as the minimum distance from the track to the center of the PMT photocathode.

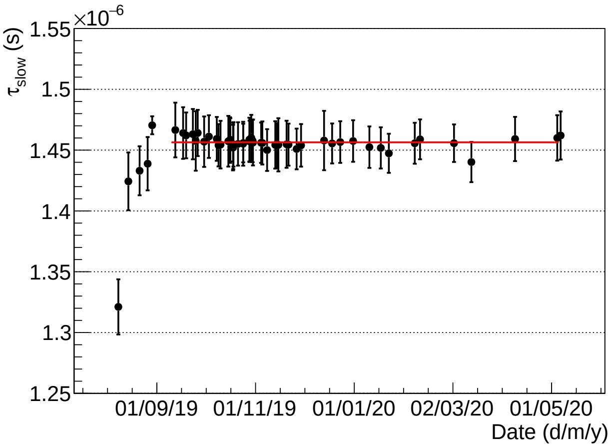

Figure 5.10: Monitoring of the τ_{slow} component of the scintillation time profile during the data-taking of ProtoDUNE Dual-Phase. Red line shows the average from September 2019 when stable operation started ($\tau_{slow} = 1.456 \pm 0.004\,\mu$s). The error bars show the STD of the measurements for the different PMT waveforms.

Only PEN PMTs placed below the trigger track are considered. The selection of 14 PEN PMTs is shown in Fig. 5.12. The light detected by other PEN PMTs show a poor correlation with the distance as it is dominated by background light. The blue points in Fig. 5.11 with error bars over the histograms represent the most probable value (MPV) for each distance. The MPV and its error are estimated by doing a Gaussian fit at each distance. The MPV is the mean of the Gaussian and the error is obtained from the fit.

Since there are more PEN PMTs than TPB PMTs and they are spread over the detector, the scintillation light attenuation is evaluated with the PEN PMTs. The curves for the PEN PMTs shown on the bottom panels of Fig. 5.11 are fitted to an exponential ($y = e^{-x/\lambda_{att}}$) to quantify the effective attenuation of the detected light with distance. The resulting parameters are summarized in Tab. 5.4. A value of $\lambda_{att} = 209 \pm 5$ cm is obtained from the S1 charge curve, and a compatible value of $\lambda_{att} = 204 \pm 5$ cm from the S1 amplitude curve. The dependence is not purely exponential since light absorption by the field cage introduces a border effect. A shoulder shape is observed at around 4.3 m, which corresponds to the PMTs placed at the centre of the detector for which this effect is reduced. This limitation is due to the fixed geometry of the triggered tracks (see Sec. 4.1.5 and Fig. 5.12). Note that the parameter λ_{att} does not correspond to the liquid-argon-light attenuation length, since the light source is not point-like but a 7-m-long track. Also the photon-path length does not correspond with the track-PMT distance, since photons do not propagate as straight lines due to the Rayleigh scattering length (see Sec. 2.5). Estimating the light attenuation in the liquid argon requires a comparison with a Monte Carlo simulation including all the effects

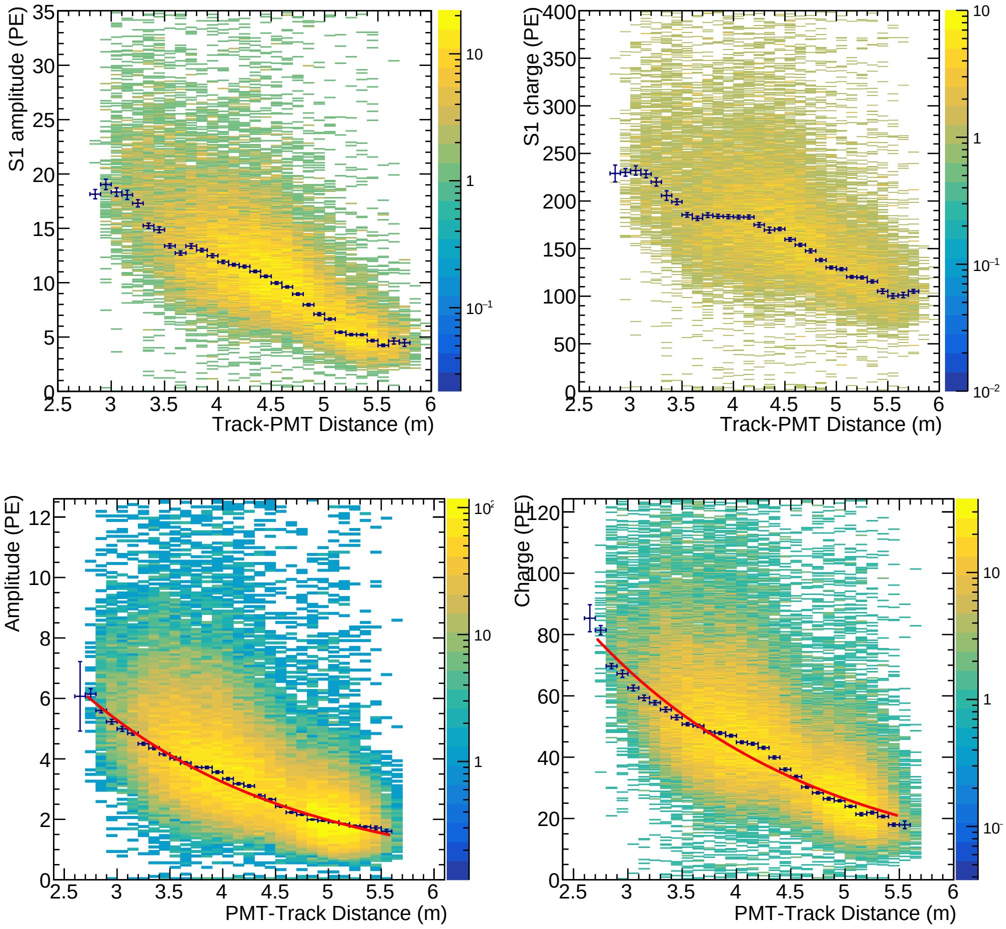

Figure 5.11: S1 amplitude (left) and charge (right) in units of detected PEs for 6 TPB (top) and 14 PEN (bottom) PMTs, per CRT-trigger event, versus track-PMT distance in pure liquid argon. Only PMTs placed below the muon-tracks are considered in the PEN selection. The colour axis represents the number of entries. There is one entry per PMT per event.

such as the absorption, the Rayleigh scattering or the light reflections. This is performed in chapter 7. However, this parameter λ_{att} is interesting since it indicates that the number of detected photons in ProtoDUNE Dual-Phase is attenuated $1/e$ each 2 m, and it will be used in chapter 9 to quantify the effect of the xenon doping in the light propagation.

	λ_{att} (cm)
S1 amplitude	209 ± 5
S1 charge	204 ± 5

Table 5.4: Effective attenuation lengths of the scintillation light in ProtoDUNE Dual-Phase from the fits shown in Fig. 5.11.

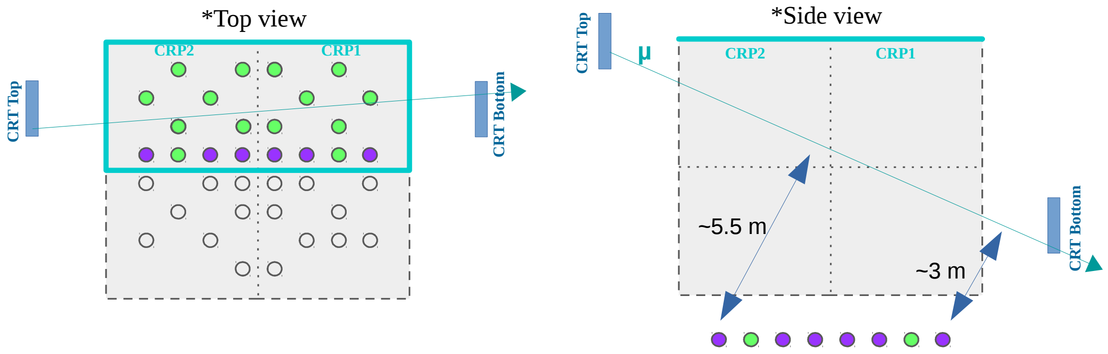

Figure 5.12: Positioning of the 14 selected PEN and 6 TPB PMTs to study the attenuation of the scintillation light with the track-PMT distance. Selected PEN PMTs are drawn in green, and TPB PMTs in magenta. Empty circles correspond to non-selected PEN PMTs. Selected PMTs are placed at a distance range of 3-5.5 m to the CRT trigger track.

5.8 Light yield suppression with the drift field

As explained in Sec. 2.3.1, the presence of an electric field suppresses the recombination of electrons and ions. As a result, the light production is quenched by the drift field. The nominal cathode voltage of 300 kV provides a drift field in the active volume of 0.5 kV/cm, which is strong enough to suppress most of the recombination (see Sec. 2.3.1). In this way, by comparing the detected light with and without drift field, the amount of produced photons from the electron-ion recombination can be estimated.

CRT-trigger events taken at full drift field during autumn 2021 (see Sec. 4.3.4) have been selected to perform this measurement. Figure 5.13 shows the dependence of the detected light for CRT-trigger events with the track-PMT distance with (red) and without (black) drift field for all PEN PMTs. The track-PMT distance is computed as the minimum distance from the PMT position to the CRT-trigger track as the track position is provided by the CRT panels. The bottom panel shows the ratio of both curves fitted to a constant, providing an average value of 0.62±0.01 for all distances. This means that 62% of the photons are produced by direct excitons, and the remaining 38% are due to the electron-ion recombination. The correlation of both curves is lost above 5.3 m, which corresponds with PMTs placed far away from the track, and the signal is dominated by background signals. To avoid this distortion, the fit is performed up to 5.3 m.

Figure 5.14 shows the comparison of this result (in magenta) with the value obtained during the operation of ProtoDUNE Dual-Phase in 2019-2020 (in yellow, considering the non-uniform drift field, see [227]), and with other values in the literature obtained for electrons ([165] in red and [228] in black) and muons ([132, 209] in blue). This measurement is quite in agreement with the values reported in the literature despite the

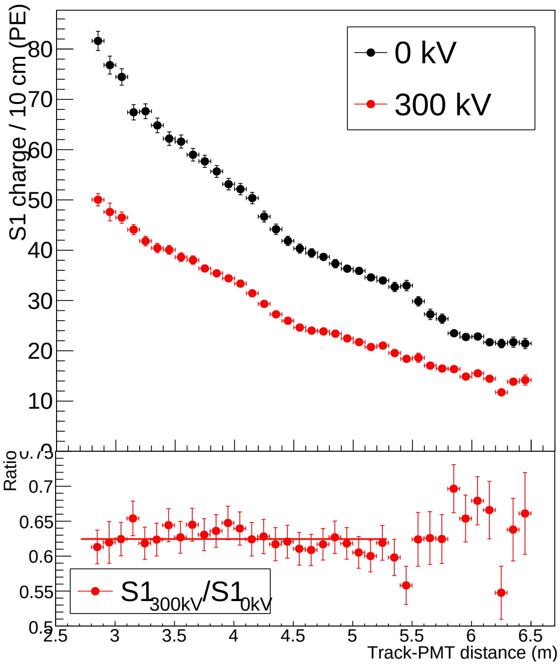

Figure 5.13: Top: S1 charge as a function of the track-PMT distance for CRT trigger muons at the nominal cathode voltage (300 kV in red) and at 0 kV (in black). Bottom: Ratio of the 300 kV over 0 kV curves.

limitations during the data-taking in 2021, since the purity was not fully stable and the uniformity of the drift field could not be verified (see Sec. 4.3.4).

5.9 Dependence of the SPE rate with the drift field

Low energy events are detected in ProtoDUNE Dual-Phase as a rate of single photoelectron (SPE) signals in the PMT waveforms. There are several sources that can contribute to the SPE rate. First, the radioactivity of natural argon. Argon isotopes such as ^{39}Ar decay depositing a small amount of energy of the order of keV and producing small scintillation light signals that contribute to the SPE background. Second, the cosmic particles crossing far away from the PMTs or depositing a small amount of energy can also contribute to the SPE rate detected by the PMTs. The PMT dark current also contributes to the SPE rate, with an average value of 1.7 kHz per PMT at cryogenic temperature [191]. When operating the detector with active electric fields, the recombination of Ar_2^+ ions with electrons and electronegative impurities can also contribute to the SPE rate as proposed in [229]. Finally, other light sources such as small discharges in the CRPs and the field cage could also contribute to the SPE rate.

The SPE rate in absence of drift field during the operation of ProtoDUNE Dual-Phase

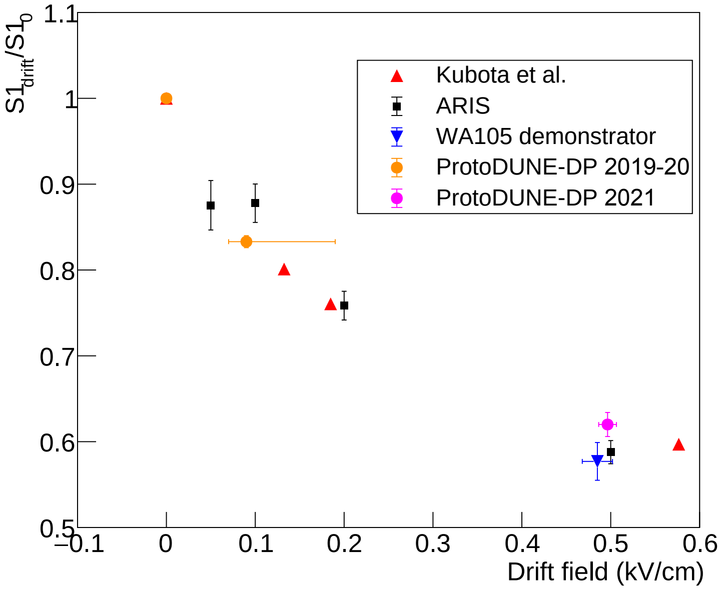

Figure 5.14: Comparison of the measured value for $S1_{300\mathrm{kV}}/S1_{0\mathrm{kV}}$ with other measurements in the literature for electrons ([165] in red, [228] in black) and muons ([132, 209] in blue).

in 2019-2020 was measured in [224, 227]. An SPE rate of 166 kHz was obtained for PEN PMTs while 345 kHz for TPB PMTs. However, due to fault in the HV system, the effect of the drift field could not be quantified (see Sec. 4.3.3). In this section, the effect of the presence of the drift field in the SPE rate is characterized by considering data taken during 2021 when the cathode was operated at its nominal voltage of 300 kV (see Sec. 4.3.4).

The rate of SPE is computed by counting the number of pulses with an amplitude between 0.5 and 2.0 times the average SPE amplitude. PMTs were operated at a gain of 2×10^7, corresponding to an average SPE amplitude of $\sim$ 16 ADC counts. Therefore, the selected pulses typically have an amplitude between ∼8 and ∼32 ADC counts. When a pulse with an amplitude above two times the SPE is found, it is considered as a potential S1 signal, and a time veto is applied to avoid SPE signals from the slow component of the S1 signal. This veto is extended until there is a time window of 3 μs without signal, when is considered that the S1 signal ended.

Table 5.5 summarizes the SPE rate results for PEN and TPB PMTs with the cathode operated at 0 kV and at 300 kV. A rate of 106 kHz and 306 kHz is obtained for PEN and TPB PMTs respectively in absence of drift field. This values are slightly below but still compatible with the values measured during the operation in 2019 and 2020 (166 kHz for PEN and 345 kHz for TPB PMTs) [227]. The difference is due to the different method used to estimate the SPE rate: the amplitude threshold of SPE candidates is slightly different (from 0.5 to 2 PEs in this study versus ∼0.2 to 1.8 PEs in [227]), and the veto window applied is much longer (100 μs in [227] versus 3 μs in this study). While the model of recombination Ar_2^+-ion recombination proposed in [229] predicts a smaller rate with the drift field, the SPE rate increases a factor of 2.7 on PEN PMTs and 1.7 on TPB PMTs when activating the drift field, as it is shown on the second and third column of Tab. 5.5.

	SPE rate (kHz)		Ratio
	0 kV	300 kV	300 kV/0 kV
PEN	$106 \pm 15(\delta_{PMTs}) \pm 20(\delta_{Runs})$	$284 \pm 55(\delta_{PMTs}) \pm 71(\delta_{Runs})$	×2.7
TPB	$306 \pm 46(\delta_{PMTs}) \pm 50(\delta_{Runs})$	$581 \pm 60(\delta_{PMTs}) \pm 95(\delta_{Runs})$	×1.7

Table 5.5: SPE rate for PEN and TPB PMTs with the cathode at 0k V and 300 kV. δ_{PMTs} is the STD among PMTs (average of the different runs), and δ_{Runs} is the STD among runs (average of PMTs).

Additionally, Fig. 5.15 shows an example waveform of a TPB PMT without (top panel) and with (bottom panel) drift field. In this case all signals are counted as SPEs, since the amplitudes are around 1 PE. The increase in the SPE rate when activating the cathode voltage is clearly visible by eye. In comparison, ProtoDUNE Single-Phase reported a drop of the SPE rate from 270 kHz to 180 kHz when activating the drift field [230]. MicroBoone also reported a drop in the SPE rate from ∼340 to ∼240 kHz when activating the drift field [231] in contrast with ProtoDUNE Dual-Phase results.

The different result in ProtoDUNE Dual-Phase could be explained by the special operation of the detector. The ProtoDUNE Dual-Phase data were taken during a high voltage test, keeping the anode out of the liquid argon and without extracting the electrons towards the gas phase. In this situation, the ionization electrons recombine at the top of the active volume as they are not collected, producing more photons that are detected as an increase of the SPE rate. Additionally, the presence of electrical discharges was reported by the cameras inside the cryostat (see Sec. 4.3.4). These electrical discharges produce visible light that would contribute also to the SPE rate.

5.10 Detection of secondary electroluminescence light

In a dual-phase TPC, the ionization electrons are extracted and amplified in the gas phase, producing a secondary scintillation light signal, called S2. This signal is proportional to the drifted charge (see Sec. 2.4).

ProtoDUNE Dual-Phase detected S2 signals during the operation of the CRPs. An example event showing an S1 and S2 signals is shown in Fig. 5.3. The primary scintillation S1 signal is followed by a continuum stream of pulses that corresponds to the electro-

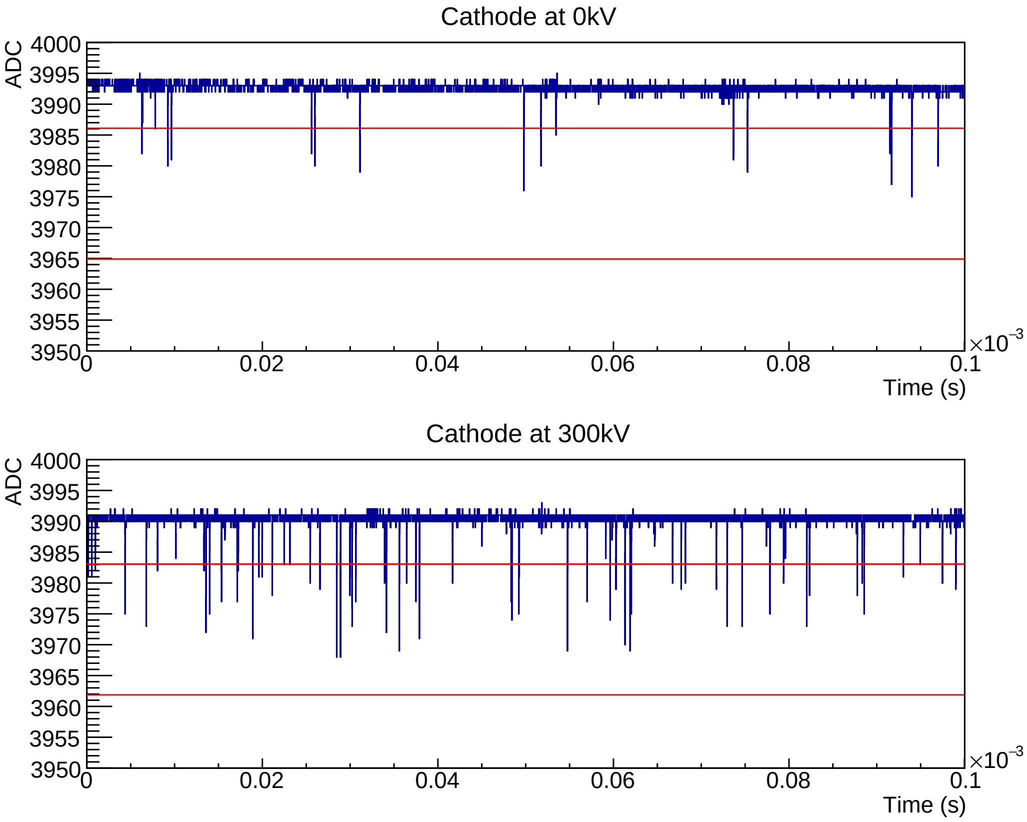

Figure 5.15: Example of two waveforms taken with random trigger in a TPB PMT. Top panel shows a waveform taken with the cathode off, bottom panel shows a waveform taken in the same PMT with the cathode at its nominal voltage of 300 kV. Red lines show the threshold of 0.5 - 2 PEs in amplitude. The increase in the SPE rate when activating the cathode is evident.

luminescence S2 signal. S2 light is originated in the gas phase around 7 m away from the PMTs, and this is the first time that light produced at such a large distance has been detected in a LAr-TPC.

Since ProtoDUNE Dual-Phase is placed on surface and exposed to a high rate of cosmic muons, the S2 signals are not easy to correlate with the S1 signal and most of the S2 signals are observed as an increase in the background rate of SPE when extraction and amplification fields are on: 350 (170) kHz for TPB (PEN) PMTs are measured in absence of S2 production while several MHz are detected (2.5 MHz for TPB and 1.1 MHz for PEN PMTs) when electroluminescence light is present [227]. In this sense, the S2 signals are an important contribution to the low-energy background in a dual-phase LAr-TPC.

Nevertheless very energetic events produce S2 signals that can be associated to their previous S1 (like in Fig. 5.3 and 5.16). These events corresponds to vertical high energy showers, that produce an S2 signal directly after the S1 signal. The S2 signals are observed to cause overshooting in the waveforms when the amount of charge collected in the

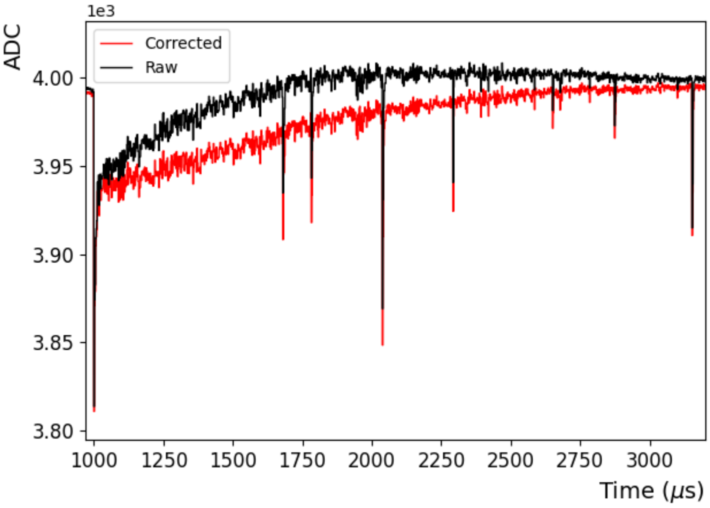

Figure 5.16: Example of a scintillation (S1) and electroluminescence (S2) light signal in a ProtoDUNE Dual-Phase PMT in liquid argon with drift, amplification and extraction fields (S1 and S2 signals). The acquired waveform is shown in black and the resulting waveform after the overshooting correction in red.

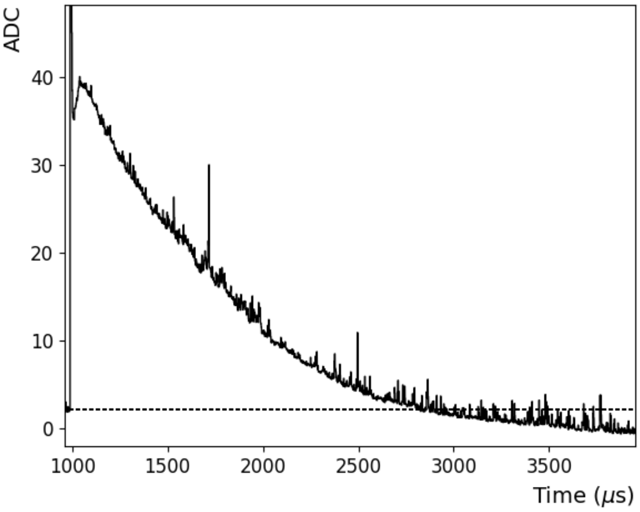

Figure 5.17: Average waveform of PEN PMTs with a S2 signal associated to a previous S1 signal. The y-axis is zoomed to focus on the S2 signal. Dotted line shows the position of the baseline. Duration of S2 signal is ∼2 ms (from 1 ms to ∼3 ms).

PMT anode exceeds the discharging rate of the combined PMT and readout circuit ($1/RC$ constant), effectively shifting the waveform baseline during the pulse. This overshooting is corrected offline by deconvoluting the capacitor response. Figure 5.16 shows the effect of this correction. The signal processing is described in [209].

Fig. 5.17 shows the average waveform for high energy vertical showers events like the one showed in Fig. 5.16. In this case, the baseline has been subtracted resulting in a positive signal. In these events the average S1 charge detected per PMT is $>$700 PE and the S2 charge $>$30 kPE. The average duration of the S2 signal determined when the baseline is recovered is $\sim$2 ms, . Considering the non-uniform drift field of $\sim$0.2 kV/cm along the first two meters of drift during the operation of ProtoDUNE Dual-Phase in 2019-2020 (see Sec. 4.3.2), and the drift velocity of $\sim$1 mm/μs [155], an S2 duration of $\sim$2 ms is expected, which is consistent with the observed time.

Chapter 6

Simulation of the scintillation light production, propagation and detection in a large LAr-TPC

In order to scale the liquid-argon TPC technology to the kiloton mass level, it is crucial to understand very well the performance of the detector at a smaller scale. This can be done by the development of a detailed Monte Carlo simulation of the detector and its validation with data, which allows identifying the main parameters that affect the detector performance, including the production, propagation and detection of the scintillation light.

The Monte Carlo simulation of ProtoDUNE Dual-Phase is based on LArSoft [232], a software package dedicated to LAr-TPC simulation. LArSoft provides a common framework used by many experiments, that allows to share simulation and reconstruction tools among them. WA105, MicroBooNE, SBND, LArIAT and DUNE among the other neutrino experiments use LArSoft as its analysis framework.

In this chapter, the work developed to simulate the scintillation light detection in ProtoDUNE Dual-Phase and in the proposed 10 kton DUNE Dual-Phase module using LArSoft is detailed. The simulation chain can be divided in three different steps as it is shown in Fig.6.1: First, the generation of the physics events, *i.e.*, the simulation of the interacting particles in the detector. Second, the Geant4 simulation of the particle interaction. This step includes the simulation of the deposited energy, and the production and propagation of scintillation photons. And finally, the simulation of the detector response and the generation of the PMT waveforms. The geometry implemented in the simulation is described in Sec. 6.1. The event generators are explained in Sec. 6.2. The Geant4 and photon-propagation simulation is summarized in Sec. 6.3. Finally, the

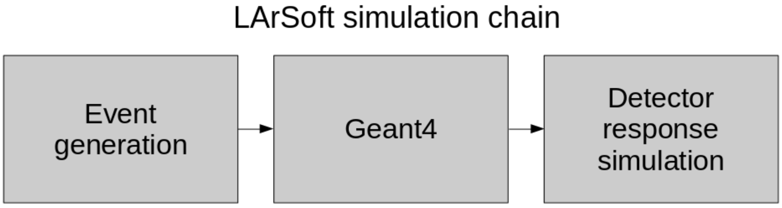

Figure 6.1: LArSoft simulation steps: Event generation, Geant4, and detector response simulation.

simulation of the photon detector system response is explained in Sec. 6.4.

6.1 Detector geometry

The detector geometry is implemented using geometry description markup language (GDML) files. It defines the position and composition of the main elements in the detector, which is important to have an accurate simulation of the deposited energy of the crossing particles. Two detector geometries have been implemented: ProtoDUNE Dual-Phase geometry and the proposed design for a 10 kiloton far detector module as defined in Sec. 3.1.3 (DUNE Dual-Phase).

6.1.1 ProtoDUNE Dual-Phase

The geometry of ProtoDUNE Dual-Phase implemented in LArSoft includes a detailed description of the cryostat containing the detector (steel support, foam insulation and inner walls), and the detector itself (cathode, field-cage, ground grid, PMTs and CRPs). The implementation of the cryostat steel support allows to simulate the energy deposition of the cosmic muons before entering the active volume. An overall view of the implemented geometry is shown in Fig. 6.2. The main dimensions are summarized in Tab. 6.1.

The main elements inside the cryostat, as the field cage, the cathode, the ground grid and the LEMs, are important in order to consider the absorption and reflection of the scintillation light:

- The LEMs are simulated as a 6 m x 6 m plane that fully absorb the light.
- The cathode and the ground grid are very important, as they are placed just on top of the PMTs. They are simulated with a great level of detail (see in Fig. 6.3). They are made of stainless steel, and the reflected light is considered. The cathode and

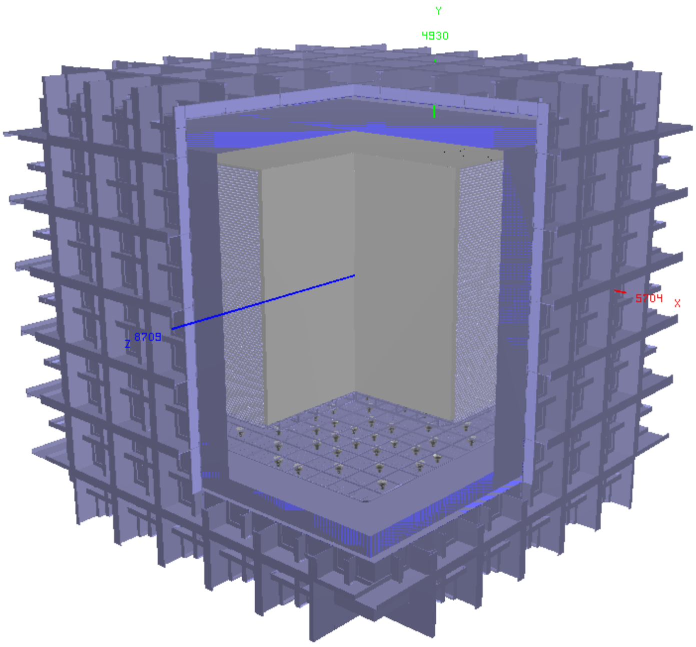

Figure 6.2: View of the ProtoDUNE Dual-Phase geometry included in the simulation.

ground grid transparency is 90%, defined as the ratio of open surface with respect to the total size.

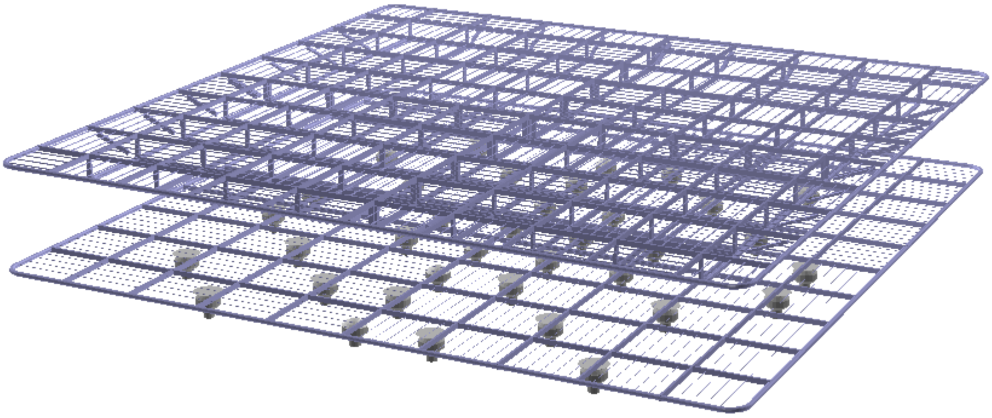

Figure 6.3: Detail of the cathode (above) and ground grid structure (below) placed on top of the PMTs as they are implemented in the simulation.

- The field cage is simulated including the 98 field-shaper rings around the active volume. A detail of the simulated field-shaper is shown in Fig. 6.4. They are made of aluminium.

	ProtoDUNE Dual-Phase	DUNE Dual-Phase
Cryostat outer size (m^3)	11.9 x 11.9 x 11.7	17.7 x 65.6 x 18.7
Cryostat inner size (m^3)	8.5 x 8.5 x 7.9	15 x 62 x 15
Active volume size (m^3)	6 x 6 x 6	12 x 60 x 12
Number of field cage (FC) rings	100	240
FC-rings separation (cm)	6	5
FC-rings radius (cm)	2.3	1.69
FC transparency	23%	33%
Cathode size (m^2)	6 x 6	12 x 60
Cathode transparency	90%	92%
Ground grid size (m^2)	6 x 6	12 x 60
Ground grid transparency	90%	92%
$R_{\mathrm{Al\ \&\ SS}}$	27%	0
PMT photocathode - cathode distance (m)	1.07	1
PMT photo-cathode diameter	20.32 cm (8 inch)	
PEN foil diameter (cm)	14	N/A

Table 6.1: Main characteristics of the main elements implemented in the LArSoft geometries.

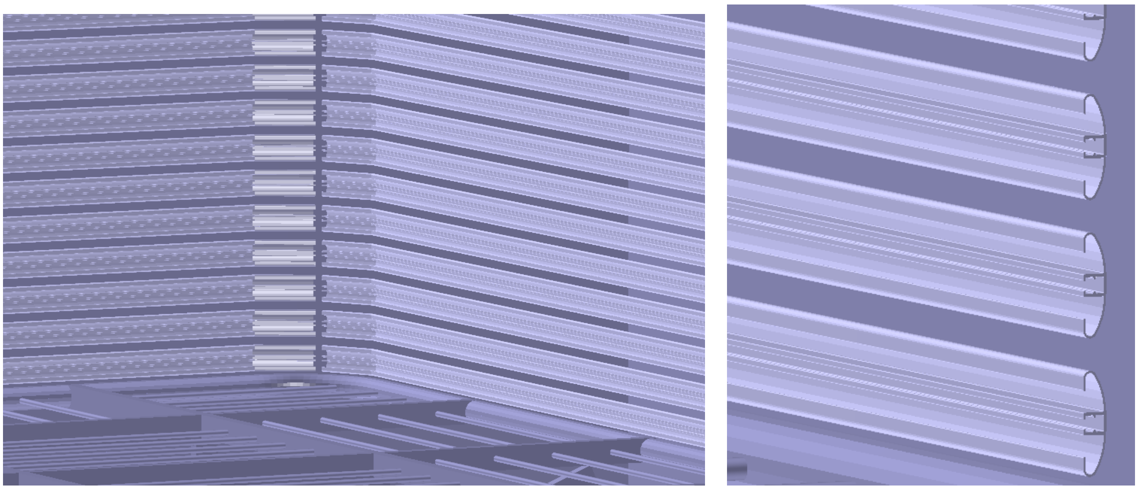

Figure 6.4: Left: Detail of a simulated field cage corner. Right: Zoom on the field-shaper rings.

- The inner cryostat walls are simulated as a simple box. They are made of stainless steel.
- The PMTs are implemented as glass volumes, with either the PEN foil or the TPB coating on top. A detail of the PMT geometry is shown in Fig. 6.5. The photons hitting the foil/coating are detected after simulating the PMT response, while those hitting the glass are absorbed/non-detected.

The baseline reflectivity of $R_{\mathrm{Al\ \&\ SS}}$=27% of the liquid argon scintillation light in the elements made of stainless-steel and aluminium (cathode, ground grid, field cage and cryostat walls) is considered in the simulation [233].

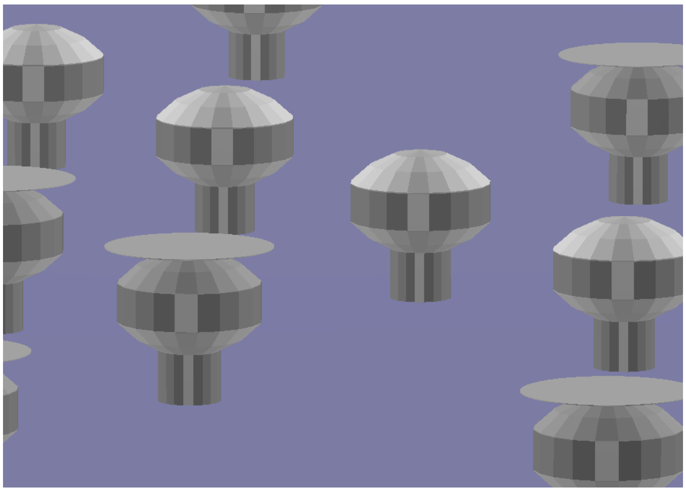

Figure 6.5: Detail of the PMTs, either with a foil or the coating on top, implemented in the simulation.

6.1.2 DUNE Dual-Phase

The DUNE Dual-Phase design is very similar to the ProtoDUNE Dual-Phase one, but scaling the size. It consists of a module of 12 m x 12 m x 60 m of active volume, with 720 PMTs placed below the cathode (keeping a density of 1 PMT/m^2 as in ProtoDUNE). The implementation of the geometry in LArSoft has been simplified with respect to ProtoDUNE. The cryostat steel support is implemented as a simple box. This is a good approximation as the Far Detector will be placed underground, and therefore cosmics depositing energy in the outer volume are not expected, unlike ProtoDUNE (the cosmic muon rate at DUNE depth is at the order of $10^{-9}\,\mathrm{cm}^{-2}\mathrm{s}^{-1}$ [234] while in surface is $1\,\mathrm{cm}^{-2}\mathrm{s}^{-1}$). The design of the cathode is also a simple grid of stainless-steel tubes, as well as the ground grid, with a transparency of 92%. The field cage is based on aluminium tubes with a pitch of 5 cm. The main dimensions are summarized in Tab. 6.1.

Due to the challenge of detecting light from more than 12 away, the use of TPB-coated reflective foils on the TPC walls is considered. The design of the reflective foils is based on the SBND reflective foils [193]: They are made of a high reflective material, VM2000, coated with TPB. In this approach, the TPB converts an incident VUV photon into a visible photon, that is later reflected by the VM2000, with a reflectivity of 93%. Three alternatives of reflective-foils layout have been proposed for the DUNE Dual-Phase studies:

- No-Foil, as a first approach.

- Foil: TPB-coated reflective foils are placed on the inner part of the field cage walls. A view of the foils in the detector is shown in Fig. 6.6 (right). A detail of the foil positioning is shown in Fig. 6.7.
- Half-Foil: TPB-coated reflective foils are placed only on the half top part of the field cage. A view of this design is shown on the left panel of Fig. 6.6.

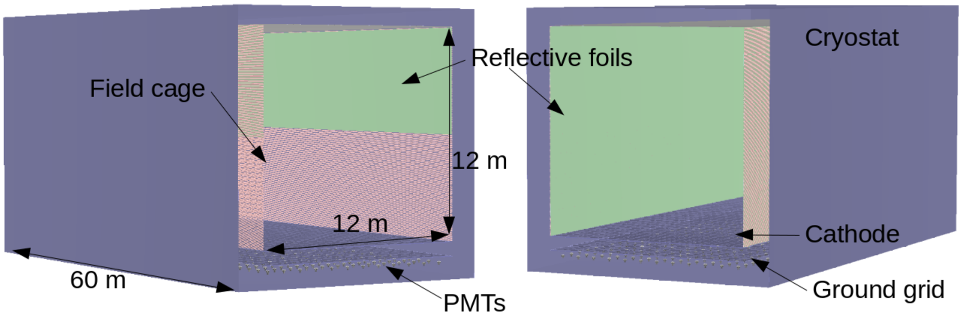

Figure 6.6: View of the simulated DUNE Dual-Phase designs. Foils covering the inner part of the field cage are drawn in green: Half Foil design on the left: Foil design on the right.

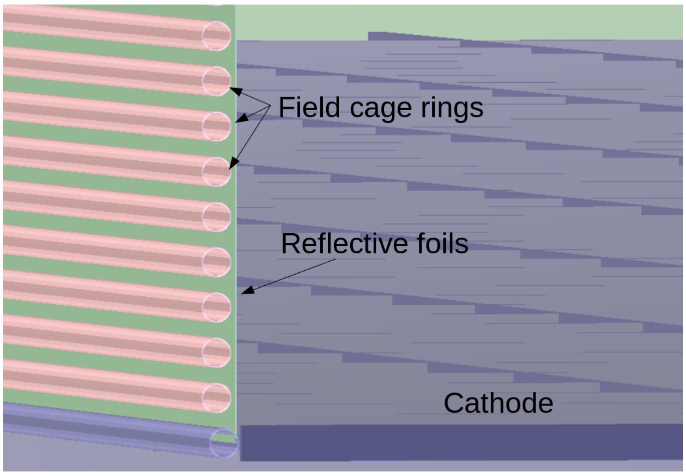

Figure 6.7: Detail of the TPB-coated reflective foil (green) covering the inner part of the field cage in the Foil geometry.

6.2 Event generation

The event generation is the first step in the LArSoft simulation chain (see Fig. 6.1). This step consists of placing the interacting particles in the simulated geometry. In this section, the different event generators developed for ProtoDUNE Dual-Phase and DUNE Dual-Phase studies are described. While ProtoDUNE Dual-Phase is exposed to cosmic rays at surface, DUNE Dual-Phase will be placed underground. Therefore, the expected type of events are very different in both detectors. A detailed simulation of the cosmic rays (Sec. 6.2.1) and CRT-triggered muons (Sec. 6.2.2) is developed for ProtoDUNE Dual-Phase studies, and the low energy background due to the radiological decays is simulated in both ProtoDUNE Dual-Phase and DUNE Dual-Phase studies (Sec. 6.2.3).

6.2.1 Cosmic rays in ProtoDUNE Dual-Phase

The main source of light inside ProtoDUNE Dual-Phase is the cosmic-ray particles reaching the active volume. Their simulation is based on CORSIKA (COsmic Ray SImulation for KAscade), a Monte-Carlo simulation package for air-showers initiated by high-energy cosmic particles (primary particles) [1].

Due to the computing cost of generating the particle showers in every simulation, many particle cascades are simulated once and stored in several files per primary particle. Five primary particles are considered: p, He, N, Mg and Fe. The detector location (CERN) altitude and latitude are taken into account in the shower generation. The hadronic interactions in the shower are simulated considering the FLUKA model [235]. Finally, a dedicated LArSoft module computes the number of expected showers per primary particle, considering the expected flux per primary particle, and places them within the detector geometry. The differential flux per primary particle is given by the power law:

$$\phi(E) = K\left(\frac{E}{1\mathrm{GeV}}\right)^{-2.7}, \tag{6.1}$$

where K depends on the primary cosmic particle. The values of K considered in the simulation are shown in Tab. 6.2. The flux composition is based on the constant mass composition (CMC) model [236]. The particle content of the showers crossing the detector is dominated by muons (57%), neutrons (24%), gammas (11%), electrons/positrons (5%) and protons (3%).

6.2.2 CRT triggered muons in ProtoDUNE Dual-Phase

A data-driven simulation has been developed for muons crossing the the CRT panels. A dedicated LArSoft module places a muon in the top CRT, with a momentum pointing towards the bottom CRT panel. The distribution of initial/final positions are shown in Fig. 6.8 and taken directly from the CRT data. The distribution shows that tilted trajectories are preferred over horizontal ones (from the top part of the top CRT panel, to the bottom

Primary particle	K (10^3 m^{-2}·s^{-1}·sr^{-1} GeV^{-1})
p	17.2
He	9.2
N	6.2
Mg	9.2
Fe	6.2

Table 6.2: Cosmic shower flux per primary particle considered in the CORSIKA simulation [1].

part of the bottom CRT panel). While data drive the direction of the muon, the energy is obtained from CORSIKA simulations (see Sec. 6.2.1). The energy distribution of muons from CORSIKA is shown in Fig. 6.9, with a most probable energy of $\sim$ 1 GeV, and an average of 6.5 GeV per muon. This histogram is used as an input to obtain the initial energy of the CRT muon.

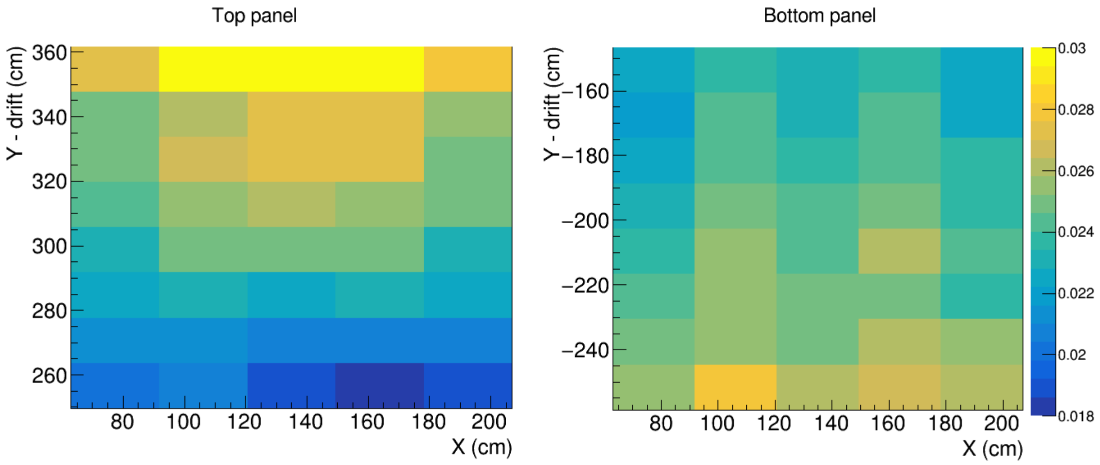

Figure 6.8: Distribution of the entry and exit point of the muon tracks collected in CRT data and used and as input to the CRT triggered muons simulation. CRT positioning is detailed in Fig. 4.8. Colour axis indicates the number of entries per bin divided by the total number of entries. There is one entry per muon track.

However, since the muons can deviate from the ideal trajectory or decay, a selection is applied to ensure that the simulated muon crosses both CRT panels.

6.2.3 Radiological backgrounds in ProtoDUNE and DUNE Dual Phase

Elements inside or around the detector can be composed of radioactive isotopes that would eventually decay and deposit energy within the active volume. This energy deposition could mimic a signal event, becoming a problem, specially when detecting low energy events such as solar or supernova neutrinos. Therefore a detailed characterization of the

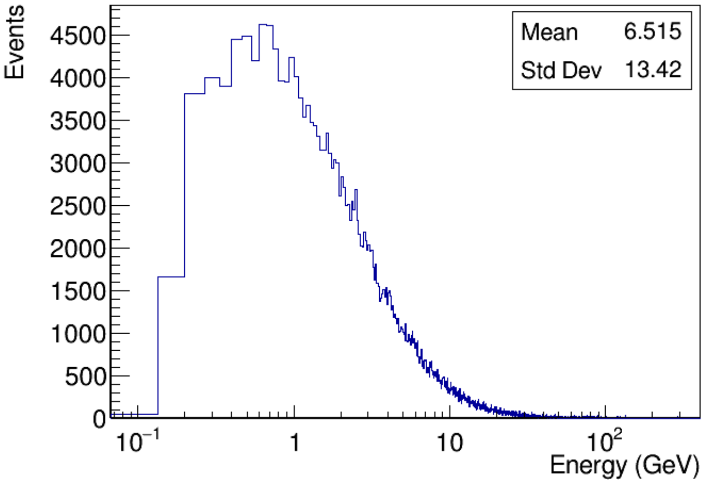

Figure 6.9: Muon energy distribution from CORSIKA, used as input of the simulated CRT-triggered muons.

isotope content of all the detector elements is needed. Two sources of radioactivity are considered in this work: The argon itself and the underground rock.

Atmospheric argon is mainly composed by the isotopes ^{40}Ar (99.60%), ^{36}Ar (0.33%) and ^{38}Ar (0.06%), which are stable. However, some radioactive isotopes are present in argon:

- ^{39}Ar is an argon isotope with a concentration of $(7.9 \pm 0.3) \times 10^{-16}$ in natural argon [237]. It undergoes a β decay into a stable ^{39}K, with a β end-point energy of 565 keV [238]. The measured activity is 1.01 Bq/kg of argon.

- ^{42}Ar is an argon isotope with a concentration of 9.2×10^{-21} atoms of ^{42}Ar/^{40}Ar [239]. It undergoes a β decay into ^{42}K which β-decays into ^{42}Ca [239], with associated gammas. The measured activity is 92 μBq/kg of argon.

- ^{85}Kr is present in the atmosphere as a fission product of uranium and plutonium, such as in nuclear bomb tests and nuclear reactors. It is present in the argon with a concentration of 4×10^{-15} g(Kr)/g(Ar) [238]. It undergoes a β decay into ^{85}Rb, with an end-point energy of 687 keV. The measured activity is 115 mBq/kg of argon.

Additionally, the radioactivity from the cavern rock has been considered for the DUNE Dual-Phase studies. Two sources are simulated:

- ^{222}Rn is the result of the ^{238}U decay chain present in the rock. It is a gas and it spreads over all the detector volume. It undergoes three α and two β decays to produce

^{210}Pb which is considered stable due to its lifetime over 22 years. In this work, an activity of 40 mBq/kg of argon is considered, as the maximum activity allowed by the detector requirements [118]. However this requirement is being reviewed, since this level of background might still compromise the detector performance.

- Neutrons produced by spontaneous fission of uranium in the rock can reach the detector and undergo eventually a neutron capture. The activity is scaled considering a flux of 10 neutrons/y/g per 10 ppm of ^{238}U in the concrete around of the detector. It corresponds to a neutron flux of 10^{-5} cm^{-2}s^{-1} on the sides of the active volume.

A summary of the background sources and activities implemented in the simulation is shown in Tab. 6.3. The ^{222}Rn activity and neutron flux are design requirements in order to allow the detector reaching its physics goals.

Particle	Activity / Flux	Origin	Reference
^{39}Ar	1.01 Bq/kg	LAr	[238]
^{42}Ar	92 μBq/kg	LAr	[239]
^{85}Kr	115 mBq/kg	LAr	[238]
^{222}Rn	40 mBq/kg	Underground rock	DUNE requirement
Neutrons	10^{-5} cm^{-2}s^{-1}	Underground rock	DUNE requirement

Table 6.3: Nominal activities of the radiological backgrounds implemented in the simulations.

The radioactivity present in the liquid argon has been considered for both ProtoDUNE Dual-Phase and DUNE Dual-Phase detectors, as it is expected in both cases. However, the radioactive sources from the rock have been only included in the DUNE Dual-Phase studies, since they are expected to be relevant only underground, and ProtoDUNE Dual-Phase is placed at the surface.

6.3 Simulation of scintillation-photon production and propagation

Once the particles produced by the event generators are placed within the detector, they are propagated using Geant4 [240]. Geant4 computes the energy deposited in the liquid argon in each position. The number of scintillation photons produced by the interacting particles are then computed considering a constant light yield of 24,000 photons/MeV at the nominal drift field of 0.5 kV/cm and 40,000 photons/MeV in absence of drift field. The scintillation time profile is simulated during the photon production, generating 23% of the photons following the fast decay time of 6 ns, and the rest 77% with the slow decay time. This corresponds to a ratio of fast over slow component photons of 0.3, as it has been measured for electrons in [162] (see Sec. 2.3). A slow decay time decay of 1.45 μs has been considered in the simulation driven by the data (see Sec.5.5).

During the propagation, photons can be absorbed by the impurities present in the liquid argon, or scatter elastically changing its direction. Both effects are implemented considering the absorption length (λ_{Abs}) and the Rayleigh scattering length (λ_{RS}), as described in Sec. 2.5. The baseline values of $\lambda_{RS} = 99.1$ cm (see Sec. 2.5.1) and $\lambda_{RS} = 20$ m (see Sec. 2.5.2) are considered in the simulation. Additionally photons can be absorbed or reflected by the elements inside the cryostat. Since the main elements inside the cryostat are made of aluminum or stainless steel, the reflectivity of these materials ($\mathrm{R}_{\mathrm{Al\ \&\ SS}}$) is considered in the simulation, with a baseline value of 27%. The parameters are summarized in Tab. 6.4.

	Parameter	ProtoDUNE-DP	DUNE-DP
Scintillation	Light yield (0 kV/cm)	40,000 ph/MeV	
	Light yield (0.5 kV/cm)	24,000 ph/MeV	
	τ_{fast}	6 ns	
	τ_{slow}	1.44 μs	
	Ratio fast/slow	30%	
Propagation	λ_{RS} (127 nm)	1 m	0.61 m
	λ_{RS} (430 nm)	N/A	480 m
	λ_{Abs}	20 m	20 m
	$\mathrm{R}_{\mathrm{Al\ \&\ SS}}$	27%	N/A
Foils response	WLS efficiency	N/A	100%
	$\mathrm{R}_{\mathrm{Foil}}$	N/A	97%

Table 6.4: Summary of the baseline parameters used in the Monte Carlo simulation.

Since the propagation of the photons towards the PMTs is very demanding in CPU power, they are simulated only once and stored in a so-called photon library. The photon library is a map of the probability for a photon produced inside the detector to reach a certain PMT, and the time smearing distribution due to the propagation.

Photon libraries are generated by dividing the full volume inside the cryostat in an array of 25 x 25 x 25 voxels (with a size of 34 x 34 x 32 cm^3). Photons are generated on each voxel with the wavelength of the scintillation photons (127 nm) and propagated through the volume. The tracking of the photons ends either when they are absorbed or they hit the PMT wavelength shifters. The ratio of the number of photons hitting the PMT wavelength shifter over the number of simulated photons provides the visibility, defined as the probability for a photon produced in a voxel to reach a certain PMT.

A view of the photon-library visibilities for the ProtoDUNE Dual-Phase geometry is shown in Fig. 6.10. Left panels shows a projection on the vertical detector axis, and right panel a projection on an horizontal axis. The black points mark the PMT positioning and the red box shows the TPC active volume. For a better understanding, the visibilities are scaled up considering an energy deposition of 40k photons/MeV, and the expected PMT detection efficiency of 0.11 on TPB PMTs and 0.018 on PEN PMTs (explained in Sec. 6.4). A minimum of 1 PE/MeV of detected light in the TPC active volume is obtained. The strong dependence of the detected light with the distance can be appreciated, going from 100 PE/MeV next to the PMT to just 1 PE/MeV in the liquid-gas interface ∼7 m above.

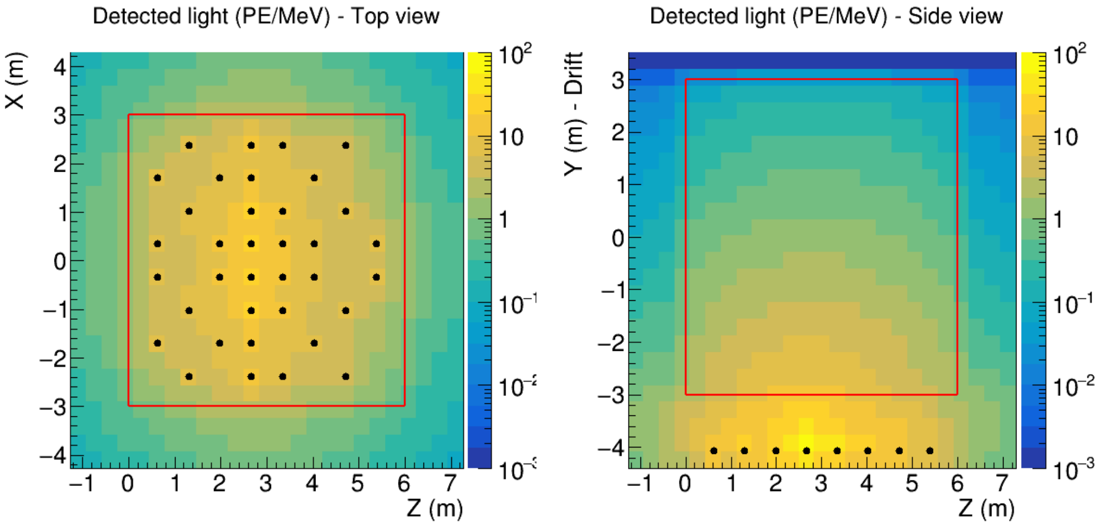

Figure 6.10: Projection of the photon-library visibilities for the ProtoDUNE Dual-Phase geometry. Visibilities are scaled assuming a light yield of 40,000 photons/MeV of deposited energy, and the parameters summarized in Tab. 6.4.

The photon library also includes the arrival times of the photons when propagating from the voxel to the PMT. An example of the photon time distribution is shown in Fig. 6.11. Each entry in the histogram represents the propagation time of a photon from the voxel to the PMT. This distribution is fitted to a Landau, and the fit parameters are stored in the photon library. One set of Landau parameters per PMT and per voxel are stored in the photon library. The voxel-PMT distance in the example shown in Fig. 6.11 is ∼3 m. The Landau MPV is 55 ns, and the σ is 10 ns. Both, MPV and σ increase with the voxel-PMT distance, as the photon propagation takes more time and the smearing is enhanced. In comparison, at 6 m the MPV is ∼100 ns and $\sigma \sim 20$ ns.

The values of the parameters that affect the production and propagation of the scintillation light considered in the simulation are summarized in Tab. 6.4. The Rayleigh scattering length considered in the DUNE studies was shorter, as it was based on a previous mea-

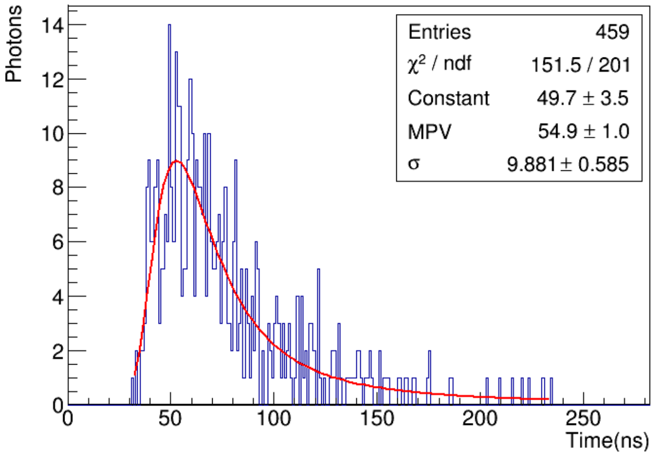

Figure 6.11: Example of a typical arrival time distribution of photons fitted to a Landau function. Photons propagate from a voxel to a PMT. One fit per PMT and per voxel are needed.

surement and taken as a more restrictive situation for the design validation. In any case, a longer Rayleigh scattering length would improve the detector performance.

6.4 Simulation of the photon detector system response

A dedicated module has been developed to simulate the photon detector system response. This modules takes as input the list of photons arriving to either the PEN foil or the TPB coating, and generates the resulting PMT waveforms. This modules has been used in both ProtoDUNE Dual-Phase and DUNE Dual-Phase studies. The simulation follows several steps:

- First, an empty waveform is generated as a uniform vector of integers with a constant value of 4000 ADC, which is near the baseline value in the data (see chapter 5.
- Second, the electronic noise is added, moving all the vector values randomly according to a Gaussian distribution with sigma 0.6 ADC. This value is obtained from data (see Sec. 5.3).
- Then, the PMT dark counts are added randomly along all the waveform, with an average rate of 1.7 kHz as it was characterized in the laboratory [191].
- Finally a loop is done over the list of photons arriving to the wavelength-shifters, adding the corresponding detected photo-electrons at its time of arrival. Each photon in the list has a probability to produce a photo-electron in the PMT photo-cathode.

> In the simulation, an effective detection efficiency (DE) is considered. This DE takes into account the wavelength-shifting efficiency, the propagation of the visible light from the wavelength-shifter towards the PMT photo-cathode, and the PMT quantum efficiency. The values used in the light simulation are explained in chapter 8: $\mathrm{DE}_{TPB} = 0.11$ and $\mathrm{DE}_{PEN} = 0.018$ (see Tab. 8.6).

The SPE response has been measured in the laboratory, by doing the average waveform for SPE signals. Left panel of Fig. 6.12 shows the average SPE response at different voltages. Note the fast response with a full-with-half-maximum (FWHM) below 4 ns. The right panel shows the distribution of the integrated SPE signal measured in the laboratory fitted to the PMT response function. The distance between the first and the second maximum corresponds to the gain of the PMT (the average area of the SPE response), and σ measures the width of the SPE distribution. The fitted function is detailed in [191]. σ have a typical value of of 0.4 times the gain.

In the simulation, waveforms are produced by adding the SPE response for each detected photon (either signal or dark count). The area of the added SPE is scaled considering the corresponding PMT gain. The scaling factor follows a Gaussian distribution with the mean in the PMT gain and a sigma of 0.4, as it is observed in the data.

Finally, an example simulated CRT triggered muon in ProtoDUNE Dual-Phase is shown in Fig. 6.13. The top panels show the energy deposition in the liquid argon in blue, black box marks the position the inner box of the cryostat, red box shows the TPC active volume. The left panel shows the top view of the detector, and the right panel shows the side view. Black circles show the PMT positioning. The energy deposition around the muon track is due to the production of delta rays and electromagnetic showers. The bottom panels show the simulated waveforms for the four selected PMTs (as red circles in the top panels). The signal amplitude detected by the PMT on the right is higher than the signal in the other PMTs, as expected since it is placed closer to the muon track.

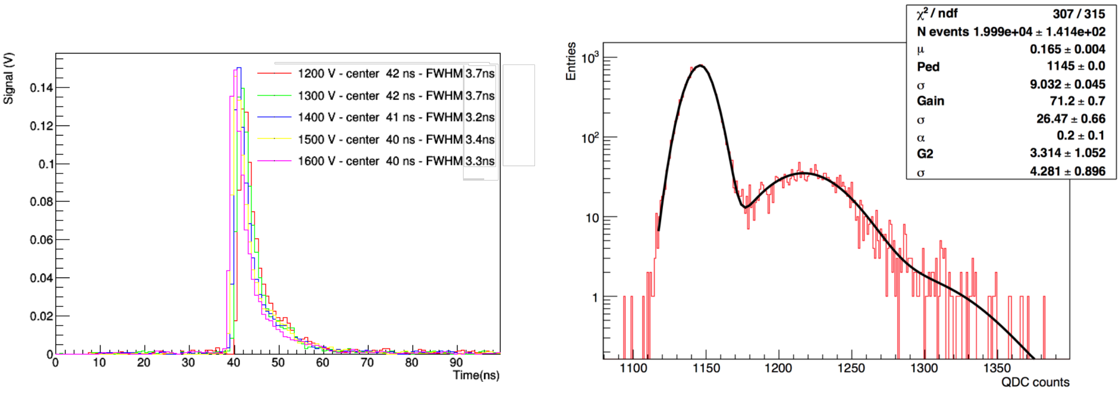

Figure 6.12: Left: PMT SPE response measured in the lab at different voltages. Right: Typical PMT SPE spectrum [191].

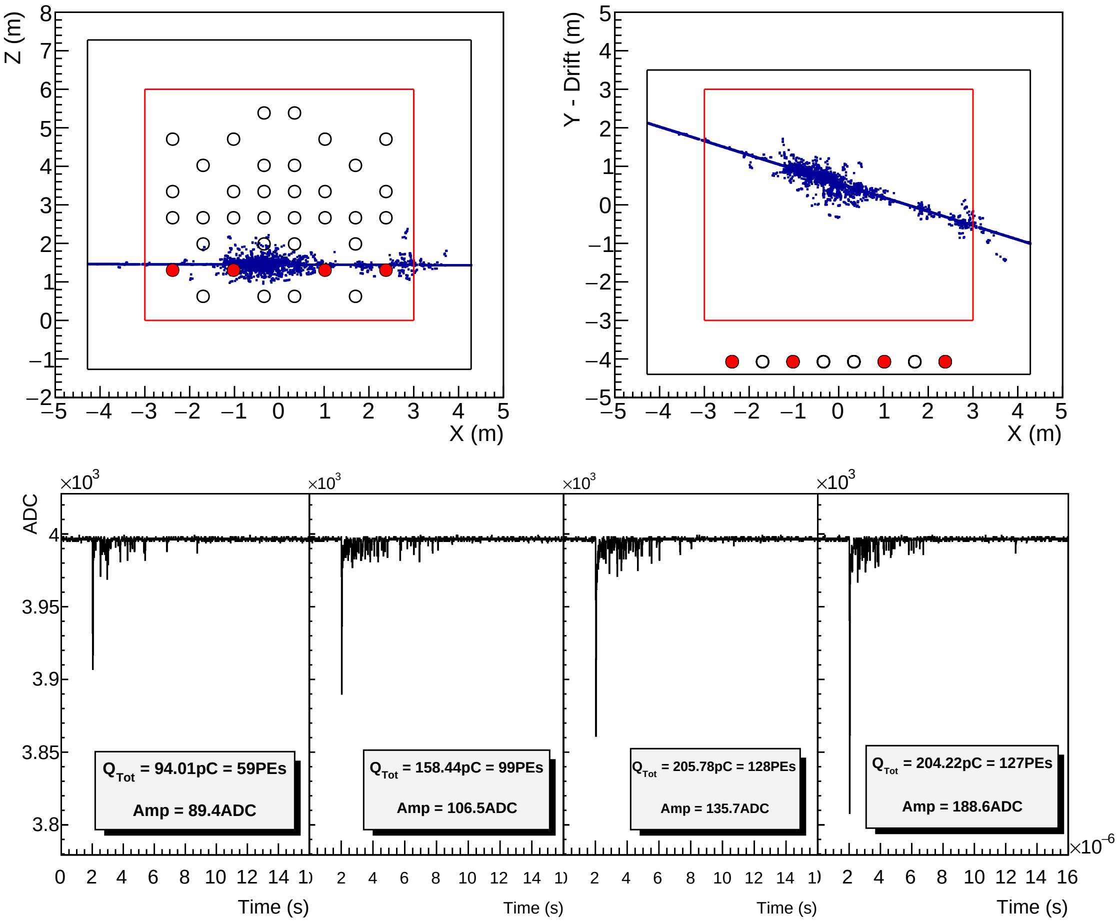

Figure 6.13: Display of a simulated CRT triggered muon in the ProtoDUNE Dual-Phase geometry. Top plots show the energy deposition in the liquid argon, plots below show the simulated waveforms for four PMTs.

Chapter 7

Study of the cosmic-muons scintillation light in ProtoDUNE Dual-Phase

As explained in Sec. 6.2.1, ProtoDUNE Dual-Phase is exposed to cosmic muons that produce scintillation light. Depending on amount of deposited energy and the distance from the deposition to the PMTs, this scintillation light can be detected as S1 signals or as background rate of SPE signals. Additionally, there is a scintillation light background produced by the decay of radioactive isotopes naturally present in argon (see Sec. 6.2.3). This radiological background mainly contributes to the rate of SPE signals.

In this chapter, scintillation light produced by cosmic muons and radiological sources in ProtoDUNE Dual-Phase is analysed and compared with simulation. First, the Monte Carlo simulation explained in chapter 6 is validated by comparing the light yield of CRT triggered muons with data in Sec. 7.1. Then the rate of scintillation light S1 signals and SPE background is evaluated and compared with the simulation of cosmic muons and radiological sources in Sec. 7.2.

7.1 Simulation validation using CRT triggered muons

In this section, the detector response is studied using CRT triggered tracks. This is the only available data for which the position of the interacting particle is known, as it is provided by the CRT panels (see Sec. 4.1.5). In this sense, the dependence of the detected light with the track-PMT distance is obtained for different sets of simulation parameters. The simulation of CRT triggered muons is explained in detail in Sec. 6.2.2. The dependence of the detected light with the simulation parameters is studied and compared with data, in order to validate the simulation.

7.1.1 Dependence of the detected scintillation light in the simulation with the photon-propagation parameters

As explained in Sec. 2.5, during their ropagation in liquid argon, scintillation photons can scatter elastically (Rayleigh scattering), be absorbed by impurities and be reflected or absorbed by the detector elements. These three effects are introduced in the simulation by three parameters: Rayleigh scattering length (λ_{RS}), absorption length (λ_{abs}) and reflectivity of aluminium and stainless steel ($\mathrm{R}_{\mathrm{Al\&SS}}$). As detailed in 6.1, $\mathrm{R}_{\mathrm{Al\&SS}}$ accounts for the reflections in the cathode, ground grid, field cage and cryostat walls. The considered baseline values are λ_{Abs}=20 m [176], λ_{RS}=99 cm [173] and $\mathrm{R}_{\mathrm{Al\&\ SS}}$=27% [233] as expected from the literature (see chapter 6). In this section, the dependence of the detected scintillation light in the simulation with the three parameters is studied. A scan in the three parameters is performed individually, by varying the target parameter and maintaining fixed the other two.

Figure 7.1 left panel shows the expected S1 charge from CRT triggered muons detected by the PMTs versus the track-PMT distance for three values of λ_{Abs} (15, 20 and 25 m). The lower panel shows the ratio of the curves with respect to the lower value of λ_{Abs}=15 m. The increasing ratio for longer track-PMT distances indicates a larger light detection at longer distances for longer values of λ_{Abs}, as expected since the absorption increases with the photon-propagation-path length (see Sec. 2.5.2).

In the same way, the right panel of Fig. 7.1 shows the S1 charge versus the track-PMT distance for three values of λ_{RS} (61 cm, 99 cm and 165 cm), and the lower panel the ratio of the curves with respect to the lower value of $\lambda_{RS} = 61$ cm. As for λ_{Abs}, a longer λ_{RS} increases the light detection at longer distances as it is shown in the lower panel. Although the Rayleigh scattering is elastic and do not reduce the number of photons directly, this dependence is expected since a shorter Rayleigh scattering length increases the photon-propagation-path length, and thus, the probability to be absorbed (see Sec. 2.5.1).

Finally, Fig. 7.2 shows the S1 charge versus track-PMT distance for four values of $\mathrm{R}_{\mathrm{Al\&SS}}$ (0%, 27%, 40% and 60%). In contrast with the results obtained for λ_{Abs} and λ_{RS}, the scan performed in $\mathrm{R}_{\mathrm{Al\&SS}}$ provides an overall variation of the detected light, with no dependence on the track-PMT distance. Only at the higher reflectivity value of 60%, a larger increase is observed at 3 m and at 5 m. These positions correspond to PMTs placed next to the field cage, and are more affected by the increase of the $\mathrm{R}_{\mathrm{Al\&SS}}$ that the PMTs placed at the center. Since the expected value of the reflectivity $\mathrm{R}_{\mathrm{Al\&SS}}$ is 27%, as measured by the ICARUS collaboration [233] and it is being used by the SBND experiment, it can be considered that the slope of the S1 charge versus the track-PMT distance do not depend on $R_{Al\&SS}$ in the expected range of values.

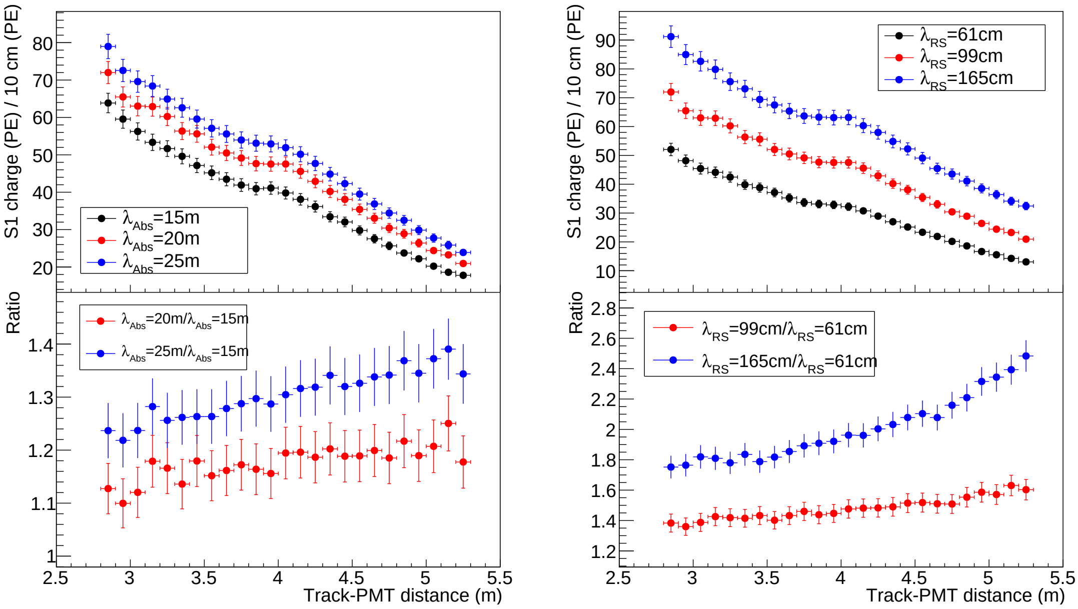

Figure 7.1: Simulated S1 charge versus the track-PMT distance for three different values of λ_{Abs} (λ_{RS}) on the left (right). The ratio of the curves are shown in the lower panels.

In conclusion, this study shows that the dependence of the S1 charge with the track-PMT distance in the simulation is affected mainly by λ_{RS} and λ_{Abs}, but not by $R_{Al\&SS}$.

7.1.2 Validation of the S1 charge simulation.

Since the previous study showed that the variation of the S1 charge with the track-PMT distance depends on two parameters only, a 2D scan in λ_{RS} and λ_{Abs} is performed in order to find the values that best fit to data. A simulation of CRT-triggered tracks has been done for every pair of values of λ_{RS} = 61, 99 and 165 cm, and λ_{Abs} = 15, 20 and 25 m, nine simulations in total. The value $R_{Al\&\ SS}$ is kept constant at 27% [233].

Figure 7.3 shows the simulated S1 charge versus the track-PMT distance plotted together with the data in each case. λ_{Abs} is kept constant in each column, λ_{RS} in each row. The plot in the centre corresponds to the baseline values (λ_{Abs} =20 m and λ_{RS}=99 cm) which is clearly the best case at reproducing the data.

In order to evaluate the similarity of the data and simulation curves, the ratio is obtained in each case. Figure 7.4 shows the ratio of the simulation over data for the nine cases. If the simulation reproduces well the data, the curve would be a constant centred in one. Therefore a fit to a constant function is performed in every curve (shown in red). The value of the fit and the χ^2 value is shown in the legend. The χ^2 values allow to discard

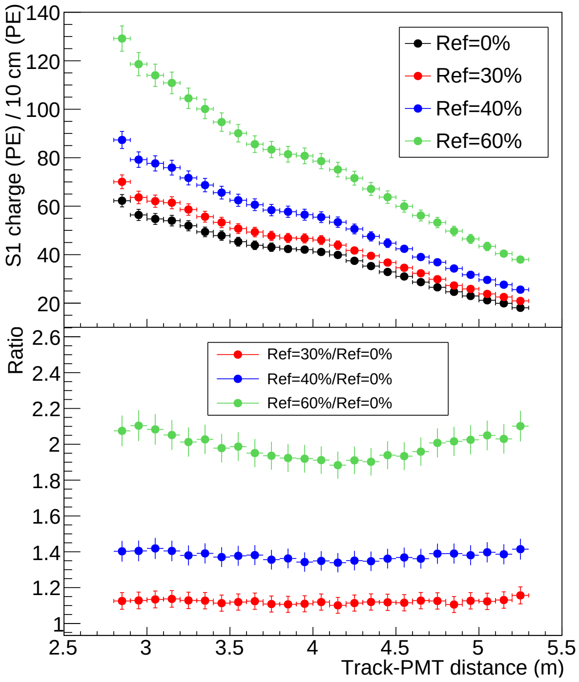

Figure 7.2: Simulated S1 charge versus the track-PMT distance for four different values of reflectivity. The ratio of the curves is shown in the lower panel.

the simulations considering λ_{RS}=61 cm (first row) and λ_{RS}=165 cm (third row), since the curves are not flat. The value of λ_{RS}=99 cm provides a good χ^2 for all three values of λ_{Abs} (15, 20 and 25 m). The lower χ^2 is obtained for the situation with an increased absorption (or lower absorption length, λ_{Abs}=15 m) and λ_{RS}=99 cm. However, the average value of the ratio of 0.88 is clearly underestimating the detected light in the simulation, in contrast with the value of 1.03 obtained for the baseline situation. In the case of considering a value of λ_{Abs}=15 m, other simulation parameters would need to be tuned in order to reproduce the data curve (for example increasing $R_{\text{Al\&SS}}$ or the PMT detection efficiency).

Therefore, a good agreement between data and simulation has been found for the baseline set of parameters and the simulation of the S1 charge is considered to be validated.

7.1.3 Validation of the S1 amplitude simulation

Apart from the S1 charge, the simulation of the S1 amplitude must be also validated. This is important since the S1 amplitude is the first observable used to distinguish scintillation light signals from low energy backgrounds, and a trigger based on the PMT signal also relies on the amplitude of the S1 signal over a certain threshold.

Figure 7.5 shows the dependence of the S1 amplitude for CRT triggered muons with the track-PMT distance for data (black) and simulation. Two values of τ_{fast} are considered

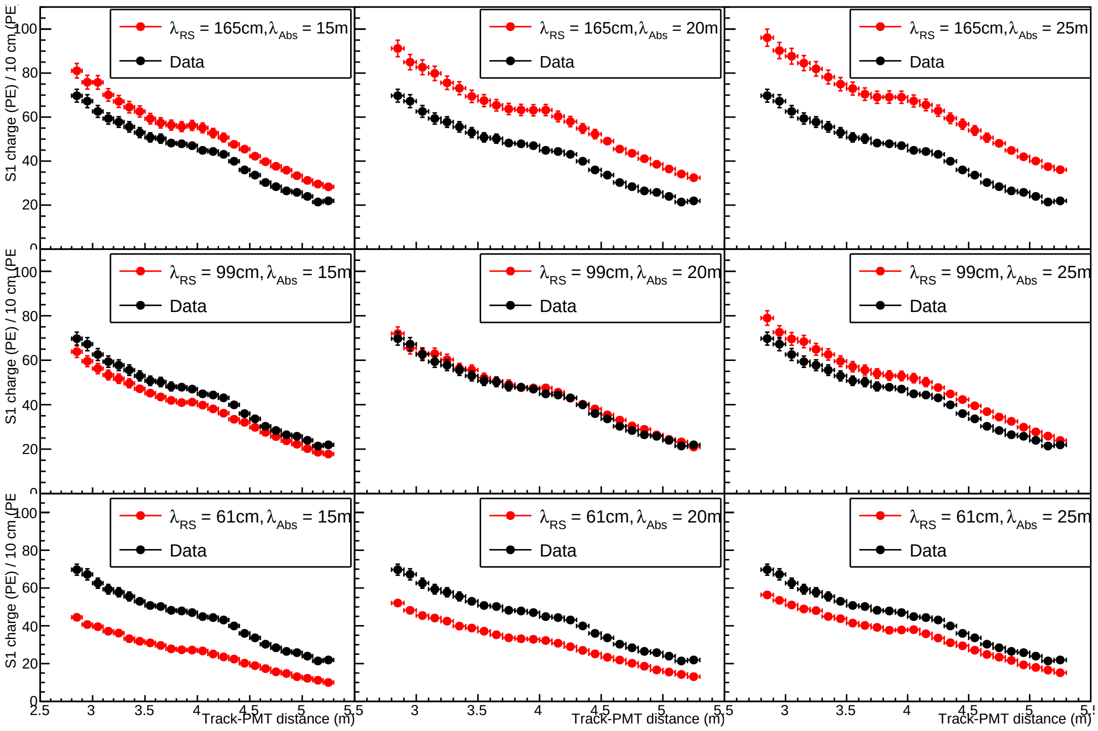

Figure 7.3: Data (black) and simulated (red) S1 charge versus the track-PMT distance for nine different values of λ_{RS} and λ_{Abs}.

in the simulation, the theoretical value of 6 ns (red), and the data-driven value of 50 ns (blue) which includes the intermediate component as obtained for the PEN PMTs in data (see Tab. 5.3). A value of τ_{slow}=1.45 μs is considered in both simulations, as measured in data (see Tab. 5.3). The ratio of the simulation over data is shown in the lower panel. The theoretical value of 6 ns overestimates by a factor of two the S1 amplitude. This discrepancy is expected and it is due to the presence of an intermediate component τ_{int} in the data (see Sec. 5.5). In order to better reproduce the S1 amplitude, the simulation has been repeated considering the effective value of τ_{fast} =50 ns as obtained in the data for the intermediate component (see Sec. 5.5). This value reproduces better the amplitude of the signal, with an agreement better than 30% in the full range.

In summary, the simulation of the S1 charge achieves a good agreement between data and simulation (better than 10% in the full range of distances), while a larger discrepancy is found in the S1 amplitude. This is due to the approximations considered in the simulation that must be addressed in future improvements: First, the time response of the wavelength-shifters is assumed as instantaneous in the simulation. Indeed, the re-emission of the fast component at slower times is the origin of the τ_{int} observed in the data, as it is pointed in the literature [225]. This is mitigated by using the effective parameter of τ_{fast} = 50 ns,

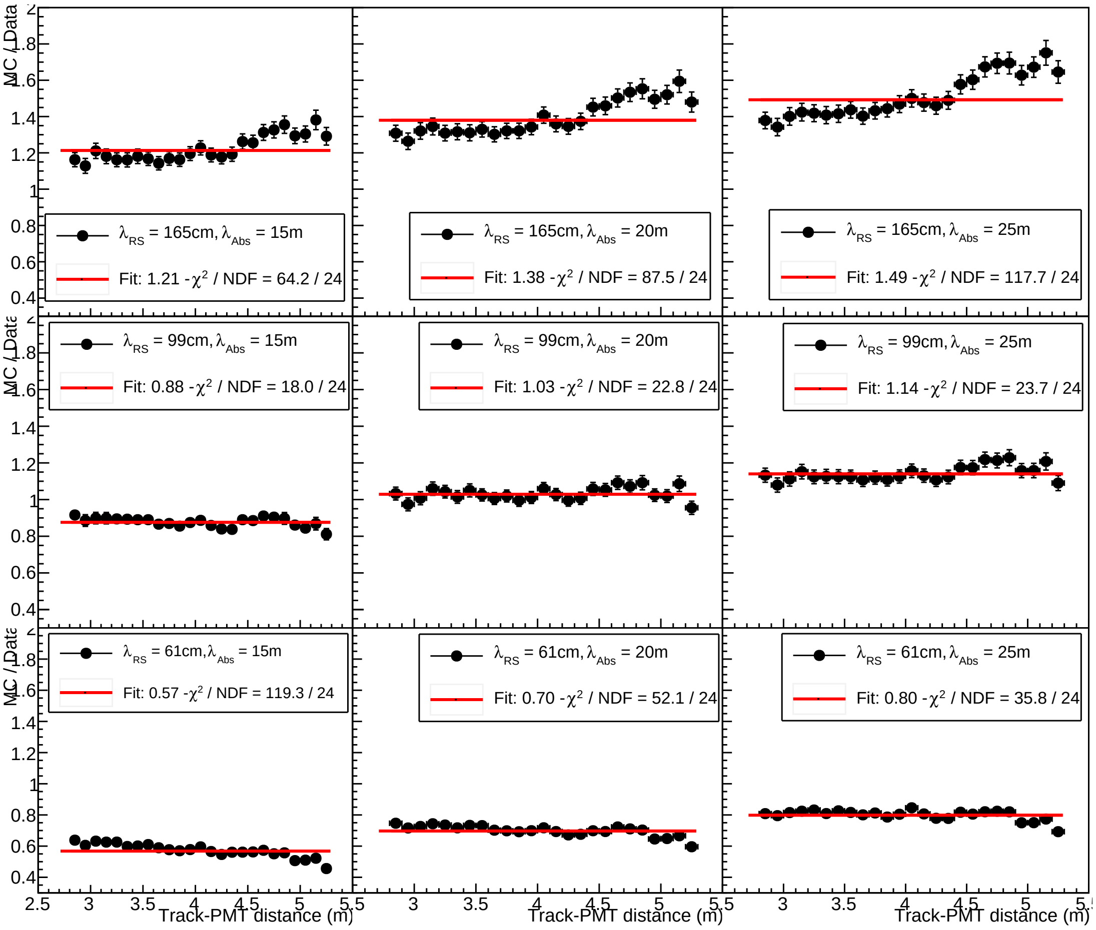

Figure 7.4: The ratio of simulated S1 charge over data versus the track-PMT distance for nine different values of λ_{RS} and λ_{Abs}.

however are more realistic simulation of the re-emission, convoluting the detected-photons arrival time with the wavelength-shifter time response function would provide a better agreement with the data. The wavelength-shifter time response is found in the literature for TPB [225] but it has not been measured for PEN yet. .Finally, the signal divider placed between the PMT and the digitizer also modifies the signal: It acts as a high-pass filter that stretches the signal and introduces a waving effect (see Sec. 5.5) and an overshooting in large signals that are not included in the simulation. The stretching of the signal results in an increase the S1 amplitude.

In summary, the S1 charge is well reproduced by the simulation considering the baseline simulation parameters (λ_{RS}=99 cm, λ_{Abs}=20 m and $\mathrm{R_{Al\&SS}}$), and the S1 amplitude is reasonably well reproduced if considering an effective value of the τ_{fast} of 50 ns to correct the not-simulated wavelength-shifting re-emission. This allows validating the simulation in order to compare with data in Sec. 7.2.

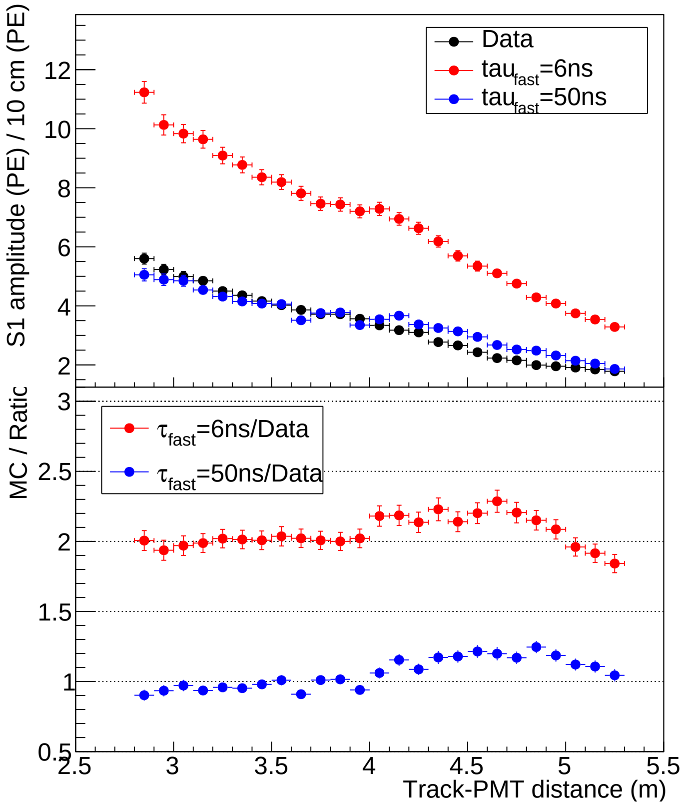

Figure 7.5: S1 amplitude versus the track-PMT distance. Data is shown in black, simulation is shown is red (considering a theoretical value of τ_{fast} =6 ns) and blue (considering the data-drive value of τ_{fast} =50 ns).

7.2 Cosmic muon and SPE rate data-MC comparison

The scintillation light detected by ProtoDUNE Dual-Phase has two main origins: First, cosmic muons crossing the liquid argon as the detector is placed at the surface. Second, the argon itself: either from the decay of argon isotopes (^{39}Ar and ^{42}Ar) or radioactive contaminants (^{85}Kr). These events, either a crossing muon or a radioactive decay, can produce an S1 signal or contribute to the background of SPE signals. On the one hand, although most of the muons will produce an S1 signal, a muon crossing far away from a PMT or depositing a small amount of energy also contributes to the SPE background. On the other hand, although most of the radioactive decays contribute to the SPE background due to the small amount of energy deposited (below the MeV range), some of them can happen next to a PMT, producing a signal large enough to mimic a small S1.

In this section, the rate of S1 and SPE signals is measured and compared with simulations. The simulation of the cosmic muons is generated with CORSIKA and the radiological backgrounds with custom generators as explained in detail in 6.2.1 and 6.2.3

respectively. The simulation is performed considering the parameters validated in Sec. 7.1, λ_{Abs}=20 m, λ_{RS}=99 cm and $\tau_{fast} = 50$ ns.

In a detailed study by A. Gallego in [227], the S1 and SPE rates in ProtoDUNE Dual-Phase are measured, and a reasonable agreement is found for the S1 rate when compared with simulation. According to [227], the average S1 rate measured in the data is 5.5 kHz in the PEN PMT while 8.8 kHz for the TPB PMTs. The values obtained in the simulation are 6.1 kHz on the PEN PMTs and 10.2 kHz on the TPB PMTs, obtaining a ratio of the simulated S1 rate over data of 110%. The measured SPE rates are 345 kHz on TPB PMTs and 166 kHz on PEN PMTs, which is largely above the expected SPE rate produced by the cosmic muons and the radiological background [227, 241].However, in [227, 241] the simulation of the S1 amplitude considered a value of $\tau_{fast} = 6$ ns, leading to a wrong simulation of the S1 amplitude that is later corrected offline. In this study, this correction is applied in the simulation, by considering a value of $\tau_{fast} = 50$ ns (see Sec. 7.1). Additionally, slightly different values of the effective detection efficiencies for PEN and TPB PMTs are considered in this work, based on the dedicated study presented in chapter 8.

As explained in chapter 6, each light source is simulated with a different event generator. In this way, each source of light can be freely activated and five simulation samples are generated: One for each of the light sources individually (CORSIKA, ^{39}Ar, ^{42}Ar and ^{85}Kr), and another one with all the light sources activated (CORSIKA + ^{39}Ar + ^{42}Ar + ^{85}Kr). Random-trigger data from ProtoDUNE Dual-Phase are used for the comparison with the simulation. Both data and simulation consider a time acquisition window of 1 ms, and a PMT gain of 1×10^7. At this gain, the amplitude of the SPE is $\sim$7.5 ADC. The simulation sample used as a reference in the following corresponds to the sample with all the light sources activated (CORSIKA + ^{39}Ar + ^{42}Ar + ^{85}Kr), and it will be referred simply as the simulated sample. The reference of any other sample will be mentioned explicitly.

Figure 7.6 top panel shows a typical data waveform from a PEN PMT, and the bottom panel shows a typical waveform in the simulation. Both waveforms look similar, although it is clear that there is more activity of SPE signals on the data waveform.

A typical simulation event is shown in Fig. 7.7. The top panels show the deposited energy in the detector. The top-left panel shows the top view and the top-right panel is the side view. The energy deposition is shown in black for cosmic muons from CORSIKA, in red for ^{39}Ar and blue for ^{85}Kr. No activity from ^{42}Ar is seen in this event since the activity is very small in comparison with the other sources (see Sec. 6.2.3). The black box marks the inner box of the cryostat, and the red box the TPC-active volume. Circles show the PMT positioning in the detector geometry. The bottom panels show the simulated

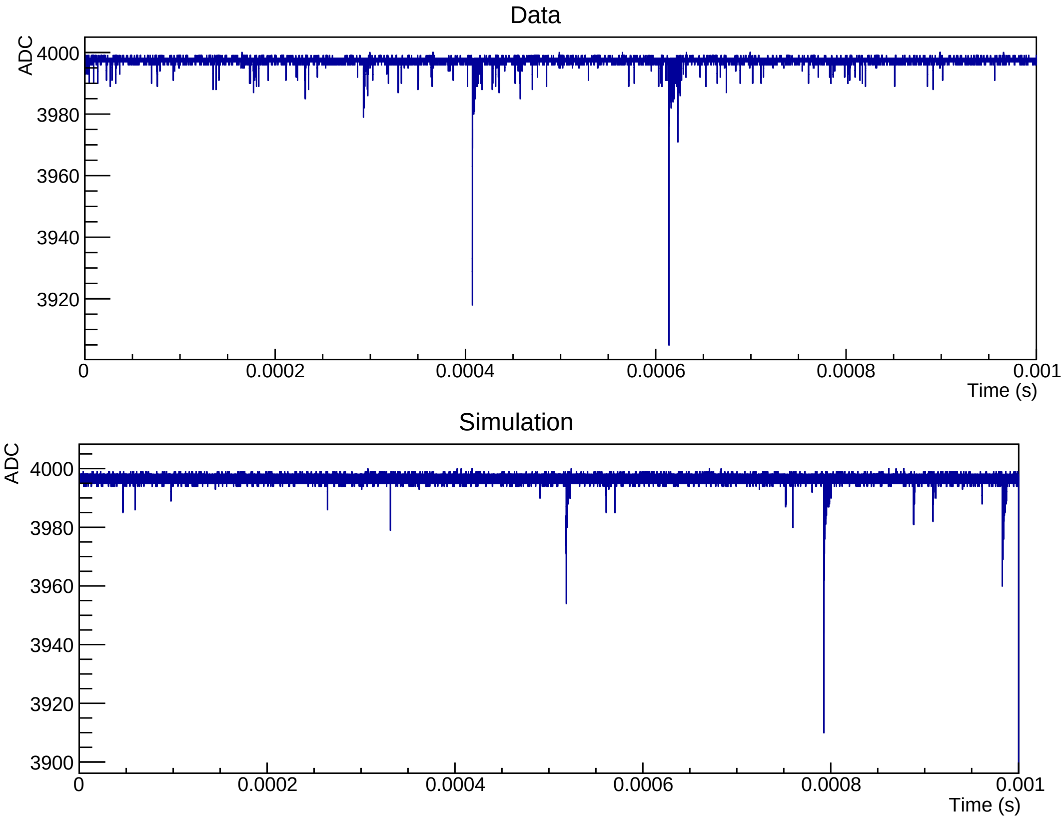

Figure 7.6: Example of data (top panel) and simulated (bottom panel) waveforms considered in this analysis. Simulation includes both cosmic muons and radiological background (CORSIKA + ^{39}Ar + ^{42}Ar + ^{85}Kr).

waveforms for four of the PMTs that are marked as red circles in the top panels. The waveform length is 1 ms.

The energy deposition on the top panels shows the high activity due to the cosmic muons, with long muon tracks, that produce the S1 signals that are seen in the PMT waveforms on the bottom panels. In this example event, 22 muons cross the liquid argon volume, depositing 900 MeV per muon on average. The PMTs detect 4-6 S1 signals each that correspond to the longer muon tracks depositing energy nearby. The small scatter dots of energy deposition in the liquid argon correspond to the low-energy radiological activity. Despite the large activity seen by the ^{39}Ar, there is no an equivalent activity in the waveforms. This is due to the small energy deposited by the ^{39}Ar decays. In this example, there is 824 ^{39}Ar decays depositing 215 keV each on average. The contribution of the different sources (CORSIKA, ^{39}Ar, ^{42}Ar and ^{85}Kr) will be disaggregated in Sec.7.2.3 and 7.2.4.

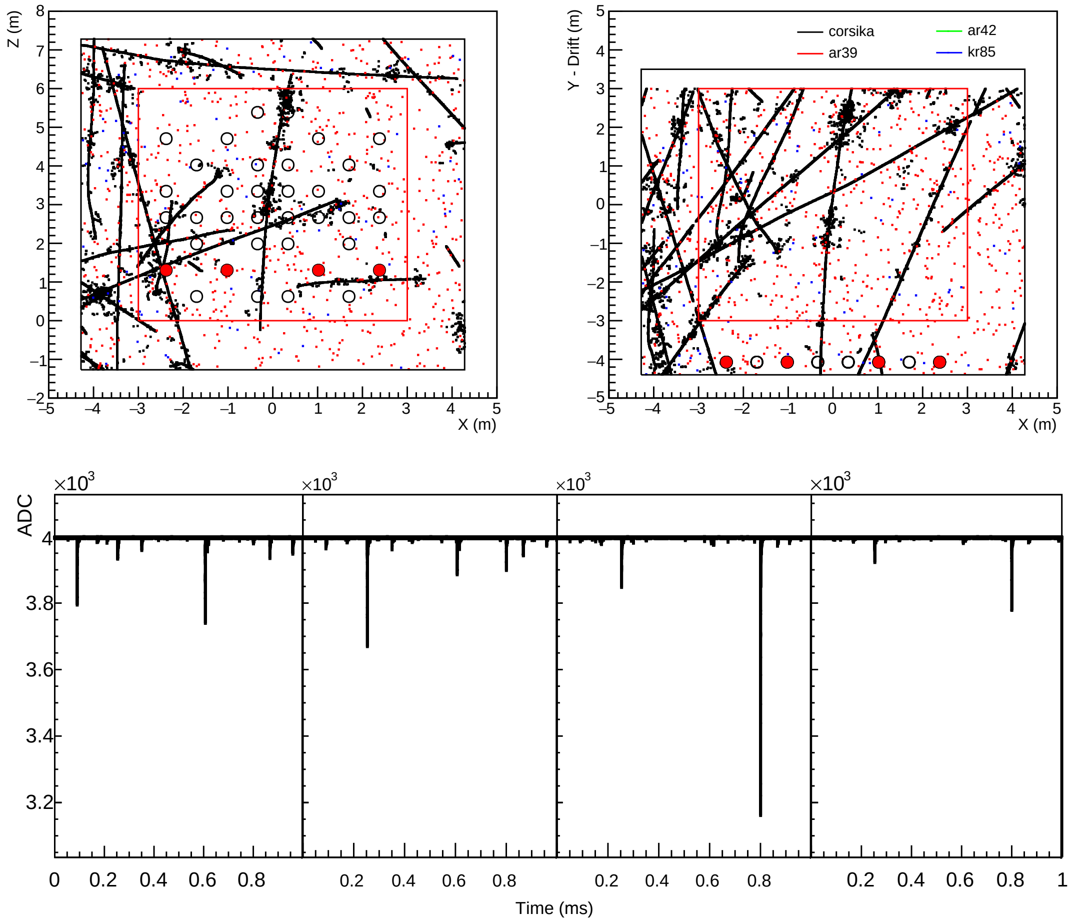

Figure 7.7: Typical event in the reference simulation sample, CORSIKA + ^{39}Ar + ^{42}Ar + ^{85}Kr. The top panel shows the energy deposition in the liquid argon during 1 ms. The top view of the cryostat is shown on the left panel and the side view on the right panel. The energy deposition colour corresponds to each generator (black for CORSIKA, red for ^{39}Ar and blue for ^{42}Ar). No activity of ^{42}Ar is seen in this event since the activity is very low (see Sec. 6.2.3). Circles show the PMT positioning in the detector geometry. The bottom panels show the four PMT waveforms which correspond to the red circles on the top panels.

7.2.1 Waveform processing: Hit finding and clustering

The analysis of data and simulation samples follows the same steps. First, hits are identified as any deviation of the signal from the baseline. The signal is integrated until it reaches the baseline again. Any signal above 4 ADC counts is identified as a hit (around half of the amplitude of an SPE).

The top panel of Fig. 7.8 shows the hits found in the data waveform after applying the hit finding algorithm. Hits are visible in the waveform with a red marker at its maximum amplitude. Each hit is characterized by its integrated charge, maximum amplitude and time. It is clear in the figure that there are many hits that belong to the same S1 signal. Typically we observe a hit of large amplitude, corresponding to the fast component of the scintillation light, followed by many hits of decreasing amplitudes from the slow component. Most of the hits of small amplitude are SPEs.

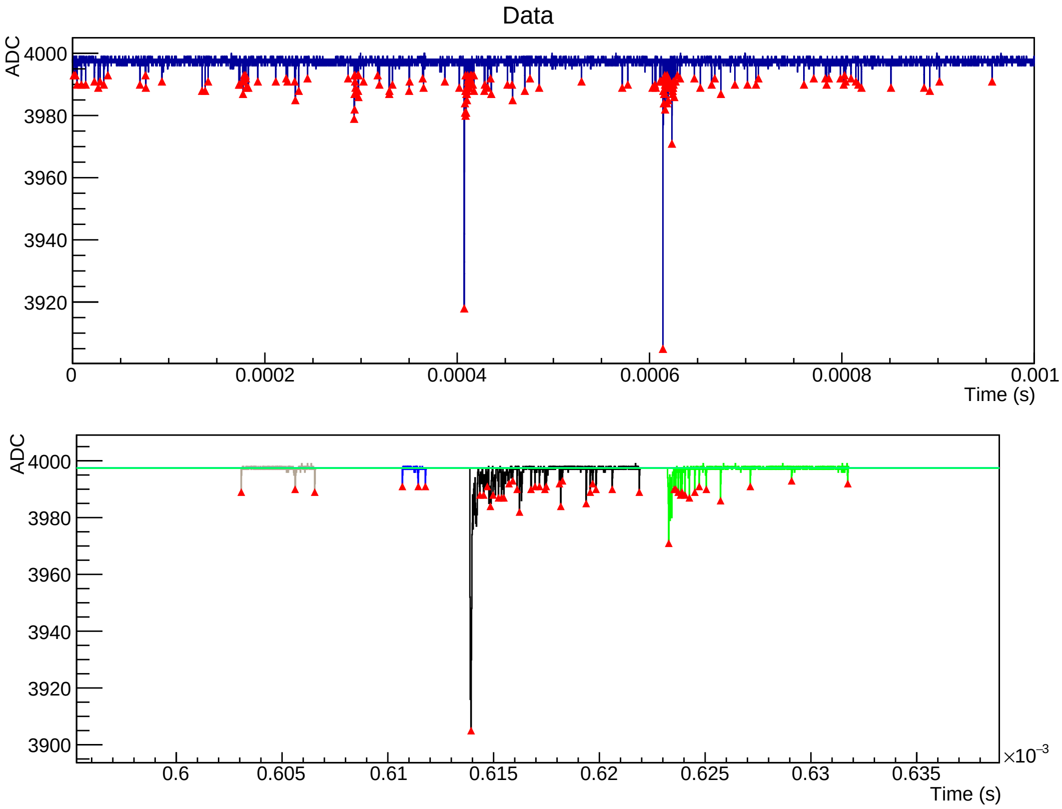

Figure 7.8: Top: Example of the hits found in a data waveform. Each hit is marked with a red marker. The window length is 1 ms. Bottom: Zoom of the waveform above after the hit clustering algorithm. Hits are grouped in clusters. Four clusters are identified (grey, blue, black and green). The window length is ∼40 μs.

In a second step, the hits are grouped by looking for time correlations to form clusters. Clusters group all hits belonging to the same physics event, *i.e.* an S1 signal. All hits with a time distance smaller than 3 μs are grouped in the same cluster. Additionally, in order to deal with the pile-up of signals, hits are added chronologically, and only if the new-hit amplitude is around the same amplitude of the previous added hit. Therefore, if the new-hit amplitude is three times larger than the last added hit, the cluster is closed and a new cluster is created with the new hit. In this way, if a second S1 arrives later, the algorithm allows the separation of both signals. An example of the clustering results is shown in the bottom panel of Fig 7.8. A time distance of 3 μs and a hit amplitude threshold of three are chosen as they provide a good separation of signals. Since the decay time of the slow component is around half of this value, this time distance ensures that signals from different physics events are well separated. This waveform zooms in around the maximum signal seen on the top panel waveform (around 0.6 and 0.64 ms). Four clusters are found in this window, and they are shown in different colours: black, green, brown and blue. Black and green clusters are two S1 signals, and they are well-separated thanks to the amplitude requirement explained above. Grey and blue clusters are streams of SPEs.

7.2.2 Data-simulation comparison

Once the clusters are identified, the cluster frequency is compared in data and simulation. The top panel of Fig. 7.9 shows the frequency of clusters versus the cluster charge for data and simulation samples in a PEN PMT. Blackline shows the data sample and magenta the simulation including all light sources (CORSIKA + ^{39}Ar + ^{42}Ar + ^{85}Kr). Isolated hits are also included as clusters of 1 PE. The x axis is drawn in logarithmic scale on the top panel, to focus on the rate of small charge clusters, and in linear scale on the bottom panel, to better compare clusters of high charge. For clusters with charge below 40 PEs, there is a clear deficit in the simulation of almost one order of magnitude compared to data (top panel). The red, green, blue and brown curves show respectively the CORSIKA, ^{39}Ar, ^{42}Ar and ^{85}Kr samples. Most of the clusters are due to muons generated by CORSIKA, as can be seen by comparing the red and magenta lines. The ^{39}Ar, ^{42}Ar and ^{85}Kr generators only contribute at small energies, below $\sim$40 PEs, however, this is not enough to reproduce the data. This deficit points to an underestimation of the low energy events in the simulation.In the bottom panel, a small excess in the event rate above $\sim$ 40 PEs can be appreciated in the simulation. In this case, since there is no radiological events above 40 PEs, the excess is entirely due to the CORSIKA simulation. This excess points to an overestimation of the muon rate in the CORSIKA simulation. Similar plots are obtained for the rest of the PMTs. However, while radiological decays contribute with clusters of up to a maximum of 40 PEs in the PEN PMTs, they provide up to 100 PEs in the TPB PMTs, due to their better efficiency.

7.2.3 S1 rate

In order to quantify the muon rate excess in the CORSIKA simulation, the S1 rate is computed per PMT in data and simulation. Any cluster with an amplitude larger than 2 PEs is initially considered as an S1 muon candidate. Additionally, since the radiological decays producing a relatively large S1 are expected to happen near the PMT, it is unlikely that another PMT would detect the same S1 signal. Therefore, any S1 signal must be

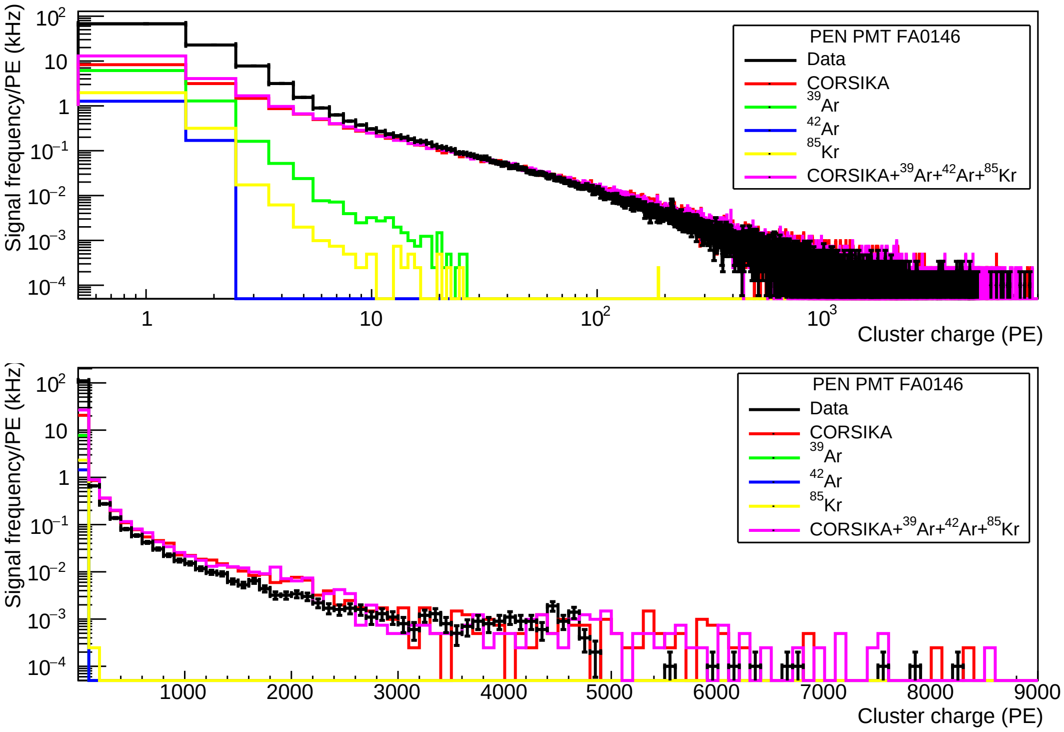

Figure 7.9: Frequency of the clusters versus the cluster charge for a PEN PMT. The x axis is drawn in logarithmic scale on the top panel, to focus on the rate of small charge clusters and in linear scale on the bottom panel, to focus on the rate of large charge clusters.

detected in at least two PMTs to be considered as an S1 muon candidate. The maximum amplitude of the signals must be coincident in time within 100 ns. Figure 7.10 shows the frequency of the selected S1 muon signals versus the S1 charge for a PEN PMTs. By comparing with the top panel of Fig. 7.9, it can be appreciated that this selection has successfully suppressed the contribution by the radiological backgrounds.

The data and simulation S1 rates for each PMT are shown in Fig. 7.11. The data rates are shown on the left panel and simulation rates on the right panel. Each bin corresponds to a PMT at its position in the detector. TPB PMTs are indicated with a red square. The colour axis represents the average S1 rate. The S1 rate in data is around 7 Hz in TPB PMTs and 4 Hz in PEN PMTs. For an easy comparison, the S1 rate ratio of simulation over data for each PMT is shown on the bottom panel. The average S1 charge per selected muon candidate is 150 PEs on PEN PMTs and 470 PEs on TPB PMTs. A slightly higher rate is measured in PMTs placed at the center of the detector in both data and simulation samples, as expected since they are more exposed to the muon tracks. The simulated S1 rate is around 30% above the value measured in the data. No correlation of this excess with the PMT positioning is observed (see bottom panel of Fig. 7.11).

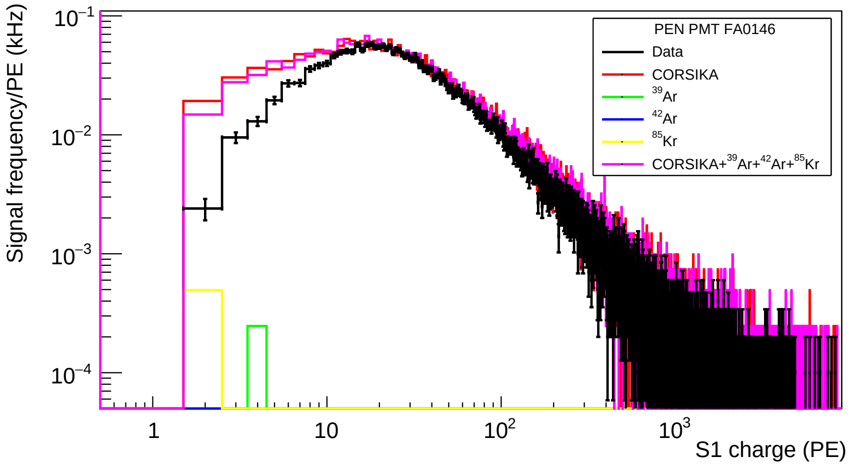

Figure 7.10: Frequency of the S1 muon signals versus the S1 charge for a PEN PMT. Radiological backgrounds are strongly suppressed by the S1 muon signal definition.

The S1 rate for PEN and TPB PMTs is shown on Fig. 7.12. Coloured histograms show the data (blue for PEN and grey for TPB PMTs) while the simulation is shown by lines (red for PEN and magenta for TPB PMTs). The average values are summarized in Tab. 7.1. The average S1 rate for PEN PMTs is 4.3 kHz in data while 5.5 kHz in the simulation, showing the simulation an excess of 28%. A similar excess of 20% is found for TPB PMTs, with an average S1 rate of 6.6 kHz in the data and 8.0 kHz in the simulation.

Sample	S1 rate (kHz)	
	PEN	TPB
Data	$4.3 \pm 0.4(\pm 0.2)$	$6.6 \pm 0.4(\pm 0.1)$
(1) CORSIKA+^{39}Ar+^{42}Ar+^{85}Kr	5.5±0.5	8.0±0.4
CORSIKA	5.5±0.4	8.0±0.5
^{39}Ar	<0.01	0.02±0.01
^{42}Ar	<0.01	<0.01
^{85}Kr	<0.01	<0.01
Ratio simulation (1) / data	1.28±0.06	1.20±0.02

Table 7.1: Average S1 rate for PEN and TPB PMTs in data and simulation samples. Errors are the STD among PMTs. Error in brackets are the STD among different data sets.

In comparison, the study by A. Gallego presented in [227, 241] obtained slightly higher S1 rates that are in reasonable agreement with the results presented in this thesis, considering the different S1 selection algorithms and thresholds. Additionally, the study in [227, 241] obtained a similar excess of 10% of the S1 rate in the simulation with respect to the data, which can be explained by the different effective detection efficiencies for PEN

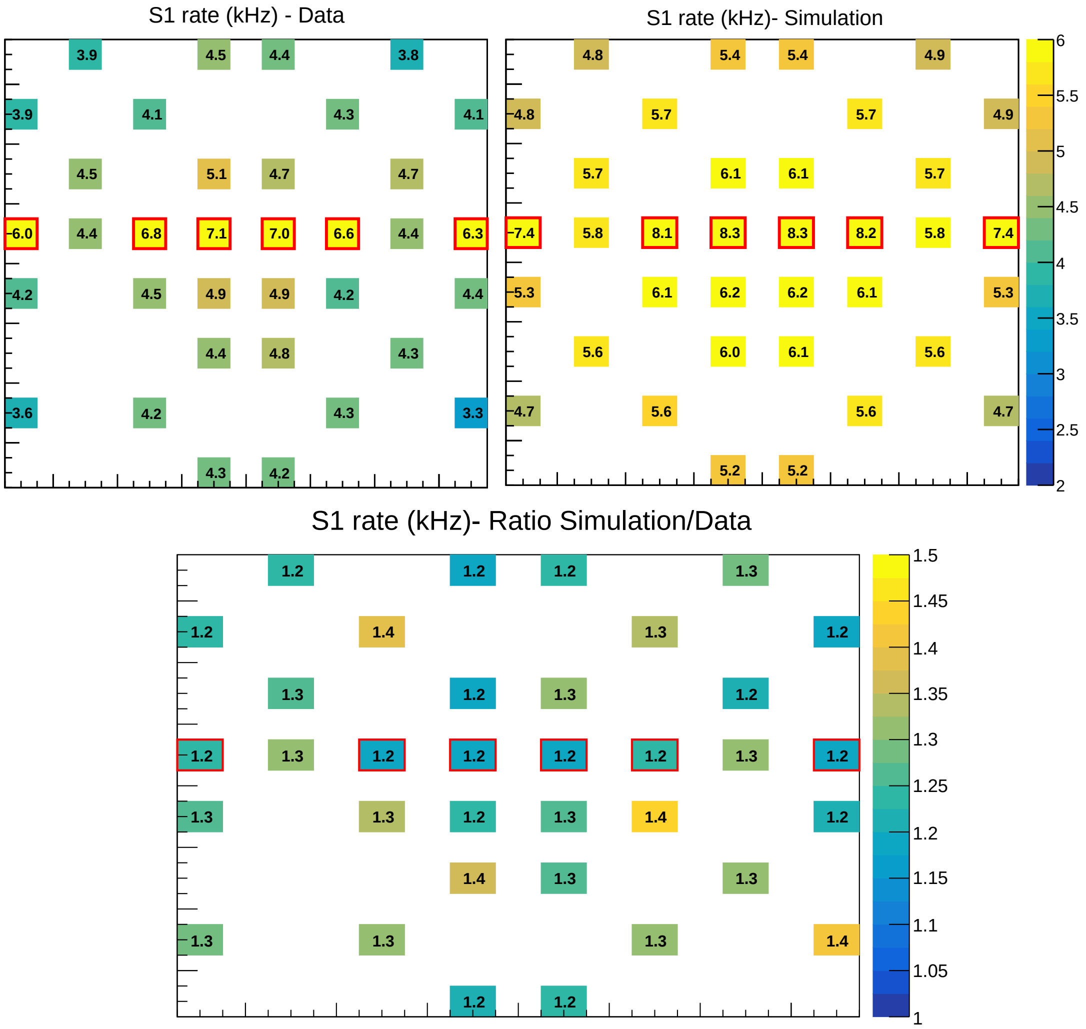

Figure 7.11: Rate of S1 signals per PMT. Data are shown on the top-left panel, simulation on the top-right panel. The bottom panel shows the ratio of simulation over data. Each bin corresponds to a PMT at its position in the detector layout. The colour axis indicates the S1 rate in kHz, which for readability has been included as a number in the bin centre. Red squares indicate the TPB PMTs.

and TPB PMTs considered in the simulation.

In summary, an excess of ∼25% is found in the simulated muon rate when compared with the data. It is significant that μBooNE also found a 26% excess in the simulated cosmic muon rate based on the constant mass composition (CMC) model, the same used here, with respect to the data ([242]). Therefore, this excess points to an overestimation of the muon flux in the selected model. However, there are also some possibilities that could contribute to this discrepancy independently from the model. First, the simulation does not consider the exact positioning of the cryostat, since it is not exactly laying on the ground but a few meters below the surface. As the detector is housed on the underground floor

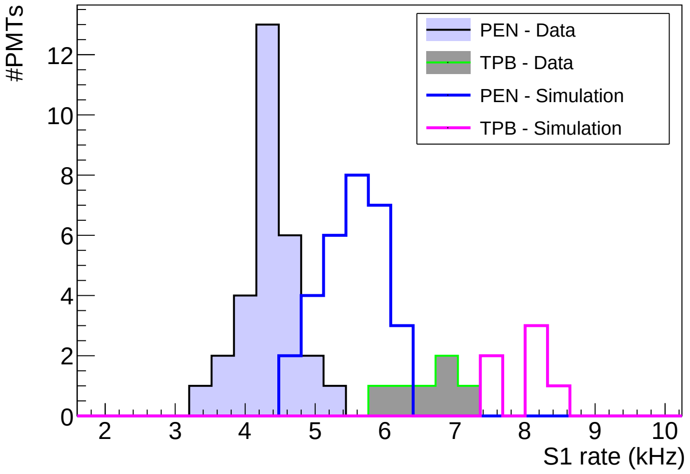

Figure 7.12: S1 rate for PEN and TPB PMTs. Data (blue for PEN and grey for TPB) and simulation (red for PEN and magenta for TPB).

of the EHN1 building, the ground behind the sides of the building and the building itself are probably shielding the cosmic muon flux. Also, the Jura mountains at the northwest of Prevessin also affect the muon flux, and this is not included in the simulation. These hypotheses could be tested by looking for a bias in the geometry of the tracks using the TPC data. However, this is not possible due to the limitations of the TPC operation in ProtoDUNE Dual-Phase (see Sec. 4.3.3).

7.2.4 SPE rate

As pointed out in Sec. 7.2.2, there is a clear deficit of low-charge clusters in the simulation in comparison with the data (see Fig. 7.9).In order to quantify the deficit of low energy events, the rate of SPE signals is measured in the data and simulation samples. The clusters with an amplitude below 2 PEs are considered as SPE background, and they are counted in order to estimate the SPE rate.

The data and simulation SPE rate for each PMT is shown on Fig. 7.13. Data rates are shown on the left panel and simulation rates on the right panel. Each bin corresponds to a PMT at its position in the detector. TPB PMTs are indicated with a red square. The colour axis represents the average SPE rate in kHz. The SPE rate in data is around 350 Hz in TPB PMTs and 120 Hz in PEN PMTs. No significant dependence is observed with the PMT position. For an easy comparison, the ratio of simulation over data for each PMT is shown on the bottom panel.

The average SPE rates for PEN and TPB PMTs are summarized in Tab. 7.2. The reported SPE rates in the data are compatible with the previous study presented in [227,241]. The average SPE background measured in data is 125 kHz versus 40 kHz in the simulation for PEN PMTs, and 350 kHz in data versus 54 kHz in the simulation for TPB PMTs. The simulation is clearly underestimating the SPE rate by a factor of three on PEN PMTs and a factor of six on TPB PMTs. It is significant that the radiological backgrounds contribute with 30% of the SPE rate in the case of the simulated TPB PMTs, while they only represent 10% of the rate of the simulated PEN PMTs. Also, CORSIKA seems to contribute equally with a rate of 35 Hz in both wavelength-shifters.

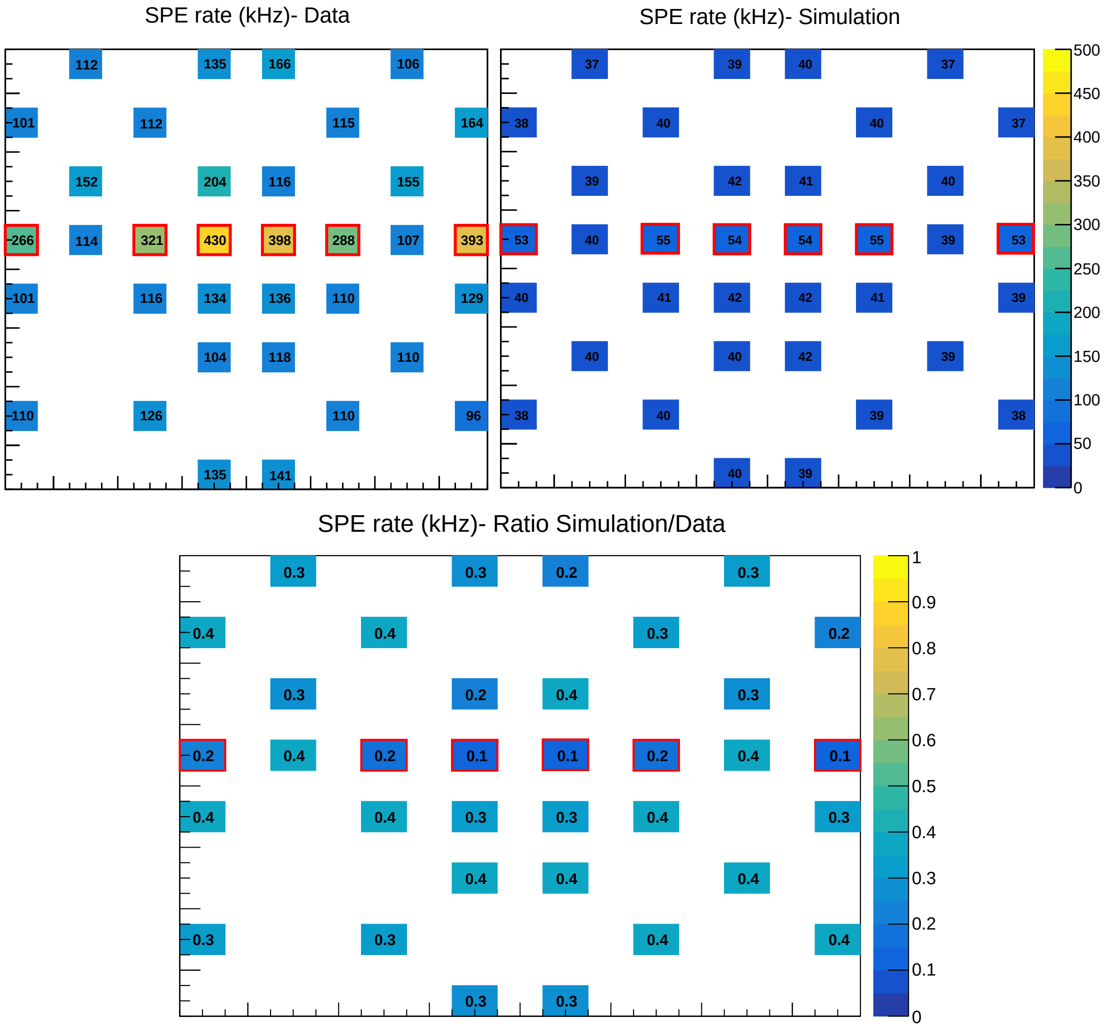

Figure 7.13: SPE rate for PEN and TPB PMTs. Data are shown on the top-left panel, simulation on the top-right panel. The bottom panel shows the ratio of simulation over data. Each bin corresponds to a PMT at its position in the detector layout. The colour axis indicates the SPE rate in kHz, which for readability has been included as a number in the bin centre. Red squares indicate the TPB PMTs.

Other experiments such as μbooNE or ProtoDUNE Single-Phase have also measured

Sample	SPE rate (kHz)	
	PEN	TPB
Data	$125 \pm 24(\pm 25)$	$350 \pm 60(\pm 90)$
(1) CORSIKA+^{39}Ar+^{42}Ar+^{85}Kr	39.7±1.4	54.1±0.7
CORSIKA	35.2±0.4	36.3±0.5
^{39}Ar	5.39±0.01	20.23±0.01
^{42}Ar	0.79±0.05	0.79±0.05
^{85}Kr	1.4±0.1	3.3±0.1
Ratio simulation (1) / data	0.33±0.05	0.16±0.03

Table 7.2: Average SPE rate for PEN and TPB PMTs in data and simulation samples. Errors are the STD among PMTs. Error between brackets are the STD among the different data sets.

an unexpectedly high SPE rate, and an ion transport model has been proposed in [229] to explain it. However, the model in [229] is based on the recombination of Ar_2^+ ions drifted by an electric field, and the analysis developed here uses data in absence of a drift field. It is not clear the contribution of the ion recombination in absence of the drift field, since most of the ions should recombine with the ionization electrons. However, it is possible that the delayed recombination of the electrons escaping the Coulomb potential of the Ar_2^+ ions could contribute to the SPE rate. In any case, further studies are needed in order to estimate this contribution.

Since there is an excess at high energies and a deficit at low energies (see Sec. 7.2.2 and 7.2.3), a possible reason to explain this discrepancy is that part of the low energy signals that are measured as small S1 signals in the simulation are actually contributing to the SPE rate in the data. However, due to the small difference in the S1 rate (below 2 Hz) versus the large difference found in the SPE rate (above 100 Hz), this is clearly not sufficient to explain the discrepancy. Another possible contribution to the SPE background is Cherenkov photons in the visible range produced by the cosmic muons crossing the liquid argon, as the production of Cherenkov photons is not included in the simulations. However, a detailed study performed by ICARUS collaboration estimated that the amount of Cerenkov photons is just 770 photons per cm of track length in comparison with 24,700 scintillation photons per cm [243]. Also, the Cherenkov signal is fast and it would foreseeably contribute to the fast component of the S1 signal, not to the SPE background. Furthermore, the same study [243] underlines the effect of the Cherenkov light in the trigger as it is indeed a fast signal. Therefore, although a dedicated simulation would be desirable to discard this possibility, the Cherenkov photons do not explain the excess observed in the SPE rate. Additionally, the fact that the deficit of signals in the simulation is seen in the energy range of the radiological generators, below 40 PEs (see Fig. 7.9), might point to an underestimation of the radiological activity in ProtoDUNE argon. However, the activity of the ^{39}Ar, the largest contributor to the SPE background, would need to increase by a factor of ten in order to reproduce the data. It does not seem likely to have such a high level of activity in ProtoDUNE Dual-Phase liquid argon. Finally, it must be considered that the radioactivity of the elements inside the cryostat has not been measured. For example, ^{60}Co is present in the stainless-steel of which is made the cathode and ground grid placed just above the PMTs, and inner walls of the cryostat. ^{60}Co undergoes beta decay, emitting a 300 keV electron and two gammas. However, due to the low activity of this isotope at the order of mBq/kg [244], its contribution would be still insufficient to explain the excess.

In summary, a large excess of the SPE rate has been measured in the data with respect to the rate predicted by the DUNE radiological model. Other experiments have measured a similar excess, that might point to a delayed recombination of the ionization electrons escaping the Coulomb potential of the Ar_2^+ ions. Further studies are needed in order to understand this excess and its consequences when considering a larger module placed underground. Radioactivity measurement of the elements inside the cryostat would be desirable for the next steps. Also, further studies using combined information from both scintillation light and ionization charge would help to clarify this excess in the future.

Chapter 8

Measurement of the PEN wavelength-shifting efficiency

As introduced in Sec. 2.3, scintillation light in liquid argon is produced by radiative decay of molecular argon excimers. It has an emission peak at 127 nm where most photosensors are not sensitive. To efficiently detect this light, fluorescent materials are needed to shift the wavelength of the scintillation photons towards the visible range. Two wavelength-shifters are used in ProtoDUNE Dual-Phase: Tetraphenyl butadiene (TPB) and polyethylene naphthalate (PEN).

Tetraphenyl butadiene (TPB) is an organic compound broadly used in particle physics as a wavelength shifter (WLS) and its effectiveness is well established [143] [177] [245]. TPB is usually deposited on surfaces with a dedicated evaporation system, which is hard to scale to large surfaces as it is required by large-scale detectors. TPB coatings are also very delicate, as they can be detached [217] or affected by VUV light. In this sense, other materials easier to handle are being explored, such as PEN, pTP [246] or bis-MSB [247] and alternative techniques, such as the use of xenon doped liquid argon (see chapter 9)

A promising alternative is polyethylene naphthalate (PEN), a fluorescent thermoplastic similar to PET. The PEN performance has been studied in the literature [184] [248], however its WLS efficiency has been only measure relatively to TPB, with a wide dispersion among measurements.

In this chapter, the WLS efficiencies of PEN and TPB are measured in real operating conditions in liquid argon using ProtoDUNE Dual-Phase data. First, the current knowledge of the TPB and PEN performance is reviewed in Sec. 8.1 and 8.2. The wavelength-shifters installed in ProtoDUNE Dual-Phase are explained in Sec. 8.3 and a model to compute the wavelength-shifting efficiency is presented in Sec. 8.4. Two types of physics events are used to measure the WLS efficiencies: S1 scintillation light signals from cosmic muons triggered by the PMTs are analyzed in Sec. 8.5.2, and cosmic muons selected by the CRT panels in Sec. 8.5.3. The results are discussed in Sec. 8.6 and the conclusion is summarized in 8.7. Preliminary results of this analysis were presented in the XXIX International Conference on Neutrino Physics and Astrophysics (Neutrino2020) [249].

8.1 Tetraphenyl butadiene (TPB)

Tetraphenyl butadiene (TPB) is an organic chemical compound. It is the wavelength-shifter most extensively used in liquid argon detectors. It is deposited over a substrate, or directly over the photosensors (as in ProtoDUNE Dual-Phase) as an evaporated coating. The maximum wavelength-shifting efficiency is reported for a thickness of 0.2 mg/cm^2 [245].

The emission spectrum is shown in Fig. 8.1, for different wavelengths of the incident light in the range from 45 ns to 250 nm. The maximum of the emission spectrum is at 420 nm. No significant dependence of the emission spectrum with the incident-light wavelength is found.

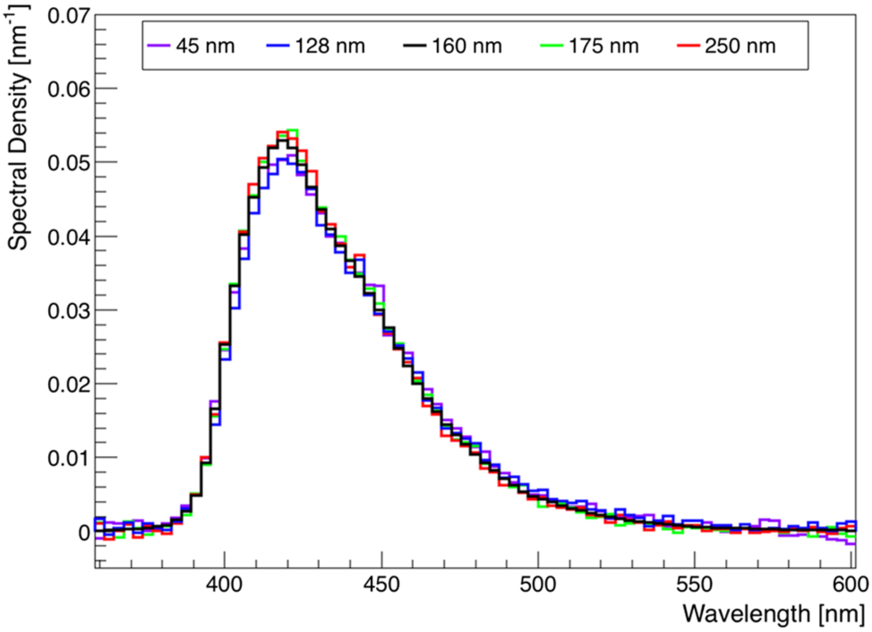

Figure 8.1: TPB emission spectrum for different incident-light wavelengths. Figure taken from [245].

The TPB wavelength-shifting efficiency at 127 nm has been measured using four ProtoDUNE Dual-Phase TPB-coated PMTs by comparing the currents given by the PMT under test and by a reference calibrated photodiode in a dedicated setup at room temperature [217]. Table 8.1 summarizes the measurements, reporting an effective detection efficiency of DE=0.14 ± 0.02 (detected photoelectrons per incident VUV photon), which would correspond to a TPB wavelength-shifting efficiency of 1.5 ± 0.3, as it is obtained using the model explained in Sec. 8.4. A large spread between PMTs is found when looking at the individual measurements. For example PMT FA140, with a QE just 2% higher than PMT FA0123, has a Detection Efficiency 26% higher. This indicates that the TPB deposited on PMT FA0140 is more efficient. These efficiencies above 100% are attributed to the TPB ionization, since one absorbed photon can excite more than one TPB molecule [225].

PMT	QE (430 nm)	DE (127 nm)	ε_{TPB}
FA0120	0.168	0.14	1.7
FA0123	0.189	0.115	1.2
FA0140	0.192	0.145	1.5
FA0143	-	0.165	
Average	0.183±0.013	0.14±0.02	1.5±0.3

Table 8.1: PMT quantum efficiency (QE) at 430 nm and TPB-coated PMT effective detection efficiency (DE) for 127 nm photons measured in the laboratory [217].

However, the TPB wavelength-shifting efficiency at 127 nm remains controversial in the literature, with reported values going from 50% up to 200%. First, a comprehensive study using different light sources with a monochromator covering a wide range of incident-light wavelengths (from 50 to 250 nm), and a photodiode to measure the flux of VUV incident light as well as the flux of reemitted light from WLS samples reported an efficiency of ∼140% for 127 nm photons at room temperature [250]. However a following paper [245] corrected this measurement after a re-calibration of the photodiode, reporting an efficiency of only ∼50% at 127 nm. The dependence of the wavelength-shifting efficiency with the incident light wavelength provided in [245] is shown in Fig. 8.2. However a more recent study reported efficiencies up to 200% [251], followed by a deterioration when the coating is exposed to air, as it is shown in Fig. 8.3. A summary of values found int the literature is presented in Tab. 8.2. A possible factor that would explain the disagreement within the reported values in the literature is the deterioration of the wavelength-shifting performance with time, as it is shown in Fig. 8.3.

ε_{TPB}	Comment	Reference
0.50±0.02	127 nm, room temperature	[245]
0.8±0.1	160 nm, room temperature	[252]
0.6–2.0	127 nm, room temperature	[251]
1.5±0.3	127 nm, room temperature	[217]

Table 8.2: Summary of values of the TPB wavelength-shifting efficiency (ε_{TPB}) that are found in the literature.

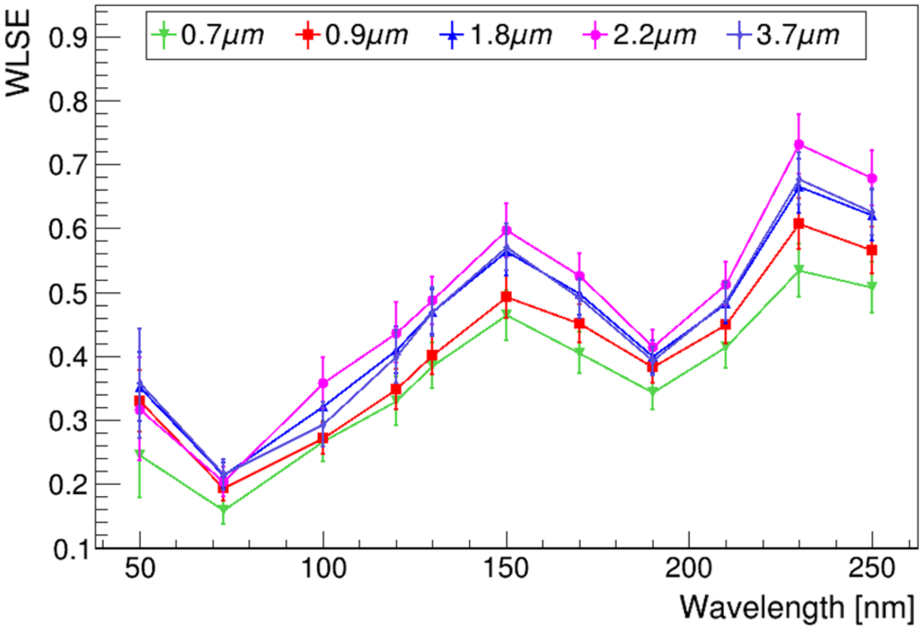

Figure 8.2: TPB wavelength-shifting efficiency at different wavelengths for different coating thicknesses. Figure taken from [245].

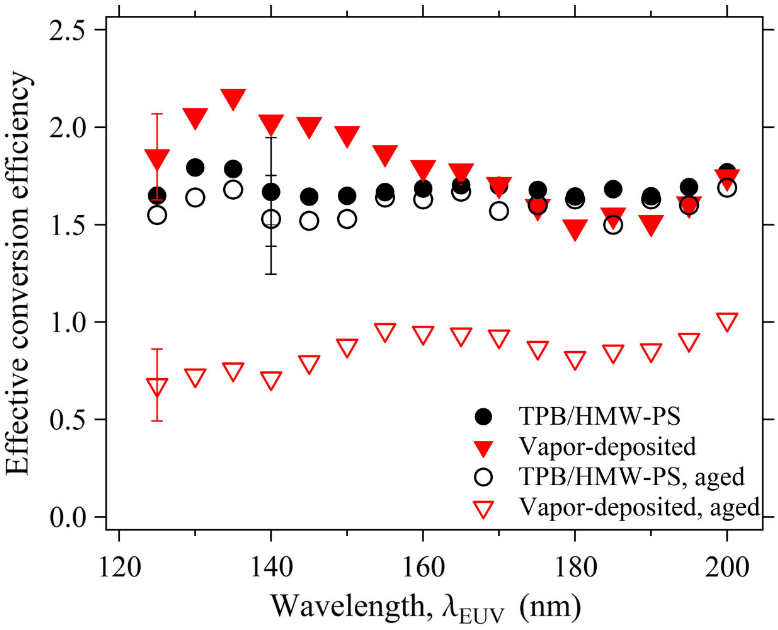

Figure 8.3: Wavelength-shifting efficiency for spin-coated (black circles) and vapor-deposited (red triangles) TPB, before (filled markers) and after 100 days of aging under atmospheric conditions (empty markers). Figure taken from [251].

Additionally, all the studies mentioned before are performed at room temperature. It is not clear the impact of the liquid argon temperature (87K) on the wavelength-shifting efficiency. An increase of 20% in the emission intensity is reported in [216], as it is shown in Fig. 8.4.

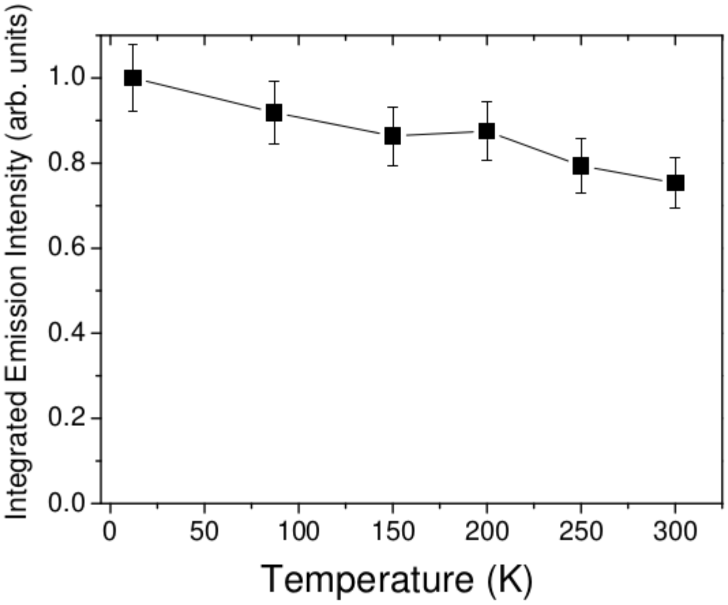

Figure 8.4: TPB emission intensity at different temperatures. Figure taken from [216].

The decay time of the TPB is very fast, and it is usually described as a single exponential of 1-10 nanoseconds. However, there is experimental evidence of several delayed TPB decay times [132]. As reported by Segreto [225] and it is summarized in Tab. 8.3, 40% of the light is converted with longer decay times. 30% of the light corresponds to a 50 ns decay component, that is usually reported as an intermediate component (see Sec. 5.5). Additionally, 8% of the photons have a longer decay component at the level of μs.

The TPB time response function is shown in Fig. 8.5 with the fit in red to the four exponential decay components shown in Tab. 8.3. The time response is obtained by averaging the TPB response signal to a very fast incident light signal at 127 nm. The very fast signal is obtained by exposing the TPB to a ^{60}Co gamma source in liquid argon doped with 3000 ppm of nitrogen. The high level of nitrogen suppresses the slow component of the scintillation light and reduces the fast component time decay at the level of 2 ns (see Sec. 2.3.2) [225].

In summary, the TPB is an efficient wavelength shifter widely used in liquid-argon experiments. However, its wavelength-shifting efficiency remains unclear as attested by the large spread of the values reported in the literature. This seems to be caused by several factors, such as the difficulty of the measurement, a possible dependence on the deposition

Time decay (ns)	Relative abundance (%)
1-10	60%
49	30%
3550	8%
309	2%

Table 8.3: Decay times and relative abundances of TPB emitted light when excited with 127 nm photons. Taken from [225].

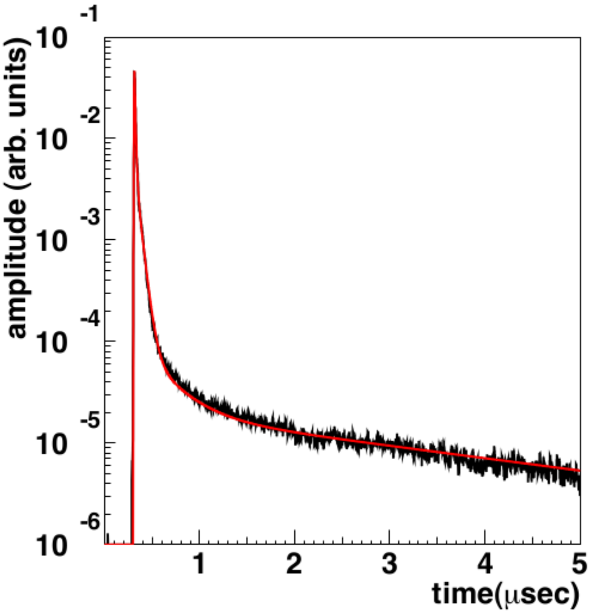

Figure 8.5: Time response function of TPB for 127 nm incident photons at liquid argon temperature. Red line is the fit to four exponential decay components shown in Tab. 8.3. Figure taken from [225]

technique, significant ageing effects and the dependence on the temperature.

8.2 Polyethylene naphthlate (PEN)

Polyethylene naphthalate is a fluorescent thermoplastic similar to PET [183]. Due to its chemical properties, it is industrially produced for large-scale applications like beverage bottling. Figure 8.6 shows its photoluminescence spectrum, which is similar to TPB, with a maximum around 430 nm.

The use of PEN as wavelength-shifter for liquid argon detectors is quite recent, being ProtoDUNE Dual-Phase the first detector that has implemented it at large scale. The PEN wavelength shifting efficiency is not well established yet. A first paper in 2019 [184] provided a wavelength-shifting efficiency relative to TPB at 127 nm of 28% at room temperature. In 2021, [248] reported a relative efficiency with respect to TPB for several

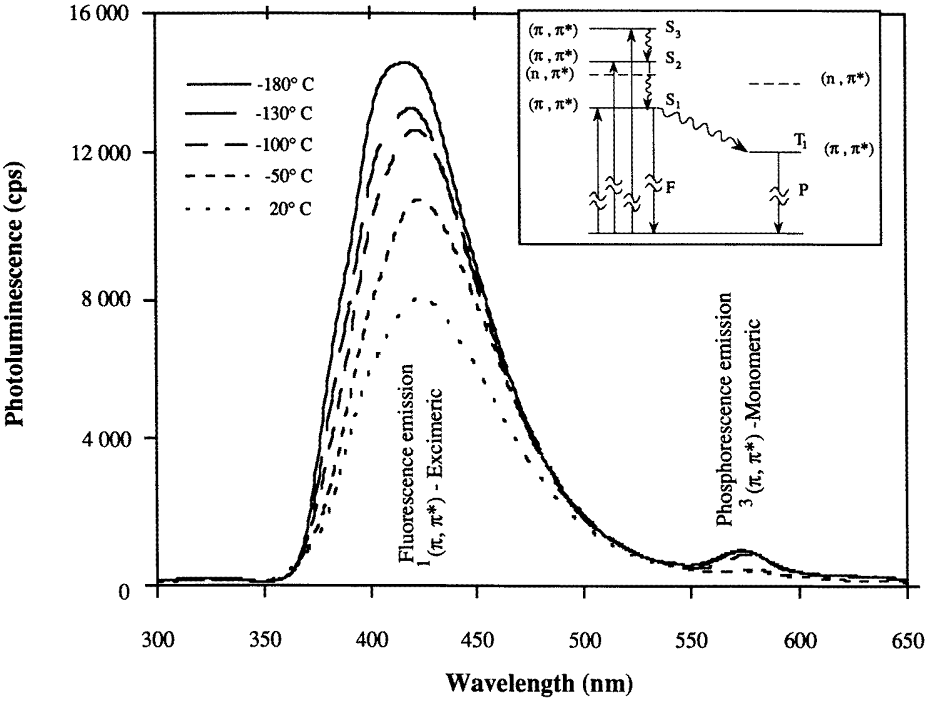

Figure 8.6: PEN photoluminescence as a function of the photon wavelength at different temperatures. An increase of the emission is observed at lower temperatures. Figure taken from [183].

samples in liquid argon, with values in the range from 0.4%-34% depending on the sample. Finally a pre-print [253] reported a relative efficiency with respect to TPB of 47% in LAr. There is a large spread in the reported values, which seems to depend on the PEN sample used. Also, the measurements are relative to the TPB, whose efficiency is not clear yet, as explained in section 8.1. Additionally, a deterioration of the photoluminescence yield under the exposure of incident light in the range of 230-380 nm has been reported in [254]. The PEN wavelength-shifting efficiency values relative to TPB found in the literature are summarized in Tab. 8.4.

Model	$\varepsilon_{PEN}/\varepsilon_{TPB}$	Comment	Reference
Teonex Q83	28%	RT	[184]
Teonex Q65FA	0.4%	LAr	[248]
Teonex TN-8065S	9.1%	LAr	[248]
Teonex Q53	24.7%	LAr, Fixed with adhesive	[248]
Teonex Q53	**34.0%**	LAr, Mechanically fixed	[248]
Teonex Q51	47%	LAr	[253]

Table 8.4: Summary of PEN wavelength-shifting efficiencies relative to TPB ($\varepsilon_{PEN}/\varepsilon_{TPB}$) at 127 nm found in the literature. The PEN model used in ProtoDUNE Dual-Phase is marked in bold. RT stands for Room Temperature.

There are not recent comprehensive studies of the PEN wavelength-shifting at different wavelengths and at cryogenic temperature. [255] provides a dependence of the intensity with the wavelength in Fig. 8.7 at room temperature, that seems to decrease at large wavelengths.

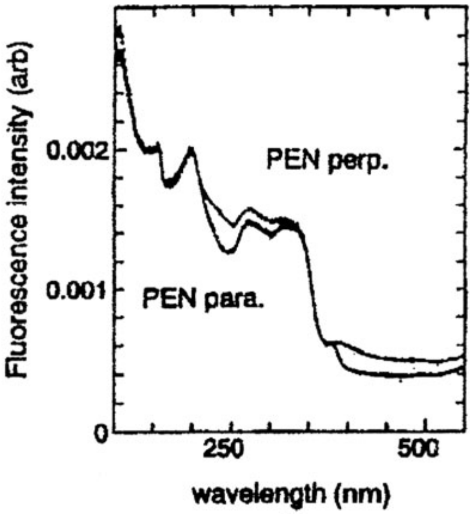

Figure 8.7: Integrated excitation spectra for PEN at different wavelengths. Parallel and perpendicular indicate that the draw direction of the uniaxial film is parallel or perpendicular, respectively, to the electric vector of the incidence beam. Figure taken from [255].

The fluorescence lifetime of PEN is 20 ns at room temperature [184], fast enough to be used in liquid argon detectors, but slower than TPB (see Sec. 8.1).

8.3 Wavelength shifting in ProtoDUNE Dual-Phase

ProtoDUNE Dual-Phase photon detection system uses both wavelength-shifters (PEN and TPB) in order to evaluate and compare the performance of both systems in real operating conditions.

The PEN sample used in ProtoDUNE Dual-Phase is transparent and biaxially oriented, manufactured by GoodFellow [215], with reference ES361090/6. It is installed as circular foils of 240 mm diameter and 0.125 mm thickness placed tangent to the PMT glass surface.

TPB is deposited over the PMT polished surface, using a dedicated evaporation system developed by the ICARUS collaboration [181]. The coating density is 0.2 mg/cm^2, which corresponds to a coating thickness around 0.2 μm.

The 36 Hamamatsu PMTs used in ProtoDUNE Dual-Phase have been fully characterized both at room and at cryogenic temperatures [191]. 6 PMTs were coated with TPB on the PMT glass, and 30 have a PEN foil placed on top. A picture of two PMTs placed inside the detector is shown in figure 8.8.

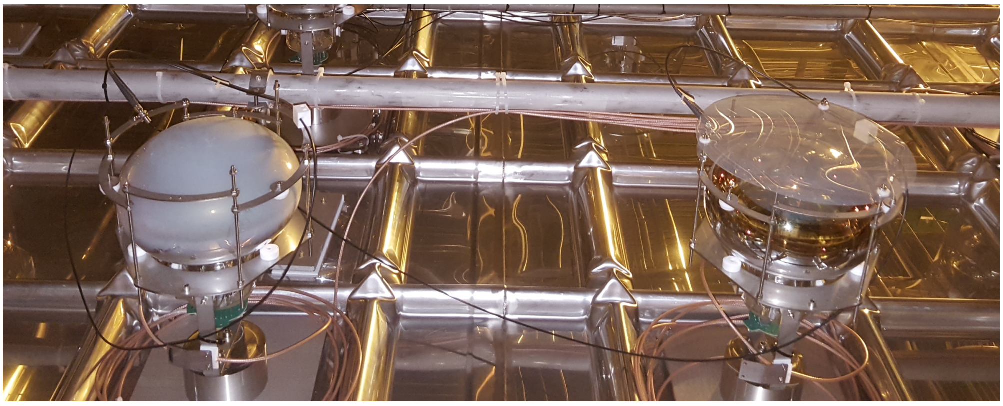

Figure 8.8: View of two PMTs inside the detector. TPB-coated PMT is on the left, PEN-foil PMT is on the right.

8.4 Wavelength-shifting calculation

Cosmic particles crossing the detector interact with the liquid argon, producing scintillation light along their track. Some of these VUV photons will arrive to the WLS of the PMTs (either PEN or TPB), being converted into visible light that can be detected by the PMTs producing a signal. The integral of this signal is the S1 charge (Q), and it provides the number of photoelectrons (PEs) detected by the PMT. If two PMTs with different WLS are placed at the same distance to the crossing track, the relative performance of both systems, PEN-foil PMT and TPB-coated PMT can be evaluated by comparing the number of photoelectrons detected by the two PMTs ($\mathrm{Q}_{PEN}/\mathrm{Q}_{TPB}$).

Additionally, to compute the WLS efficiency of the material itself, a simple model is proposed in Eq. 8.1, to separate the different contributions of the light signal. In Eq. 8.1, Q is the number of detected photoelectrons which is computed by integrating the PMT signal; γ is the number of VUV photons arriving to the wavelength shifter; ε is the WLS efficiency at 87K, defined as the number of visible photons re-emitted per incident VUV photon; Δ represents the photon transport losses from the wavelength shifter (either the coating or the foil) to the photocathode, and it is defined as the number of photons arriving to the PMT photocathode per visible photon emitted by the WLS; QE is the PMT quantum efficiency.

$$\mathrm{Q} = \gamma\, \varepsilon\, \Delta\, \mathrm{QE} \tag{8.1}$$

Based on this definition, the relative WLS efficiency of both materials (PEN and TPB) at 87K can be obtained by dividing Eq. 8.1 for PEN and TPB, as it is shown in Eq. 8.2. Q can be measured directly in the data, and γ and Δ can be determined using simulations.

$$\frac{\varepsilon_{PEN}}{\varepsilon_{TPB}} = \frac{\mathrm{Q}_{PEN}\ \gamma_{coat}\ \Delta_{coat}}{\mathrm{Q}_{TPB}\ \gamma_{foil}\ \Delta_{foil}} \tag{8.2}$$

Additionally, considering $\varepsilon_{PEN}/\varepsilon_{TPB}$ from Eq. 8.2, and the TPB WLS efficiency measured in the laboratory ($\varepsilon_{TPB,Lab}$), the absolute PEN WLS efficiency (ε_{PEN}) can be obtained (Eq. 8.3). It has been assumed that $\varepsilon_{TPB,\mathrm{Lab}}$ does not change when going from room to cryogenic temperature. Although an increase of ε_{TPB} is reported at cryogenic temperature, also a decrease when TPB is exposed to air is reported in the literature. In this analysis, it is assumed that both effects are compensated.

$$\varepsilon_{PEN} = \frac{\varepsilon_{PEN}}{\varepsilon_{TPB}} \varepsilon_{TPB,\mathrm{Lab}} \tag{8.3}$$

Finally, an effective PMT photon-detection efficiency (DE) is defined as the number of photoelectrons detected by the PMT per incident VUV photon. DE depends on the WLS efficiency (ε), the photon-transport losses (Δ) and the PMT quantum efficiency (QE) as it is defined in Eq. 8.4.

$$\mathrm{DE} = \frac{\mathrm{Q}}{\gamma} = \varepsilon\ \Delta\ \mathrm{QE} \tag{8.4}$$

DE has been measured for TPB-coated PMTs at room temperature at the University of Pavia for four of the PMTs by comparing the current given by the PMT under test with a reference calibrated photodiode in a dedicated setup (see Sec. 8.1 and Tab. 8.1). They measured an average value of $\mathrm{DE}_{TPB,Lab}$ = 0.14 ± 0.02, meaning that only 14% of the VUV photons received by the TPB coating will produce a photoelectron. This number includes the TPB WLS efficiency at room temperature ($\varepsilon_{TPB,Lab}$), photon-transport losses (Δ_{coat}), and the PMT quantum efficiency (QE), as it is defined in Eq. 8.4. This measurement is larger but still compatible with the value obtained for ICARUS's PMTs of 0.12 ± 0.01 using the same setup [181].

Also, the value of QE was measured in the laboratory at room temperature by the manufacturer (Hamamatsu) for 3 of the PMTs. They measured a value of $QE = 0.183 \pm 0.013$ at 430 nm which has been shown that is stable when going to cryogenic temperature [256] [214].

Additionally, the photon-transport losses (Δ) can be estimated. Since the TPB is directly coated over the PMT glass, it has been considered that 50% of the photons will reach the photocathode, since the re-emission is isotropic (Δ_{coat} = 0.5). As the PEN foil is placed tangent but not covering the PMT glass as the TPB, these transport losses have been computed using LArSoft (see Sec. 6). It has been found that only 24.7% of the photons re-emitted by the PEN foil would arrive to the PMT photocathode (Δ_{foil} = 0.247).

Therefore, considering Eq. 8.4 and the values of $\mathrm{DE}_{TPB,Lab}$, QE and Δ_{coat} described above, a value for the TPB WLS efficiency at room temperature of $\varepsilon_{TPB,Lab} = 1.5 \pm 0.3$ is obtained.

8.5 Measurement of the wavelength-shifting efficiency

The PEN and TPB wavelength-shifting efficiencies can be obtained using protoDUNE Dual-Phase data from cosmic muons in pure liquid argon. Two types of events are considered. First PMT-trigger muon data are considered in Sec. 8.5.2, where the track event geometry is not known, and therefore the comparison between PEN-foil and TPB-coated PMTs is done using PEN-TPB PMT pairs placed symmetrically with respect to the trigger PMT. This data is used to provide a data-driven measurement of $\varepsilon_{PEN}/\varepsilon_{TPB}$, by considering the calculations presented in Sec. 8.4. Second, CRT-trigger muon data are analysed in Sec. 8.5.3. In this case, the position of the muon tracks is provided by the CRT trigger system and they can be simulated to compute the number of photons arriving to each PMT. Then, the absolute value of ε_{PEN} and ε_{TPB} is obtained by comparing data and simulation.

8.5.1 PMT gain calibration

For every data acquisition with the photon detection system, all PMTs are set at the voltages corresponding to the target gain based on a calibration performed some weeks before using the Light Calibration System (see Sec. 4.2.2 and 5.4). Additionally, for this study, a dedicated calibration is performed in order to take into account small variations in the gain.

The PMTs are calibrated by looking for single photo-electron signals (SPE) in the pre-trigger region of the events. The origin of these signals is mainly dark current and some late light from previous crossing muons. The charge of these signals is integrated and stored in a histogram to obtain the average SPE charge. Figure 8.9 shows an example of a SPE signal in the pre-trigger range (0–3.0μs), and the resulting SPE charge histogram with a Gaussian fit around the second maximum. The first maximum represent the electronic noise, with average charge around zero, and the second maximum shows the SPE signal charge.

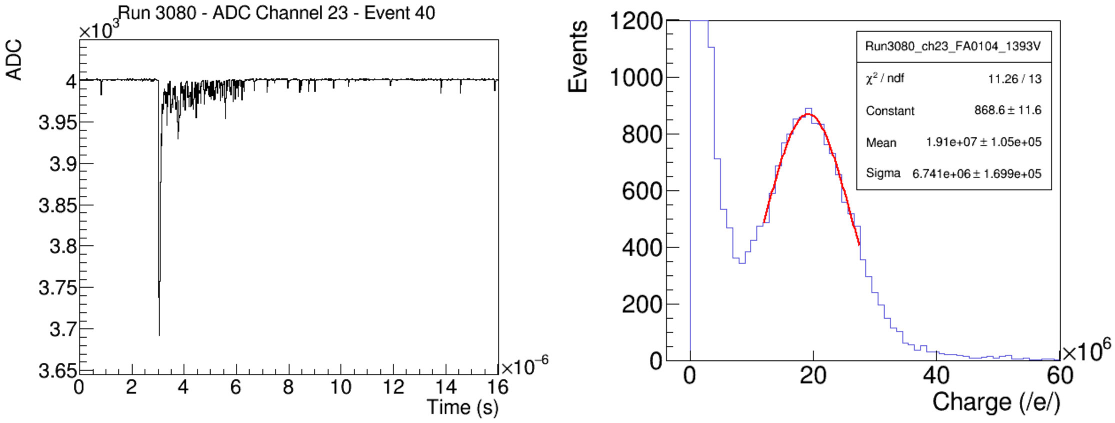

Figure 8.9: Left: Example of a waveform of a PMT signal, with a small SPE in the pre-trigger range (at 1 μs). Right: Integrated charge histogram of the SPE signals in number of electrons, with a gaussian fit around the SPE average charge showing a gain of 1.9×10^7 for target gain of 2×10^7.

Thanks to this dedicated calibration, a gain drop with respect to the target gain is detected in five of the PMTs in the CRT data. This gain drop does not allow to measure the gain properly, since both maximums (SPE charge and electronic noise) overlap. Therefore this five PMTs are excluded from this analysis to avoid introducing a bias (Sec. 8.5.3).

8.5.2 PMT trigger muons

As explained in Sec. 8.4, every cosmic particle crossing the detector produce scintillation light that can be detected by the PMTs. The number of detected photoelectrons depends on the track distance to the PMT, having more photons detected if the track passes closer to the PMT. The number of detected photoelectrons also depends on the track geometry, having more photons if a large part of the track is contained within the active volume. Therefore, PMTs placed closer to the centre of the detector will detect on average more photons, as the border effect is smaller.

The relative photon-detection efficiency of PEN-foil and TPB coated PMTs ($\varepsilon_{PEN}/\varepsilon_{TPB}$) can be obtained by comparing the number of photoelectrons detected by both systems for the same number of photons arriving to the foil and the coating (Q_{PEN}/Q_{TPB}), see Eq. 8.2. Since the track position is not known, the number of photons arriving to the PMTs cannot be compared in an event by event basis. However assuming a flux of cosmic particles radially symmetrical within the horizontal PMT plane, and considering two PMTs placed at the same distance to the triggering PMT and to the detector centre, it can be assumed that the amount of photons arriving to both PMTs on average is the same.

Two PMTs placed at the centre of the detector are selected as triggering PMTs, and the comparison is performed between the PMTs placed nearby. Therefore two dedicated data-sets were acquired: a first set of 4 runs triggering on PMT FA0132 channel 20, and a second set of 4 runs triggering on PMT FA0139, channel 21. Both PMTs are TPB-coated, and they are placed at the center of the detector, as it is shown on figure 8.10. Each run within the set is taken at a different gain (10^7, 2×10^7, 5×10^7 and 10^8). All PMTs are set at the same gain, except for the triggering PMT which is kept at a constant gain of 10^6 in all 4 runs.

Therefore, the average charge per run detected by each PMT is compared. Figure 8.10 shows the selection of PEN-TPB PMT pairs to be compared in the two sets of runs. Note that only two pairs are selected in the first set of runs, because PEN-foil PMT channel 11 has been reported to have a non-linear behaviour. Therefore, this channel will not be considered.

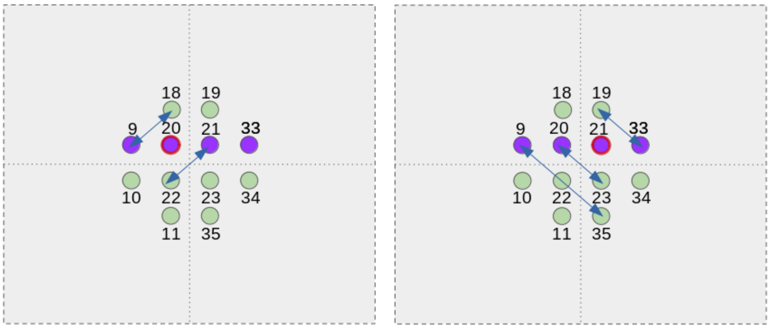

Figure 8.10: Top view of the PEN-TPB PMT pairs to be compared in the analysis. PEN-foiled PMTs are shown in green, TPB-coated PMTs are shown in purple. PMT pairs are placed symmetrically with respect to the triggering PMT (in red) and the detector center. The first configuration is shown on the left and the second configuration is shown on the right.

The trigger threshold is kept constant in all runs, set at a minimum amplitude of 50 ADC counts, which corresponds to an amplitude of $\sim$ 12,PEs on the trigger channel. Each run contains 200k events and the digitisation provides 1000 samples per event at a frequency of 62.5 MHz, meaning waveforms of 16 μs and samples of 16 ns (see Sec.4.2.4).

No electric field was applied in the detector during the data taking (drift, amplification or extraction). First set of data was taken on February 2020 and second set on May 2020.

Data selection

Since PEN and TPB have a very different efficiency (being TPB more efficient), TPB PMTs saturate the ADC dynamic range (4000 ADC counts) much more often than PEN

PMTs. As these events would bias the average amount of photo-electrons differently for PEN and TPB PMTs, they must be taken into account.

To avoid this bias, a selection based on the amplitude in the triggering PMT is applied to remove the events saturating the ADC: Events with a signal amplitude larger than 100 ADC counts are not considered. This selection keeps around 30% of the total number of events, reducing the saturating events below 1% for most of the PMTs in all runs. Figure 8.11 shows the amplitude distribution in the triggering PMT and in a nearby PMT before and after the data selection.

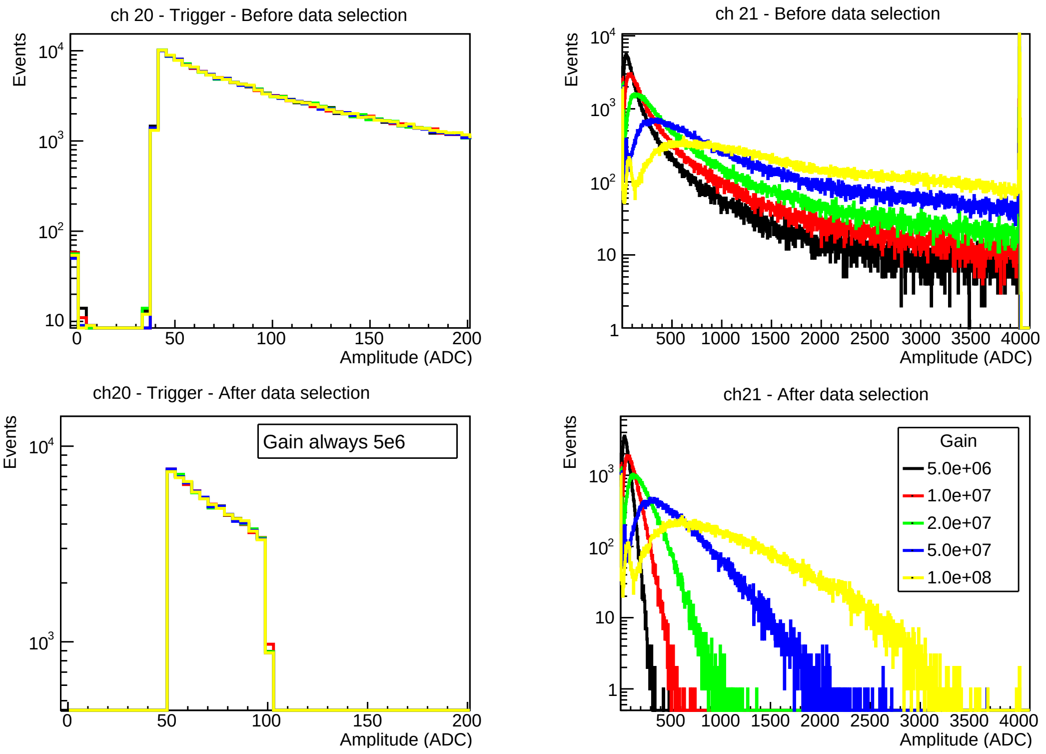

Figure 8.11: Amplitude distribution in the triggering PMT (left) and the TPB PMT placed next to it, channel 21, (right) before (up), and after the data selection (down) for the first set of runs. Note how the saturation at 4000 ADC counts is reduced at all gains.

To obtain the average number of photons detected by any PMT, the signal is integrated in a fixed range of 112 ns (7 bins), 1 bin before and 6 bins after the maximum. Tests have been done by varying this range and similar results have been obtained.

Relative performance of the PEN-foil and TPB-coated PMTs

The average S1 charge is obtained for each PMT in each run. Table 8.5 shows the average Q_{PEN}/Q_{TPB} for every PMT pair for the two dataset (being each dataset four runs at different gains), and the error is the standard deviation. The standard deviation is in general below 1.5%, showing a consistent result for every PMT pair at different gains. The average Q is in the order of 10-20 PEs for PEN-foil PMTs and 50-70 PEs for TPB PMTs, considering a range of integration of 112 ns (7 bins), as explained in section 3.2.

Set	PMT Pair (PEN - TPB)	S1 charge ratio (Q_{PEN}/Q_{TPB})
1	22 - 21	0.233 ± 0.009
	18 - 9	0.262 ± 0.005
2	23 - 20	0.223 ± 0.002
	19 - 33	0.299 ± 0.015
	35 - 9	0.227 ± 0.003
Average		0.25 ± 0.03

Table 8.5: PEN/TPB ratio of the S1 charge for the different PMT pairs considered in this analysis.

The average value of Q_{PEN}/Q_{TPB} is 0.25 ± 0.03, being the error the standard deviation for all the PMT pairs which coincides with the expected uncertainty due to the PMT QE (see Tab. 8.1). This means that the TPB-coated PMTs are 4 times more efficient detecting VUV photons than the PEN-foil PMTs.

Geometrical corrections using simulations

To obtain the relative performance of the materials themselves ($\varepsilon_{PEN}/\varepsilon_{TPB}$), the setup differences must be corrected (see Eq. 8.2). This correction is performed by simulating a detailed geometry of both systems using LArSoft (see chapter 6). A screenshot of the simulated PMT geometry is shown on figure 8.12.

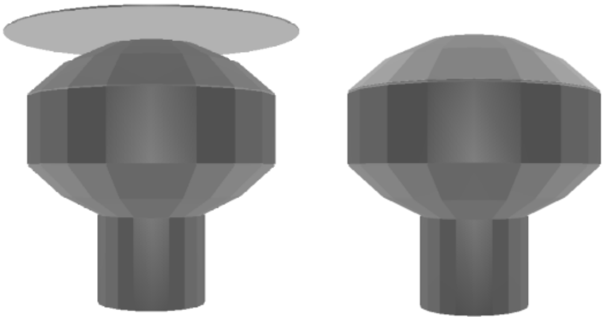

Figure 8.12: Detail of the PEN-foiled PMT (left) and TPB-coated PMT (right) geometry included in the simulation.

The CORSIKA [1] event generator has been used to simulate the cosmic particles crossing the detector, as it is described in Sec. 6.2.1. CORSIKA uses as an input a database of pre-simulated showers generated from different primary particles, computes the expected number of showers in a given time window and place the resulting particles crossing the detector. Then the deposited energy in the liquid argon is simulated in the Geant4 [240] step. An example of the deposited energy in a CORSIKA event is shown on the top panel of Fig. 8.13. Each simulated event considers a time window of 8 ms. In total, a sample of ~9 s is considered.

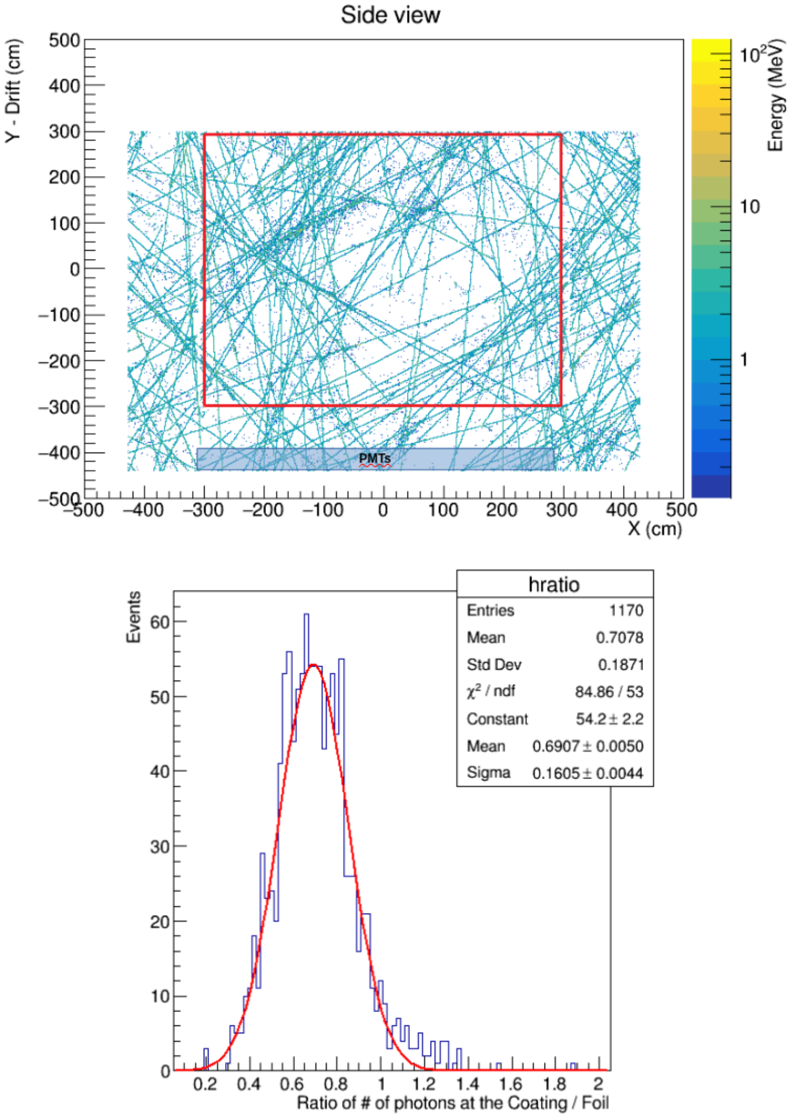

Figure 8.13: Top: Example of the deposited energy in a CORSIKA event. The red box marks the position of the active volume, and the blue square indicates the position of the PMTs at the bottom of the detector. Bottom: Ratio of photons arriving to a TPB coating over PEN foil ($\gamma_{coat}/\gamma_{foil}$). The time window is 8 ms.

Considering a scintillation light yield of 40k photons per MeV of deposited energy and a Rayleigh scattering length of 99.9 cm [257], photons are propagated from the energy deposition point up to the wavelength shifters, where they are counted. The ratio of photons arriving to the TPB coating over the PEN foil is shown on the bottom panel of Fig. 8.13, being on average $\gamma_{coat}/\gamma_{foil} = 0.69 \pm 0.16$. That means that the TPB coating is receiving on average only 69% of the photons received by the PEN foil. This is expected since the foil has the two sides exposed to the liquid argon in opposition to the TPB twhich only has one side exposed to the liquid .

WLS efficiency result

From Eq. 8.1, and considering the value of $Q_{PEN}/Q_{TPB} = 0.25 \pm 0.03$ previously measured and the values of $\gamma_{coat}/\gamma_{foil} = 0.69 \pm 0.16$, $\Delta_{coat} = 0.5$ and $\Delta_{foil} = 0.247$ (see Sec. 8.4, a relative WLS efficiency of $\varepsilon_{PEN}/\varepsilon_{TPB} = 0.35 \pm 0.09$ is obtained.

From Eq. 8.3, and considering the TPB WLS efficiency at room temperature ($\varepsilon_{TPB,Lab} = 1.5 \pm .0.3$, see Sec. 8.4), an absolute PEN WLS efficiency of $\varepsilon_{PEN} = 0.50 \pm 0.17$ is derived. It must be noticed that the resulting ε_{PEN} depends on in the considered $\varepsilon_{TPB,RT}$. A different $\varepsilon_{TPB,RT}$ value, as appears in the literature (see Sec. 8.1), would lead to a different ε_{PEN}.

8.5.3 CRT trigger muons

In this analysis, the PEN and TPB wavelength shifting efficiencies (ε_{PEN} and ε_{TPB}) are obtained directly by comparing muon data from ProtoDUNE Dual-Phase and simulations.

Five long CRT runs with the PMTs operating at a gain of at least 2×10^7 have been selected. Typically these runs contain 15 hours of data, which correspond to ~ 5000 events per run. No electric field was applied in the detector during the data taking (drift, amplification or extraction).

A data selection is applied to avoid noisy events and the pile-up of signals. The selection criteria are explained in Sec. 5.2. Around 30% of the acquired events are not considered.

Analysis

The light signal is integrated around the maximum, to obtain a S1 charge histogram with the number of detected photo-electrons per PMT. The typical distributions obtained for two example PMTs (PEN and TPB) are shown on the right panel of Fig. 8.14. Additionally, a sample of events with the same geometry as the CRT trigger events are simulated in LArSoft (see Sec. 6), in order to obtain the number of VUV photons arriving to the wavelength shifters of each PMT. The typical distributions obtained for the same two example PMTs are shown on the left panel of Fig. 8.14. A Gaussian function is fitted around the maximum of each distribution, in order to obtain the Most Probable Value (MPV). The MPV is a better observable to compare both distributions than to the mean, since the latter is biased by high energy vertical showers that trigger the CRTs and are not included in the simulation, as described in [227]. The MPV is very stable when comparing different data runs, with a variation below 5%.

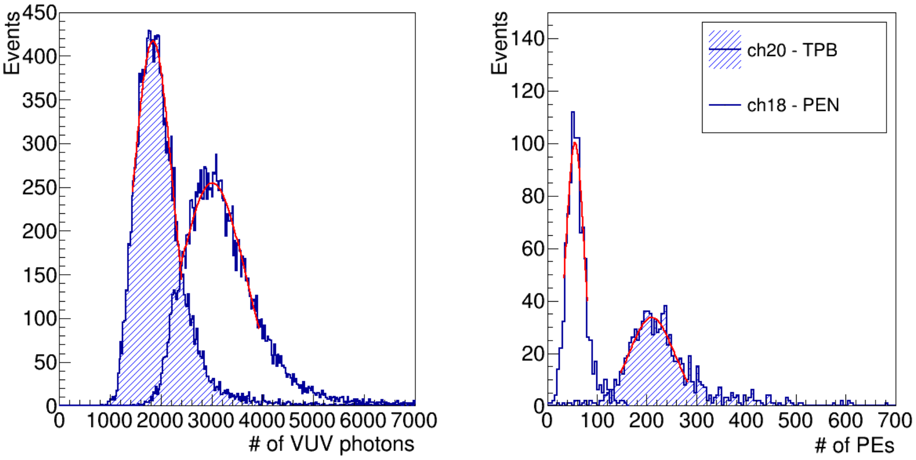

Figure 8.14: Left: Number of VUV photons computed from the Monte Carlo simulation arriving to the wavelength-shifter of two PMTs (PEN and TPB) placed a the center of the detector. Right: Number of detected photo-electrons in the same PEN and TPB PMTs in the data. TPB (PEN) PMT variables are shown with shadowed (transparent) area histogram. A Gaussian fit (red curve) is performed around the maximum to obtain the Most Probable Value (MPV) of the distribution.

Figure 8.15 shows the MPV of the distributions shown in 8.14 for each PMT. The left panel shows the number of VUV photons arriving to each wavelength-shifter from the simulation. The geometry of the track can be easily appreciated. More photons arrive to the PMTs on the top-right corner, as they are placed near the track. The right panel shows the number of photoelectrons detected by each PMT from the data. In this case, the distribution is dominated by the different PEN and TPB efficiencies, since TPB-coated PMTs detect ∼200 PEs, while PEN-foil PMTs only detect ∼40 PEs on average.

The ratio between the number of detected photoelectrons and the number of VUV photons arriving to each PMT would provide the effective detection efficiency (DE) for each PMT, as described in Eq. 8.4. This is shown in Fig. 8.16, where the left panel shows the DE of each PMT, and the right panel the DE distribution for PEN-foil PMTs (in blue) and TPB-coated PMTs (in red). An average of $\mathrm{DE}_{PEN} = 0.018 \pm 0.002$ and $\mathrm{DE}_{TPB} = 0.11 \pm 0.02$ is obtained, where the error is the standard deviation for all the PMTs. It must be noted the large dispersion of the TPB-coated PMTs (20%) unlike the dispersion between PEN-foil PMTs (only 5%). On the one hand the PEN PMT detects ∼50 PEs in the data from ∼3000 photons arriving to the foil in the simulation. On the

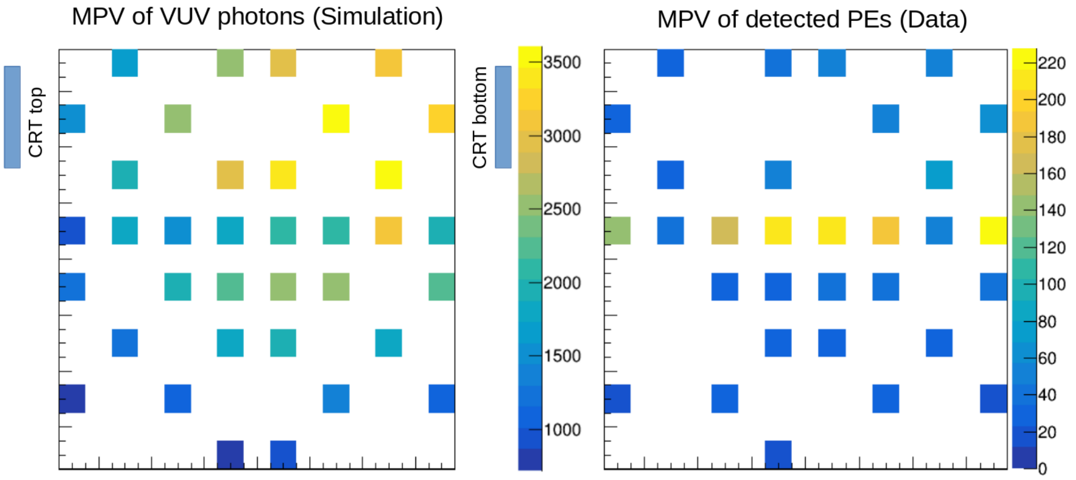

Figure 8.15: Left: MPV of the number of VUV photons arriving to each wavelength-shifter from the Monte Carlo simulation (γ). Right: MPV of photo-electrons detected by each PMT from the data (Q). Each bin corresponds to a PMT at its position in the detector (top view). The approximate position of the CRTs is also drawn on the left panel.

other hand, the TPB PMT detects ~200 PEs in the data from ~2000 photons arriving to the coating the simulation.

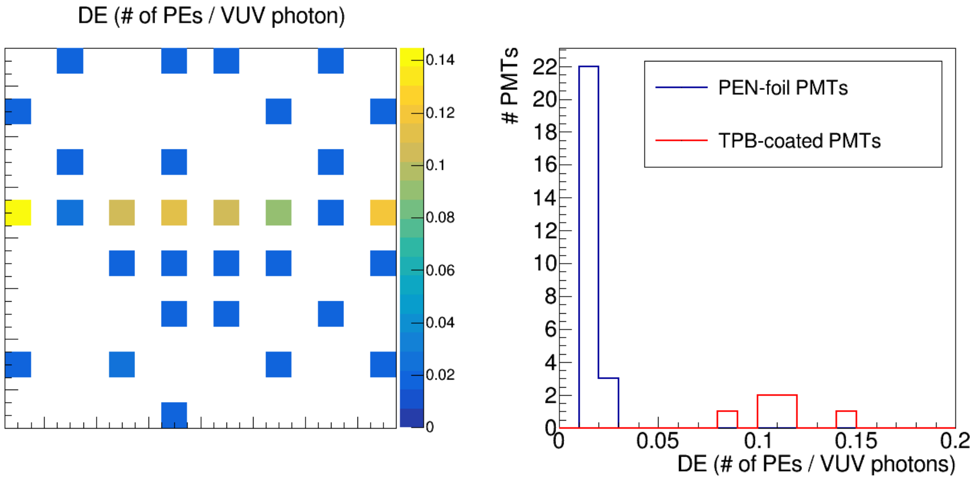

Figure 8.16: Left: Detection Efficiency (DE) for each PMT as they are placed in the detector. Right: PEN-foil (TPB-coated) PMTs DE in blue (red). $< \mathrm{DE}_{PEN} >= 0.018 \pm 0.002$ and $< \mathrm{DE}_{TPB} >= 0.11 \pm 0.02$

WLS efficiency results

Finally, by correcting the photon-transport losses from the wavelength-shifter to the photocathode (Δ), the absolute wavelength-shifting efficiency can be obtained (ε_{PEN} and ε_{TPB}), as described in Eq. 8.2. Figure 8.17 left panel shows the value of ε for each PMT wavelength-shifter at its position in the detector, and the right panel the distribution of the

ε for PEN (blue) and TPB (red) wavelength-shifters. The average of the distributions is $\varepsilon_{PEN} = 0.39 \pm 0.05$ and $\varepsilon_{TPB} = 1.2 \pm 0.2$, where the error is the standard deviation of the distributions.

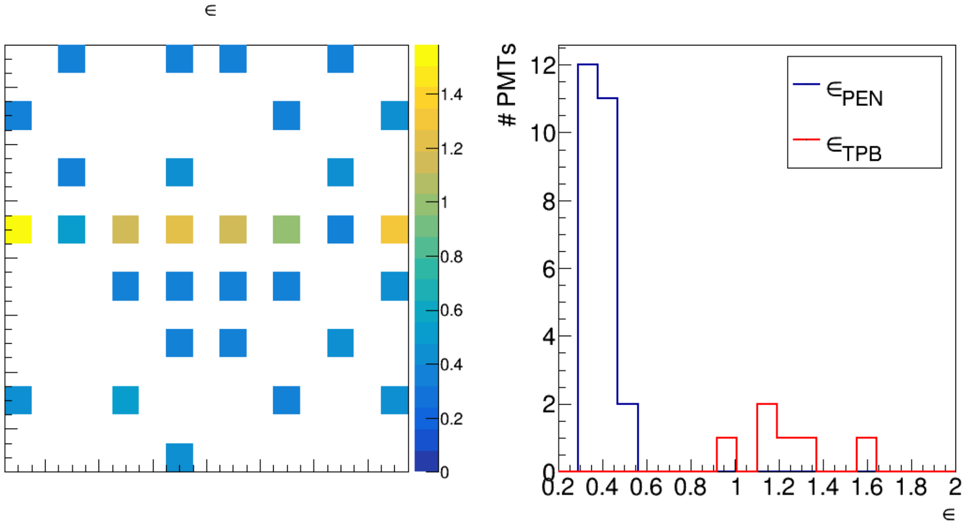

Figure 8.17: Left: PEN and TPB Wavelength Shifting Efficiency (ε) for each PMT as they are placed in the detector. Right: PEN WLS efficiency (ε_{PEN}) in blue and TPB WLS efficiency (ε_{PEN}) in red. $< \varepsilon_{PEN} >= 0.39 \pm 0.05$ and $< \varepsilon_{TPB} >= 1.2 \pm 0.2$

Figure 8.18 shows the stability of ε_{TPB} and ε_{PEN} obtained for different runs. The variations are compatible with the errors. Two PEN PMTs seem to have a higher efficiency than the rest above 0.5 (0.53 ± 0.03 and 0.52 ± 0.03, see the top-right and the bottom-left panels), but most of them are close to the average value of 0.39.

The values obtained for these absolute efficiencies (ε_{PEN} and ε_{TPB}) are in agreement with the values found in the literature. However, as they are computed directly using the number of photons arriving to the wavelength-shifters, they depend highly on the simulation parameters. For example, an hypothetical over/under estimation of the reflected light, would reduce/increase this WLS efficiency values accordingly. Therefore, a better estimator would be the relative value to reduce any systematic bias introduced by the simulation. The resulting relative value of $\varepsilon_{PEN}/\varepsilon_{TPB}$ is $= 0.32 \pm 0.07$, which is in agreement with the value computed in the previous section, and with the values reported in the literature.

Table 8.6 summarizes the results obtained using the CRT-triggered data.

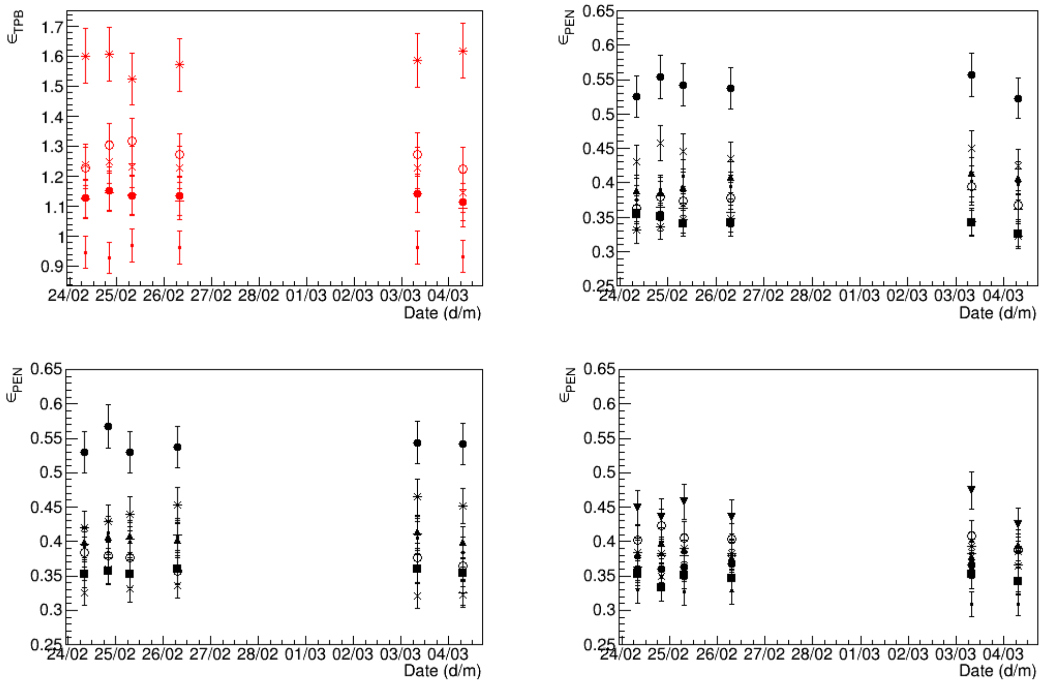

Figure 8.18: TPB (red) and PEN (black) wavelength-shifting efficiency (ε_{TPB} and ε_{PEN}) for the selected 31 PMTs at different times. Each symbol correspond to a PMT. Six TPB PMTs are drawn in the top-left, eight PEN PMTs are shown on the top-right and bottom-left panels, and nine on the bottom right panel.

Value	Result
DE_{PEN}	0.018 ± 0.002
DE_{TPB}	0.11 ± 0.02
ε_{PEN}	0.39 ± 0.05
ε_{TPB}	1.2 ± 0.2
$\varepsilon_{PEN}/\varepsilon_{TPB}$	0.32 ± 0.07

Table 8.6: PEN and TPB efficiencies obtained using CRT data.

8.6 Results and discussion

Finally, table 8.7 summarizes the WLS efficiencies obtained in these studies and presented in the previous sections. The relative values $\varepsilon_{PEN}/\varepsilon_{TPB}$ obtained in both studies are compatible, resulting in a weighted average of 0.33 ± 0.05. This value is compatible with the value of 34% efficiency reported in the [248] for a sample similar to the one used in ProtoDUNE Dual-Phase.

The value ε_{TPB} derived from the laboratory measurement (1.5 ± 0.3 as detailed in Sec. 8.4) is higher but still compatible with the value obtained in the CRT trigger study (1.2 ± 0.2). These large errors are due to the large spread in the individual PMT measurements of DE_{TPB}, from which the ε_{TPB} values are derived (see Tab. 8.1 and Eq. 8.1).

Analysis	Value	Result	Comment
Lab measurement[1]	ε_{TPB}	1.5 ± 0.3	
PMT-trigger data	$\varepsilon_{PEN}/\varepsilon_{TPB}$	0.35 ± 0.09	
	ε_{PEN}	0.50 ± 0.17	Assuming 1
CRT-trigger data	$\varepsilon_{PEN}/\varepsilon_{TPB}$	0.32 ± 0.07	
	ε_{PEN}	0.39 ± 0.05	From simulation
	ε_{TPB}	1.2 ± 0.2	From simulation
Weighted average	$\varepsilon_{PEN}/\varepsilon_{TPB}$	0.33 ± 0.05	

Table 8.7: Summary of WLS efficiencies obtained in ProtoDUNE Dual-Phase. The measurement of ε_{PEN} using PMT-trigger data assumes the measurement of ε_{TPB} in the laboratory. The measurement of ε_{PEN} and ε_{TPB} using CRT-trigger data depends directly on the simulation.

This spread can be observed in the wide distribution of the DE$_{TPB}$ shown in Fig.8.19, that overlaps the values obtained in this study. Some causes that would explain the discrepancy between both distributions are:

- The measurements in the lab were done on the spare PMTs that were not installed in the detector. It may happen that the small sample of PMTs measured in the lab had a larger QE than the PMTs installed in the detector.
- The laboratory measurements were done in 2018, more than one year before the operation of ProtoDUNE Dual-Phase started. During this time, the PMTs were stored in boxes with black plastic bags protecting the TPB coating. Some small deterioration of the WLS performance while exposed to the air inside the plastic bag, and during the installation could reduce the WLS performance, as it is reported in the literature [251].
- The reflectivity of the elements inside the detector might be overestimated in the simulation. A smaller reflectivity would reduce the number of VUV photons arriving to the wavelength shifters in the Monte Carlo simulation, and this would directly increase the value of DE obtained in this study, improving the agreement of both measurements.

The first two hypotheses are hard to test without direct measurements. However, to test the last hypothesis, the dependence of DE and ε with the reflectivity has been studied performing a scan on this value. A 27% reflectivity for VUV photons was considered as a baseline value in the aluminum and stainless steel surfaces in the detector. The study has been repeated for 0%, 40%, 60% and 90% reflectivities. Figure 8.20 shows the dependence of the DE, ε and $\varepsilon_{PEN}/\varepsilon_{TPB}$ with the reflectivity implemented in the

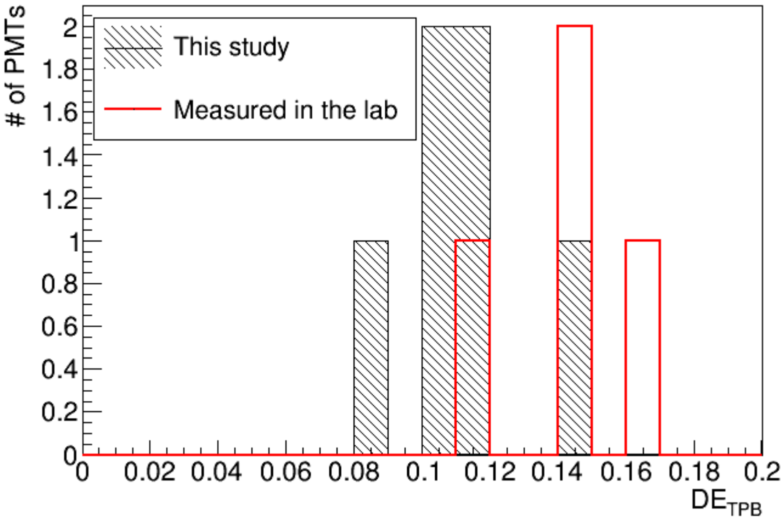

Figure 8.19: TPB-coated PMTs detection efficiency (DE$_{TPB}$) obtained in this study in liquid argon (shaded black) and measured in the laboratory at RT (red).

simulation for PEN (black) and TPB (red). A larger reflectivity reduces the values for DE and ε as expected. A slightly larger value of DE$_{TPB} = 0.12 \pm 0.02$ is obtained when having full absorption (left panel of Fig. 8.20), which is closer but still below the average value of DE$_{TPB} = 0.14 \pm 0.02$ measured in the lab. Therefore, a smaller reflectivity would not explain by itself the larger efficiency measured in the lab, and it might be a combination of factors. Additionally, ICARUS collaboration measured a value of DE$_{TPB,RT} = 0.12 \pm 0.01$ on their PMTs [181], using a similar model of PMT, the same coating setup and the same experimental setup to measure DE. It is meaningful that the value obtained in this study is perfectly compatible with their measurement.

Finally, it must be noted that despite the large dependence of DE and ε with the reflectivity, the variation of the ratio $\varepsilon_{PEN}/\varepsilon_{TPB}$ with the reflectivity is small, with a 15% decrease when going from the baseline reflectivity (27%) to the maximum and unrealistic value considered (90%), which is still within the errors.

A final comment on the dependence of the ε_{TPB} with the temperature: It must be noted that the $\varepsilon_{TPB,Lab}$ is derived from a measurement at room temperature, and [216] measured a 20% increase of ε_{TPB} at liquid argon temperature with respect to room temperature, as it is shown in Fig. 8.4. This correction would increase the disagreement with the data. However, the measurement in this reference is done using a cold finger of a closed-cycle helium cryostat, and not in liquid argon. Since the measurement might be affected by the use of a different medium, the correction has not been applied.

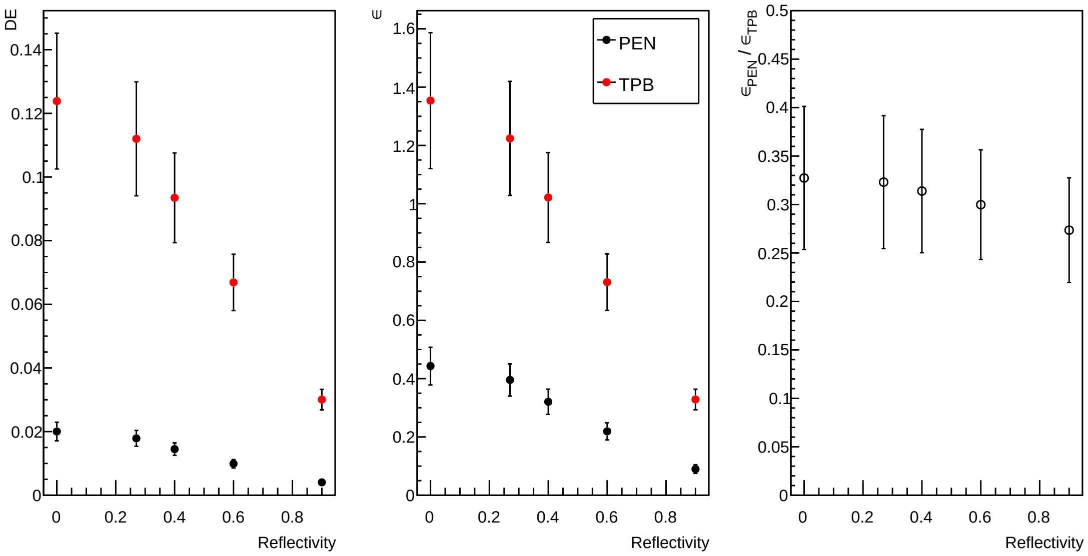

Figure 8.20: Dependence of the PEN and TPB Detection efficiency (left), PEN and TPB WLS Efficiency (center), and the $\varepsilon_{PEN}/\varepsilon_{TPB}$ ratio with the reflectivity.

8.7 Conclusions

Polyethylene naphthalate is a thermoplastic similar to PET with potential applications in large liquid argon detectors like DUNE. It has a similar photo-luminescence spectrum as TPB, with an emission peak around 430 nm. It has potential advantages over TPB, since it is produced as a plastic foil very easy to manipulate and to install under large surfaces. It is also stable and easy to store without risk of damage. On the contrary, TPB is a powder that needs dedicated evaporation setups. While the good performance of TPB is well established and it is broadly used in many noble element detectors, the performance of PEN has not been well characterized yet.

In this work, the performance of the PEN foils as WLS has been measured for the first time in a large LAr-TPC detector, ProtoDUNE Dual-Phase. The performance of PMTs covered with PEN foils on the top has been compared with PMTs with TPB directly coated over the glass. The results indicate that PEN-foil PMTs detect only 25% of the 127 nm photons detected by TPB-coated PMTs, at 87K.

Taking into account geometrical differences due to the position of the foil and the coating, a relative PEN/TPB WLS efficiency of $\varepsilon_{PEN}/\varepsilon_{TPB} = 0.33 \pm 0.05$ is obtained, meaning that TPB would emit three times more visible photons than PEN for the same incident amount of VUV photons. This value is in agreement with some measurements found in the literature [248].

By comparing data and simulation, the effective detection efficiency of TPB-coated and

PEN-foil PMTs are obtained: $DE_{\mathrm{TPB}} = 0.11 \pm 0.02$ and $DE_{\mathrm{PEN}} = 0.018 \pm 0.002$, making the TPB coated-PMT six times more efficient. However, positioning the PEN foil directly over the PMT glass, as the TPB coating, would double its effective efficiency. The value obtained for the TPB is below but still compatible with the direct measurement performed in the laboratory in our four spare PMTs. It is also in agreement with the measurements performed by the ICARUS collaboration for a similar model of PMT using a larger sample of PMTs and the same coating setup (0.12 ± 0.01 at room temperature).

Using a simulation to compute the number of photons arriving to the wavelength-shifters, the absolute WLS efficiency of $\varepsilon_{PEN} = 0.39 \pm 0.05$ and $\varepsilon_{TPB} = 1.2 \pm 0.2$ are obtained.

Finally, concerning the possibility of using PEN as wavelength shifter in DUNE, it will be shown in chapter 10 that a system based exclusively on TPB as WLS would be needed to accomplish the DUNE physics program goals due to the small efficiency of PEN measured in ProtoDUNE Dual-Phase data. Nonetheless, PEN can be taken into account as an alternative when the detection efficiency is not critical compared to the benefits of an easy installation.

Chapter 9

Impact of the presence of xenon and nitrogen in the liquid argon scintillation light

The use of liquid argon of high purity is required in LAr-TPCs, otherwise electrons are trapped by electronegative impurities (see Sec. 2.2) and the photon production is quenched by impurities like nitrogen atoms (see Sec. 2.3.2). Additionally, impurities also absorb photons during their propagation, reducing the detected light with the propagation distance (see Sec. 2.5.2). The use of xenon-doped liquid argon is a promising alternative for large-scale LAr-TPCs since it mitigates the light reduction due to impurities and it also improves the photon-detection uniformity. However, xenon-doping has been used in small prototypes only [258], and the performance of large scale LAr-TPC using xenon-doped liquid argon is not clear yet. This chapter presents the results of the pioneering ProtoDUNE Dual-Phase xenon-doping data-taking campaign and provide valuable inputs for the design of the future xenon-doping based Vertical Drift Far Detector module of DUNE(see 3.1.3).

Xenon doping is a novel technique to shift the wavelength of the 127-nm photons to 178 nm [259], the wavelength of the xenon scintillation light [260]. In the presence of xenon, the scintillation light is quickly shifted to longer wavelengths, reducing the quenching introduced by impurities. Additionally, the longer Rayleigh Scattering Length (RSL) for the 178-nm photons enhances the light detection with the distance, improving the photon detection uniformity. However, xenon-doping also presents some drawbacks to be studied. First, it has been reported that xenon absorbs argon scintillation photons during propagation [261]. Also, a longer RSL would reduce the collection of light at short distances.

In July 2020 ProtoDUNE Dual-Phase was re-filled with 230 tons of xenon-doped liquid argon contaminated with nitrogen from ProtoDUNE Single-Phase [202]. After the filling dedicated nitrogen injections were performed in order to study the light attenuation. Data were taken during all the processes of re-filling and nitrogen injection. The concentrations were in the range of 0-5.8 ppmm of xenon and 0-5.3 ppmv of nitrogen (see Chapter 4).

This study describes the analysis of the ProtoDUNE Dual-Phase data with xenon-doped liquid argon contaminated with nitrogen. The production and propagation of scintillation light in liquid argon containing xenon and nitrogen are explained in Section 9.1, including a model for the scintillation light production in xenon-doped liquid argon contaminated with nitrogen which has been developed. The data used in the analyses are described in Section 9.2. The effect of the presence of xenon and nitrogen in the light yield is shown in Section 9.3. The impact on the shape of the average waveform is analysed in Section 9.4. Data is compared with a dedicated Monte Carlo simulation including xenon and nitrogen in Section 9.5. Finally, the conclusions of the study are summarized in Section 9.6.

9.1 Scintillation light in xenon, nitrogen and argon mixtures

The scintillation light production and propagation processes have been reviewed in this thesis in the case of pure liquid argon in chapter 2 (see Sec. 2.3 for the production and 2.5 for the propagation). In this section, the case of xenon-doped liquid argon and liquid argon contaminated with nitrogen are described. Then, a model is developed and presented for the scintillation light production of xenon-doped liquid argon contaminated with nitrogen. Finally, a summary of the expected effect of adding xenon and nitrogen in pure liquid argon in the detected scintillation light is summarized.

9.1.1 Effects of xenon in liquid argon

Photon production

In the presence of xenon, molecular argon excimers Ar_2^* in the triplet state live long enough to transfer its energy to the xenon atoms creating argon-xenon excimers ($ArXe^*$) and xenon-xenon excimers (Xe_2^*), as explained in [262]. Argon excimers in the singlet state decay too fast to be affected by the xenon species at concentrations of a few ppm. The re-emission of the fast component occurs at the level of 500 ppm of xenon [263] which is not the case under study. A detailed description of the involved processes can be found in [264] [265]. However, a simplified model is proposed here, based on the processes summarized in Eq. 9.1.

$$\begin{aligned} Ar_2^*(^{1,3}\Sigma_u^+) &\rightarrow 2Ar + \gamma(127nm) \\ Ar_2^*(^{3}\Sigma_u^+) + Xe &\rightarrow ArXe^* + Ar \\ ArXe^* &\rightarrow Ar + Xe + \gamma(150nm) \\ ArXe^* + Xe &\rightarrow Xe_2^*(^{1,3}\Sigma_u^+) + Ar \\ Xe_2^*(^{1,3}\Sigma_u^+) &\rightarrow 2Xe + \gamma(178nm) \end{aligned} \tag{9.1}$$

In this model, Ar_2^* excimers in the triplet state can either decay producing 127-nm photons or produce $ArXe^*$ excimers. Then $ArXe^*$ excimers can decay producing 150-nm photons, as it has been shown in [266]. The time decay of $ArXe^*$ is not reported in the literature. $ArXe^*$ excimers can also produce Xe_2^* in singlet and triple state. $Xe_2^*(^1\Sigma_u^+)$ and $Xe_2^*(^3\Sigma_u^+)$ decay times are 3 ns at 27 ns respectiveley, and the wavelength of the emitted photon is centered in 178 nm [262]. Therefore, in the presence of xenon, the slow component of the scintillation light is not monochromatic, having three components: 127 nm, 150 nm and 178 nm. However the light component at 150 nm is usually negligible, being significant only at concentrations below 1 ppm (see upper-left panel of Fig. 9.1).

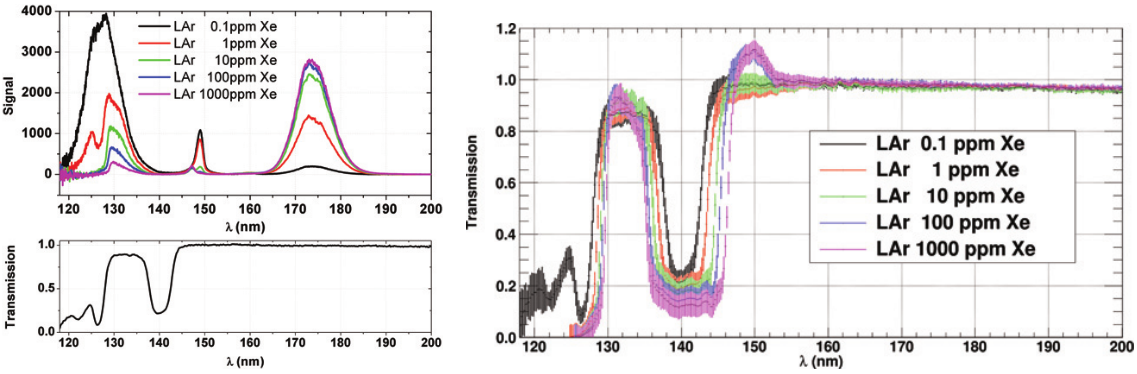

Figure 9.1: Left: The VUV emission of electron-beam excited liquid argon doped with 0.1, 1, 10, 100, 1000 ppm xenon is shown (upper panel). The lower panel shows the transmission of liquid argon doped with 0.1 ppm xenon measured with a deuterium light source and an optical path length of 116 mm. Figure is taken from [267]. Right: Transmission of doped liquid argon at different xenon concentrations. Figure taken from [261].

As a result, scintillation light in xenon doped liquid argon is composed of a fast component at 127 nm, and a slow component at 127, 150 and 178 nm. An example of the time structure is shown in Fig. 9.2. The green line shows the component at 127 nm, the black line at 178 nm. The component at 1182 nm (red line) is not considered in this analysis, since the PMTs are not sensitive to this wavelength. The time structure at 127 nm is similar as in pure liquid argon, described by two exponential decays. At 178 nm the time structure shows a slower rise time resulting in a much smaller signal amplitude (note the log y axis).

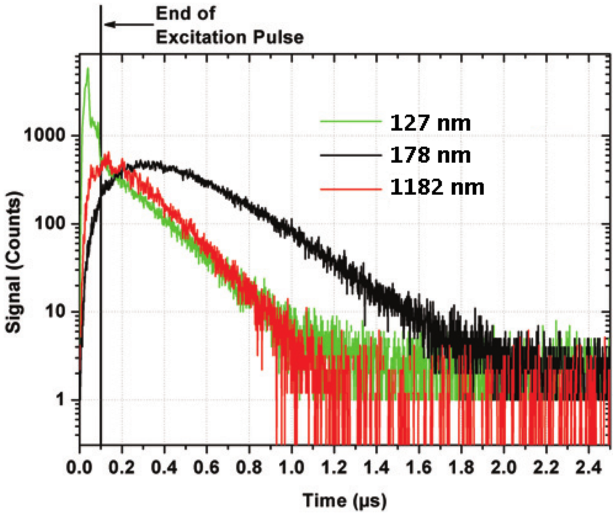

Figure 9.2: The time structures of electron-beam–induced scintillation at different wavelengths in liquid argon doped with 10 ppm of xenon. Figure is taken from [261].

In this situation, the photon production rate can be described by the sum of three exponential functions as it is shown in equation 9.2. A third exponential is added with respect to pure liquid argon, with a characteristic time of $\tau_{Transfer}$, that describes the effective migration from Ar_2^* to $ArXe^*$ and Xe_2^* [262]:

$$f(t) = \frac{A_{Fast}}{\tau_{Fast}} e^{-t/\tau_{Fast}} + \frac{A_{Slow}}{\tau_{Slow}} e^{-t/\tau_{Slow}} - \frac{A_{Transfer}}{\tau_{Transfer}} e^{-t/\tau_{Transfer}}, \tag{9.2}$$

where A_{Fast} is the total number of photons from the fast component, i.e. produced from the decay of excimers in the singlet state, and (A_{Slow}-$A_{Transfer}$) is the total number of photons from the slow component (from the excimers in the triplet state).

Photon propagation

Xenon atoms also affect photon propagation. On the one hand, it has been reported that xenon acts as an impurity, suppressing part of the spectrum at 127 nm even at the low concentration of 0.1 ppm (see lower-left panel of Fig. 9.1) and a propagation distance of $\sim$ 12 cm [267]. This absorption does not depend much on the xenon concentration, as it is shown in the right panel of Fig. 9.1, since the transmission curve remains similar when increasing the xenon concentration. Absorption by xenon is due to the presence of two spectral lines of the xenon atoms at 125 and 129.6 nm [268], and it reduces mainly the fast component of the detected signal since it is composed of 127-nm photons only. The lower-left panel of Fig. 9.1 shows that the transmission is similar to a step function centred in 128 nm, being the xenon-doped liquid argon transparent for $>$128 nm photons, and opaque for $<$128 nm photons. As a result, the wavelength spectrum initially centred in 127 nm in pure liquid argon is slightly shifted towards 130 nm when adding xenon (as it is observed in the top-left panel of Fig. 9.1). This shifting happens during the photon propagation, but right after the photon production, since it is observed by [267] for a short photon-propagation distance of 12 cm.

On the other hand, photons produced at longer wavelengths (150 and 178 nm) are not absorbed during propagation, as it is shown in the transmission curves of Fig. 9.1.

The Rayleigh scattering induced by xenon atoms is neglected due to the relatively small amount of xenon atoms, and only the scattering with argon atoms is considered. The Rayleigh scattering length (λ_{RS}) for 150 and 178 nm photons in liquid argon is $\sim$ 3.5 and $\sim$ 8.3 m respectively, much longer than $\sim$1 m for 127 nm. As stated before, this results in an enhancement of the detection of the light produced at long distances.

9.1.2 Effects of nitrogen in liquid argon

The presence of nitrogen contaminants in liquid argon leads to the reduction of the scintillation light production due to a quenching process, as it is explained in Sec. 2.3.2. Additionally, absorption of scintillation photons by nitrogen during propagation increases with the nitrogen concentration, as detailed in Sec. 2.5.2.

At the nitrogen concentrations under study, the reported absorption lengths (λ_{Abs}) for 127-nm photons are 28 m at 2.4 ppm, 20 m at 3.4 ppm and 12.4 m at 5.3 ppm (see Eq. 2.15) [176]. There are no direct measurements in the literature at other wavelengths in liquid argon. However, an absorption close to zero at 150 and 178 nm can be expected, since the absorbance in solid nitrogen is almost zero at these wavelengths in comparison to 127 nm, as it is shown in Fig. 9.3 from [269].

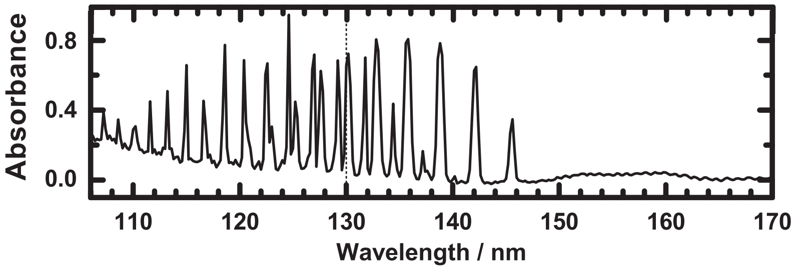

Figure 9.3: VUV absorption spectra of pure solid nitrogen [269].

9.1.3 Scintillation light production model for argon, xenon and nitrogen mixtures

Considering the processes described in the previous sections, a simple model is proposed to evaluate the liquid argon scintillation light in the presence of both xenon and nitrogen. As in Sec. 9.1.1, this model assumes a concentration of xenon and nitrogen in the range of 1-10 ppm, and therefore the production of fast-component photons is not affected. Table 9.1 collects the processes involved in xenon-doped liquid argon contaminated with nitrogen. Figure 9.4 shows the sequence of the processes: First, the medium excitation by a crossing muon produces Ar_2^* in two levels of energy, singlet and triplet. While the excimers in the single state decay directly producing 127-nm photons, the excimers in the triple-state can either decay (producing 127-nm photons), collide with a nitrogen molecule or produce $ArXe^*$. This $ArXe^*$ can either decay (producing 150-nm photons), collide with a nitrogen molecule or produce Xe_2^*. Xe_2^* excimers decay directly producing 178-nm photons.

	Process	Time	Reference values
1	$Ar_2^*(^3\Sigma_u^+) \rightarrow 2Ar + \gamma\,(127\text{ nm})$	τ_{127}	$\sim 1.5 \pm 0.1 \mu s$ [270]
2	$Ar_2^*(^3\Sigma_u^+) + Xe \rightarrow ArXe^* + Ar$	τ_{ArXe}	Not measured
3	$ArXe^* \rightarrow Ar + Xe + \gamma\,(150\text{nm})$	τ_{150}	Not measured
4	$ArXe^* + Xe \rightarrow Xe_2^*(^{1,3}\Sigma_u^+) + Ar$	τ_{Xe_2}	$\frac{9.7-11.4}{[Xe]}\mu\text{s ppm}$ [262,271]
5	$Xe_2^*(^{1,3}\Sigma_u^+) \rightarrow 2Xe + \gamma\,(178\text{ nm})$	τ_{178}	$\sim ns$ [262]
6	$Ar_2^*(^3\Sigma_u^+) + N_2 \rightarrow 2Ar + N_2$	τ_{N_2,Ar_2}	$\frac{9\ \mu\text{s ppm}}{[N2]}$ [166]
7	$ArXe^* + N_2 \rightarrow Ar + Xe + N_2$	$\tau_{N_2,ArXe}$	Not measured

Table 9.1: List of scintillation light production processes in xenon-doped liquid argon contaminated with nitrogen that are included in our model. The singlet-decay to 127-nm photons is not included.

A new process arises due to the presence of xenon and nitrogen at the same time that was not considered previously when studying the effect of nitrogen and xenon individually. It is the quenching process induced by the collision of $ArXe^*$ with N_2 (process 7 in Tab. 9.1). This process reduces the amount of $ArXe^*$, suppressing the production of 150-nm and 178-nm photons. No quenching is considered for Xe_2^* due to its short lifetime (~ns). τ_{127}, τ_{ArXe}, τ_{150}, τ_{Xe_2}, τ_{178}, τ_{N_2,Ar_2} and $\tau_{N_2,ArXe}$ included on Tab. 9.1 are the characteristic times of the processes found in the literature. τ_{ArXe} and τ_{Xe_2} depend on the xenon concentration ([Xe]), and τ_{N_2,Ar_2} and $\tau_{N_2,ArXe}$ on the nitrogen concentration ([N_2]) in a similar way as in

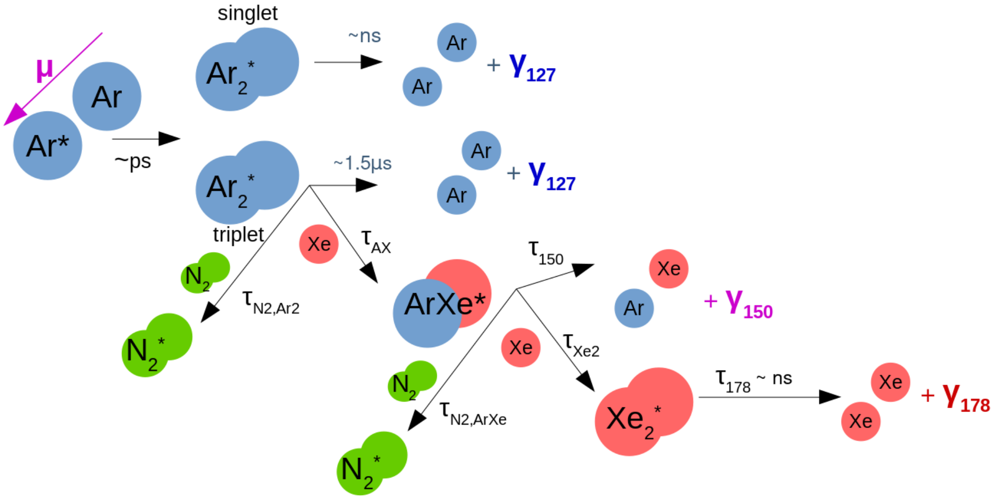

Figure 9.4: Diagram of the processes involved in the scintillation light production of argon, xenon and nitrogen mixtures.

the quenching by nitrogen (see Eq. 2.10), where k_α are constants:

$$\begin{aligned} \frac{1}{\tau_{ArXe}} &= k_{ArXe}[Xe], \\ \frac{1}{\tau_{Xe_2}} &= k_{Xe_2}[Xe], \\ \frac{1}{\tau_{N_2,Ar_2}} &= k_{N_2,ArXe}[N_2] \\ \text{and } \frac{1}{\tau_{N_2,ArXe}} &= k_{N_2,ArXe}[N_2]. \end{aligned} \tag{9.3}$$

Taking into account the processes described in Tab. 9.1, a model describing the deexcitation rates, and thus the light production is given in equation 9.4, where $[Ar_2]$, $[ArXe]$, and $[Xe_2]$ are respectively the concentration of Ar_2^*, $ArXe^*$ and Xe_2^* excimers.

$$\begin{aligned} \frac{d[Ar_2]}{dt} &= -\frac{[Ar_2]}{\tau_{127}} - \frac{[Ar_2]}{\tau_{N_2,Ar_2}} - \frac{[Ar_2]}{\tau_{ArXe}} \\ \frac{d[ArXe]}{dt} &= +\frac{[Ar_2]}{\tau_{ArXe}} - \frac{[ArXe]}{\tau_{150}} - \frac{[ArXe]}{\tau_{N_2,ArXe}} - \frac{[ArXe]}{\tau_{Xe_2}} \\ \frac{d[Xe_2]}{dt} &= +\frac{[ArXe]}{\tau_{Xe_2}} - \frac{[Xe_2]}{\tau_{178}} \end{aligned} \tag{9.4}$$

The system of equations in 9.4 can be solved analytically. Then, by summing the three light contributions, and considering that the Xe_2^* decays much faster than the rest of the processes, the solution can be expressed as a sum of two exponential functions of τ_{TA} and τ_{TX} as it is shown in equation 9.5. τ_{TA} and τ_{TX} are defined in equation 9.6, and they depend on [Xe] and [N$_2$]. τ_{TA} can be interpreted as the lifetime of Ar_2^* excimers and τ_{TX}

as the lifetime of $ArXe^*$ excimers. τ_{TA} and τ_{TX} can be directly extracted by fitting the average waveform of S1 signals produced by an ionizing particle. A_1 and A_2 are constants left as free parameters.

$$\begin{aligned}
&\frac{d[Ar_2]}{dt}(127\text{ nm}) + \frac{d[ArXe]}{dt}(150\text{ nm}) + \frac{d[Xe_2]}{dt}(178\text{ nm}) \approx \\
&\qquad\qquad\qquad\qquad \overset{\tau_{178} \ll \tau_{TA}, \tau_{TX}}{\approx} -A_1 e^{-t/\tau_{TA}} + A_2 e^{-t/\tau_{TX}}
\end{aligned} \tag{9.5}$$

$$\begin{aligned}
\frac{1}{\tau_{TA}} &= \frac{1}{\tau_{N_2,Ar_2}} + \frac{1}{\tau_{ArXe}} + \frac{1}{\tau_{127}} = k_{N_2,Ar_2}[N2] + k_{ArXe}[Xe] + \frac{1}{\tau_{127}} \\
\frac{1}{\tau_{TX}} &= \frac{1}{\tau_{N_2,ArXe}} + \frac{1}{\tau_{Xe_2}} + \frac{1}{\tau_{150}} = k_{N_2,ArXe}[N2] + k_{Xe_2}[Xe] + \frac{1}{\tau_{150}}
\end{aligned} \tag{9.6}$$

Additionally, by considering the analytical solution to equations 9.4, the number of photons produced at each wavelength can be computed at any [Xe] and [N_2]. Table 9.2 shows the dependence of the number of photons produced at each wavelength and the number of quenched excimers with the time constants defined in Tab. 9.1 and equation 9.6 as predicted by the model. They depend on [Xe] and [N_2] through τ_{TA} and τ_{TX} as proposed in equation 9.3 and 9.6.

# of Ar_2^*	k
# of 127 nm photons	$k\frac{\tau_{TA}}{\tau_{127}}$
# of 150 nm photons	$k\frac{\tau_{TA}\tau_{TX}}{\tau_{ArXe}\tau_{150}}$
# of 178 nm photons	$k\frac{\tau_{TA}\tau_{TX}}{\tau_{ArXe}\tau_{Xe_2}}$
# of missing photons due to process 6	$k\frac{\tau_{TA}}{\tau_{N_2,Ar_2}}$
# of missing photons due to process 7	$k\frac{\tau_{TA}\tau_{TX}}{\tau_{ArXe}\tau_{N_2,ArXe}}$

Table 9.2: Number of photons produced at each wavelength and lost due to nitrogen predicted by the proposed model. They depend on [Xe] and [N_2] through τ_{TA} and τ_{TX} as proposed in equation 9.6. Process 6 and 7 are described in Tab. 9.1.

9.1.4 Expected effects on the detected liquid-argon scintillation light when adding xenon and nitrogen

The presence of xenon and nitrogen in liquid argon affects both the production and propagation of the scintillation light. Since the scintillation light is always detected after its propagation, both effects must be taken into account when comparing the detected light in argon, xenon and nitrogen mixtures with pure liquid argon. In this section, the expected effects on the detected liquid-argon scintillation light is summarized when adding xenon and nitrogen in ProtoDUNE Dual-Phase, quantifying the effect when it is possible.

As explained in Sec. 9.1.1 and Sec. 9.1.2, the fast component of the scintillation light is not affected during the photon production by the presence of xenon and nitrogen. However, it is partially suppressed by xenon right after its generated, in the first centimetres of propagation and not depending on the xenon concentration. The fast component is also absorbed by the nitrogen atoms during propagation, with an absorption length depending on the nitrogen concentration. Therefore, an overall reduction of the fast component of the detected scintillation light is expected when adding xenon, and an additional reduction depending on the photon-propagation distance when adding nitrogen.

Fortunately, the expected fast component reduction when adding only nitrogen can be quantified. In the case of ProtoDUNE Dual-Phase, the two nitrogen injections would reduce the absorption length (λ_{Abs,N_2}) at 127-nm from 28 m for 2.4 ppm to 12.4 m for 5.3 ppm (see Sec. 2.5.2 and [176]). Considering these values, a reduction in the fast component of $\sim$16% ($\sim$20%) is expected for photons produced at 4 m (5 m) from the PMTs. This estimation assumes an exponential attenuation of the signal $e^{-d/\lambda_{Abs}}$, with d the photon-propagation distance. The impact can be also quantified using the attenuation length (λ_{att}). Assuming a $\lambda_{att} = 204 \pm 5$ cm in pure liquid argon (as it will be obtained later in Sec. 9.3.3), the attenuation length would be reduced to 190 ± 5, 185 ± 4 and 175 ± 4 cm when adding 2.4, 3.4 and 5.3 ppm of nitrogen respectively. This estimation assumes $1/\lambda'_{att} = 1/\lambda_{att} + 1/\lambda_{Abs,N_2}$.

Since the fast component reduction happens during the propagation, the time profile of the signal should not be affected. This means that the value of τ_{fast} should remain constant when adding xenon or nitrogen.

The slow component of the scintillation light is affected in both steps: photon production and propagation. First, the presence of xenon shifts the wavelength of some 127 nm photons to 150 nm and 178 nm, and the presence of nitrogen reduces the number of photons produced at the three wavelengths as explained in Sec. 9.1.3. Second, only 127 nm photons are absorbed during propagation due to xenon and nitrogen. On the contrary, 150 and 178 nm photons are neither absorbed by xenon nor nitrogen during propagation and additionally, they have a longer λ_{RS} than 127 nm photons. The considered values of λ_{RS} and λ_{Abs,N_2} are summarised in Tab. 9.3. Longer λ_{RS} and reduced absorption enhance light detection at long distances. Therefore, an increase of the slow component of the detected scintillation light mainly from 178-nm photons is expected depending on the photon-propagation distance when adding xenon (being larger at long distances), and an overall reduction not depending on the photon-propagation distance when adding nitrogen.

	$[N_2]$ (ppmv)	127 nm	150 nm	178 nm
λ_{RS} (m)	n/a	1	3.5	8.3
λ_{Abs,N_2} (m)	0	$\sim$km	n/a	
	2.4	28	$\sim$km	
	3.4	20	$\sim$km	
	5.3	12.4	$\sim$km	

Table 9.3: Summary of the parameters affecting the propagation of scintillation photon in xenon-doped liquid argon contaminated with nitrogen. The Rayleigh scattering lengths (λ_{RS}) at different wavelengths are shown at the top, and the absorption lengths due to nitrogen (λ_{Abs,N_2}) at different wavelengths and nitrogen concentrations are given in the bottom.

9.2 Xenon-doped liquid argon data in ProtoDUNE Dual-Phase

As described in Section 4.3.3, ProtoDUNE Dual-Phase was refilled with xenon-doped liquid argon contaminated with nitrogen from ProtoDUNE Single-Phase. Later on, nitrogen was injected in order to study its effect on the light attenuation. As a result, four situations with different concentrations of xenon and nitrogen for the same volume of liquid are studied in this section. They are summarized in Tab. 9.4.

Situation	[Xe] (ppmm)	$[N_2]$ (ppmv)
LAr	0	0
LAr + Xe + N_2	5.8	2.4
1^{st} N_2 injection	5.8	3.4
2^{nd} N_2 injection	5.8	5.3

Table 9.4: Summary of the xenon and nitrogen concentrations for the same level of liquid argon in ProtoDUNE Dual-Phase.

9.2.1 Summary of the collected data

Two types of data have been studied: CRT-trigger events, which correspond to muons crossing the CRTs, and PMT-trigger events, which correspond to muon tracks triggered by a PMT placed at the centre of the detector. Each event is composed of 36 waveforms, one per PMT. A run is a group of events taken at the same time with the detector in stable conditions.

PMT and CRT trigger runs were taken during the evaporation, re-filling and nitrogen injections. During the evaporation, the level of liquid argon decreased by 2.3 m, but the purity of the liquid argon remained stable. During the filling, the concentration of xenon and nitrogen increased proportionally to the increase of the liquid level. Since this level is constantly monitored by level meters, it is possible to interpolate the concentration of xenon and nitrogen for runs taken during the filling. Each point in Fig. 9.5 represents a data-set at a given xenon and nitrogen concentration.

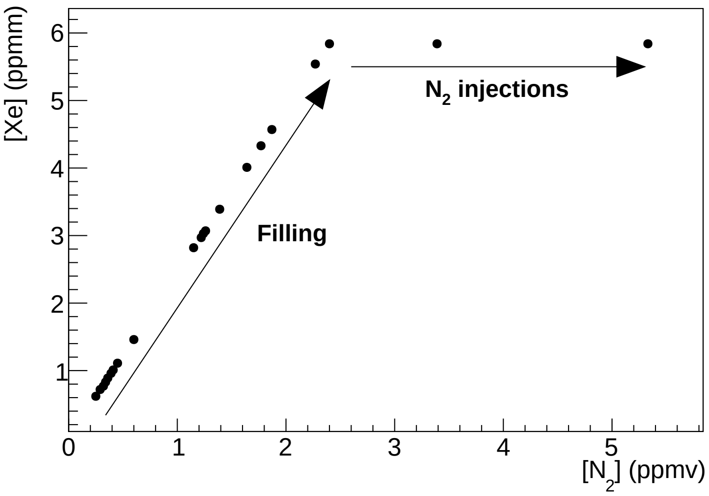

Figure 9.5: Xenon and nitrogen concentrations for the data sets under study. Both concentrations are proportional during the filling, while the xenon concentration is fixed during the nitrogen injections.

CRT triggered cosmic-muons

CRT panels described on Sec. 4.1.5 provide an external trigger signal to the Photon Detection System for muons crossing both CRTs. This allows identifying the scintillation light produced by a diagonally crossing muon. Additionally, for each trigger signal the CRT panels provide the entry and exit point of the track, which allows reconstructing the track in 3D. On average, the distance from the centre of the CRT-trigger tracks and the PMTs is ~4 m. In the CRT triggered data, the PMTs are typically biased to provide an equalized gain of 2×10^7, providing SPE signals of 15 ADC.

Typically a PEN-foil PMT detects on average around 50 PEs, and a TPB-coated 200 PEs from a CRT trigger run. In total 33 CRT-trigger runs, representing ~150k events, have been taken and analyzed.

PMT triggered cosmic-muons

When triggering on a PMT, the selected events correspond to any ionizing particle, typically cosmic muons, providing a scintillation light signal on the trigger PMT larger than the chosen trigger threshold. In these data, all PMTs are biased to provide an equalized gain of 5×10^6. The trigger threshold is set at a minimum amplitude of 100 ADC counts, which corresponds to an amplitude of $\sim$ 25 PEs on a TPB-coated PMT placed at the centre of the detector. This threshold selects signals from tracks passing near the trigger PMT, at the bottom of the detector. Although the track geometry of each PMT trigger event is not known, the average PMT-track distance for the PMT-trigger events is shorter than for the CRT-trigger events. An average PMT-track distance of $\sim$2 m is estimated for the PMT-trigger events, based on the light detected. Each PMT trigger run contains 200k events.

In a PMT trigger run, a PEN PMT detects on average 200 PEs (PEN) and and a TPB PMT detects 1000 PEs. In total 76 PMT-trigger runs, representing $\sim$15M events, have been taken and analyzed.

9.3 Measurement of the impact of xenon and nitrogen on the scintillation light yield

As described in the previous sections, the presence of xenon and nitrogen in the liquid argon introduces new physical processes that modify the number of photons produced and detected. In this section the signals at different xenon and nitrogen concentrations are characterized and compared, using CRT and PMT trigger events. Since CRT and PMT trigger events have a different photon propagation distance (4 m in the CRT versus 2 m in the PMT trigger events), comparing both triggers allows to understand the effect of the photon propagation in the detected light.

The signals are characterized by the S1 amplitude and charge as defined in Sec. 5.2. An example of a typical scintillation light signal in pure liquid argon is shown on the left panel of Fig. 9.6, and in xenon-doped liquid argon contaminated with nitrogen on the right panel. The S1 amplitude is composed by 127-nm photons only, as it is dominated by the fast component of the scintillation light. Under the presence of xenon, the S1 charge will include the contribution of the three light components: 127 nm, 150 nm and 178 nm. Due to the expected suppression of the fast component and the enhancement of the slow (see Sec. 9.1.4), the S1 charge is dominated by the slow component.

The monitoring of the scintillation light during the evaporation, filling and nitrogen

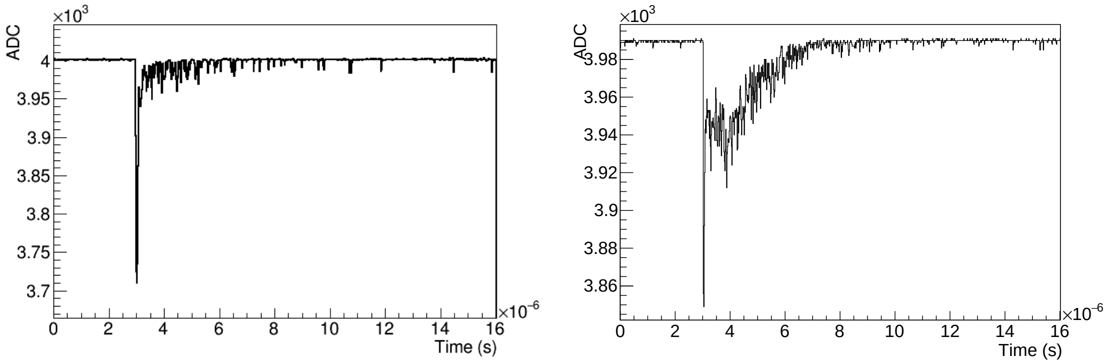

Figure 9.6: Example of a scintillation light signal in pure liquid argon (left) and in xenon-doped liquid argon contaminated with nitrogen (right).

injections is presented in Sec. 9.3.1. Then, the impact of the presence of xenon and nitrogen with the detector full of liquid is quantified in Sec. 9.3.2. Finally, the effective attenuation length in the detector is evaluated at the different xenon and nitrogen concentrations using CRT-trigger data in Sec 9.3.3.

9.3.1 Light monitoring during evaporation, filling and nitrogen injections

Figure 9.7 shows the evolution of the total S1 charge detected by all PMTs as a function of time during the LAr evaporation from 7.4 m to 5.1 m of liquid level (from May to July 2020), re-filling and nitrogen injection steps. Around 12 kPEs are detected on average per PMT-trigger event, compared to only 2 kPEs per CRT-trigger event in LAr. After the filling, the S1 charge increased as expected due to the longer λ_{RS} for the xenon light, and it is reduced with the nitrogen injections due to the increased nitrogen quenching for both triggers as expected (see Sec. 9.1.4).

Figure 9.8 shows the evolution of the average S1 amplitude and S1 charge per event per PMT relative to its initial value in pure liquid argon conditions during the processes of evaporation, filling and nitrogen injections. PMT-trigger runs are shown in black and CRT-trigger runs are shown in red. Only channels placed near the trigger PMT have been selected for the PMT trigger runs, to focus on PMTs at a similar distance to the track. Only the 18 PMTs placed below the CRT tracks are considered for the CRT-trigger runs since the level of detected light in the other PMTs is reduced, and dominated by the background light. This selection is drawn in the small diagrams in Fig. 9.8, representing the geometrical position of the PMTs in the detector. Error bars represent the standard deviation for the PMT selection. S1 charge and amplitude are reduced during the evaporation in the CRT-

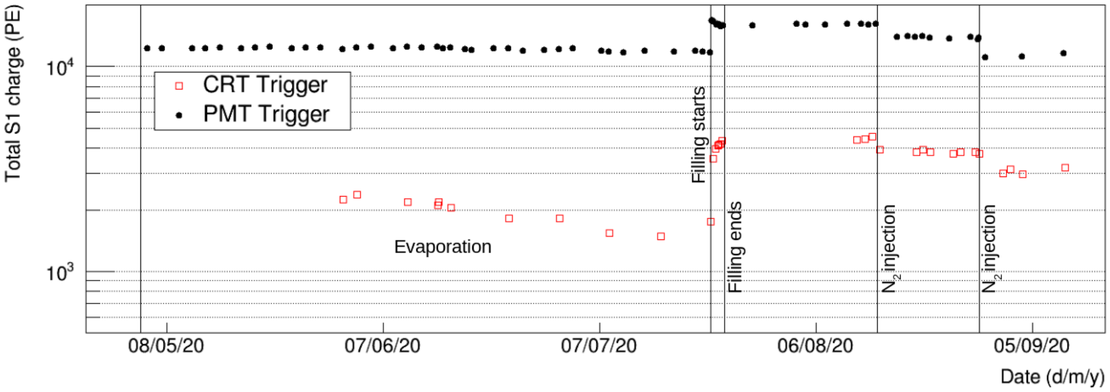

Figure 9.7: Evolution of the average S1 charge per event detected in all the PMTs for PMT(CRT)-trigger data in black (red) during the evaporation, filling and nitrogen injections. The processes are described in section 9.2.

trigger events, since part of the CRT-track gets out of the liquid, while in the PMT-trigger events is stable. This confirms that the PMT-trigger events are dominated by tracks passing near the PMTs, far from the liquid-gas inter-phase.

The S1 amplitude is reduced after the filling in both triggers as expected mainly because of the pressence of xenon (see Sec. 9.1.4). However, it remains stable after the N_2 injections. This is something unexpected that will be discussed in more detail in Sec. 9.3.2 and 9.3.3.

Figure 9.9 shows a zoom of Fig. 9.8 during the filling. Only PMT trigger data are shown since they do not depend on the liquid level variation. As the filling flow was uniform, the estimated xenon concentration is drawn in the secondary top axis, assuming an instantaneous mixing of the new liquid entering the cryostat. It is significant that most of the S1 amplitude reduction happens at the very beginning of the filling, still at xenon concentrations below 1 ppm. This points to the photo-absorption of 127-nm photons by xenon, which does not depend on the concentration, as it was pointed in Sec. 9.1.4.

9.3.2 Average S1 charge and amplitude on PMT and CRT triggered muons

To quantify the impact of the presence of xenon and nitrogen in the S1 charge and amplitude with respect to its value in pure liquid argon, data taken with the same liquid level are selected. Therefore only four situations are fully comparable which are summarized in Tab. 9.4.

The average S1 amplitude and S1 charge with respect to pure liquid argon are shown in Fig. 9.10. Again, as in the previous section, only channels placed near the trigger PMT

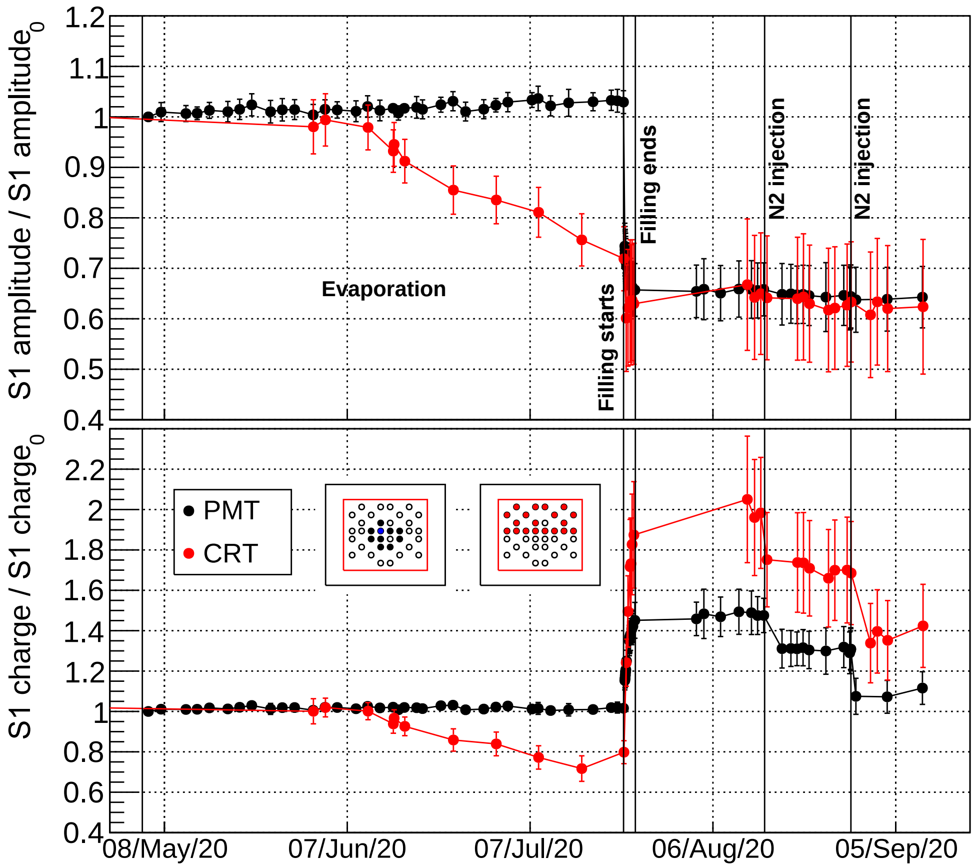

Figure 9.8: Evolution of the average S1 amplitude and S1 charge per event per PMT during the evaporation, filling and nitrogen injections. Each point is normalized with respect to the initial value in pure liquid argon with the full detector. PMT (CRT) trigger runs are shown in black (red). Each point is the average of the selected PMTs indicated in the small diagrams with full circles.

are selected for the PMT trigger runs, to focus on PMTs placed near the triggered track, and only channels placed below the track beam have been considered on CRT trigger runs. The error bars show the standard deviation for the selected PMTs.

Both triggers show a similar decrease in the S1 amplitude of 35% when adding xenon. This decrease is due to the photo-absorption of 127-nm photons by the xenon atoms, as anticipated in Sec. 9.1.4. Having the same decrease in both triggers means that there is no dependence on the photon-propagation distance (longer for CRT-trigger events), and this absorption happens locally, right after the photon production, as expected.

Whilst a 16% decrease of the fast component (S1 amplitude) for the CRT-trigger data is expected when adding nitrogen according to [176] (see Sec. 9.1.4), we observe the fast component remains constant for the two nitrogen injections. A possible explanation for this discrepancy is that the assumption of the fast component being monochromatic

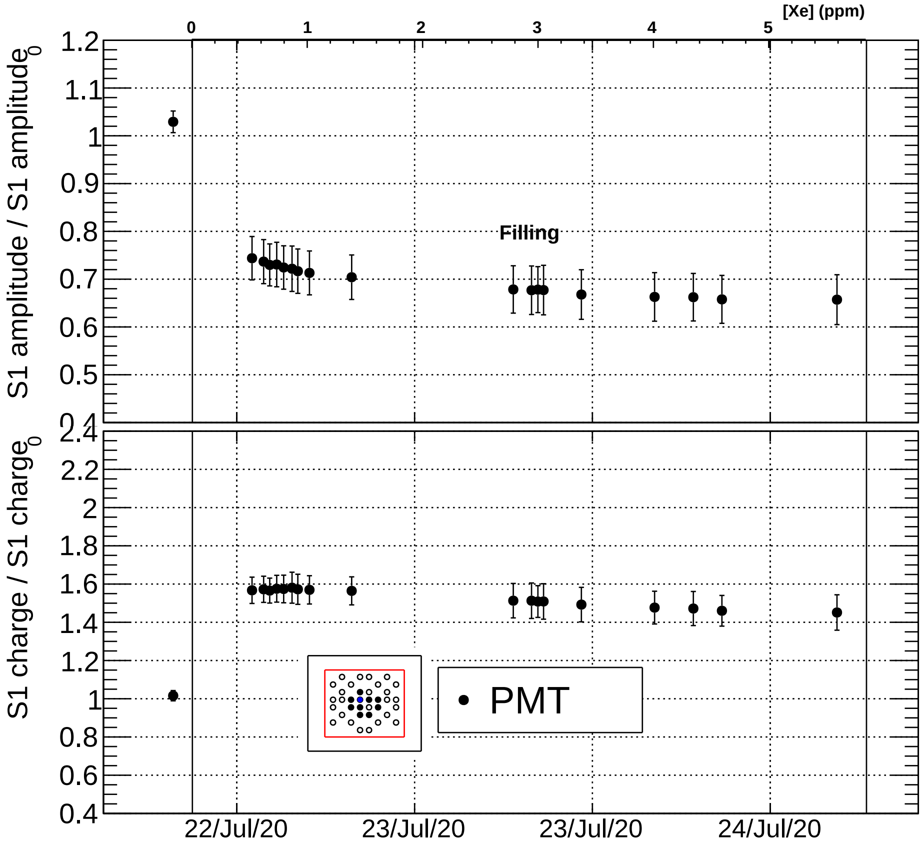

Figure 9.9: Detail of figure 9.8 during the filling process. Vertical lines mark the start and the end of the filling (from 0 ppm to 5.8 ppm of Xe).

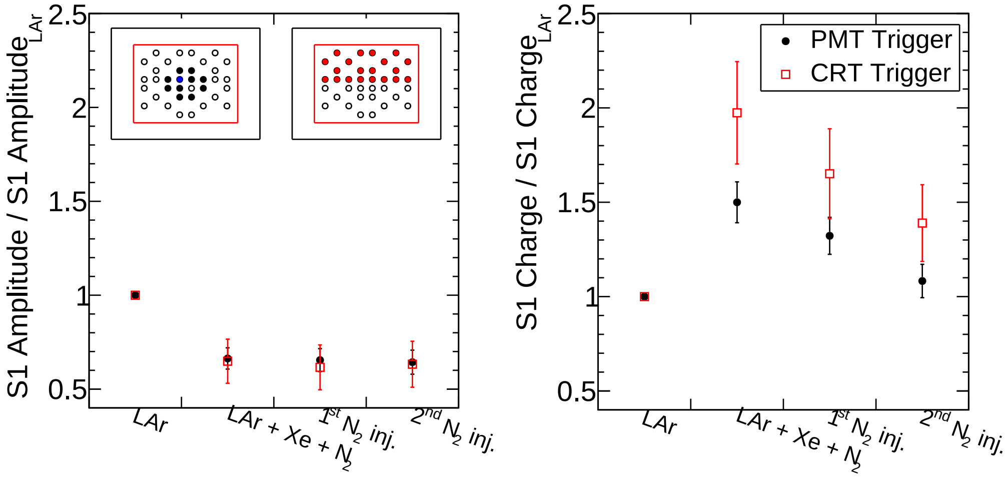

Figure 9.10: Average S1 amplitude and charge in the three doping situations relative to pure liquid argon. PMT (CRT) trigger is shown in black (red). PMT selection is shown in the diagrams indicating its geometrical position in the detector.

at 127 nm is not accurate, and an additional light contribution at a different wavelength, that is not absorbed by the nitrogen, is masking the expected absorption at 127 nm. This discrepancy between our observations in ProtoDUNE Dual-Phase and [176] will be estimated more precisely in Sec. 9.3.3, where the dependence of the detected light with the photon-propagation distance is studied.

The collected S1 charge increases 100% for the CRT-trigger data, while only 50% for the PMT-trigger data. This difference is understood as an improvement of the detection uniformity, since CRT-trigger muons are on average farther away from the PMTs, and the longer λ_{RS} of the xenon photons improves their collection at long distances.

The decrease of the S1 charge due to the presence of nitrogen is the same for both triggers (30%), meaning that there is no dependence of the detected light suppression on the PMT-track distance. This indicates that the reduction is mainly due to the quenching of the Ar excimers by nitrogen rather than photo-absorption.

9.3.3 Measurement of the attenuation length in xenon-doped LAr: Detected light versus distance

In order to evaluate the effect of the xenon doping on the attenuation length (λ_{att}), a study of the dependence of the collected light per PMT with the track-PMT distance is performed for muon tracks crossing the CRT panels.

The dependence of the S1 amplitude and charge detected with the PMT-Track distance for the PEN PMTs is obtained at the different concentrations under study (following the same procedure as in pure liquid argon, as explained in Sec. 5.7). Again, since there are more PEN-foil PMTs and they are spread over the detector, the analysis is developed with the 18 PEN-foil PMTs placed below the CRT tracks. Left (right) panel of Fig. 9.11 shows the dependence of the S1 amplitude (charge) with the Track-PMT distance at the different concentrations under study. The curves are fitted to an exponential ($y = exp^{-x/\lambda_{att}}$) to estimate the effective attenuation length, which values are summarized in Tab. 9.5. While λ_{att} is the effective attenuation length for the combination of photons at 127, 150 and 178 nm, λ_{att}^{127} is the attenuation length for 127 nm photons only. λ_{att} is obtained from the fit to the S1 charge and λ_{att}^{127} is obtained from the fit to the S1 amplitude. As explained in Sec. 5.7, the dependence is not purely exponential since the light absorption by the field cage introduces a border effect: a shoulder shape is observed at around 4.3 m, which corresponds to the PMTs placed at the centre of the detector, where this effect is reduced. This limitation is due to the fixed geometry of the triggered tracks. The expected values for λ_{att}^{127} are also included in Tab. 9.5. As anticipated in Sec. 9.1.4, the expected values are obtained assuming that the attenuation length at different nitrogen concentration follows the function $1/\lambda_{att}^{127} = 1/\lambda_{att,LAr}^{127} + 1/\lambda_{Abs}$, where $\lambda_{att,LAr}^{127}$ is the attenuation length in pure liquid argon, and the values of λ_{Abs} are obtained from the literature [176], which values are summarized in Tab. 9.3.

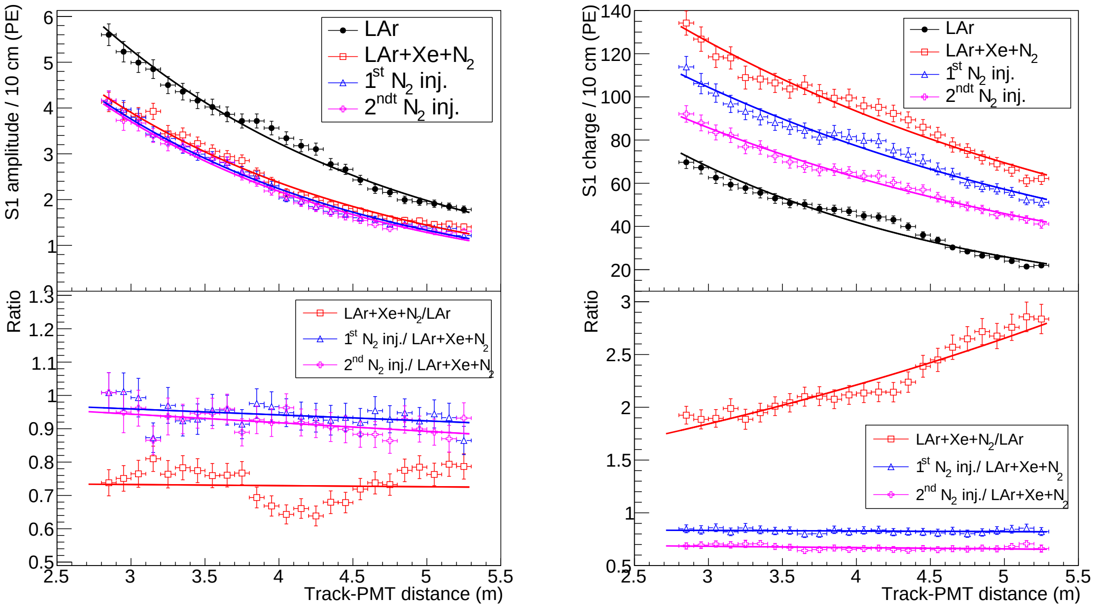

Figure 9.11: The top-left (top-right) panel shows the S1 amplitude (charge) versus PMT-Track distance at the different doping concentrations. Bottom panels: Ratio between the data shown in the top panels.

Situation	[Xe](ppmm)	[N$_2$] (ppmv)	λ_{att} (cm)	λ_{att}^{127} (cm) Measured	Expected
LAr	0	0	209 ± 5	204 ± 5	n/a
LAr + Xe + N$_2$	5.8	2.4	338 ± 13	201 ± 5	190 ± 5
1st N$_2$ injection	5.8	3.4	332 ± 13	193 ± 5	185 ± 4
2nd N$_2$ injection	5.8	5.3	320 ± 12	189 ± 5	175 ± 4

Table 9.5: Attenuation lengths at the different concentrations extracted from the fits shown in Fig. 9.11, and expected (see Sec. 9.1.4).

Results show an increase of 60% of λ_{att} when adding 5.8 ppm of xenon and 2.4 ppm of nitrogen (see Tab. 9.5). This increase can be better appreciated on the bottom-right panel of Fig. 9.11, which shows the ratio of the curves. The red curve shows the improved detection uniformity when adding xenon, with a gain of a factor of $\sim$3 for tracks at 5 m and a factor of $\sim$2 at 3 m. As anticipated in Sec. 9.1.4, this is attributed to the longer Rayleigh scattering length and the reduced absorption of 150 and 175 nm photons. In comparison, a decrease of λ_{att}^{127} to 190 ± 5 is expected due to the additional 2.4 ppm of nitrogen (see Sec. 9.1.4), however, we are not sensitive to this variation for the S1 amplitude (see Tab. 9.5).

A small 5% decrease of λ_{att} is observed after the two nitrogen injections (see Tab. 9.5). This small variation can be seen in the blue and magenta curves on the bottom-right panel of Fig. 9.11. The ratio is below one and do not depend on the distance. This means that there is an overall decrease of the detected light due to the photon-production quenching by the additional nitrogen, but this does not affect the photon propagation.

A small 6% decrease of λ_{att}^{127} from 201 ± 5 to 189 ± 5 cm is observed after the two nitrogen injections. In this case, we expected a larger decrease of λ_{att}^{127} to 175 ± 4 cm (see Sec. 9.1.4). The values are compatible within 2σ. This discrepancy can be also appreciated on the bottom-left panel of Fig. 9.11, where the magenta curve shows the relative attenuation of the detected light after the two nitrogen injections. At a track-PMT distance of 5 m the magenta curve is at 0.9, meaning an attenuation of only 10%, while a 20% was expected. This estimation assumes an exponential attenuation of the signal $e^{-d/\lambda_{Abs}}$, with d the photon-propagation distance (see Sec. 9.1.4).

In conclusion, a 60% increase of the λ_{att} due to the longer Rayleigh scattering length on the xenon photons is observed. On the other hand, a decrease of λ_{att}^{127} smaller than expected is measured. However, the expected reduction of λ_{att}^{127} computed before assumes that the fast component remains at 127 nm. However, under the presence of xenon, the light at 127 nm (and thus, the fast component), is shifted to 130 nm (see Fig. 9.1 and Sec. 9.1.4). Therefore, the discrepancy measured in λ_{att}^{127} using ProtoDUNE Dual-Phase data is pointing to a smaller absorption of 130 nm photons by nitrogen with respect to 127 nm photons.

9.4 Measurement of the impact of xenon and nitrogen on the scintillation time profile

As described in the previous sections, the presence of xenon and nitrogen in the liquid argon introduces new physical processes that modify not only the number of photons produced and detected but also their time profile. Therefore, information of the physics involved with adding xenon and nitrogen can be extracted by studying the variation of the scintillation time profile (see Sec. 9.1.3).

In this section the scintillation time profile at different doping situations will be characterized and compared. The data selection and processing are described in Sec. 9.4.1. The resulting time constants obtained from the fit to the time profile function are summarized in Sec 9.4.2. Finally, in Sec. 9.4.3, the data time profiles are fitted to the scintillation light model proposed in Sec. 9.1.3. The results from this section are used as an input for the simulation described in Sec. 9.5.

9.4.1 Scintillation time profile and data selection

The scintillation time profile is obtained by adding signals from many events. Only a selection of 6 PMTs has been taken into account: PMTs placed next to the trigger PMT to reduce the PMT-track distance and minimize any possible distortion introduced by the photon-propagation. 3 are PEN-foil and 3 TPB-coated PMTs. Signals are added after a time alignment of the waveforms to correct the expected trigger jitter.

Additionally, a data selection is required in order to avoid noise and background distortions. Most of the applied selection criteria are described in Sec. 5.2. Just an additional selection criterion is applied:

- MaxAmplitudeRange: Events with a maximum amplitude in the trigger range below 10 ADC counts are removed. These events have less than three photo-electrons in amplitude and the time profile cannot be appreciated due to the low statistics.

The selection efficiency is shown in Fig. 9.12. On average 86% of the events are selected.

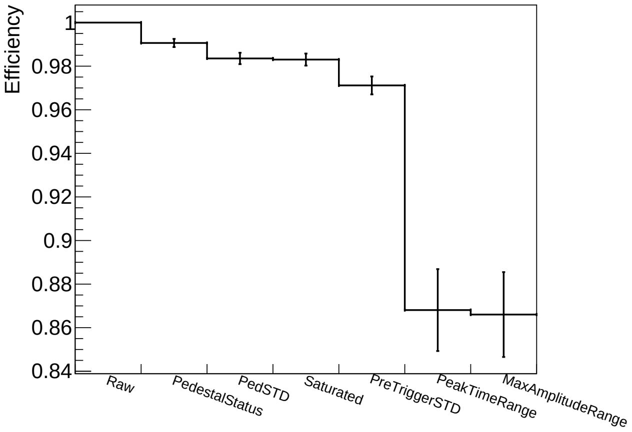

Figure 9.12: Efficiency of the selection criteria. Error bars show the standard deviation for all the PMTs and runs. Selection names are defined in the text.

9.4.2 Measurement of the scintillation time profile parameters

Figure 9.13 shows the time profile evolution of the average PMT waveform normalized to the maximum amplitude during filling with xenon-doped liquid argon and the nitrogen injections. First the slow component increases largely at the very beginning of the filling, even though the xenon concentration is still very small (from the black to the red curve). Then a secondary bump appears as more xenon atoms are available to create excimers (red to green). Finally, the slow component shrinks back when the nitrogen is injected (green to blue and magenta).

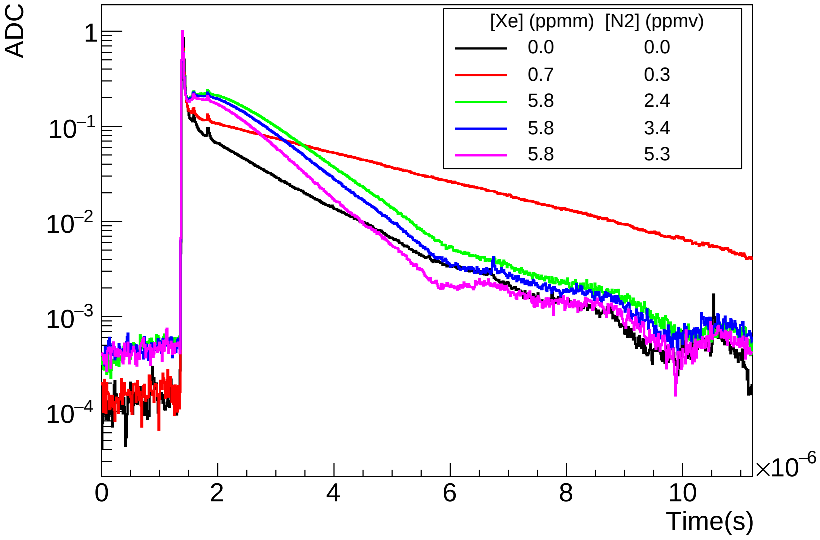

Figure 9.13: Evolution of the time profile normalized to the maximum amplitude at different doping concentrations for a PMT in ProtoDUNE Dual-Phase. Black: Pure liquid argon. Red: With a small xenon concentration. Green: When the detector is filled with xenon-doped liquid argon contaminated with nitrogen. Blue: First nitrogen injection. Magenta: Second nitrogen injection.

The scintillation time profiles in pure liquid argon are fitted to the sum of two exponential functions (with constants τ_{fast} and τ_{slow}) convoluted with a Gaussian (with standard deviation σ), as explained in Sec. 5.5. In order to fit the waveform with the secondary bump due to xenon, a third exponential is introduced ($\tau_{transfer}$), as shown in equation 9.7, to model the raise of the bump. Figure 9.14 shows the fit separated in the fast (black) and the slow components (green). As it was introduced in Sec. 9.1.1, A_{fast} is the number of photons from the fast component, and (A_{slow}-$A_{transfer}$) is the number of photons from the slow component. At low concentrations (< 1 ppm of nitrogen), when the second bump is not visible yet, the fit is performed to two exponentials only, as in pure liquid argon. t_0 is the initial time.

$$f(t) = \sum_{j=\text{fast,slow,transfer}} \frac{2A_j}{\tau_j} exp\left[\frac{\sigma^2}{2\tau_j^2} - \frac{t-t_0}{\tau_j}\right]\left(1-\text{Erf}\left[\frac{\sigma^2-\tau_j(t-t_0)}{\sqrt{2}\,\sigma\tau_j}\right]\right) \tag{9.7}$$

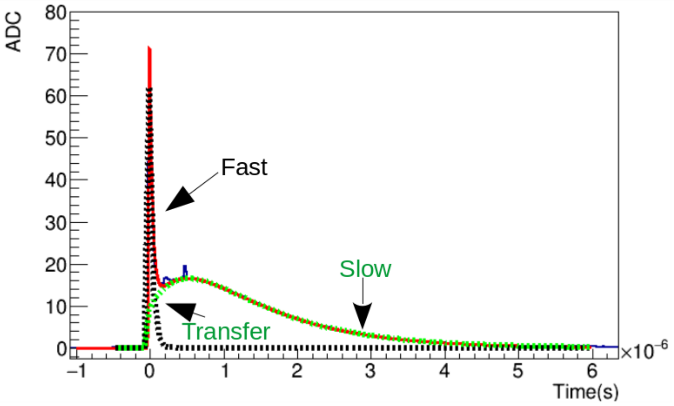

Figure 9.14: Example of a fit of data to Eq. 9.7 separating the fast (red) and the slow (green) components. The rise of the slow component corresponds to the $\tau_{transfer}$.

Figure 9.15 shows some fit examples of scintillation time profiles at different doping concentrations to Eq. 9.7. Figures 9.16 and 9.17 show the summary results of the fit parameters at the different doping concentrations, where the error bars show the standard deviation of the PMTs. τ_{fast} decreases with the xenon and nitrogen concentration in Fig. 9.16 left. This dependence of the fast component with the xenon concentration is not expected (see Sec. 9.1.4) and it has not been observed in other experiments (see Fig. 7 in [263]). The systematic difference of τ_{fast} for PEN and TPB is due to the different fluorescence decay times of both materials (see chapter 8). τ_{slow} jumps from 1.4 μs in pure liquid argon to 3.3 μs at low xenon concentrations, and then it is reduced. At $\sim$ 1 ppm of nitrogen and $\sim$ 3 ppm of xenon, τ_{slow} recovers a similar level as in pure liquid argon. No differences between PEN and TPB PMTs are found on τ_{slow} and $\tau_{transfer}$. The relative number of fast over slow photons ($A_{\text{fast}}/(A_{\text{slow}} - A_{\text{transfer}})$) decay similarly on PEN and TPB PMTs, keeping a higher ratio on PEN PMTs. This difference between PEN and TPB is not fully understood, it might be a systematic bias introduced in the fit by the different values of τ_{fast} for PEN and TPB.

9.4.3 Global fit to the scintillation light model

Considering the scintillation light model proposed for the xenon-doped liquid argon in Sec. 9.1.3, the scintillation time profiles are fitted to the equations 9.6. A global fit is performed over the selected PMTs, fitting simultaneously 21 histograms at different xenon concentrations for every PMT. A simple three exponential fit is used in this case, without the Gaussian convolution, since the global fit do not converge with so many free parameters. The global fit is performed PMT per PMT. Results are stable, and no differences are seen between PEN-foil and TPB-coated PMTs. An example of a global fit performed over one

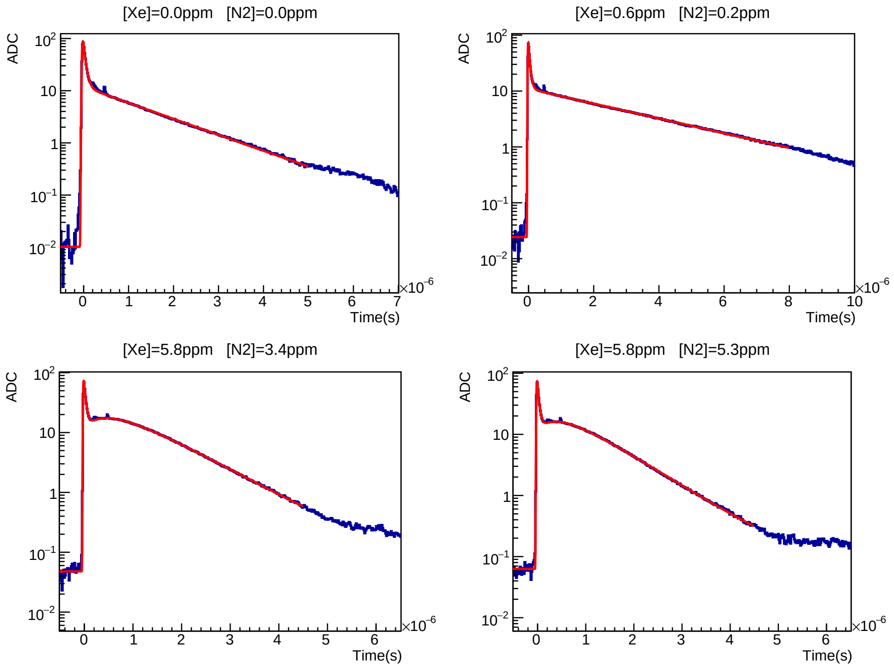

Figure 9.15: Example of scintillation time profiles fitted to equation 9.7. At low doping concentration, the third exponential ($\tau_{transfer}$) is not present (top right and top left).

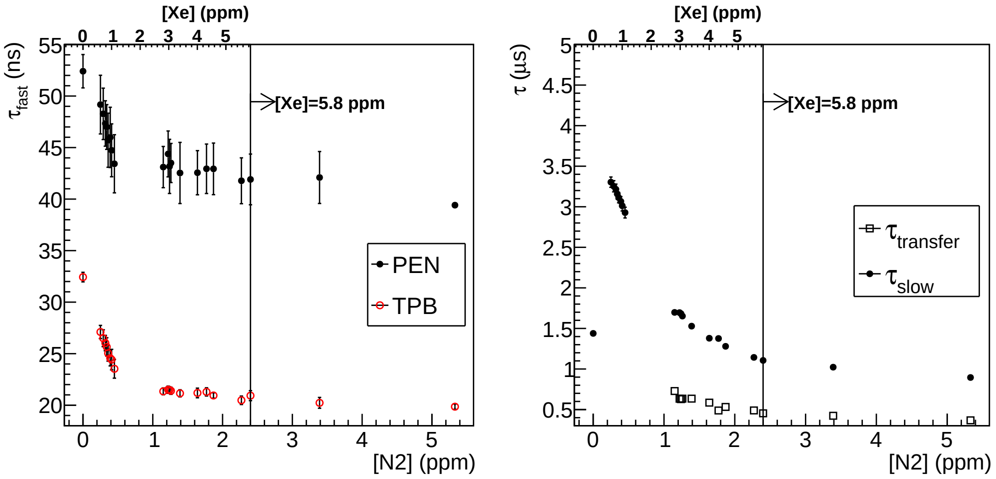

Figure 9.16: Left: $\tau_{\rm fast}$ versus nitrogen concentration for PEN and TPB PMTs. Right: $\tau_{\rm transfer}$ and τ_{slow} versus nitrogen concentration for PEN and TPB PMTs. Xenon concentration (top horizontal axis) increases proportionally during the filling and is fixed at 5.8 ppm for the last three points.

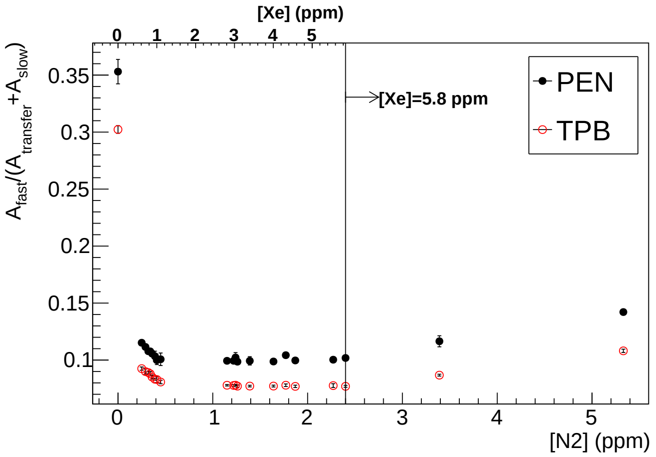

Figure 9.17: Ratio of fast over slow component photons ($A_{\mathrm{Fast}}/(A_{\mathrm{Slow}} - A_{\mathrm{Transfer}})$) versus nitrogen concentration for PEN and TPB PMTs. Xenon concentration (top horizontal axis) increases proportionally during the filling and is fixed at 5.8 ppm for the last three points.

example PMT is shown in Fig. 9.18.

The global fit allows to extract the values of the time constants of all the involved processes. Figure 9.19 shows the global fit result $\pm 1\sigma$ (shaded areas) plotted together with the individual fits (points) obtained in Sec. 9.4.2 (see right panel of Fig. 9.16). The parameters obtained are shown in Tab. 9.6, comparing with the reference value in the literature when possible. Some of them are measured in this work for the first time. The time decay of the ArXe* excimer is measured for the first time, being $\tau_{150} = 4.7 \pm 0.1 \mu s$. The rate of $ArXe^*$ collision with N_2 is also measured for the first time, obtaining a value of $\tau_{N_2,ArXe}$ [N_2] = 20.4±0.6 μs ppm. A value compatible with the literature is obtained for τ_{Xe_2}, even though the xenon concentrations under study are very different. The rate constant of the quenching process for the Ar_2^* collision with N_2 (τ_{N_2,Ar_2}) is five times faster than for $ArXe^*$ ($\tau_{N_2,ArXe}$), and also two times faster than the value reported by [166].

Constant	ProtoDUNE-DP	Literature
τ_{127} (μs)	1.44	~ 1.5 [270]
τ_{ArXe} [Xe] (μs ppm)	6.4 ± 0.4	Not measured
τ_{150} (μs)	4.7 ± 0.1	Not measured
τ_{Xe_2} [Xe] (μs ppm)	9.7 ± 0.1	11.4 [271] - 9.7 [262]
τ_{N_2,Ar_2} [N_2] (μs ppm)	4.1 ± 0.1	9.1 ± 0.1 [166]
$\tau_{N_2,ArXe}$ [N_2] (μs ppm)	20.4 ± 0.6	Not measured

Table 9.6: Results from the global fit to the scintillation model presented in Sec. 9.1.3. The dependence of τ with the xenon and nitrogen concentration ([Xe] and [N_2]) is explicit in the table. τ_{127} and τ_{150} do not depend on [Xe] and [N_2].

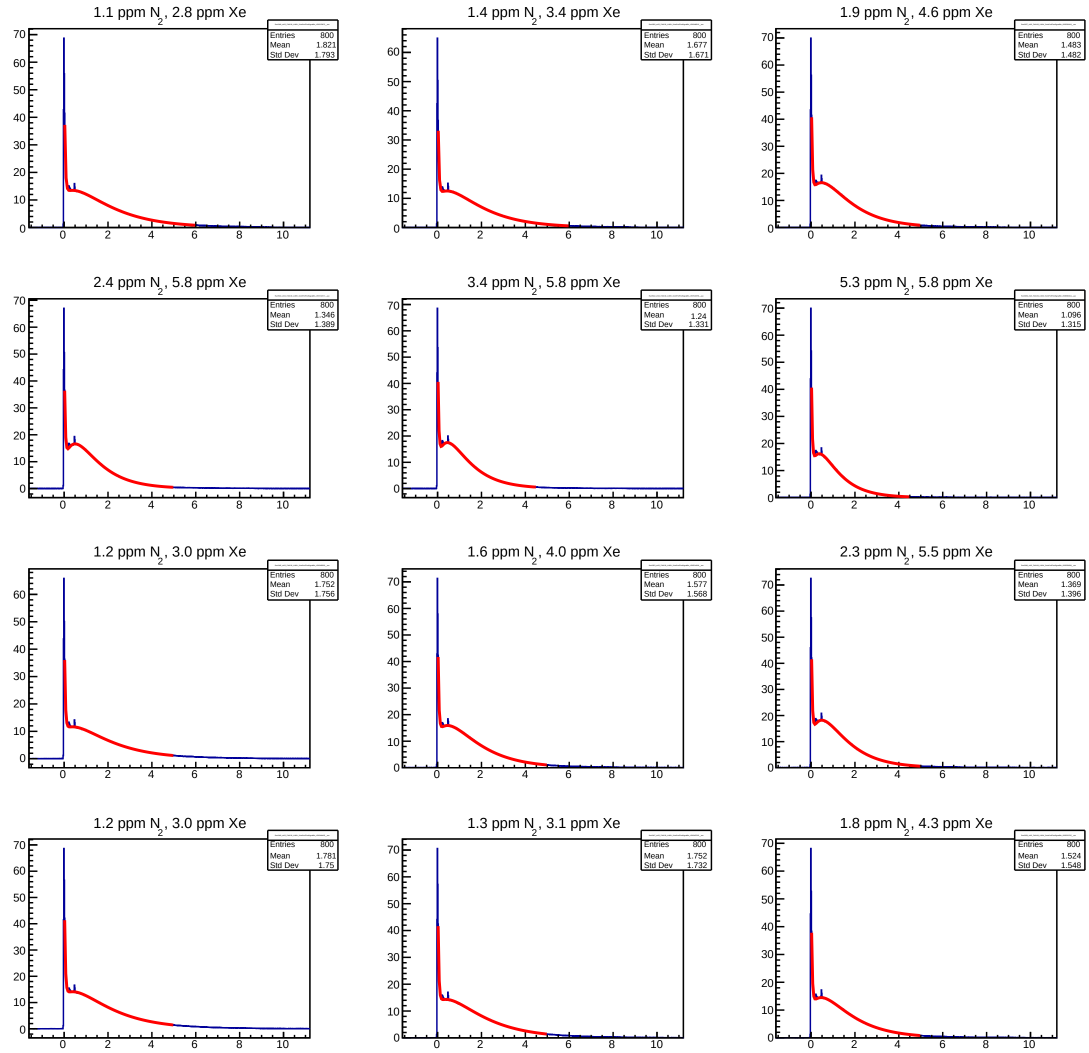

Figure 9.18: Example of a global fit of twelve PMT waveforms at different doping concentrations. Horizontal axis is in μs and vertical axis in ADC counts.

Figure 9.20 shows the values predicted by the model for τ_{slow} (τ_{TX}) and $\tau_{transfer}$ (τ_{TA}) at 0 ppm of nitrogen (solid line) together with values provided in the literature for electrons, gammas, neutrons and alphas (data points taken from [263]). Although the model is tuned for low xenon concentrations (<5.8 ppm), the extrapolation at higher xenon concentrations are not far from the reference experimental values. The saturation effect that appears at 100 ppm on the right panel of Fig. 9.20, when all the Ar light is already transferred to xenon light is not included in our model. The larger discrepancy on the $\tau_{transfer}$ values (left plot) is due to the limited sensitivity to this component in the fit, due to the overlap with the fast signal.

As a result of this analysis, the rate of all the processes included in the model (see Sec. 9.1.3) has been measured (values are summarized in Tab. 9.6). This measurement

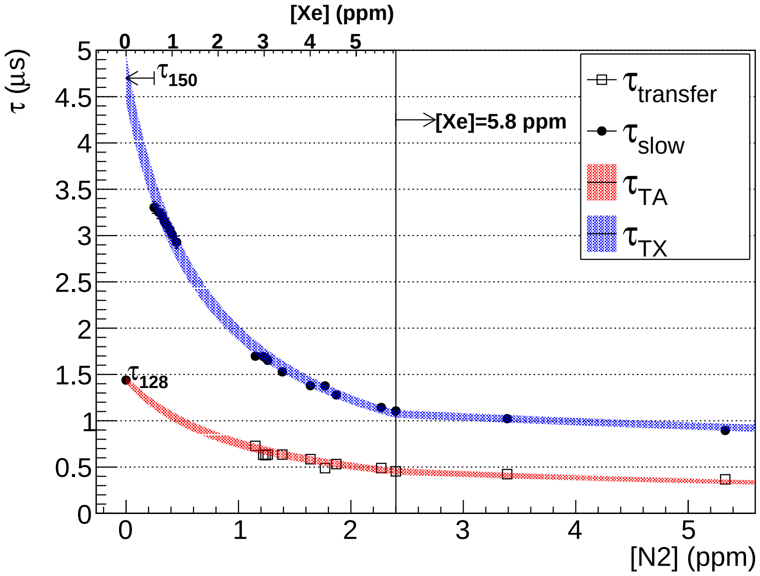

Figure 9.19: Time constants versus xenon (top axis) and nitrogen (bottom axis) concentration. Black points show the result from the individual fits. The blue and red shaded areas show the result from the global fit to Eq. 9.6 $\pm 1\sigma$.

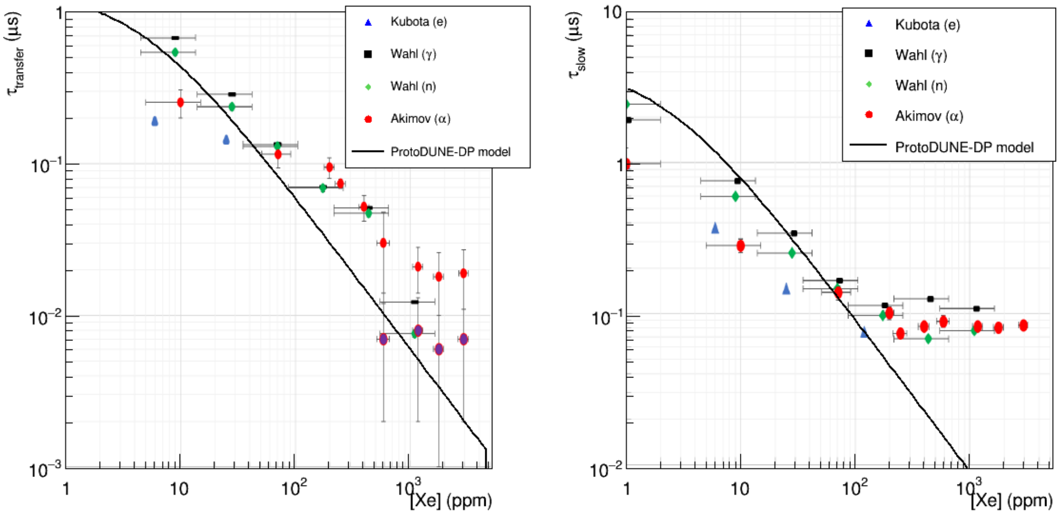

Figure 9.20: Comparison of $\tau_{transfer}$ (left) and τ_{slow} (right) provided by [263] (data points) with the dependence predicted by the model (solid line) tuned with ProtoDUNE Dual-Phase data extrapolating at higher xenon concentrations. Electrons, gammas, neutrons and alphas are provided in [263]. ProtoDUNE Dual-Phase measurement is based in muons. Even though the model is tuned for low xenon concentrations (<5.8 ppm), the extrapolations are not far from the reference values.

relies only on the change of the scintillation time profile with the xenon and nitrogen concentrations. This allows us to solve the model and estimate the photon production for the three different wavelengths at any xenon and nitrogen concentration. This will be done in Sec. 9.5 when comparing the ProtoDUNE Dual-Phase data with the simulation.

9.5 Development of a Monte Carlo simulation of xenon-doped liquid argon

The scintillation light model presented in Sec. 9.1 allows to compute the number of scintillation photons produced at each wavelength for any given doping concentration. This model depends on the time constants that are obtained from the data through the fit to the time profile presented in Sec. 9.4.

In this section, the photon production predicted by the model is compared with the ProtoDUNE Dual-Phase data by simulating CRT-trigger muons. The energy deposited by the muons is simulated using LArSoft as explained in Sec. 6. The photon production is proportional to the deposited energy, with a light yield in pure liquid argon of 40k photons per MeV in absence of drift field. In the presence of xenon and nitrogen, it is assumed that part of the light yield will remain at 127 nm, part will be transferred to 178 nm and the rest will be quenched. The photons at 150 nm are treated as the 178-nm ones for simplicity. Therefore, the sum of the light yields at 127 and 178 nm should be below 40k photons per MeV.

The light yield at the different xenon and nitrogen concentrations is estimated using equations in Tab. 9.2 and the time parameters obtained in Sec. 9.4 (see Tab. 9.6 with the results). The dependence of the photon production with the concentrations at different wavelengths predicted by the model is shown in Fig. 9.21. Note that the 127-nm photons from the fast component is not affected by the xenon and nitrogen concentrations.

Table 9.7 summarizes the photon production at each wavelength predicted by the model at the concentrations under study. These values are obtained from the curves in Fig. 9.21, by summing the 127-nm photons (from both fast and slow component) for the argon light, and the 150 and 178 nm photons for the xenon light, as in the simulation are treated equally. The values in the table are relative to the total light yield in pure liquid argon (40k photons per MeV).

These numbers (Tab. 9.7) are used to simulate the argon and xenon light for different xenon and nitrogen concentrations.

The photon propagation is simulated using Geant4 from the production point until the

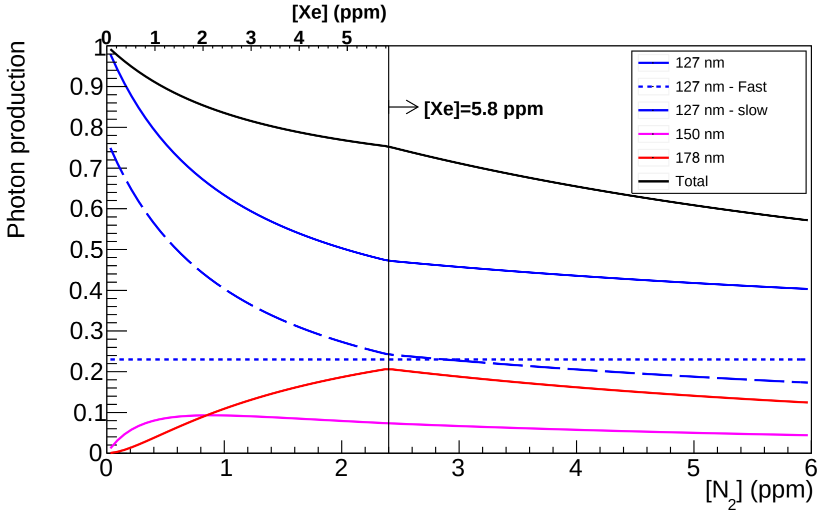

Figure 9.21: Dependence of the total photon production at each wavelength with the xenon and nitrogen concentrations. Xenon concentration (top horizontal axis) increases proportionally during the filling and is fixed at 5.8 ppm after the vertical line.

Concentrations		Light production (% of 40kph/MeV)		
[Xe] (ppmm)	[N$_2$] (ppmm)	Ar (127 nm)	Xe (178 nm)	Total
0.0	0.0	100	0	100
5.8	2.4	47.2±0.9	28.0 ±0.9	75.3±1.2
5.8	3.4	44.8±0.7	24.0±0.8	68.8±1.0
5.8	5.3	41.3±0.5	18.3±0.6	59.6±0.8

Table 9.7: Light yield at each wavelength as predicted by the model at the concentrations under study. Values are relative to the light yield in pure liquid argon. Errors are propagated from the parameter errors obtained in the global fit (see Sec. 9.4.3).

photon hits a PMT or it is absorbed. Since the simulation of the propagation of all the produced photons would require a huge computing time, the propagation is simulated only once, and the results are stored in the so-called photon libraries (see Sec. 6.3).

The parameters involved in the photon-propagation are the Rayleigh scattering length (λ_{RS}), the absorption length (λ_{Abs}) and the reflectivity of aluminum and stainless steel within the cryostat ($R_{Al\&SS}$). The values considered for 127-nm photons are $\lambda_{RS} = 1$ m, $\lambda_{Abs} = 20$ m and $R_{Al\&SS} = 27\%$. The three parameters are fixed in this study since they provide a good agreement between data and simulation in pure liquid argon (see Sec. 7.1). An 35% reduction of the signal at 127 nm is considered due to the absorption of 127 nm photons by the xenon atoms, as it is shown in the fast component reduction in Sec. 9.3. Since this absorption is considered to happen locally, the number of 127-nm photons (47% of 40kph/MeV in the case of 2.4 ppmm of nitrogen) is scaled directly by a factor of 0.65 prior to propagation. This factor is driven by the data (see Sec. 9.3.2).

The Rayleigh scattering length at 178 nm is 8.3 m. It is extrapolated from the spectrum provided in [173], as it is done at 127 nm. Two different sets of values are considered for the absorption length and reflectivity of the 178-nm photons. First, both parameters are kept constant as for 127-nm as a baseline approach. However, since the 178-nm photons are not absorbed (see Sec. 9.1.4), a second situation with a longer absorption length of 1.8 km is considered. Since this value is largely above the detector size length, it effectively removes the absorption on 178-nm photons (see Tab. 9.8).

	127 nm				178 nm		
	Scaling	λ_{RS}	λ_{Abs}	$\mathrm{R}_{\mathrm{Al\&SS}}$	λ_{RS}	λ_{Abs}	$\mathrm{R}_{\mathrm{Al\&SS}}$
1. Baseline	65%	1 m	20 m	27%	8.3 m	20 m	27%
2. No absorption	65%	1 m	20 m	27%	8.3 m	1.8 km	27%

Table 9.8: Sets of photon-propagation parameters considered in the simulation. Values are explained in the text.

Finally, after the photon propagation and having the list of photons hitting the PMTs, the simulated waveforms are generated by adding the corresponding detected photo-electrons at its arrival time. Each photon has a probability to produce a photo-electron in the PMT photo-cathode, defined as the effective detection efficiency (DE). This DE takes into account the wavelength-shifting efficiency, the propagation of the visible light from the wavelength-shifter towards the PMT photo-cathode, and the PMT quantum efficiency. The value considered is $\mathrm{DE}_{TPB} = 0.11$ and $\mathrm{DE}_{PEN} = 0.018$ (See Sec. 6.4). The DE is considered to be the same at 127 nm and 178 nm. Dark counts and electronic noise are also included in the simulation.

9.5.1 Comparison of cosmic muon data and simulation in ProtoDUNE Dual-Phase

A first data-MC comparison is done considering the CRT-trigger events taken at 5.8 ppm of xenon and 2.4 ppm of nitrogen. Figure 9.22 shows the S1 charge versus PMT-track distance for data and simulation. As in Sec. 7.1), a selection of PMTs placed below the CRT track is applied. The simulation assumes the baseline photon-propagation parameters described in Tab. 9.8. A relative light yield of 47.2% for 127 nm photons (prior the 65% scaling) and 28% for 178 nm photons is assumed in the simulation, as predicted by the scintillation model at the first doping concentration of 5.8 ppm of xenon and 2.4 ppm of nitrogen. It is clear in the figure that the data show an excess of photons in comparison with the simulation in the baseline configuration.

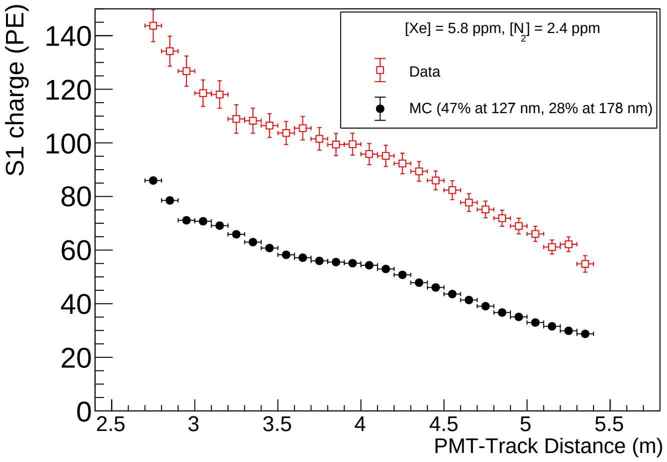

Figure 9.22: S1 charge versus PMT-track distance in xenon-doped liquid argon contaminated with nitrogen for data (red) and simulation (black). The baseline photon-propagation parameters described in Tab. 9.8 are assumed in the simulation.

In order to find the pair of values that reproduce the data, a scan is performed in the relative light yield at 127 and 178 nm. For each pair of values, a curve of average S1 charge versus PMT-track distance is obtained as the one shown in Fig. 9.22. To evaluate the agreement between the data and simulation, a likelihood (L) is defined in Eq. 9.8. A smaller L would mean a better agreement between data and simulation.

$$L = \sum_{\text{bins}} \left(\frac{Q_{Data} - Q_{MC}}{Q_{Data}}\right)^2 \tag{9.8}$$

Figure 9.23 shows the value of the likelihood in the light yield pairs scan considering the two sets of photon-propagation parameters ("baseline" and "no absorption", see Tab. 9.8). The bins in blue show the pair of values with a smaller L and thus a better agreement with the data. Black stars show the photon production predicted by the model. The black line marks the limit at which the sum of the light yields is 100% of 40kph/MeV. The region above the line is forbidden because it implies the production of more photons than excimers are generated.

The left panel of Fig. 9.23 shows that the region in blue is largely above the black line in the baseline set of photon-propagation parameters. This means that, in order to reproduce the data, the light yields in the simulation must be set above the limit of 40k photons per MeV. Since this is not possible, it indicates that the absorption of 178 nm photons is being overestimated, as expected. The right panel of Fig. 9.23 shows the likelihood for the second set of parameters that effectively removes the absorption of 178 nm photons. In this case, the blue region of data-simulation agreement reaches more reasonable values, but it is still largely above the predicted value by the scintillation model: ∼60% of the light yield must be transferred to xenon light in order to reproduce the data in comparison with the predicted value of 28%. The right panel of Fig. 9.23 might indicate that the contribution of the xenon light is underestimated. Two possibilities are explored in order to reconcile data and model: First, a recovery of the light absorbed by the xenon atoms, and second, a larger reflectivity for the xenon light.

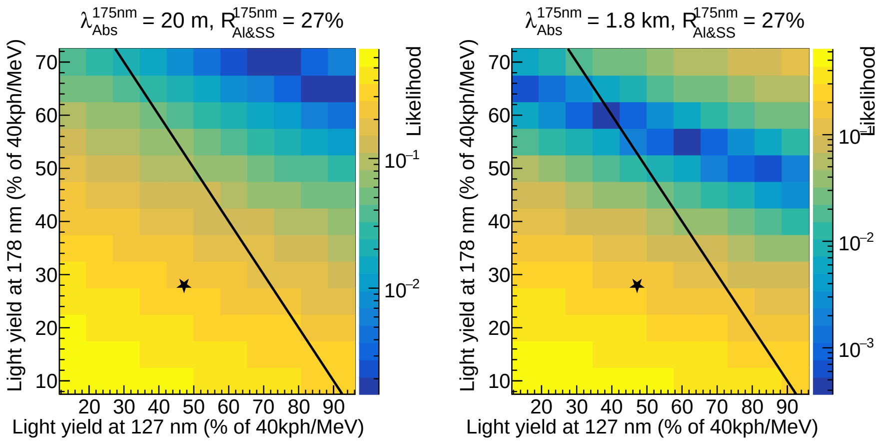

Figure 9.23: Likelihood of the Data-Monte Carlo agreement for different light yield pairs at 127 nm and 178 nm at 5.8ppm of Xe and 2.4 ppm of N_2, for the first (left) and second (right) set of photon-propagation parameters described in Tab. 9.8. The black line marks the limit at which the sum of the light yields is 40kph/MeV. The region above the line is very unrealistic. Black stars shows the photon production predicted by the model.

Xenon atoms absorb the argon light due to two xenon spectral lines at 125 and 129.5 nm respectively. Under the first hypothesis, these xenon atoms would be in an excited state that would contribute to the excimer formation and the light production:

$$\gamma_{127} + \mathrm{Xe} \rightarrow \mathrm{Xe}^* \tag{9.9}$$

According to the literature, this process is possible and it has been proposed in [263]. However, the maximum number of photons produced by this additional path is limited to the number of 127-nm photons being absorbed. This process would allow a maximum recovery of 17% of the light yield, which is closer but still insufficient to reconcile the data with the model. Figure 9.24 shows the likelihood (L) assuming an extreme case of a full transfer of the 127-nm photons absorbed by the xenon atoms to 178 nm, for the three doping concentrations under study. Although in the first case (left panel, at 5.8 ppm of xenon and 2.4 ppm of nitrogen), the model would be still below the number of photons observed in the data, the model would improve the agreement with the data in the second and third doping concentrations (at 5.8 ppm of xenon and 3.4 and 5.3 ppm of nitrogen in the center and right panel).

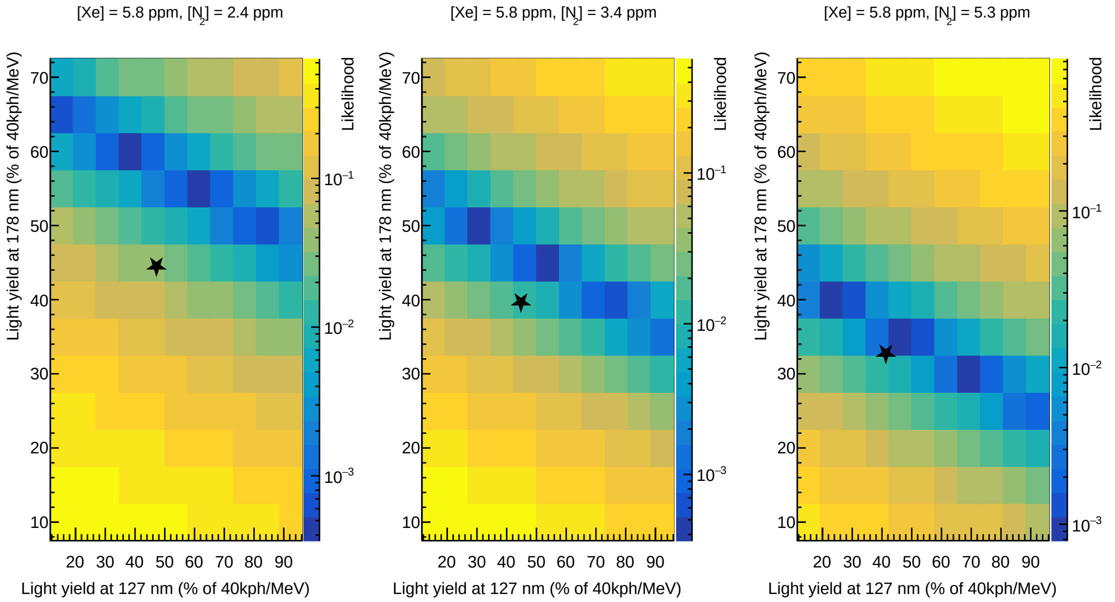

Figure 9.24: Likelihood of the Data-Monte Carlo agreement for different light yield pairs at 127 nm and 178 nm, for the three doping concentrations under analysis. Black stars show the photon production predicted by the model, assuming a hypothetical full recovery of the 127-nm photons absorbed by the xenon atoms.

The second hypothesis that would enhance the contribution of the 178-nm photons is a larger reflectivity of the aluminum and stainless-steel surfaces inside the cryostat. In this case, the photon propagation parameters are maintained as in the second set (without absorption on the 178 nm photons), and only the reflectivity of the 178 nm photons is increased from 27% to 70%. Although there is not a dedicated measurement of the reflectivity of these materials in the laboratory, it can be found in the literature a large increase of the aluminium reflectance at 178 nm with respect to 130 nm. In Fig. 3 of [272], the aluminium reflectance goes from 56% to 84%. These values cannot be extrapolated directly to our case, since they depend on the specific composition or the surface termination. However, it is a good indication that an increase of the reflectivity at 178 nm can be expected as the data seems to point.

The left panel of Fig. 9.25 shows that the photon-propagation considering a reflectivity of 70% for 178 nm photons in the aluminum and stainless-steel surfaces inside the cryostat allows reconciling the model and the data. The centre and right panels of Fig. 9.25 show the good agreement between the model and the data also for the other two doping concentrations under study (at 2.7 and 4.7 ppm of N_2).

The second hypothesis of having a 70% reflectivity provides a better agreement between the data and the simulation. The S1 charge versus PMT-track distance for data and simulation, for the three doping concentrations, considering this hypothesis are shown in

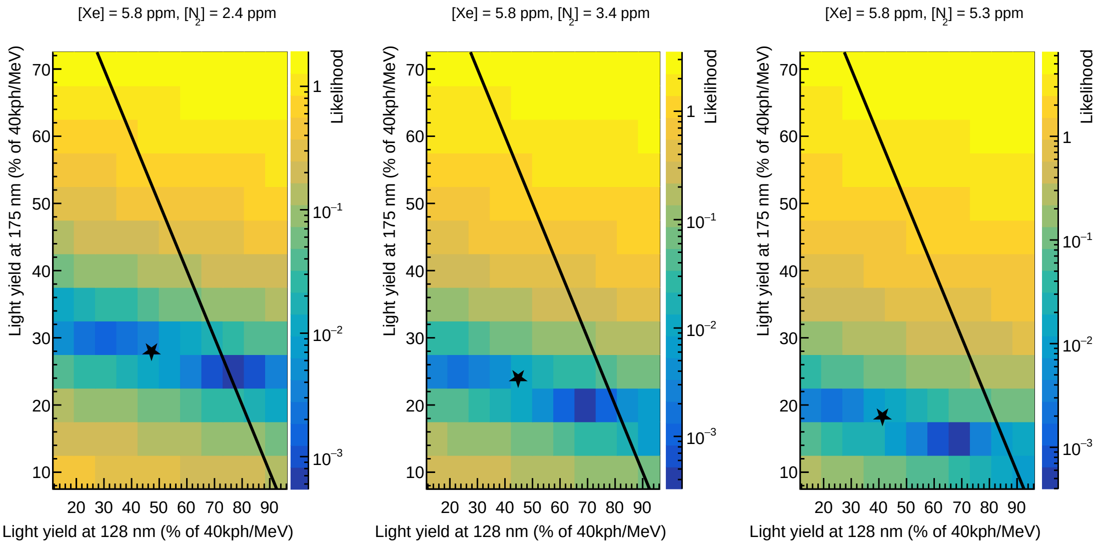

Figure 9.25: Likelihood of the Data-Monte Carlo agreement for different light yield pairs at 127 nm and 178 nm, for the three doping concentrations under analysis assuming a reflectivity of 70% for the 178 nm photons. The black line marks the limit at which the sum of the light yields is 40kph/MeV. The region above the line is forbidden. Black stars show the photon production predicted by the model.

Fig. 9.26. Data and simulation are in good agreement for the three doping conditions, with a discrepancy below 10% in the full range.

In summary, the simulation of the photon-propagation shows that the longer λ_{RS} for the 178 nm photons cannot explain *per se* the large increase of the detected light observed in the data. If assuming no absorption on 178 nm photons, a transfer of ~60% of the light yield to 178 nm is required to reproduce the data, at 5.8 ppm of xenon. However this transfer is too high and does not agree with the model. Two hypotheses are explored that reconcile the data and the model: A full recovery of the light absorbed by the xenon atoms and a high reflectivity of 70% for the xenon light. Although a better agreement is found for the second hypothesis, a combination of both mechanisms might be operating at the same time.

9.6 Conclusions

Xenon doping is a promising technique for large-scale detectors like DUNE since it mitigates the light suppression due to impurities and it also increases the collected light at long distances. ProtoDUNE Dual-Phase performed a xenon-doping data-taking campaign in summer 2020 by re-filling the detector with 230 tons of xenon-doped liquid argon contaminated with nitrogen and performing dedicated nitrogen injections. The concentrations

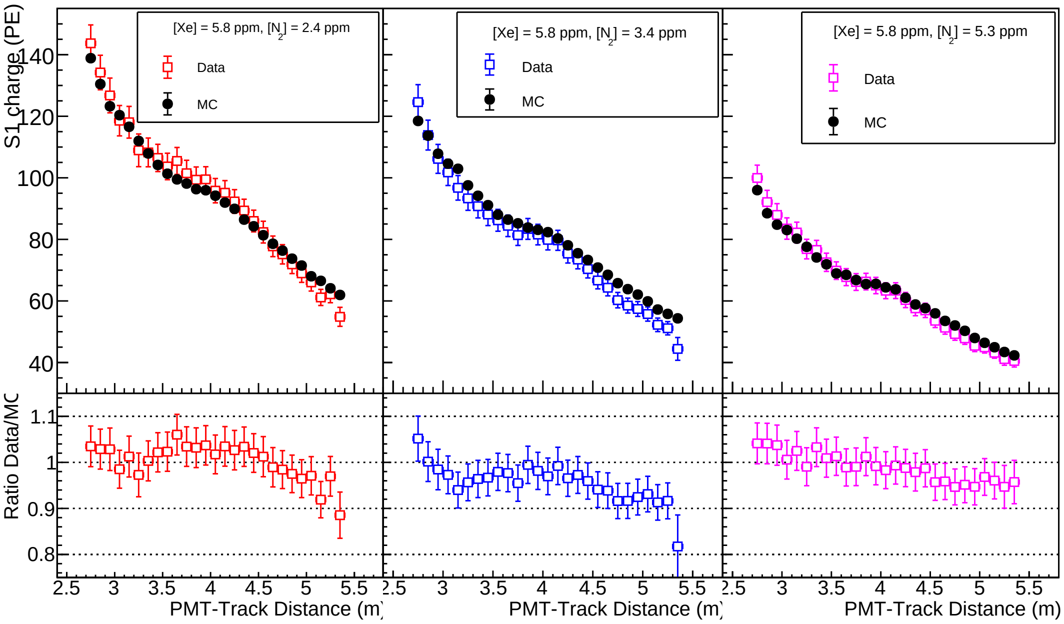

Figure 9.26: S1 charge versus PMT-track distance in the three doping situations, for data (red) and simulation (black). A reflectivity of 70% for the 178 nm photons is assumed in the simulation.

were in the range of 0-5.8 ppmm of xenon and 0-5.3 ppmv of nitrogen.

With a small doping level of 5.8 ppm of xenon (and even in the presence of 2.4 ppm of nitrogen), an enhancement in the light detection efficiency (a factor of two increase for muons crossing at a distance of 3−5 m from the PMTs) and a better uniformity (attenuation length 60% longer) is measured. Additionally, a 35% reduction of the signal amplitude has been observed, which is attributed to the photo-absorption by xenon atoms. The subsequent nitrogen injections of 1 and 2 ppm reduced the collected light a 30% due to the quenching, but unexpectedly they did not affect the signal amplitude (Fig. 9.10).

The impact on the scintillation time profile is also studied. At small concentrations ($\sim$1 ppm of xenon), the slow component increased largely. Then, as the xenon concentration increases, a secondary bump appears. Finally, the slow component shrinks back as the nitrogen is injected (Fig. 9.13).

A model of the scintillation light production in the presence of xenon and nitrogen is proposed and analytically solved. This model proposes the photon-production transfer from the Ar_2^* excimers to the Xe_2^* excimers through an intermediate $ArXe^*$ excimer. These excimers can decay producing photons at a different wavelength: Ar_2^* excimers produce photons at 127 nm, $ArXe^*$ at 150 nm and Xe_2^* at 175 nm.

The photon-production model is fitted using the time profile of the scintillation light obtained from the average signals. The fit provides the time constants of each physics process. The time decay of the ArXe* excimer ($\tau_{150} = 4.7 \pm 0.1 \mu s$) and rate of $ArXe^*$ collision with N_2 ($\tau_{N_2,ArXe}$ $[N_2]$ = 20.4±0.6 μs ppm) are measured for the first time. The is also measured for the first time, obtaining a value of . The model allows to extrapolating the time constants removing the effect of the nitrogen showing that the values obtained are not far from the literature (Fig. 9.20).

As the model predicts a certain composition of the produced light (see Fig. 9.21), a Monte Carlo simulation is developed in order to reproduce the effect of the photon-propagation in the three light components (127, 150 and 178 nm) and compare with the data observations. This comparison shows that the large increase of the detected light cannot be explained only by the longer Rayleigh scattering length for the xenon light (150 and 178 nm photons), and other factors must take in place. In particular assuming no absorption and a reflectivity of 70% of stainless-steel and aluminum for the xenon light would reconcile the data and the model, providing a good agreement between data and simulation at the different doping concentrations under study.

As a result, ProtoDUNE data shows that xenon-doping is a promising technique to enhance light detection in large detectors where the photon propagation distance is long. However, the reduction of the fast component that is seen in the data might compromise the performance of a light-based trigger.

Chapter 10

Validation of the design of the DUNE Dual-Phase Photon Detection System to perform proton decay searches

One of the primary goals of the DUNE physics program is the search for proton decay. Forbidden in the Standard Model, the observation of proton decay could explain the matter-antimatter asymmetry in the universe. DUNE would have a better performance than other detectors in proton decay channels involving a charged kaon in the final state. This is due to the excellent imaging capabilities of the LAr-TPC, that allow identifying the kaon and measure its energy with high efficiency.

In this sense, the photon detection system is crucial for proton decay searches, since it provides the exact time when event was produced that allows a full 3D reconstruction of the event (it provides the coordinate in the drift direction). And this event time is crucial for two reasons: First, it allows to correct the smearing of the energy deposition due to the electron drift, enhancing the energy resolution of the TPC. And second, it allows the suppression of atmospheric muons background: as most cosmic ray activity will cross the detector from the top, the way to suppress this background is to require the event candidate to be fully contained within the detector. Hence, in order to remove the events happening in the detector borders, a full 3D reconstruction is needed.

Since the capability to provide the event time is unique of the photon detection system, a primary DUNE design requirement is that the photon detection system must provide an event time with 90% efficiency throughout the TPC active volume for proton decay signal events. Additionally, some flashes of light produced by radiological activity within the same event readout window can introduce some ambiguity in the time determination.

Therefore, it is also required a 90 % purity among all the reconstructed proton-decay-candidate flashes.

In order to reconstruct the event time, signals from different PMTs are associated by looking at time and space correlations. To perform this task, the system must be able to provide the PMT signals with a time alignment among PMTs better than 100 ns. This will allow the photon detection system to group signals from different PMTs produced by the same physics event. As the proposed photon detection system design for a Dual-Phase Far Detector of DUNE (DUNE Dual-Phase) is similar to the photon detection system used in ProtoDUNE Dual-Phase, this requirement can be tested using ProtoDUNE Dual-Phase data. It is validated through the study of the signal time of every PMT with respect to a reference PMT for the same physics event.

In this chapter, the capability of the DUNE Dual-Phase photon detection system to provide an event time to proton decay events is validated. First, in Sec. 10.1, proton decay studies in DUNE are introduced. The capability of the photon detection system of providing the event time in proton decay events with a 90% efficiency and 90% purity is validated by using Monte Carlo simulated samples in Sec. 10.2. In Sec. 10.3 the time alignment among PMTs is shown to be below 16 ns in ProtoDUNE Dual-Phase data, the sampling frequency of the acquisition system, validating the capability of the DUNE-DP photon detection system design for grouping light signals from different PMTs. Finally, the conclusions are summarized in Sec. 10.4.

10.1 Proton decay searches in DUNE

Grand Unification Theories (GUT) aim to encompass three of the four fundamental forces in nature: electromagnetic, weak and strong forces. Many GUT theories that extend the Standard Model to include a unified gauge symmetry at high energies (more than 10^{15} GeV), predict nucleon decay [273–275]. While supersymmetric GUTs predict the proton decaying into a kaon as a the dominant channel (Eq. 10.1), non-supersymmetric GUTs prefer the proton decaying into a positron (Eq. 10.2). These decays violate the baryon number conservation, and are forbidden in the Standard Model.

$$p \to K^+ + \bar{\nu} \tag{10.1}$$

$$p \to e^+ + \pi^0 \tag{10.2}$$

Proton decay has not been observed yet, and the current best limits for most of the channels have been set by Super-Kamiokande [276–278]. DUNE will be able to detect both decay modes. Although it is unlikely that DUNE would be more competitive than the next generation of water Cherenkov experiments such as Hyper-Kamiokande in the second decay mode (Eq. 10.2), its sensitivity to the nucleon decay channels involving a kaon (such as Eq. 10.1) will be unique. While water Cherenkov detectors cannot detect the kaon but its decaying products, since the kaon momentum is below the Cherenkov threshold, in a LAr-TPC the kaon can be clearly detected. Due to the excellent imaging resolution of LAr-TPCs, the kaon can be identified by the analysis of the energy loss profile, and its momentum can be measured with high precision.

Since the presence of an isolated kaon with a well-defined momentum of 339 MeV/c is the key signature for $p \rightarrow K^+ + \bar{\nu}$, the observation of a single event with such level of detail would provide a clear evidence of a proton decay. Due to the unique capabilities of DUNE to identify kaons, the initial proton decay sensitivity studies have been focused in the nucleon decay modes including kaons. Therefore, the key signature of this channel (see Eq. 10.1) is a monoenergetic kaon of 339 MeV/c, that stops and decay. However, in a bound proton the momentum of the outgoing kaon is smeared by the Fermi motion of the protons inside the nucleus. These final state interactions (FSI) between the kaon and the nucleus can also reduce the kaon momentum and modify the final state, for example, by ejecting nucleons. The two dominant kaon decay modes are the kaon decaying into a muon ($K^+ \rightarrow \mu^+ + \nu_\mu$), and the production of two pions ($K^+ \rightarrow \pi^+ + \pi^0$).

The backgrounds for proton decay searches are atmospheric muons and neutrinos. If a muon crosses through the detector borders, then the event can be easily identified and rejected. However, muons passing near the detector would also contribute to the background. Among these events, neutral kaons produced outside the TPC by background muons and undergoing inelastic scattering inside the TPC would result in a single positive kaon detected. Also the atmospheric neutrinos undergoing CC ($\nu_\mu + n \rightarrow \mu^- + K^+ + n$) and NC ($\nu + p \rightarrow \nu + K^+ + \Lambda$) would contribute to this background, since they are around the energy range relevant for proton decay. Nevertheless, these background events can be removed thanks to the good imaging capabilities of the technology, and the use of dedicated reconstruction and particle identification techniques, as it is shown in [200]. However, it is important to remark that these studies assume that the photon detection system correctly determines the event time, as this is a design requirement: the photon detection system should provide an event time with a 90% purity and efficiency throughout all the TPC active volume. This is demonstrated in Sec. 10.2, for the DUNE-DP photon detection system design.

As a result, DUNE will be able to set a lower limit on the lifetime of the decay $p \to K^+ + \bar{\nu}$ channel for 400 kt year exposure at 90% confidence level of 1.3×10^{34} years. In comparison, the best current limit in this channel has been set by the Super-Kamiokande collaboration at 90% confident level of 5.9×10^{33} years [278].

Another potential nucleon decay mode is $n \to e^- + K^+$, for which DUNE will be able to set a limit of 1.1×10^{34} years. In comparison, the current best limit of 3.2×10^{31} years has been set by the FREJUS collaboration [279].

The DUNE sensitivity studies for nucleon decay searches, as well as other BSM searches are explained in detail in [200, 280].

10.2 Event time reconstruction for proton decay searches in DUNE

In this section, the capability of the DUNE Dual-Phase photon detection system to provide an event time to proton decay events is validated. This is required in order suppress proton decay backgrounds and enhance the energy resolution of the detector (see Sec. 10.1). The photon detection system should provide an event time with 90% efficiency and 90 % purity throughout the TPC active volume for proton decay signal events.

While the backgrounds for proton decay searches are atmospheric muons and neutrinos (see Sec. 10.1), the background for the event time determination is the low energy decay of radiactive isotopes that are continuously producing background light inside the detector. These radiological backgrounds were reviewed in detail in Sec. 6.2.3. They are the decay of ^{39}Ar, ^{42}Ar, ^{85}Kr that are present in natural argon, and radon and neutrons produced by the decay of the uranium in the underground rock.

The proton decay channel studied is $p \to K^+ + \bar{\nu}$. In this channel, the event time is provided by the scintillation light signal (S1) produced by the kaon and its decay products. This signal is detected right after the kaon is produced, due to the fast propagation of the photons in comparison with the drift of the electrons. Also radiological backgrounds produce scintillation light in the liquid argon that can hinder the event time determination. While the kaon and its decay products have a well defined energy of the order of hundreds of MeV, the energy of the radiological backgrounds is of the order of hundreds of keV, what makes the signal events very different and easy to separate from the backgrounds. However, the high rate of the background decays can difficult the detection of the signal when it happens far away from the photon detector system (up to 13 m away from the PMTs in DUNE-DP). The most significant radiological background is ^{39}Ar, emitting betas with an end-point energy of 565 keV and an activity of 1.01 Bq/kg. This means a high rate of 17 MHz in 17 kton of liquid argon which can compromise the performance of the event time determination.

In this study, the scintillation light production, propagation and detection of proton decay signal and radiological backgrounds is simulated. Then, an algorithm to separate signal from backgrounds is developed, and the efficiency in the event time determination is evaluated. The simulation of the proton decay events is explained in Sec.10.2.1. The simulation of the radiological backgrounds and the detector response is similar as for ProtoDUNE Dual-Phase studies and were already explained in chapter 6. The Monte Carlo samples used in this study are described in Sec. 10.2.2. Then, the signal reconstruction and its optimization to separate proton decay events from backgrounds are explained in Sec. 10.2.3. Finally, the event time reconstruction performance is described in Sec. 10.2.4.

10.2.1 Proton decay event simulation

The simulation of proton decay events is performed using GENIE [281]. Even though GENIE can simulate 68 nucleon decay channels, the study presented in this thesis has been focused on $p \to K^+ + \bar{\nu}$.

If a proton decay occurs within a bound nucleus, the remaining nucleus would be in an excited state and will de-excite by emitting nuclear fission fragments, nucleons, and photons. The nucleon binding energy and momentum distribution are simulated using the Fermi gas model implemented in GENIE. The decay products then propagate in the nucleus. This is simulated using an hadron-transport model. The kinetic energy of a primary charged kaon for a proton decay at rest is 105 MeV (or a momentum of 339 MeV/c). In bound proton decay, such as in the argon nucleus, the energy of the kaon is smeared by the Fermi motion of the protons inside the nucleus. GENIE model this process using the hA2015 model, and empirical, data-driven method for this final-state interactions (FSI). This results in a small smearing of the kaon energy, as it can be seen in Fig. 10.1 that shows the kinetic energy of a kaon from $p \to K^+ + \bar{\nu}$ before and after FSI.

10.2.2 Simulated samples: Signal and radiological backgrounds

Proton decay signal events in the channel $p \to K^+ + \bar{\nu}$ have been simulated using GENIE (see Sec. 10.2.1) and the radiological backgrounds using a dedicated LArSoft module as explained in Sec. 6.2. The signal and background events are simulated as separated samples.

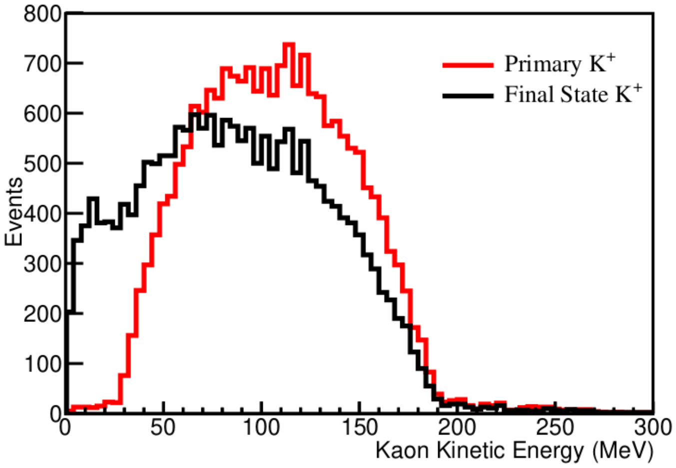

Figure 10.1: Simulated kinetic energy of kaons in the proton decay channel $p \rightarrow K^{+} + \bar{\nu}$, before (red) and after (black) final state interactions in the argon nucleus [117].

Each signal event contains a single $p \rightarrow K^{+} + \bar{\nu}$ decay interaction, that is simulated randomly within all the active volume. The simulated readout window for signal events is 16 μs, which is large enough to collect all the scintillation light produced by the kaon and its decay products. The left panel of Fig. 10.2 shows the energy distribution of the resulting charged kaons and $\bar{\nu}$ obtained in the simulation. The total energy of the K^{+} is around 0.6 GeV, which is stopped and decay. The total energy deposit of the kaon and its decay products is around $\sim$ 500 MeV, with results in production of $\sim 12 \times 10^{6}$ scintillation photons per proton decay event.

Since the maximum drift length is 12 m in DUNE-DP, the maximum delay between charge and light signal is 8 ms. Therefore, if a proton-decay candidate event is triggered, the correlated light signal (and thus, the event time) must be searched in the previous 8 ms of photon-detection-system readout window. For this reason, the time window of the background events should be 8 ms. However, due to computing limitations the background time window is divided in eight events of just 1 ms. Hence eight background events are considered per signal event. Each background event contains a certain number of background interactions. The number and position of the background interaction depends on its origin (as described in Sec. 6.2). While radioactive isotopes present in natural argon (^{39}Ar, ^{42}Ar and ^{85}Kr) are produced uniformly in all the liquid argon volume, the radon and neutrons from the underground rock enter from the sides of the cryostat. The right panel of Fig. 10.2 shows the number background interactions per background event of 1 ms of readout window. The dominant backgrounds by number of interactions are the ^{39}Ar, ^{85}Kr and Rn, with $\sim$ 20,000 $\sim$2,000 and $\sim$800 events per ms respectively.

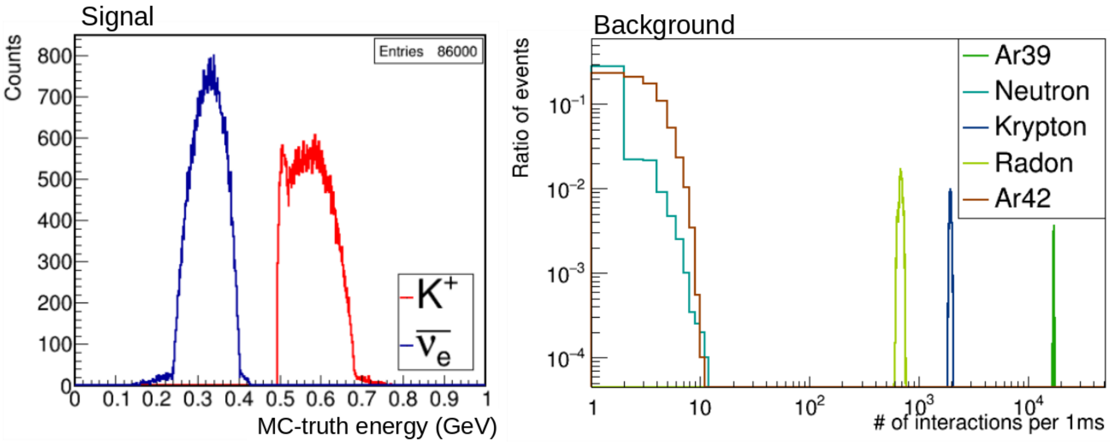

Figure 10.2: Left: MC-truth energy of the resulting kaon and $\bar{\nu}$ in the simulated $p \to K^+ + \bar{\nu}$ events. Right: Number of background interactions simulated per ms of readout window.

As anticipated in Sec. 6.1, three different geometries are evaluated depending on the coverage of field cage with wavelength-shifting reflective foils: No foil, half foil, and full foil. While the full-foil geometry has the inner part of the field cage fully covered with reflective foils, in the half-foil geometry, only the top half is covered, and the no-foil geometry does not include any foil.

Left panel of Fig. 10.3 shows the number of photoelectrons (PE) detected by all PMTs per signal event as a function of its drift position. The drift length goes from -6 m to +6 m. PMTs are at -7 m and the CRPs are at +6 m. The non uniformity of the light detection in the no-foil geometry can be appreciated on the left panel of Fig. 10.3, being three orders of magnitude the difference between the bottom part of the active volume and the top part (10^4 versus 10 PEs). The wavelength-shifter reflective foils increase the detected light by almost two orders of magnitude at the top of the field cage. While the full-foil geometry increases the collected light at all drift positions, the increase in the half-foil geometry is focused on the top part of the field cage. However, this increase in the detection efficiency is also reflected in the background light detection. The right panel of Fig. 10.3 shows the number of photoelectrons detected per background event by all PMTs. The background light increases almost a factor of two when comparing no-foil with full-foil geometry (~ 34 versus ~ 50 kPEs). In comparison, the background light increase is below 10% in the half-foil geometry with respect to the no-foil geometry. The sources of the background light are shown in Fig. 10.4 for the half-foil geometry case. The PMT dark counts are shown in black. The main contribution comes from the ^{39}Ar with $\sim$30k PEs per ms followed by ^{85}Kr and PMT dark counts.

In total 40k events are simulated for the no-foil geometry, and 20k events for both, the half-foil and full-foil geometry. In comparison, 86k events of signal events are simulated.

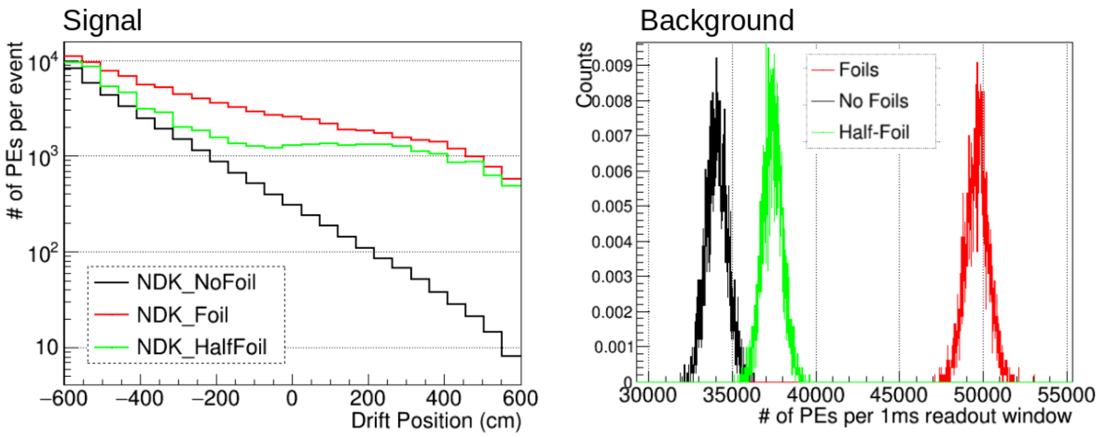

Figure 10.3: Left: Number of detected PEs by all PMTs per $p \to K^+ + \bar{\nu}$ event vs drift position. Right: Total number of detected PEs by all PMTs from background interactions per ms of readout window.

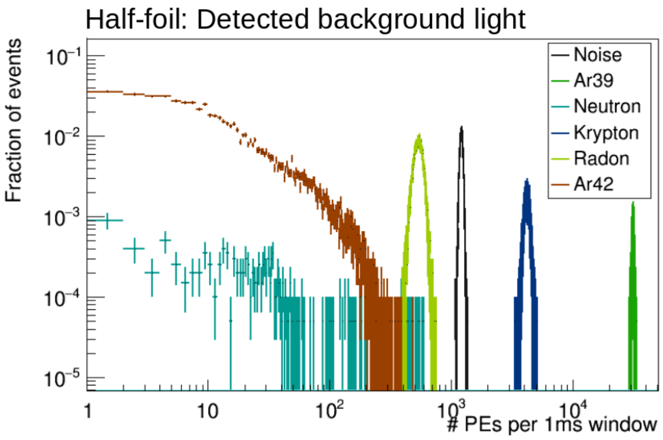

Figure 10.4: Number of detected PEs in 1 ms readout window per background source. Noise (in black) stands for the PMT dark counts.

10.2.3 Signal reconstruction: Hit and flash finding

The PMT waveforms are processed in order to reconstruct the scintillation light from the proton decay signal that provides the event time. This reconstruction is based on hits and flashes. One hit is just one pulse in a PMT waveform. Using a dedicated algorithm, any pulse with an amplitude larger than 10 ADC counts is identified as a hit, being the amplitude of one PE around 25 ADC counts. Each hit is characterized by one time, amplitude, integrated charge (in number of PEs) and the PMT position in the detector.

One flash is a collection of hits from different PMTs that are grouped following a nearest-neighbour algorithm, considering time and space correlations among hits. The grouping starts with the selection of the largest hit (*i.e.* that one with the largest integrated charge in the time window) as a flash seed, then the nearest hits are added to the flash if they satisfy the following four criteria defined by four clustering parameters:

- Maximum hit time difference: The hit is added if its time is below a certain value with respect to the closest hit in the flash.
- Maximum hit distance: The hit is added if the PMT detecting this hit is closer than a certain distance to the nearest hit in the flash.
- Maximum flash duration: The flash cannot grow in time more than a certain duration.
- Minimum flash charge: The group of hits must contain a minimum integrated charge in order to consider it a flash.

The purpose of the flash is to reconstruct the S1 signal that would provide the event time (t_0). Since the background light can also be reconstructed as a flash, the clustering parameters are chosen to optimize the selection of the flash originated by a signal event over the flashes originated by the background light. Therefore a scan on the maximum time difference (test values: 50, 100, 200, 400 and 800 ns), the maximum hit distance (1.5, 2.5, 3.5, 4.5 and 5.5 m) and maximum flash duration (test values: 0.063, 0.125, 0.25, 0.5, 1, 2, 4, 8 and 16 μs) is performed. For each combination of these values, a list of signal and background flashes is generated. Then the minimum flash charged is adapted to provide the same rate of background flashes for each set of parameters, in order to compare its performance.

The different combination of clustering parameters provides very different results when the clustering is applied. For example, a short maximum flash duration of 125 ns splits the signal event into several flashes when the duration of the scintillation light is of the order of μs. However, a long maximum flash duration of 16 μs groups hits from many different background signals creating large background flashes that would compromise our signal discrimination. Therefore, a balance is needed. To find the optimal configuration, the signal efficiency is defined as the fraction of signal events with at least one reconstructed flash. The clustering parameters that maximize the signal efficiency for the same rate of background flashes is selected as the optimal combination. The dependence of the signal efficiency with two of the clustering parameters is shown in Fig. 10.5. In these figures, a scan in the maximum hit distance and the maximum flash duration is performed. The maximum hit time difference is kept constant, and the minimum flash charged is adapted to provide the same background rate of 10 background flashes, as a first approach, per signal event in each bin.

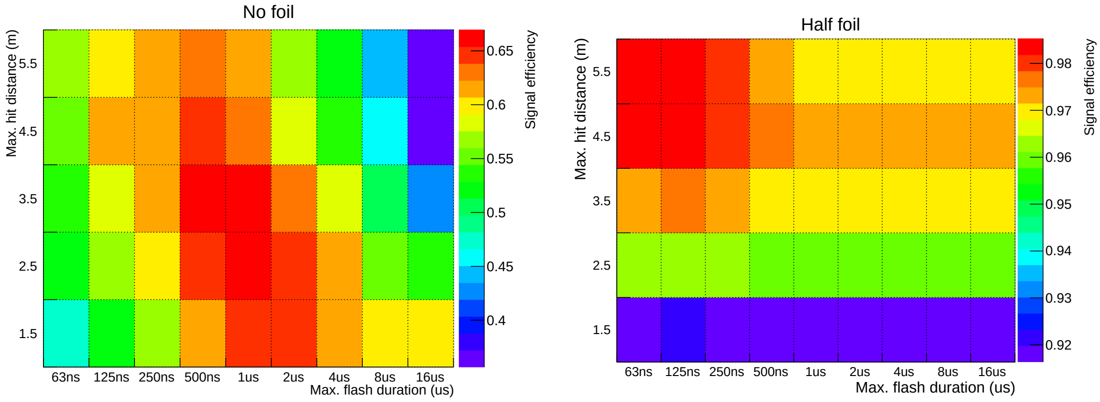

Figure 10.5: Clustering parameters optimization for the no foil (left) and half foil (right) geometry. The histograms show a scan in the maximum flash duration (in x) and the maximum hit distance (in Y). The maximum hit time difference is kept constant at 800 ns (100 ns) on the left (right) plot. Colour shows the signal efficiency.

The optimal combination of the clustering parameters for the three DUNE-DP geometries is summarized in Tab. 10.1. An efficiency of 65% is obtained for the no foil geometry, while an efficiency of 98% is obtained for the foil and half-foil geometries, allowing a background rate of 10 background flashes per signal event. In the no foil case, the photon hits are detected in a well defined position, therefore the optimal configuration requires a strong spatial correlation and a more relaxed correlation in time. On the contrary, in the foil and half foil cases, hits belonging to the same cluster are required to be nearly coincident in time, but only loosely correlated in space.

Geometry	Max. hit distance	Max. time difference	Max. flash duration	Efficiency
No foil	2.5 m	800 ns	1 μs	65%
Half foil	5.5 m	100 ns	100 ns	98%
Foil	5.5 m	100 ns	100 ns	98%

Table 10.1: Optimal combination of clustering parameters for the three DUNE-DP geometries.

10.2.4 t_0 reconstruction efficiency and purity for proton decay events

In general, the event flash reconstruction described in the previous section would provide several flashes per event: Those originated by the signal interactions and those from background radiological activity. However, not all the flashes are considered as t_0 candidates. Only those reconstructed in the vicinity of the signal event are taken into account to reconstruct the event interaction time. Since the TPC provides a precise reconstruction of the position of the proton decay interaction in the plane perpendicular to the drift, it is possible to ignore the flashes that are reconstructed far away. For this, the position of the flash is defined as the barycenter of the hits belonging to the same flash. The barycenter is computed by weighting the hits by its integrated charge. Therefore, the position of a reconstructed flash must be within a certain distance from the proton-decay interaction vertex in the plane perpendicular to the drift in order to be considered as a t_0. The value of this maximum flash-vertex distance is optimized in a separate step, in order to maximize the rejection of flashes from background origin.

To perform this optimization, two parameters are defined: t_0 reconstruction efficiency and purity. The reconstruction efficiency measures the fraction of events with at least one t_0 candidate originated by a signal proton-decay interaction. If there is more than one t_0 candidate, the event time will be associated to the t_0 candidate with the highest charge. The purity is defined as the probability for the highest charge t_0 candidate in the event to correspond with the proton-decay signal interaction time. It measures the fraction of the event times well reconstructed. A value of purity below one is obtained if the highest charge t_0 candidate is due to radiological activity.

Figure 10.6 shows the scan of the efficiency (black curve) and purity (red curve) considering different values for the maximum flash-vertex distance for the half-foil case. Green curve shows the Efficiency x Purity as a figure of merit to maximize both values. The maximum flash-vertex distance that provides the maximum efficiency and purity is 1.5 m in the half-foil case.

Finally, Fig. 10.7 shows the proton-decay t_0 reconstruction efficiency (left panel) and purity (right panel) as a function of the nucleon decay vertex position in the drift direction (with the cathode plane placed at -600 cm, and the PMTs at -700 cm). In the no foil configuration (black curves), the efficiency is above 85% in most of the active volume (up to 10 meters drift out of 12), while the purity drops to zero (at 50% at 8 meters drift). This means that above 10 m from the cathode there is a t_0 candidate originated by the signal interaction, however the background interactions are creating other candidates with more integrated charge. This multiplicity of flashes creates ambiguities that reduce the purity.

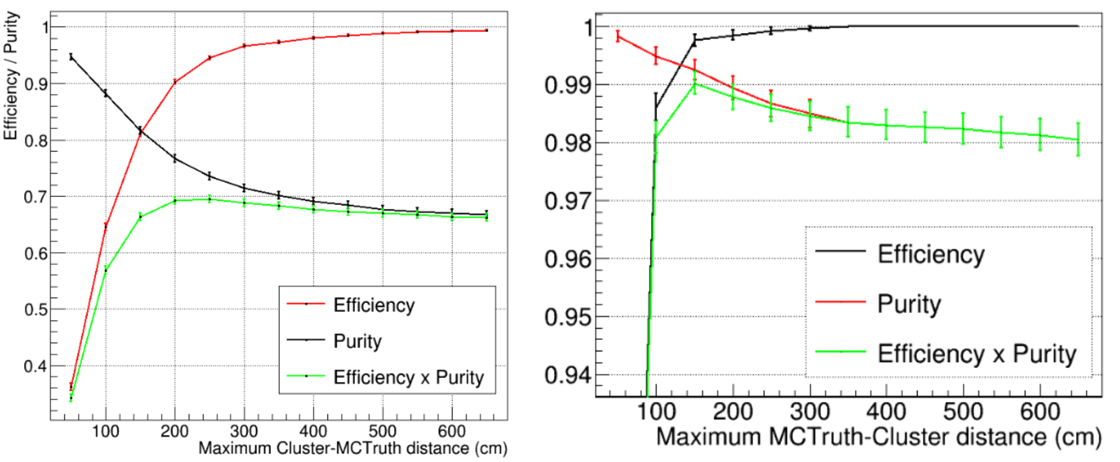

Figure 10.6: Efficiency (black), purity (red) and Efficiency x Purity (green) versus maximum flash-vertex distance in cm. No-foil geometry is shown on the left, and half-foil geometry on the right. The distance of 250 (150) cm provides the optimal Efficiency x Purity in the no-foil (half-foil) geometry case.

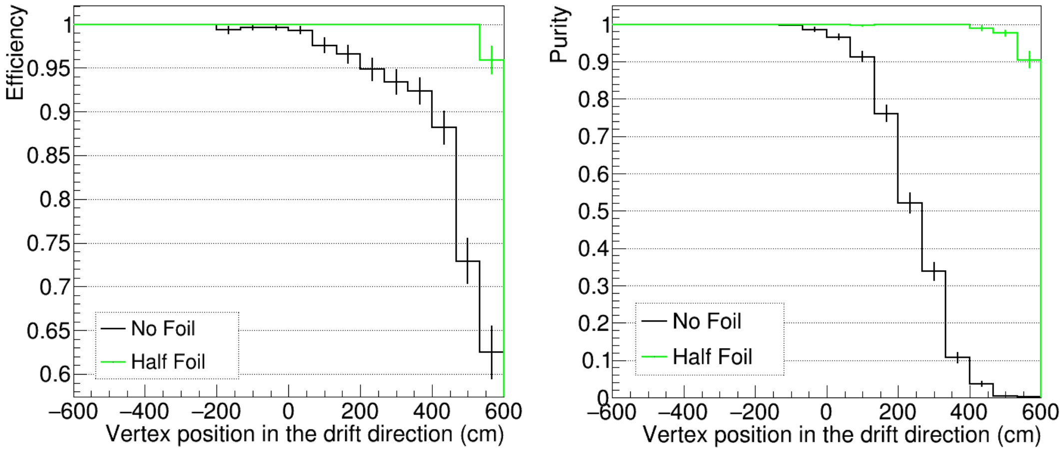

Figure 10.7: Proton decay t_0 reconstruction efficiency and purity as a function of the nucleon decay vertex position in the drift direction.

Nevertheless, an efficiency and purity above 90% throughout the TPC active volume is obtained for the half-foil geometry, satisfying the detector requirements. The foils on the top part of the TPC allow to increase the detected light at long distances from the cathode, without amplifying the background flashes that could happen at short distances.

This large improvement in the t_0 reconstruction is the main motivation of introducing the reflective foils in the field cage. Additionally, since the time correlations are critical to reconstruct the event time, this analysis has also motivated the introduction of a requirement in the photon detection system design: A time alignment among PMT signals better than

100 ns, which is the maximum time difference allowed by the clustering algorithm (see Tab. 10.1). This requirement is validated in Sec. 10.3, showing an alignment below 16 ns in ProtoDUNE Dual-Phase data, which is the sampling frequency of the acquisition system.

10.3 Study on the time alignment among PMT signals in ProtoDUNE Dual-Phase

In order to reach the DUNE physics goals, the photon detection system of the DUNE Dual-Phase Far Detector must fulfil some requirements established in the DUNE Dual-Phase Technical Design Report (TDR) [190]. The time alignment among PMTs signals should be better than 100 ns [190]. This requirement will allow the photon detection system to group signals from different PMTs produced by the same physics event, which is later used to reconstruct the event time (as it has been demonstrated in Sec. 10.2) or to trigger on the light signals (such as for supernovae burst detection, [227]). The maximum time difference that provides the optimal event time reconstruction efficiency is 100 ns (see Tab. 10.1), therefore the time alignment should be better than this value.

Possible sources of time misalignment among PMT signals are different signal-cable lengths or failures in the DAQ system. Also time differences due to the topology of the event are expected, since a particle crossing the detector takes some time to cross the volume, and the scintillation light also takes some time to arrive from the production point to the position of the photo-sensor.

A study on the alignment in time of signals of every PMT with respect to a reference PMT has been performed using the data of ProtoDUNE Dual-Phase (4).

The ProtoDUNE Dual-Phase photon detection system is carefully designed to avoid any source of time misalignment. The delay introduced by every PMT cable has been measured during the installation using an oscilloscope and a signal generator, obtaining an average value for all PMTs of 496.8 ± 0.4 ns, and a maximum difference between PMTs of 2 ns. Additionally the PMTs introduce a jitter in the signal given by the Transit Time Spread (TTS) of 3 ns [282]. These two factors are negligible compared with the sampling frequency of the digitizer of 16 ns.

Additionally, physics can also introduce some time differences: A relativistic particle takes 20 ns to cross the 6 meters ProtoDUNE Dual-Phase width, and the scintillation light would take around 45 ns (considering a speed of light of 7.5 ns per meter in Ar [173]) in the worst case arriving to a PMT placed on the other side of the detector.

Triggering on a specific PMT, light signals corresponding to the same physics event can be identified by looking for the nearest signal in time in the rest of the PMTs. An algorithm to identify and characterize these signals has been developed, also taking into account the case of two particles crossing at the same time. Finally the distribution of the time difference of the signal with respect to the trigger PMT is fitted to a Gaussian. The relative timing accuracy is obtained from the fitting parameters and compared to the TDR requirement.

For completeness, the analysis has been repeated using data triggered with the external cosmic ray taggers (CRTs, see Sec. 4.1.5).

10.3.1 Description of the data

The run selected to perform this analysis has been acquired triggering on PMT FA0132, a TPB-coated PMT placed in the centre of the detector, as it is shown on figure 10.8. All PMTs were operated at the same gain of 5 10^6, being the expected SPE amplitude around 4 ADC counts. The trigger threshold is set at a minimum amplitude of 100 ADC counts, which corresponds to an amplitude of 25 PEs on the trigger channel. The run contains 200k events and the digitisation provides 1000 samples per event at a frequency of 62.5 MHz, meaning waveforms of 16 μs and samples of 16 ns. No electric field was present during the data taking.

As explained in Sec. 10.3, the topology of the particle track can introduce time differences due to the light propagation: photons will arrive faster to the PMTs placed closer to the photon production point, where the energy is deposited. In the worst case of a vertical track passing next to a PMT in a corner, the time difference with respect to a PMT placed 6 m away would be 45 ns.

To mitigate this effect, a PMT placed in the centre has been selected as the trigger (see Fig.10.8) since the PMT will trigger on tracks passing nearby. In this case, the light propagation distance would be around 3 m maximum, making the time difference due to the geometrical position negligible, around 22 ns.

In the case of the CRT triggered run, the topology of the selected tracks is known, being the average PMT-track distance approximately constant for every PMT. This distance goes from around 3 m to around 6 m as it is shown in figure 10.8. Again, to mitigate this effect, the same PMT placed in the centre has been selected as a reference, with an average PMT-track distance of around 4.5 m. Therefore the difference between this PMT and the rest will be around 2 m maximum, which corresponds to a difference in time due to the geometrical position of 15 ns, below our digitization frequency of 16 ns which makes this factor negligible in this analysis.

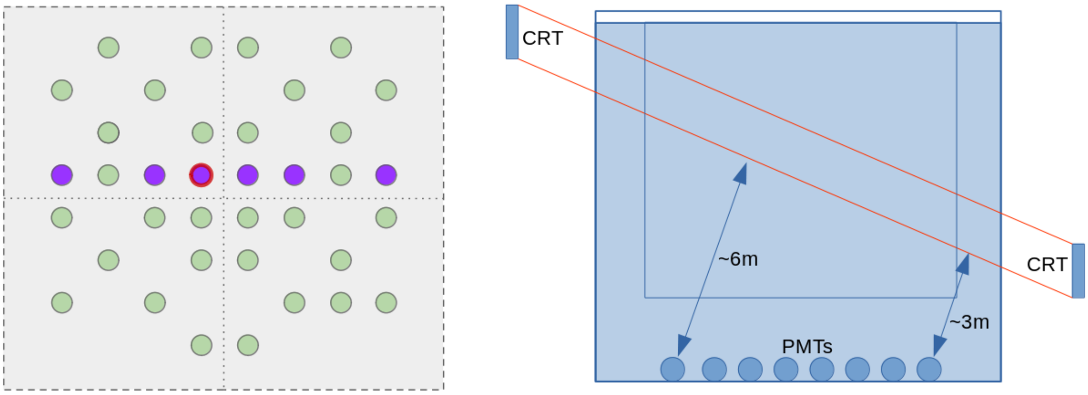

Figure 10.8: Left: Top view of the PMT positioning. PEN-foiled PMTs are shown in green, TPB-coated PMTs are shown in purple. The red circle indicates the triggering PMT used as a reference. Rigt: Side view of the detector and the position of the selected tracks in the CRT triggered data.

10.3.2 Description of the method

As explained in Sec. 2.3 cosmic muons crossing the detector produce primary scintillation light (S1) that can be detected by the PMTs. Scintillation light is produced by the decay of argon excimers, with two time decays, a fast decay of 7 ns, and a slow decay of $\sim$1.4s μ. As a consequence, the S1 signals have a prompt component of a few nanoseconds width, and a subsequent tail of small pulses, as can be appreciated on Fig. 10.9.

By identifying the corresponding S1 signals in different PMTs, the difference in time between the two signals can be measured. Figure 10.9 shows an hypothetical example of two overlapped S1 signals in two PMTs (in blue and red). Assuming that the signal on both PMTs has been produced by the same track, the difference in time between the two minima, δt in the figure, would correspond to the timing accuracy among these two PMTs.

10.3.3 Pulse finder algorithm.

The data processing consists of identifying S1 light signals within each PMT waveform. Since we can have several signals produced by different particles in the same waveform, we need an algorithm to identify them and separate one from another.

The DAQ places the triggered signal around 3μs in the time acquisition window. Therefore we will look for signals in the range from 2.8 to 3.3 μs in the rest of the PMTs. This time range is set large enough to consider possible time differences due to the event topology or any hardware effect, but also small enough to reduce the chance of having two particles in time coincidence. S1 signals (*Pulses*) are found in the PMT waveform, by following these steps:

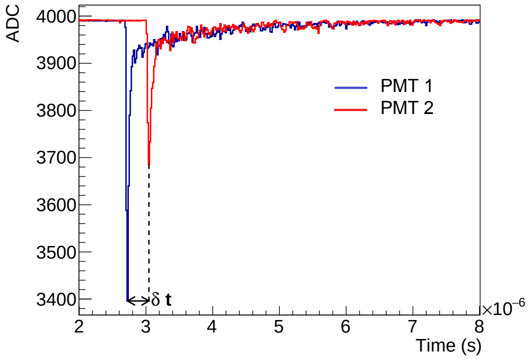

Figure 10.9: Example of two scintillation light waveforms of two PMTs for the same event. By comparing the timing of both S1 scintillation light signals, the relative timing accuracy among these two PMTs can be measured. S1 signal on the second PMT has been manually shifted to illustrate the example.

1. Once the baseline is measured, the sample with minimum value in the trigger range is taken. The S1 *Pulse* is found if this is more than 3 ADC counts with respect to the baseline.This amplitude is saved as the *Pulse Amplitude* and its time position as the *Maximum Peak Time*, shown as t_{max} on the left panel of Fig. 10.10.

2. The time where the baseline is first lost (within a 1 ADC count tolerance) is found by going backwards in the waveform. This is the *Pulse Start Time*, shown as t_{start} on the left panel of Fig. 10.10.

3. The time where the baseline is recovered (within 1 ADC count tolerance) is found by going forward in the waveform. If the baseline is not recovered, the end of the time window is considered. This is the *Pulse End Time*, shown as t_{end} on the left panel of Fig. 10.10.

4. The first time sample with signal is saved, meaning the first bin of the *Pulse* with a value >3 ADC counts with respect to the baseline. This is the *First Peak Time*, shown as t_{first} on the left panel of Fig. 10.10.

5. The *Pulse* is removed from the waveform by setting all bins of the pulse (from t_{start} to t_{end}) to the baseline value.

6. We go back to step 1 until no more *Pulses* are found.

With this algorithm definition, there will be some cases for which it is not possible to identify and separate different S1 signals. As shown on the right panel of Fig. 10.10, when two muons arrive very close in time, the baseline is not recovered between the two signals and they are identified as a single *Pulse*. However, they can be tagged by the large time difference between t_{max} and t_{first} (marked as A and D respectively on the right panel of Fig. 10.10).

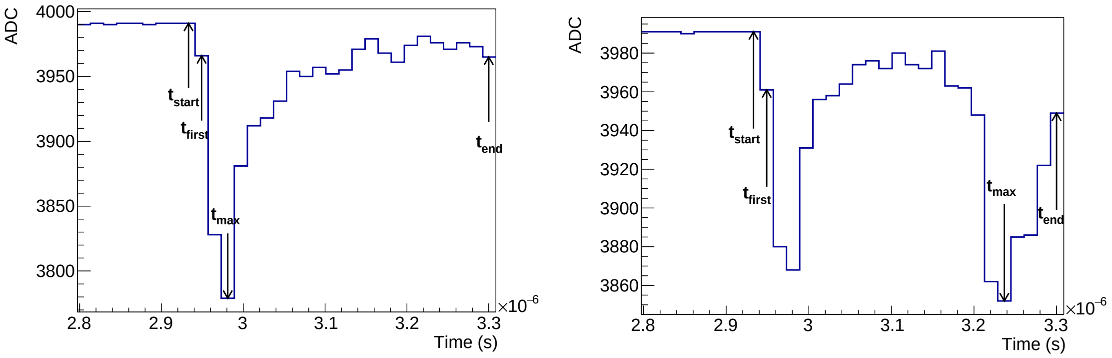

Figure 10.10: Left: Example of *Pulse* found in a waveform using the Pulse Finder algorithm. Definitions of t_{start}, t_{first}, t_{max} and t_{end} are provided in the text. Right: Example of a typical case where two S1 are not well identified. As two muons arrive close to each other in time, the baseline is not recovered in between and they are identified as a single *Pulse*.

10.3.4 Computation of δt

Once the *Pulse* finder is applied, a collection of *Pulses* is obtained in every waveform for each PMT. Starting with a simple approach, the t_{max} of the *Pulse* with maximum *Pulse Amplitude* in the waveform is compared with t_{max} of the *Pulse* with maximum *Pulse Amplitude* in the triggering channel to obtain a raw distribution of the δt:

$$\delta t = t_{max} - t_{max}^{trigger}. \tag{10.3}$$

Figure 10.11 shows this δt distribution for all channels. From figure 10.11 some observations can be made:

- Most of the δt values are around zero as expected.
- There is a flat contribution (uncorrelated with time) mainly at lower amplitudes. This is consistent with a background of muons in coincidence where δt is not correctly measured. An example of this type of events is shown in Fig. 10.12.
- There is an extra contribution at low amplitudes for positive δt (signals delayed with respect to the trigger), that looks like a tail after zero. An example of these events in the tail is shown in Fig. 10.13. The shape of the waveform does not look like a standard S1. The t_{max} of the signal appears retarded with respect to the beginning of

the signal, producing a larger δt's. Hypotheses about the origin of these events are explained in Sec. 10.3.5.

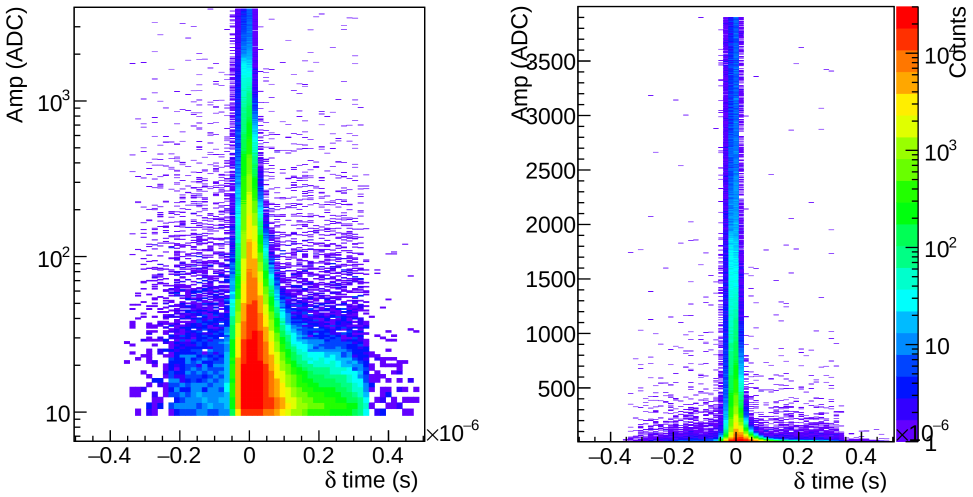

Figure 10.11: Distribution of raw δt (as defined in Eq. 10.3) versus the *Pulse Amplitude* for all PMTs. Signals saturating the ADC and with *Pulse Amplitude* below 10 ADC ($\sim$3 PE) have been removed to avoid dark counts. Linear (right) and logarithmic (left) plots are shown.

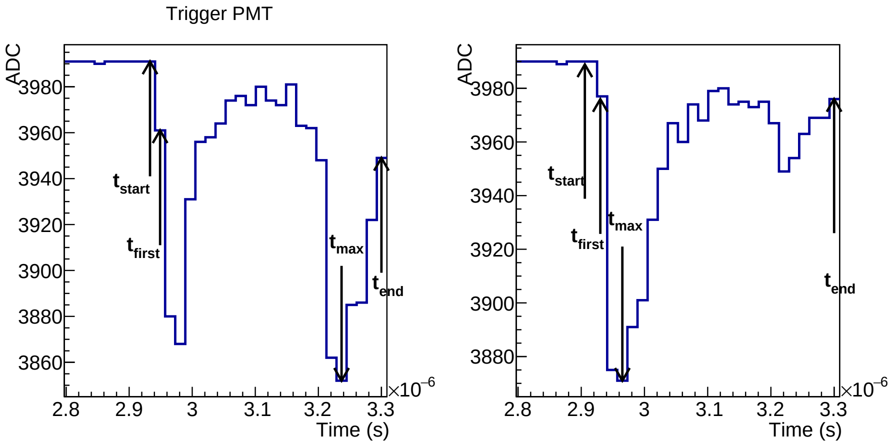

Figure 10.12: Example of an event with two muons in coincidence seen by two PMTs. We are triggering on the first muon, but the second provides a larger signal on the trigger PMT (left plot). If the t_{max} is considered in both PMTs, an unrealistically large δt will be obtained, because these are signals from different muons.

Seen the high level of events with muons in coincidence and with retarded light, δt must be recomputed to take them into account. This is done by computing δt in the following way:

- First, the reference time (t_0) is obtained in the trigger PMT: If several *Pulses* are found within the triggering PMT (channel 20) waveform, the one closer to the trigger

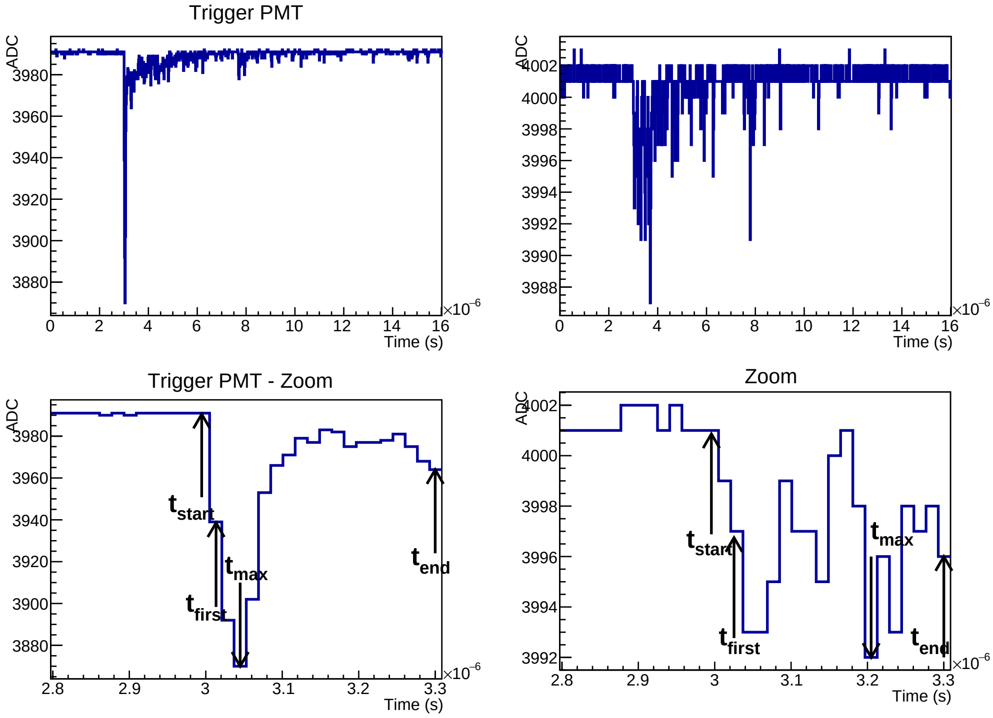

Figure 10.13: Example of a retarded light event producing a larger δt seen by two PMTs. The bottom panels show a zoom of the waveforms above around the trigger range. The waveform on the right shows an anomalous shape, being the t_{max} retarded with respect to the beginning of the signal. This is corrected in the algorithm by considering t_{first} instead.

time will be consider (instead of the larger in amplitude). For this *Pulse*, the distance between the t_{max} (A in Fig. 10.10) and the t_{first} (D) is required to be below 5 bins (80 ns). This allows to remove many of the overlapping muons (as in the right panel of Fig. 10.10), and the t_{max} is the t_0 to compare with the rest of the channels:

$$t_0 = t_{max}^{trigger};\ \text{if}(t_{max} - t_{first} < 80\text{ns}). \tag{10.4}$$

- Once identified the t_0 from the triggering channel, if many *Pulses* are found in the rest of the PMT channels, the *Pulse* closer in time to t_0 will be considered (instead of the larger in amplitude). Then δt will be computed considering the closest time to t_0 among the t_{max} and the t_{first}. This process corrects the bias introduced by the retarded light events, and avoiding additional distortions due to dark counts or photons arriving before the signal due to the single photo-electron background and to the slow component of muons crossing before the signal:

$$\delta t = \begin{cases} t_{max} - t_0 & \text{if} |t_{max} - t_0| < |t_{first} - t_0| \\ t_{first} - t_0 & \text{if} |t_{max} - t_0| > |t_{first} - t_0|. \end{cases} \tag{10.5}$$

Finally, the following selection criteria have been applied:

- Waveforms with an amplitude larger than 4000 ADC saturate the dynamic range of the DAQ and have not been considered. This represents only 0.1% of the data.
- Pulses with an amplitude below 10 ADC counts are rejected, to avoid considering the background of single photo-electrons. This removes around 3 – 30% of the events, being this cut larger for PEN PMTs, since they see on average less light than TPB PMTs.

10.3.5 Retarded light events

Waveforms with a particular shape, different from a standard S1, have been identified. Since they show the maximum of the signal retarded with respect to the beginning of the signal, as it is shown on figure 10.13, they are called *retarded light events*.

We can make two appreciations concerning these events:

- They have a relatively small amplitude. As it can be appreciated on the left panel of Fig. 10.11, the amplitude is smaller than 20 ADC counts for most of them.
- They are only observed by PEN PMTs, as we can see in Fig. 10.14. However, it is not clear if these retarded light events are specific to PEN PMTs, or they are directly related to the amount of light seen by the PMTs. TPB PMTs detect on average more light than PEN PMTs and the contribution of the retarded light might be masked by a prominent fast signal. As it can be seen in Fig. 10.14, the peak of the maximum of the distribution is around 100 ADC on TPB PMTs while for PEN PMTs is only around 20 ADC.

The hypotheses about the possible origin of these events are:

- A possible explanation is light produced from reflections of the primary light in the elements inside the cryostat, like the field cage or the cathode.
- Since retarded events are only seen on PEN PMTs, they might be related with the slower wavelength-shifting response of the PEN, as the measured τ_{int} is higher for PEN with respect to TPB (see Sec. 5.5).
- They might be caused by a small amount of Cherenkov photons arriving before the scintillation light, since photons in the visible range, as Cherenkov photons are, propagate faster than VUV light.

- Since retarded light events show up at low amplitudes, they might be caused by probability fluctuations when having just a few photons detected. Under this hypothesis, the limited amount of photons detected by the PMT does not allow the fast component to be seen but only the slow component. This is possible since the number of fast photons are only 30% of the slow photons (see Sec. 2.3).

Even though the origin of the retarded light events is not clear, the distortion that they introduce in the δt distribution is corrected by assuming that they are produced by the same energy deposition (or physics event), and taking t_{first} as the Pulse time as it is explained in Sec. 10.3.4.

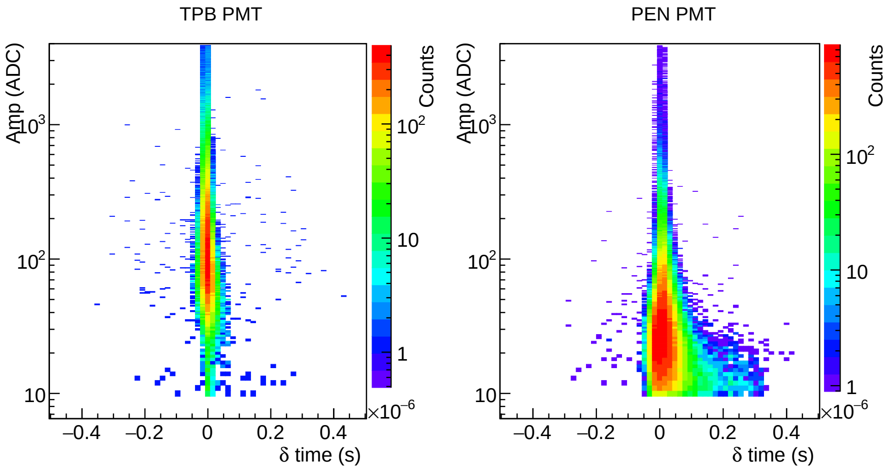

Figure 10.14: δt distribution for PEN (right) and TPB (left) PMTs. PEN PMTs show δt distribution different from TPB PMTs. Retarded light events are not detected by TPB-coated PMTs.

10.3.6 Resulting δt distributions

The distribution of δt versus the *Pulse Amplitude* for all PMTs is shown in Fig. 10.15. The amount of events out of the main peak around zero has been reduced. Only 0.13‰ of events show a negative δt below 64 ns (before the first black line in the figure). 0.6‰ of events show a positive δt above 64 ns (after the second black line in the figure). Two observations about Fig. 10.15 can be made:

- A small contribution of the uniform background (uncorrelated with time and of low amplitude) is still present. This is due to muons that are detected by the triggering PMT and not seen by the second PMT. However, the second one detects a secondary muon in the time coincidence. An example of this type of events is shown in Fig. 10.16.

- A small remnant of the retarded light tail is still present in the distribution. This is due to a few events with very low level of light, for which the S1 fast component is not detected and only some retarded photons (probably from the slow component) are detected. An example of this type of events is shown on figure 10.17.

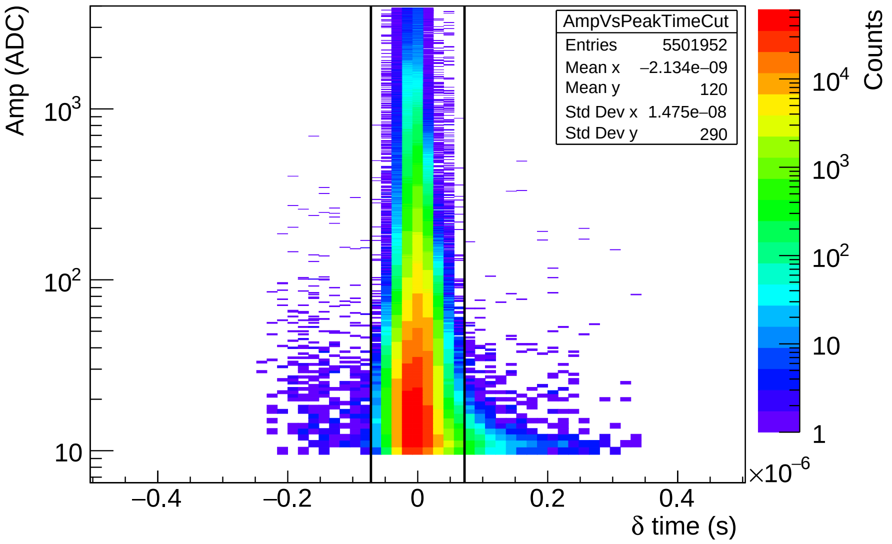

Figure 10.15: δt distribution vs *Pulse Amplitude*. Vertical lines are placed in ± 64 ns.

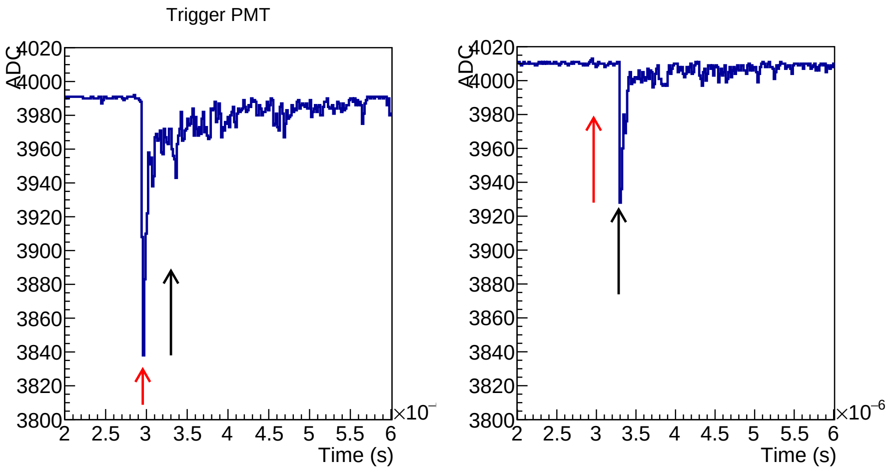

Figure 10.16: Example of event providing a large δt. Here the trigger signal is only seen in the triggering channel (left), and not seen in the secondary channel (right). Red arrow shows where the trigger signal is expected. Black arrow shows a second S1 signal.

10.3.7 Results and discussion

The distribution of δt is shown for two example PMTs on Fig.10.18. A TPB PMT is shown on the left panel and a PEN PMT in the right panel. All PMTs show a similar

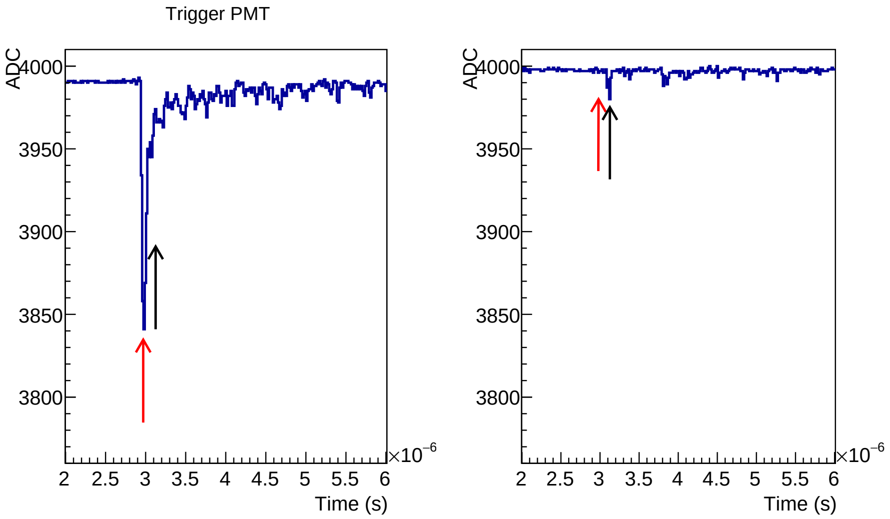

Figure 10.17: Example of event providing δt in the right tail in figure 10.15. Here the signal seen in the channel (right) is so small ($\sim$4 PEs), that probably only the slow component is seen and the S1 fast component is missed.

Gaussian distribution around zero.

A Gaussian fit is performed on every δt distribution to obtain the mean and width of the distribution around zero. Figure 10.19 shows the distribution of the δt mean and σ for all PMTs with respect to the reference PMT. The mean value of δt is -3 ± 3 ns and σ is 12 ± 2 ns. Both values are below the sampling time of the data acquisition system (16ns).

Therefore, the DUNE requirement of a relative timing accuracy among PMTs below 100 ns is fulfilled.

For completeness, the same study has been performed with a run taken triggering on CRT panels and considering as reference PMT a TPB PMT placed at the center of the detector. Results are consistent with the stated above, below the systematic uncertainty of 16 ns, showing a mean value of $\delta t = -8 \pm 4$ ns and $\sigma = 15 \pm 3$ ns.

10.4 Conclusions

The photon detection system in a LAr-TPC is an important subsystem in charge of providing the event time for non-beam events and contributing to the calorimetric reconstruction. In particular, there is a requirement for the Far Detectors of DUNE that the photon detection system must provide the event interaction time with 90% efficiency and 90% purity throughout the TPC active volume for proton decay signals.

The estimation of the time reconstruction efficiency and purity is performed using simulated samples of proton decay events in the channel $p \to K^+ + \bar{\nu}$ and radiological

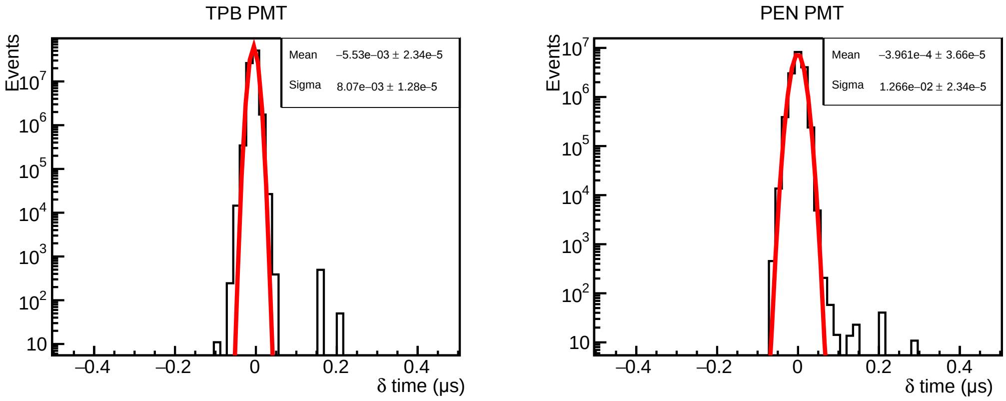

Figure 10.18: δt distribution for two example PMTs. A TPB PMT is shown on the left panel and a PEN PMTs on the right panel.

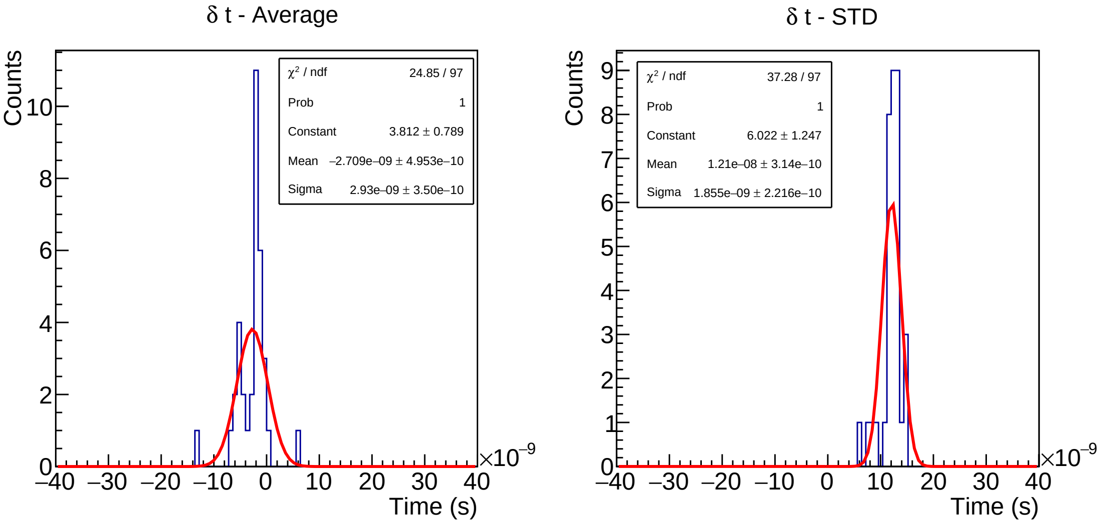

Figure 10.19: Average δt and σ distribution for all PMTs.

backgrounds. The light signals are reconstructed by looking at time and space correlations, grouping them in light flashes. Then the flashes are considered as event-time candidates if they are detected near the interaction point provided by the TPC. Thanks to the presence of reflective foils on the top-half part of the field cage (see Section 3.1.3), the DUNE Dual-Phase photon detection system is able to provide the event interaction time with an efficiency and purity above 90% in all the TPC active volume. 90% efficiency corresponds to the worst case, 12 m away from the cathode.

Since the event time reconstruction is performed by grouping light signals correlated in time and space, the time alignment among PMT signals must be better than 100 ns. Possible sources of timing misalignment among PMT signals are different signal-cable lengths or failures in the DAQ system. A study on the alignment in time of signals of every PMT with respect to a reference PMT has been performed using the data of ProtoDUNE

Dual-Phase. The time alignment has been estimated measuring the time difference per event between the signal in each PMT and in a reference PMT that was used as the trigger during the data taking. It has been shown that the time alignment achieved in the ProtoDUNE Dual-Phase photon detection system is below 16 ns, which is the sampling time of the system, fulfilling the requirements.

Conclusions

The Deep Underground Neutrino Experiment (DUNE) is the best-in-class neutrino experiment of the coming years. DUNE is a high precision long-baseline neutrino oscillation experiment, aiming at measuring the CP violation phase in the leptonic sector, to determine the neutrino mass ordering and to measure with very good precision all the oscillation parameters. It will also perform beyond standard model searches and detect supernova neutrinos if a galactic supernova collapse occurs during the detector operation. DUNE will consist of the most powerful neutrino beam in the world, a Near Detector placed downstream, and a Far Detector placed 1.5 km underground at 1,300 km from the beam source. To reach their physics goals, the DUNE collaboration is bringing the LAr-TPC technology to an unprecedented large scale, as they plan to build four 17 kton LAr-TPCs as Far Detector.

The construction and operation of the 750 ton ProtoDUNE Dual-Phase LAr-TPC during 2019 and 2020 is a milestone in the development of the LAr-TPC technology at the multi-ton scale. It is the largest Dual-Phase LAr-TPC ever constructed. The difficulties arising during the detector operation, such as the non-uniform electric drift field or the issues when extracting and amplifying the charge signal in the gas phase, have indicated that the technology is not yet mature to be implemented as a DUNE Far Detector module. Despite these problems, the ProtoDUNE Dual-Phase photon detection system based on PMTs has demonstrated excellent performance, detecting scintillation and even electroluminescence light signals more than six meters away from the PMTs, and taking data in stable conditions during the whole detector operation. The analysis of the ProtoDUNE Dual-Phase light data is the main object of this thesis. The time profile of the scintillation light has been characterized and monitored during the detector operation. The monitoring of the scintillation light provides valuable information, such as the liquid argon purity, which is critical in a LAr-TPC since electronegative impurities trap the ionization electrons, suppressing the signal. ProtoDUNE Dual-Phase light data have shown that the liquid argon purity remained stable during the full operation. The dependence of the scintillation light with the drift field is measured, and the electroluminescence light signals are also characterized. The light detection at a distance of more than six meters away represents the longest light detection distance in a LAr-TPC up to date, and it validates its design for larger detectors like the DUNE Far Detector modules.

A dedicated Monte Carlo simulation of the scintillation light production, propagation and detection has been developed. The simulation includes the scintillation light produced by the comic muons traversing the detector, and the low energy radioactivity present in natural argon. The simulation is validated with muon data with a well-known track geometry, triggered by two Comic Ray Taggers placed at the detector sides. Three key parameters rule the dependence of the detected light with the distance: the absorption length (λ_{Abs}), the Rayleigh scattering length (λ_{RS}), and the reflectivity of aluminum and stainless-steel elements inside the cryostat ($\mathrm{R_{Al\&SS}}$). The best agreement between data and simulation is found for a set of values of $\lambda_{RS} = 99\,\mathrm{cm}$, $\lambda_{Abs} = 20\,\mathrm{m}$ and $\mathrm{R_{Al\&SS}} = 27\%$. The obtained values are in agreement with the measurements in the literature, which ensures our well-understanding of the detector performance.

Once validated the simulation with single muons, the cosmic muon flux and the radiological backgrounds are simulated. The simulated cosmic-muon flux is based on the constant mass composition (CMC) model [236] and CORSIKA [1], and the simulated radiological backgrounds rely on the published radioactivity measurements. On the one hand, a 28% excess of the cosmic muon rate has been observed in the simulation when compared with data. However a similar excess in the model has been measured by other experiments, which points to an overestimation of the flux in the model. On the other hand, a significant excess of a factor of six on TPB PMTs and of a factor of three on PEN PMTs, of the background single photoelectron rate is measured in the data with respect to the simulation. This excess has been observed also by other experiments and it is not yet understood, although it might by related with a delayed recombination of Ar_2^+ ions. The understanding of this excess is critical, since it is directly related with the detector performance at low energies, which affects an important part of the DUNE physics program, such as the capability of detecting solar or supernova neutrinos. Further studies and dedicated measurements are desirable in order to understand this excess and its implications for the DUNE program.

Since scintillation light is produced at 127 nm, fluorescent materials are placed on the top of the PMTs to shift the photon wavelength to the visible range, at which the PMTs have maximal detection efficiency. ProtoDUNE Dual-Phase has thirty PMTs with a PEN foil on top, and six PMTs coated directly on the PMT glass. TPB is widely used as a wavelength shifter due to its high efficiency, however, its installation requires delicate work in dedicated coating setups. This is the reason to explore novel materials, such as PEN, a thermoplastic very stable and easy to install. ProtoDUNE Dual-Phase is the first detector using PEN as a wavelength-shifter at such a large scale. Using ProtoDUNE Dual-Phase data, the efficiency of PEN-foil PMTs with respect to the TPB-coated PMTs is measured for the first time: PEN-foil PMTs detect only 25% of the 127 nm photons detected by TPB-coated PMTs in liquid argon at 87K. By taking into account geometrical differences due to the position of the foil and the coating, the relative PEN/TPB wavelength-shifting efficiency of the material itself of $\varepsilon_{PEN}/\varepsilon_{TPB} = 0.33 \pm 0.05$ is estimated: TPB emits three times more visible photons than PEN for the same incident amount of VUV photons, in agreement with recent measurements found in the literature [248]. Additionally, the stability of both systems, PEN and TPB, is verified after more than one year of operation. This study has shown that PEN is a reliable wavelength shifter that can be considered as an alternative to TPB only when the detection efficiency is not critical, which is not the case for the DUNE detectors.

The use of xenon-doped liquid argon is a promising technique for large-scale detectors. Under the presence of xenon, the wavelength of part of the scintillation photons is quickly shifted to longer wavelengths. In this way, xenon doping mitigates the light suppression due to impurities and it also increases the collected light at long distances, improving the photon detection uniformity. ProtoDUNE Dual-Phase performed a full xenon-doping campaign, being the first time that xenon doping is tested at such a large scale in a monolithic detector. With a small doping level of 5.8 ppm of xenon, and even with the presence of 2.4 ppm of nitrogen, an enhancement in the light detection efficiency (100% increase for muons crossing at a distance of $3-5$ m from the PMTs) and a better detection uniformity (attenuation length 60% larger) are measured. However, a 35% reduction of the signal amplitude has been observed, which is attributed to the photo-absorption by xenon atoms. A model of the scintillation light production in the presence of xenon and nitrogen is proposed and analytically solved. The photon-production model is fitted using the time profile of the scintillation light obtained from the average PMT waveforms. The fit provides the time constants of each physics process, some of them are measured for the first time in this work. Furthermore, the proposed model allows to extrapolate the wavelength composition of the light produced at any xenon and nitrogen concentration. The proposed model has been also validated by comparing with a Monte-Carlo simulation including the effect of the photon propagation at different wavelengths. This is the most comprehensive study up to date of the light scintillation production and propagation mechanisms in xenon-doped liquid argon. The results of this study are used as an input for the design studies of the future xenon-doped based Vertical Drift Far Detector module of

DUNE.

The photon detection system is a critical part of any LAr-TPC, since it provides the interaction time for non-beam events, which is needed to reconstruct the tracks in three dimensions and to improve the particle identification capabilities. Therefore, it is a design requirement for the Far Detectors of DUNE that the photon detection system can provide the event interaction time with 90% efficiency and 90% purity throughout the TPC active volume for proton decay signals. A photon detection system based on TPB coated PMTs placed below the cathode, as in ProtoDUNE Dual-Phase but also including TPB-coated reflective foils, is proposed for a DUNE Far Detector module. Despite the fact that the TPC active volume in the proposed design would be a huge monolithic volume of 12 m x 12 m x 60 m , it is shown that the photon detection system would be able to provide the interaction time with 95% efficiency and 90% purity throughout the TPC active volume for proton decay signals.

In summary, thanks to its high precision technology and its large scale, DUNE promise to bring neutrino physics to a new era. A huge prototyping work done by the DUNE collaboration is making possible the construction of such a challenging experiment. This project is already a reality, since the construction has already started, and thrilling times are about to come in the near future, when the detector operation will start.

Conclusiones

El experimento DUNE (Deep Underground Neutrino Experiment) será el más potente experimento de su tipo de los próximos años. DUNE es un experimento de oscilación de neutrinos de alta precisión, que pretende medir la fase violación CP en el sector leptónico, determinar el orden de la masa de los neutrinos y medir con muy buena precisión todos los parámetros de oscilación. Además realizará búsquedas de física más allá del modelo estándar y detectará neutrinos de una supernova, si una supernova colapsara en la galaxia durante el funcionamiento del detector. DUNE consistirá en el haz de neutrinos más potente del mundo, un detector cercano situado a continuación, y un detector lejano instalado a bajo tierra a una profundidad de 1,5 km y a 1.300 km del haz. Para alcanzar sus objetivos de física, la colaboración DUNE está llevando la tecnología de las LAr-TPC a una escala enorme, ya que planean contruir cuatro LAr-TPC de 17 kilotoneladas como detector lejano.

La construcción y el funcionamiento de ProtoDUNE Dual-Phase, una LAr-TPC de 750 toneladas, durante 2019 y 2020 es un hito en el desarrollo de las LAr-TPC a la escala de centenares de toneladas. Es la LAr-TPC de doble fase más grande jamás construida. Las dificultades surgidas durante el funcionamiento del detector, como el campo eléctrico de deriva no uniforme o los problemas para extraer y amplificar la señal de carga a la fase gas indican que la tecnología no está lista para ser implementada como un módulo del detector lejano de DUNE. A pesar de estos problemas, el sistema de detección de fotones de ProtoDUNE Dual-Phase basado en PMTs ha mostrado un rendimiento excelente, detectando señales de luz de centelleo e incluso de electroluminiscencia producidas a más de seis metros de los PMTs, y tomando datos de forma estable durante todo el funcionamiento del detector. El análisis de los datos de ProtoDUNE Dual-Phase es el principal objetivo de esta tesis. El perfil temporal de la luz de centelleo ha sido caracterizado y monitorizado durante todo el funcionamiento del detector. La monitorización de la luz de centelleo proporciona información valiosa, como la pureza del argón líquido, que es crucial en una LAr-TPC dado que las impurezas electronegativas atrapan los electrones de ionización suprimiendo la señal. Los datos de ProtoDUNE Dual-Phase muestran que la pureza del argón líquido permaneció estable durante todo el funcionamiento del detector. Además, se ha medido la dependencia de la luz de centelleo con el campo de deriva, y se han caracterizado las señales producidas por la luz de electroluminiscencia. La detección de luz producida a una distancia de más de seis metros supone la mayor distancia de detección de luz en una LAr-TPC hasta la fecha, y valida el diseño del sistema de detección de fotones para diseños más grandes, como los módulos del detector lejano de DUNE.

Una simulación Monte Carlo dedicada de la producción, propagación y detección de luz ha sido desarrollada. La simulación incluye la luz de centelleo producida por los muones cósmicos que atraviesan el detector, y por la radioactividad de baja energía del argón natural. La simulación es validada con datos de muones con una trayectoria conocida, ya que han sido disparados por dos CRTs (Cosmic Ray Taggers) situados a los lados del detector. Tres parametros clave gobiernan la dependencia de la luz detectada con la distancia: la longitud de absorción (λ_{Abs}), la longitud de dispersión de Rayleigh (λ_{RS}) y la reflectividad de los elementos de aluminio y el acero inoxidable situados dentro del criostato ($\mathrm{R}_{\mathrm{Al\&SS}}$). El conjunto de valores de $\lambda_{RS} = 99\,\mathrm{cm}$, $\lambda_{Abs} = 20\,\mathrm{m}$ y $\mathrm{R}_{\mathrm{Al\&SS}} = 27\%$ proporcionan la mejor concordancia entre datos y simulación. Los valores obtenidos están así mismo en concordancia con otras medidas de la literatura, lo que asegura nuestra buena compresión del comportamiento del detector.

Una vez validada la simulación con muones individuales, se ha simulado el flujo de muones cósmicos y los fondos radiactivos. El flujo de muones cósmicos simulado está basado en el modelo CMC (Constant Mass Composition) [236] y CORSIKA [1], y los fondos radiactivos se basan en medidas publicadas de la radiactividad del argón. Por un lado, se observa un exceso del 28% en el ritmo de detección de muones simulado al compararlo con los datos. Sin embargo, un exceso similar ha sido observado en otros experimentos, lo que apunta a una sobreestimación del flujo de muones en el modelo. Por otro lado, se ha medido un exceso importante de un factor seis en los PMTs con TPB, y de un factor tres en los PMTs con PEN, del ritmo de detección del fondo de señales de un fotoelectrón en los datos con respecto a la simulación. Este exceso ha sido observado también por otros experimentos y no está entendido aún, aunque podría estar relacionada con la recombinación de iones Ar_2^+. La compresión de este exceso es clave, ya que está directamente relacionado con el rendimiento detector a bajas energias, lo que afecta a una parte importante de los objetivos de física de DUNE, como la capacidad de detectar neutrinos solares o procedentes de una supernova. Sería deseable la realización de estudios complementarios y de medidas dedicadas de radiactividad para entender este exceso y cómo afectaría a los planes de DUNE.

Debido que la luz de centelleo se produce a una longitud de onda de 127 nm, es necesario situar materiales fluorescentes sobre los PMTs para desplazar la longitud de onda al rango visible, en el cual los PMTs tienen eficiencia de detección máxima. ProtoDUNE Dual-Phase tiene treinta PMTs con una lámina de PEN situada encima de cada uno, y seis con TPB depositado directamente sobre el vidrio del PMT. El TPB es ampliamente usado debido a su alta eficiencia, sin embargo su instalación requiere de un trabajo delicado en complejos montajes de deposición. Por esta razón se exploran nuevos materiales, como el PEN, un termoplástico muy estable y sencillo de manejar. ProtoDUNE Dual-Phase es el primer detector en usar PEN a una escala tan grande. A través de los datos de ProtoDUNE Dual-Phase, la eficiencia de detección de un PMT con una lámina de PEN encima, con respecto a la de un PMT con TPB depositado se ha medido por primera vez. Los PMTs con PEN detectan solamente el 25% de los fotones detectados por los PMTs con TPB en argón líquido a una temperatura de 87K. Considerando diferencias geometricas debido a la posición del PEN y el TPB, se ha estimado una eficiencia relativa de conversión de fotones del PEN respecto al TPB de $\varepsilon_{PEN}/\varepsilon_{TPB} = 0.33 \pm 0.05$. Por lo tanto, el TPB emite tres veces más fotones visibles que el PEN para la misma cantidad de fotones incidentes de 127 nm, en concordancia con medidas recientes disponibles en la literatura. Este estudio muestra que el PEN es una alternativa confiable al TPB, pero solamente cuando la eficiencia de detección no es algo crítico, que no es el caso para los detectores de DUNE.

El uso de argón dopado con xenón es una técnica prometedora para detectores grandes. En presencia de xenón, la longitud de onda de parte de los fotones de centelleo es desplazada rápidamente a longitudes de onda más largas. De este modo, el dopaje con xenón mitiga la supresión de la luz debida a impurezas además de incrementar la detección de luz a distancias largas, mejorando la uniformidad de la detección de fotones. ProtoDUNE Dual-Phase llevó a cabo una iniciativa completa de dopaje con xenón, siendo la primera vez que se ensaya esta técnica en un detector monolítico a una escala tan grande. Con un nivel de dopaje de solamente 5.8 ppm (partes por millón) de xenón, e incluso la presencia de 2.4 ppm de nitrógeno, se ha medido una considerable mejora de la detección de luz (incremento del 100% para muones cruzando a una distancia de 3-5 m de los PMTs) y de la uniformidad de detección (una longitud atenuación un 60% mayor). Sin embargo, también se ha observado una reducción del 35% en la amplitud de la señal, lo que es atribuido a la absorción de fotones por los átomos de xenón. Se ha propuesto un modelo de la producción de luz de centelleo en argón liquido dopado con xenón y contaminado con nitrógeno, y se ha resulto analíticamente. El modelo de producción de fotones es ajustado usando el perfil temporal de la luz de centelleo obtenido al promediar las señales de los PMTs. El ajuste proporciona las contantes temporales de cada uno de los procesos físicos propuestos en el modelo. Alguna de estas constantes se ha medido por primera vez en este trabajo. Por otra parte, el modelo propuesto permite extrapolar la composición de la longitud de onda de la luz a cualquier concentración de xenón y nitrógeno. El modelo propuesto ha sido además validado comparando con una simulación Monte Carlo, incluyendo el efecto de la propagación de los fotones a diferentes longitudes de onda. Este es el estudio más detallado hasta la fecha de los mecanismos de producción y propagación de la luz de centelleo en argón líquido dopado con xenón. Así mismo, los resultados de este trabajo son una contribución valiosa para los estudios del diseño del futuro módulo del detector lejando de DUNE basado en argón dopado con xenón.

El sistema de detección de fotones es una parte crítica de una LAr-TPC, ya que proporciona el tiempo de interacción para eventos que no tienen origen en el haz. El tiempo de interacción es necesario para reconstruir las trazas en tres dimensiones y para mejorar la capacidad de identificar partículas del detector. Por lo tanto, es un requisito del detector lejano de DUNE que el sistema de detección de fotones proporcione el tiempo de interación del evento con una eficiencia del 90% y una pureza del 90% en cualquier parte del volumen activo de la TPC para eventos de decaimiento del protón. Se ha propuesto un sistema de detección de fotones para un módulo del detector lejano de DUNE. Este sistema está basado en PMTs con TPB depositado situados bajo el cátodo, como en ProtoDUNE Dual-Phase, pero también incluyendo láminas reflectantes recubiertas de TPB. A pesar de que el diseño propuesto supone un descomunal volumen monolítico de 12 m x 12 m x 60 m, se ha demostrado que el diseño propuesto sería capaz de proporcionar el tiempo de interacción con una eficiencia del 95% y una pureza del 90% en todo el volumen activo para señales del decaimiento del protón.

En resumen, gracias a su tecnología de alta precisión y su enorme tamaño, DUNE promete lleva a la física de neutrinos a una nueva era. Esto será posible gracias al enorme trabajo de prototipado realizado por la colaboración DUNE, que está haciendo posible la construción de un experimento tan exigente. Este proyecto es ya una realidad, dado que la contrucción del experimento ya ha comenzado. Así, un periodo emocionante para la comunidad de física de neutrinos está por arrancar en un futuro próximo, cuando el detector empiece a funcionar.

Bibliography

[1] D. Heck, J. Knapp, J. Capdevielle, G. Schatz, and T. Thouw. Corsika: A monte carlo code to simulate extensive air showers. Technical report, Institut für Kernphysik (IK), 1998. 51.02.03; LK 01; Wissenschaftliche Berichte, FZKA-6019 (February 98).

[2] W. Pauli. Dear radioactive ladies and gentlemen. *Phys. Today*, 31N9:27, 1978.

[3] J. Chadwick. The intensity distribution in the magnetic spectrum of beta particles from radium (B + C). *Verh. Phys. Gesell.*, 16:383–391, 1914.

[4] E. Fermi. An attempt of a theory of beta radiation. 1. *Z. Phys.*, 88:161–177, 1934.

[5] F. Reines and C. L. Cowan. Detection of the free neutrino. *Phys. Rev.*, 92:830–831, 1953.

[6] C. L. Cowan, F. Reines, F. B. Harrison, H. W. Kruse, and A. D. McGuire. Detection of the free neutrino: A Confirmation. *Science*, 124:103–104, 1956.

[7] C. Quigg. *Gauge Theories of the Strong, Weak, and Electromagnetic Interactions: Second Edition*. Princeton University Press, USA, 9 2013.

[8] M. E. Peskin and D. V. Schroeder. *An Introduction to quantum field theory*. Addison-Wesley, Reading, USA, 1995.

[9] D. H. Perkins. *Introduction to high energy physics*. CAMBRIDGE UNIVERSITY PRESS, 1982.

[10] P. W. Higgs. Broken Symmetries and the Masses of Gauge Bosons. *Phys. Rev. Lett.*, 13:508–509, 1964.

[11] P. Minkowski. $\mu \to e\gamma$ at a Rate of One Out of 10^9 Muon Decays? *Phys. Lett. B*, 67:421–428, 1977.

[12] M. Gell-Mann, P. Ramond, and R. Slansky. Complex Spinors and Unified Theories. *Conf. Proc. C*, 790927:315–321, 1979.

[13] R. N. Mohapatra and G. Senjanovic. Neutrino Mass and Spontaneous Parity Nonconservation. *Phys. Rev. Lett.*, 44:912, 1980.

[14] K. Zuber. *Neutrino Physics, Second Edition*. Series in High Energy Physics, Cosmology and Gravitation. Taylor & Francis, 2011.

[15] J. A. Formaggio, A. L. C. de Gouvêa, and R. H. Robertson. Direct measurements of neutrino mass. *Physics Reports*, 914:1–54, 2021. Direct measurements of neutrino mass.

[16] M. Aker et al. Improved upper limit on the neutrino mass from a direct kinematic method by katrin. *Phys. Rev. Lett.*, 123:221802, Nov 2019.

[17] W. H. Furry. On transition probabilities in double beta-disintegration. *Phys. Rev.*, 56:1184–1193, 1939.

[18] F. Boehm and P. Vogel. *Physics of massive neutrinos*. Cambridge Univ. Press, 1992.

[19] M. J. Dolinski, A. W. P. Poon, and W. Rodejohann. Neutrinoless Double-Beta Decay: Status and Prospects. *Ann. Rev. Nucl. Part. Sci.*, 69:219–251, 2019.

[20] A. Giuliani, J. J. Gomez Cadenas, S. Pascoli, E. Previtali, R. Saakyan, K. Schäffner, and S. Schönert. Double Beta Decay APPEC Committee Report. *arXiv*, 10 2019.

[21] S. Umehara et al. Neutrino-less double-beta decay of Ca-48 studied by Ca F(2)(Eu) scintillators. *Phys. Rev. C*, 78:058501, 2008.

[22] M. Agostini et al. Final Results of GERDA on the Search for Neutrinoless Double-β Decay. *Phys. Rev. Lett.*, 125(25):252502, 2020.

[23] S. I. Alvis et al. A Search for Neutrinoless Double-Beta Decay in ^{76}Ge with 26 kg-yr of Exposure from the MAJORANA DEMONSTRATOR. *Phys. Rev. C*, 100(2):025501, 2019.

[24] A. S. Barabash and V. B. Brudanin. Investigation of double beta decay with the NEMO-3 detector. *Phys. Atom. Nucl.*, 74:312–317, 2011.

[25] J. Argyriades et al. Measurement of the two neutrino double beta decay half-life of Zr-96 with the NEMO-3 detector. *Nucl. Phys. A*, 847:168–179, 2010.

[26] R. Arnold et al. Results of the search for neutrinoless double-β decay in ^{100}Mo with the NEMO-3 experiment. *Phys. Rev. D*, 92(7):072011, 2015.

[27] R. Arnold et al. Measurement of the $2\nu\beta\beta$ Decay Half-Life and Search for the $0\nu\beta\beta$ Decay of ^{116}Cd with the NEMO-3 Detector. *Phys. Rev. D*, 95(1):012007, 2017.

[28] D. Q. Adams et al. Improved Limit on Neutrinoless Double-Beta Decay in ^{130}Te with CUORE. *Phys. Rev. Lett.*, 124(12):122501, 2020.

[29] A. Gando et al. Search for Majorana Neutrinos near the Inverted Mass Hierarchy Region with KamLAND-Zen. *Phys. Rev. Lett.*, 117(8):082503, 2016. [Addendum: Phys.Rev.Lett. 117, 109903 (2016)].

[30] G. Anton et al. Search for Neutrinoless Double-β Decay with the Complete EXO-200 Dataset. *Phys. Rev. Lett.*, 123(16):161802, 2019.

[31] R. Arnold et al. Measurement of the $2\nu\beta\beta$ decay half-life of ^{150}Nd and a search for $0\nu\beta\beta$ decay processes with the full exposure from the NEMO-3 detector. *Phys. Rev. D*, 94(7):072003, 2016.

[32] N. Aghanim et al. Planck 2018 results. VI. Cosmological parameters. *Astron. Astrophys.*, 641:A6, 2020. [Erratum: Astron.Astrophys. 652, C4 (2021)].

[33] S. Alam et al. Completed SDSS-IV extended Baryon Oscillation Spectroscopic Survey: Cosmological implications from two decades of spectroscopic surveys at the Apache Point Observatory. *Phys. Rev. D*, 103(8):083533, 2021.

[34] M. M. Ivanov, M. Simonović, and M. Zaldarriaga. Cosmological Parameters and Neutrino Masses from the Final Planck and Full-Shape BOSS Data. *Phys. Rev. D*, 101(8):083504, 2020.

[35] K. Abazajian et al. CMB-S4 Decadal Survey APC White Paper. *Bull. Am. Astron. Soc.*, 51(7):209, 2019.

[36] B. Pontecorvo. Neutrino Experiments and the Problem of Conservation of Leptonic Charge. *Zh. Eksp. Teor. Fiz.*, 53:1717–1725, 1967.

[37] V. N. Gribov and B. Pontecorvo. Neutrino astronomy and lepton charge. *Phys. Lett. B*, 28:493, 1969.

[38] B. Pontecorvo. Mesonium and anti-mesonium. *Sov. Phys. JETP*, 6:429, 1957.

[39] G. Barenboim, J. F. Beacom, L. Borissov, and B. Kayser. CPT Violation and the Nature of Neutrinos. *Phys. Lett. B*, 537:227–232, 2002.

[40] G. Barenboim and J. D. Lykken. A Model of CPT Violation for Neutrinos. *Phys. Lett. B*, 554:73–80, 2003.

[41] G. Barenboim. Neutrino Physics. In *2012 European School of High-Energy Physics*, pages 161–179, 2014.

[42] P. A. Zyla et al. Review of Particle Physics. *PTEP*, 2020(8):083C01, 2020.

[43] S. P. Mikheev and A. Y. Smirnov. Resonant amplification of neutrino oscillations in matter and solar neutrino spectroscopy. *Nuovo Cim. C*, 9:17–26, 1986.

[44] L. Wolfenstein. Neutrino Oscillations in Matter. *Phys. Rev. D*, 17:2369–2374, 1978.

[45] S. P. Mikheyev and A. Y. Smirnov. Resonance Amplification of Oscillations in Matter and Spectroscopy of Solar Neutrinos. *Sov. J. Nucl. Phys.*, 42:913–917, 1985.

[46] S. P. Mikheev and A. Y. Smirnov. Neutrino Oscillations in a Variable Density Medium and Neutrino Bursts Due to the Gravitational Collapse of Stars. *Sov. Phys. JETP*, 64:4–7, 1986.

[47] H. Nunokawa, S. Parke, and J. W. Valle. Cp violation and neutrino oscillations. *Progress in Particle and Nuclear Physics*, 60(2):338–402, 2008.

[48] J. N. Bahcall, W. F. Huebner, S. H. Lubow, P. D. Parker, and R. K. Ulrich. Standard Solar Models and the Uncertainties in Predicted Capture Rates of Solar Neutrinos. *Rev. Mod. Phys.*, 54:767, 1982.

[49] J. N. Bahcall, A. M. Serenelli, and S. Basu. New solar opacities, abundances, helioseismology, and neutrino fluxes. *Astrophys. J. Lett.*, 621:L85–L88, 2005.

[50] A. M. Serenelli, W. C. Haxton, and C. Pena-Garay. Solar models with accretion. I. Application to the solar abundance problem. *Astrophys. J.*, 743:24, 2011.

[51] A. Serenelli. Alive and well: a short review about standard solar models. *Eur. Phys. J. A*, 52(4):78, 2016.

[52] B. T. Cleveland, T. Daily, R. Davis, Jr., J. R. Distel, K. Lande, C. K. Lee, P. S. Wildenhain, and J. Ullman. Measurement of the solar electron neutrino flux with the Homestake chlorine detector. *Astrophys. J.*, 496:505–526, 1998.

[53] C. Pena-Garay and A. Serenelli. Solar neutrinos and the solar composition problem. *arXiv preprint arXiv:0811.2424*, 11 2008.

[54] P. Anselmann et al. Solar neutrinos observed by GALLEX at Gran Sasso. *Phys. Lett. B*, 285:376–389, 1992.

[55] W. Hampel et al. GALLEX solar neutrino observations: Results for GALLEX IV. *Phys. Lett. B*, 447:127–133, 1999.

[56] M. Altmann et al. Complete results for five years of GNO solar neutrino observations. *Phys. Lett. B*, 616:174–190, 2005.

[57] V. N. Gavrin. Solar neutrino results from SAGE. *Nucl. Phys. B Proc. Suppl.*, 91:36–43, 2001.

[58] J. N. Abdurashitov et al. Measurement of the solar neutrino capture rate with gallium metal. III: Results for the 2002–2007 data-taking period. *Phys. Rev. C*, 80:015807, 2009.

[59] K. S. Hirata et al. Observation of B-8 Solar Neutrinos in the Kamiokande-II Detector. *Phys. Rev. Lett.*, 63:16, 1989.

[60] K. S. Hirata et al. Real time, directional measurement of B-8 solar neutrinos in the Kamiokande-II detector. *Phys. Rev. D*, 44:2241, 1991. [Erratum: Phys.Rev.D 45, 2170 (1992)].

[61] Y. Fukuda et al. Solar neutrino data covering solar cycle 22. *Phys. Rev. Lett.*, 77:1683–1686, 1996.

[62] Y. Fukuda et al. Measurements of the solar neutrino flux from Super-Kamiokande's first 300 days. *Phys. Rev. Lett.*, 81:1158–1162, 1998. [Erratum: Phys.Rev.Lett. 81, 4279 (1998)].

[63] Y. Fukuda et al. Measurement of the solar neutrino energy spectrum using neutrino electron scattering. *Phys. Rev. Lett.*, 82:2430–2434, 1999.

[64] J. Boger et al. The Sudbury neutrino observatory. *Nucl. Instrum. Meth. A*, 449:172–207, 2000.

[65] C. Arpesella et al. First real time detection of Be-7 solar neutrinos by Borexino. *Phys. Lett. B*, 658:101–108, 2008.

[66] G. Bellini et al. First evidence of pep solar neutrinos by direct detection in Borexino. *Phys. Rev. Lett.*, 108:051302, 2012.

[67] M. Agostini et al. Comprehensive measurement of *pp*-chain solar neutrinos. *Nature*, 562(7728):505–510, 2018.

[68] G. Bellini et al. Measurement of the solar 8B neutrino rate with a liquid scintillator target and 3 MeV energy threshold in the Borexino detector. *Phys. Rev. D*, 82:033006, 2010.

[69] K. S. Hirata et al. Experimental Study of the Atmospheric Neutrino Flux. *Phys. Lett. B*, 205:416, 1988.

[70] Y. Fukuda et al. Evidence for oscillation of atmospheric neutrinos. *Phys. Rev. Lett.*, 81:1562–1567, 1998.

[71] D. Casper et al. Measurement of atmospheric neutrino composition with IMB-3. *Phys. Rev. Lett.*, 66:2561–2564, 1991.

[72] K. Daum et al. Determination of the atmospheric neutrino spectra with the Frejus detector. *Z. Phys. C*, 66:417–428, 1995.

[73] M. Aglietta et al. Experimental study of atmospheric neutrino flux in the NUSEX experiment. *Europhys. Lett.*, 8:611–614, 1989.

[74] Z. Li et al. Measurement of the tau neutrino cross section in atmospheric neutrino oscillations with Super-Kamiokande. *Phys. Rev. D*, 98(5):052006, 2018.

[75] M. G. Aartsen et al. Measurement of Atmospheric Tau Neutrino Appearance with IceCube DeepCore. *Phys. Rev. D*, 99(3):032007, 2019.

[76] S. E. Kopp. Accelerator-based neutrino beams. *Phys. Rept.*, 439:101–159, 2007.

[77] S. H. Ahn et al. Detection of accelerator produced neutrinos at a distance of 250-km. *Phys. Lett. B*, 511:178–184, 2001.

[78] M. H. Ahn et al. Measurement of Neutrino Oscillation by the K2K Experiment. *Phys. Rev. D*, 74:072003, 2006.

[79] P. Adamson et al. Measurement of Neutrino and Antineutrino Oscillations Using Beam and Atmospheric Data in MINOS. *Phys. Rev. Lett.*, 110(25):251801, 2013.

[80] P. Adamson et al. Combined analysis of ν_μ disappearance and $\nu_\mu \to \nu_e$ appearance in MINOS using accelerator and atmospheric neutrinos. *Phys. Rev. Lett.*, 112:191801, 2014.

[81] P. Adamson et al. The NuMI Neutrino Beam. *Nucl. Instrum. Meth. A*, 806:279–306, 2016.

[82] C. Rubbia et al. Underground operation of the ICARUS T600 LAr-TPC: first results. *JINST*, 6:P07011, 2011.

[83] N. Agafonova et al. Final Results of the OPERA Experiment on ν_τ Appearance in the CNGS Neutrino Beam. *Phys. Rev. Lett.*, 120(21):211801, 2018. [Erratum: Phys.Rev.Lett. 121, 139901 (2018)].

[84] M. G. Catanesi. T2K Results and Perspectives. *Nucl. Phys. B Proc. Suppl.*, 237-238:129–134, 2013.

[85] K. Abe et al. Observation of Electron Neutrino Appearance in a Muon Neutrino Beam. *Phys. Rev. Lett.*, 112:061802, 2014.

[86] P. Adamson et al. First measurement of electron neutrino appearance in NOvA. *Phys. Rev. Lett.*, 116(15):151806, 2016.

[87] C. Giganti, S. Lavignac, and M. Zito. Neutrino oscillations: The rise of the PMNS paradigm. *Prog. Part. Nucl. Phys.*, 98:1–54, 2018.

[88] M. A. Acero et al. First Measurement of Neutrino Oscillation Parameters using Neutrinos and Antineutrinos by NOvA. *Phys. Rev. Lett.*, 123(15):151803, 2019.

[89] A. Aguilar-Arevalo et al. Evidence for neutrino oscillations from the observation of $\bar{\nu}_e$ appearance in a $\bar{\nu}_\mu$ beam. *Phys. Rev. D*, 64:112007, 2001.

[90] B. Armbruster et al. Upper limits for neutrino oscillations muon-anti-neutrino —> electron-anti-neutrino from muon decay at rest. *Phys. Rev. D*, 65:112001, 2002.

[91] A. A. Aguilar-Arevalo et al. Updated MiniBooNE neutrino oscillation results with increased data and new background studies. *Phys. Rev. D*, 103(5):052002, 2021.

[92] S. Ajimura et al. Technical Design Report (TDR): Searching for a Sterile Neutrino at J-PARC MLF (E56, JSNS2). *arXiv*, 5 2017.

[93] M. Antonello et al. A Proposal for a Three Detector Short-Baseline Neutrino Oscillation Program in the Fermilab Booster Neutrino Beam. *arXiv*, 3 2015.

[94] M. Apollonio et al. Search for neutrino oscillations on a long baseline at the CHOOZ nuclear power station. *Eur. Phys. J. C*, 27:331–374, 2003.

[95] F. Boehm et al. Final results from the Palo Verde neutrino oscillation experiment. *Phys. Rev. D*, 64:112001, 2001.

[96] L. Hsu. Review of experimental data: KamLAND. *Nucl. Phys. B Proc. Suppl.*, 155:158–159, 2006.

[97] F. Ardellier et al. Double Chooz: A Search for the neutrino mixing angle θ_{13}. *arXiv*, 6 2006.

[98] D. B. Collaboration. A precision measurement of the neutrino mixing angle θ_{13} using reactor antineutrinos at daya bay, 2007.

[99] R. Collaboration and J. K. Ahn. Reno: An experiment for neutrino oscillation parameter θ_{13} using reactor neutrinos at yonggwang, 2010.

[100] Y. Abe et al. Indication of Reactor $\bar{\nu}_e$ Disappearance in the Double Chooz Experiment. *Phys. Rev. Lett.*, 108:131801, 2012.

[101] F. P. An et al. Observation of electron-antineutrino disappearance at Daya Bay. *Phys. Rev. Lett.*, 108:171803, 2012.

[102] J. K. Ahn et al. Observation of Reactor Electron Antineutrino Disappearance in the RENO Experiment. *Phys. Rev. Lett.*, 108:191802, 2012.

[103] Y. J. Ko et al. Sterile Neutrino Search at the NEOS Experiment. *Phys. Rev. Lett.*, 118(12):121802, 2017.

[104] J. Ashenfelter et al. First search for short-baseline neutrino oscillations at HFIR with PROSPECT. *Phys. Rev. Lett.*, 121(25):251802, 2018.

[105] I. Alekseev et al. Search for sterile neutrinos at the DANSS experiment. *Phys. Lett. B*, 787:56–63, 2018.

[106] H. Almazán et al. Sterile Neutrino Constraints from the STEREO Experiment with 66 Days of Reactor-On Data. *Phys. Rev. Lett.*, 121(16):161801, 2018.

[107] A. P. Serebrov et al. First Observation of the Oscillation Effect in the Neutrino-4 Experiment on the Search for the Sterile Neutrino. *Pisma Zh. Eksp. Teor. Fiz.*, 109(4):209–218, 2019.

[108] Y. Abreu et al. A novel segmented-scintillator antineutrino detector. *JINST*, 12(04):P04024, 2017.

[109] B. Aharmim et al. Electron energy spectra, fluxes, and day-night asymmetries of B-8 solar neutrinos from measurements with NaCl dissolved in the heavy-water detector at the Sudbury Neutrino Observatory. *Phys. Rev. C*, 72:055502, 2005.

[110] K. Abe et al. Precise Measurement of the Neutrino Mixing Parameter θ_{23} from Muon Neutrino Disappearance in an Off-Axis Beam. *Phys. Rev. Lett.*, 112(18):181801, 2014.

[111] K. Abe et al. Indication of Electron Neutrino Appearance from an Accelerator-produced Off-axis Muon Neutrino Beam. *Phys. Rev. Lett.*, 107:041801, 2011.

[112] K. Abe et al. Constraint on the matter–antimatter symmetry-violating phase in neutrino oscillations. *Nature*, 580(7803):339–344, 2020. [Erratum: Nature 583, E16 (2020)].

[113] K. Abe et al. Improved constraints on neutrino mixing from the T2K experiment with $\mathbf{3.13 \times 10^{21}}$ protons on target. *Phys. Rev. D*, 103(11):112008, 2021.

[114] P. F. De Salas, S. Gariazzo, O. Mena, C. A. Ternes, and M. Tórtola. Neutrino Mass Ordering from Oscillations and Beyond: 2018 Status and Future Prospects. *Front. Astron. Space Sci.*, 5:36, 2018.

[115] K. Abe et al. Hyper-Kamiokande Design Report. *arXiv*, 5 2018.

[116] B. Abi et al. Deep Underground Neutrino Experiment (DUNE), Far Detector Technical Design Report, Volume I Introduction to DUNE. *JINST*, 15(08):T08008, 2020.

[117] B. Abi et al. Deep Underground Neutrino Experiment (DUNE), Far Detector Technical Design Report, Volume II: DUNE Physics. *arXiv*, 2 2020.

[118] B. Abi et al. Deep Underground Neutrino Experiment (DUNE), Far Detector Technical Design Report, Volume III: DUNE Far Detector Technical Coordination. *Journal of Instrumentation*, 15(08):T08009, 2020.

[119] B. Abi et al. Deep Underground Neutrino Experiment (DUNE), Far Detector Technical Design Report, Volume IV: Far Detector Single-phase Technology. *Journal of Instrumentation*, 15(08):T08010, 2020.

[120] B. Abi et al. Long-baseline neutrino oscillation physics potential of the DUNE experiment. *Eur. Phys. J. C*, 80(10):978, 2020.

[121] S. Adrian-Martinez et al. Letter of intent for KM3NeT 2.0. *J. Phys. G*, 43(8):084001, 2016.

[122] M. G. Aartsen et al. PINGU: A Vision for Neutrino and Particle Physics at the South Pole. *J. Phys. G*, 44(5):054006, 2017.

[123] M. A. Acero et al. An Improved Measurement of Neutrino Oscillation Parameters by the NOvA Experiment. *arXiv preprint arXiv:2108.08219*, 8 2021.

[124] A. A. Aguilar-Arevalo et al. Improved Search for $\bar{\nu}_\mu \to \bar{\nu}_e$ Oscillations in the MiniBooNE Experiment. *Phys. Rev. Lett.*, 110:161801, 2013.

[125] P. Abratenko et al. Search for an Excess of Electron Neutrino Interactions in MicroBooNE Using Multiple Final State Topologies. *arXiv*, 10 2021.

[126] M. A. Acero, C. Giunti, and M. Laveder. Limits on nu(e) and anti-nu(e) disappearance from Gallium and reactor experiments. *Phys. Rev. D*, 78:073009, 2008.

[127] C. Giunti and M. Laveder. Statistical Significance of the Gallium Anomaly. *Phys. Rev. C*, 83:065504, 2011.

[128] T. A. Mueller et al. Improved Predictions of Reactor Antineutrino Spectra. *Phys. Rev. C*, 83:054615, 2011.

[129] P. Huber. On the determination of anti-neutrino spectra from nuclear reactors. *Phys. Rev. C*, 84:024617, 2011. [Erratum: Phys.Rev.C 85, 029901 (2012)].

[130] G. Mention, M. Fechner, T. Lasserre, T. A. Mueller, D. Lhuillier, M. Cribier, and A. Letourneau. The Reactor Antineutrino Anomaly. *Phys. Rev. D*, 83:073006, 2011.

[131] J. N. Marx and D. R. Nygren. The time projection chamber. *Physics Today*, 31(10):46–53, 1978.

[132] C. F. Lastoria. *Analysis of the scintillation light production and propagation in the WA105 Dual-Phase demonstrator*. PhD thesis, Universidad Complutense de Madrid, 2021.

[133] C. Rubbia. The liquid-argon time projection chamber: a new concept for neutrino detectors. Technical report, CERN, Geneva, 1977.

[134] I. De Bonis et al. Technical Design Report for large-scale neutrino detectors prototyping and phased performance assessment in view of a long-baseline oscillation experiment. Technical report, CERN, Apr 2014. Comments: 217 pages, 164 figures, LBNO-DEMO (CERN WA105) Collaboration.

[135] V. Atrazhev and I. Timoshkin. Transport of electrons in atomic liquids in high electric fields. *IEEE Transactions on Dielectrics and Electrical Insulation*, 5(3):450–457, 1998.

[136] S. Amerio et al. Design, construction and tests of the ICARUS T600 detector. *Nucl. Instrum. Meth. A*, 527:329–410, 2004.

[137] A. M. Szelc. The ArgoNeuT Experiment. *AIP Conf. Proc.*, 1663(1):020004, 2015.

[138] R. Acciarri et al. The Liquid Argon In A Testbeam (LArIAT) Experiment. *JINST*, 15(04):P04026, 2020.

[139] S. Tufanli. The SBND experiment. *PoS*, HQL2016:070, 2017.

[140] C. Shalem, R. Chechik, A. Breskin, and K. Michaeli. Advances in thick gem-like gaseous electron multipliers—part i: atmospheric pressure operation. *Nuclear Instruments and Methods in Physics Research Section A: Accelerators, Spectrometers, Detectors and Associated Equipment*, 558(2):475–489, 2006.

[141] R. Chechik, A. Breskin, C. Shalem, and D. Mörmann. Thick gem-like hole multipliers: properties and possible applications. *Nuclear Instruments and Methods in Physics Research Section A: Accelerators, Spectrometers, Detectors and Associated Equipment*, 535(1):303–308, 2004. Proceedings of the 10th International Vienna Conference on Instrumentation.

[142] A. Buzulutskov. Advances in Cryogenic Avalanche Detectors (review). *JINST*, 7:C02025, 2012.

[143] B. Aimard et al. A 4 tonne demonstrator for large-scale dual-phase liquid argon time projection chambers. *Journal of Instrumentation*, 13(11):P11003–P11003, nov 2018.

[144] B. Aimard et al. Performance study of a 3×1×1 m3 dual phase liquid Argon Time Projection Chamber exposed to cosmic rays. *JINST*, 16(08):P08063, 2021.

[145] A. Marchionni et al. ArDM: a ton-scale LAr detector for direct Dark Matter searches. *J. Phys. Conf. Ser.*, 308:012006, 2011.

[146] E. Aprile et al. The XENON100 Dark Matter Experiment. *Astropart. Phys.*, 35:573–590, 2012.

[147] D. S. Akerib et al. The Large Underground Xenon (LUX) Experiment. *Nucl. Instrum. Meth. A*, 704:111–126, 2013.

[148] T. Doke, A. Hitachi, J. Kikuchi, K. Masuda, H. Okada, and E. Shibamura. Absolute Scintillation Yields in Liquid Argon and Xenon for Various Particles. *Jap. J. Appl. Phys.*, 41:1538–1545, 2002.

[149] L. Onsager. Initial Recombination of Ions. *Phys. Rev.*, 54:554–557, 1938.

[150] J. Thomas and D. A. Imel. Recombination of electron-ion pairs in liquid argon and liquid xenon. *Phys. Rev. A*, 36:614–616, 1987.

[151] S. Amoruso et al. Study of electron recombination in liquid argon with the ICARUS TPC. *Nucl. Instrum. Meth. A*, 523:275–286, 2004.

[152] A. Badertscher et al. First operation and drift field performance of a large area double phase LAr Electron Multiplier Time Projection Chamber with an immersed Greinacher high-voltage multiplier. *JINST*, 7:P08026, 2012.

[153] W. Walkowiak. Drift velocity of free electrons in liquid argon. *Nucl. Instrum. Meth. A*, 449:288–294, 2000.

[154] S. Amoruso et al. Analysis of the liquid argon purity in the ICARUS T600 TPC. *Nucl. Instrum. Meth. A*, 516:68–79, 2004.

[155] E. Buckley et al. A Study of Ionization Electrons Drifting Over Large Distances in Liquid Argon. *Nucl. Instrum. Meth. A*, 275:364–372, 1989.

[156] Y. Li et al. Measurement of Longitudinal Electron Diffusion in Liquid Argon. *Nucl. Instrum. Meth. A*, 816:160–170, 2016.

[157] A. Einstein. Über die von der molekularkinetischen theorie der wärme geforderte bewegung von in ruhenden flüssigkeiten suspendierten teilchen. *Annalen der Physik*, 322(8):549–560, 1905.

[158] L. Agostino et al. LBNO-DEMO: Large-scale neutrino detector demonstrators for phased performance assesment in view of a long-baseline oscillation experiment, CERN-SPSC-2014-013, SPSC-TDR-004. Technical report, CERN, 2014.

[159] J. Lekner. Motion of electrons in liquid argon. *Phys. Rev.*, 158:130–137, Jun 1967.

[160] P. Agnes et al. Electroluminescence pulse shape and electron diffusion in liquid argon measured in a dual-phase TPC. *Nucl. Instrum. Meth. A*, 904:23–34, 2018.

[161] R. Andrews, W. Jaskierny, H. Jostlein, C. Kendziora, S. Pordes, and T. Tope. A system to test the effects of materials on the electron drift lifetime in liquid argon and observations on the effect of water. *Nucl. Instrum. Meth. A*, 608:251–258, 2009.

[162] A. Hitachi et al. Effect of ionization density on the time dependence of luminescence from liquid argon and xenon. *Phys. Rev. B*, 27:5279–5285, 1983.

[163] T. Doke, K. Masuda, and E. Shibamura. Estimation of absolute photon yields in liquid argon and xenon for relativistic (1 MeV) electrons. *Nucl. Instrum. Meth. A*, 291:617–620, 1990.

[164] T. Heindl et al. The scintillation of liquid argon. *EPL*, 91(6):62002, 2010.

[165] S. Kubota et al. Dynamical behavior of free electrons in the recombination process in liquid argon, krypton, and xenon. *Phys. Rev. B*, 20:3486, 1979.

[166] R. Acciarri et al. Effect of the nitrogen and oxygen contamination in liquid argon. *Nuc. Phys. B - Proc. Supp.*, 197:70, 2009.

[167] C. M. B. Monteiro, J. A. M. Lopes, J. F. C. A. Veloso, and J. M. F. dos Santos. Secondary scintillation yield in pure argon. *Phys. Lett. B*, 668:167–170, 2008.

[168] V. Chepel and H. Araujo. Liquid noble gas detectors for low energy particle physics. *JINST*, 8:R04001, 2013.

[169] T. Lux. Charge and Light Production in the Charge Readout System of a Dual Phase LAr TPC. *JINST*, 14(03):P03006, 2019.

[170] L. R. F.R.S. Xxxiv. on the transmission of light through an atmosphere containing small particles in suspension, and on the origin of the blue of the sky. *The London, Edinburgh, and Dublin Philosophical Magazine and Journal of Science*, 47(287):375–384, 1899.

[171] N. Ishida et al. Attenuation length measurements of scintillation light in liquid rare gases and their mixture using improved reflection suppresser. *NIM A*, 384:380, 1997.

[172] J. Calvo et al. Measurement of the attenuation length of argon scintillation light in the ArDM LAr TPC. *Astropart. Phys.*, 97:186–196, 2018.

[173] M. Babicz et al. A measurement of the group velocity of scintillation light in liquid argon. *JINST*, 15(09):P09009, 2020.

[174] E. Grace et al. Index of refraction, rayleigh scattering length and sellmeier coefficients in solid and liquid argon and xenon. *NIM A*, 867:204, 2017.

[175] G. Seidel et al. Rayleigh scattering in rare-gas liquids. *NIM A*, 489:189, 2002.

[176] B. J. P. Jones et al. A measurement of the absorption of liquid argon scintillation light by dissolved nitrogen at the part-per-million level. *JINST*, 8(07):P07011–P07011, jul 2013.

[177] M. Spanu, A. Falcone, R. Mazza, A. Menegolli, M. C. Prata, G. L. Raselli, M. Rossella, and M. Torti. Study on TPB as wavelength shifter for the new ICARUS t600 light collection system in the SBN program. *Journal of Physics: Conference Series*, 956:012016, jan 2018.

[178] S. F. Pate, T. Wester, L. Bugel, J. Conrad, E. Henderson, B. J. P. Jones, A. I. L. McLean, J. S. Moon, M. Toups, and T. Wongjirad. A Model for the Global Quantum Efficiency for a TPB-Based Wavelength-Shifting System used with Photomultiplier Tubes in Liquid Argon in MicroBooNE. *JINST*, 13(02):P02034, 2018.

[179] D. Garcia-Gamez. Developing Scintillation Light Readout Simulation for the SBND experiment. *JINST*, 11(01):C01080, 2016.

[180] J. R. Graybill, C. B. Shahi, M. A. Coplan, A. K. Thompson, R. E. Vest, and C. W. Clark. Extreme ultraviolet photon conversion efficiency of tetraphenyl butadiene. *Appl. Opt.*, 59(4):1217–1224, Feb 2020.

[181] M. Bonesini, T. Cervi, A. Falcone, U. Kose, R. Mazza, A. Menegolli, C. Montanari, M. Nessi, M. Prata, A. Rappoldi, G. Raselli, M. Rossella, M. Spanu, M. Torti, W. Vollenberg, and A. Zani. An innovative technique for TPB deposition on convex window photomultiplier tubes. *Journal of Instrumentation*, 13(12):P12020–P12020, dec 2018.

[182] J. Asaadi, B. J. P. Jones, A. Tripathi, I. Parmaksiz, H. Sullivan, and Z. G. R. Williams. Emanation and bulk fluorescence in liquid argon from tetraphenyl butadiene wavelength shifting coatings. *JINST*, 14(02):P02021, 2019.

[183] D.Mary et al. Understanding optical emissions from electrically stressed insulating polymers: electroluminescence in poly(ethylene terephthalate) and poly(ethylene 2,6-naphthalate) films. *J. Phys. D: Appl. Phys.*, 30:171, 1997.

[184] M. e. a. Kuźniak. Polyethylene naphthalate film as a wavelength shifter in liquid argon detectors. *Eur. Phys. J. C*, 79:291, 2019.

[185] C. Brizzolari and S. others. Enhancement of the x-arapuca photon detection device for the dune experiment, 2021.

[186] H. V. Souza et al. Liquid argon characterization of the x-arapuca with alpha particles, gamma rays and cosmic muons, 2021.

[187] L. Paulucci, F. Marinho, A. Machado, and E. Segreto. A complete simulation of the x-arapuca device for detection of scintillation photons. *Journal of Instrumentation*, 15(01):C01047–C01047, Jan 2020.

[188] I. Ambats et al. The MINOS Detectors Technical Design Report. 10 1998.

[189] A. Abed Abud et al. Deep Underground Neutrino Experiment (DUNE) Near Detector Conceptual Design Report. *Instruments*, 5(4):31, 2021.

[190] B. Abi et al. Deep Underground Neutrino Experiment (DUNE), Far Detector Technical Design Report, Volume IV The DUNE Far Detector Dual-Phase Technology. Technical report, DUNE, 2019.

[191] D. Belver et al. Cryogenic R5912-20Mod Photomultiplier Tubes Characterization for the ProtoDUNE Dual Phase Experiment. *JINST*, 13:T10006, 2018.

[192] R. Acciarri et al. Design and Construction of the MicroBooNE Detector. *JINST*, 12(02):P02017, 2017.

[193] A. M. Szelc. Developing LAr Scintillation Light Collection Ideas in the Short Baseline Neutrino Detector. *JINST*, 11(02):C02018, 2016.

[194] DUNE. Deep Underground Neutrino Experiment (DUNE) Far Detector Conceptual Design Report, Single-Phase Vertical Drift Technology, in preparation. *arXiv*, 2021.

[195] A. Abed Abud et al. Deep Underground Neutrino Experiment (DUNE) Near Detector Conceptual Design Report. *Instruments*, 5(4):31, 2021.

[196] H.-T. Janka. Neutrino emission from supernovae. In A. W. Alsabti and P. Murdin, editors, *Handbook of Supernovae*, pages 1575–1604. Springer International Publishing, 2017.

[197] K. Hirata, T. Kajita, M. Koshiba, M. Nakahata, Y. Oyama, N. Sato, A. Suzuki, M. Takita, Y. Totsuka, T. Kifune, T. Suda, K. Takahashi, T. Tanimori, K. Miyano, M. Yamada, E. W. Beier, L. R. Feldscher, S. B. Kim, A. K. Mann, F. M. Newcomer, R. Van, W. Zhang, and B. G. Cortez. Observation of a neutrino burst from the supernova sn1987a. *Phys. Rev. Lett.*, 58:1490–1493, Apr 1987.

[198] T. Haines, C. Bratton, D. Casper, A. Ciocio, R. Claus, M. Crouch, S. Dye, S. Errede, W. Gajewski, M. Goldhaber, T. Haines, T. Jones, D. Kielczewska, W. Kropp, J. Learned, J. Losecco, J. Matthews, R. Miller, M. Mudan, L. Price, F. Reines, J. Schultz, S. Seidel, E. Shumard, D. Sinclair, H. Sobel, L. Sulak, R. Svoboda, G. Thornton, and J. Van Der Velde. Neutrinos from sn1987a in the imb detector. *Nuclear Instruments and Methods in Physics Research Section A: Accelerators, Spectrometers, Detectors and Associated Equipment*, 264(1):28–31, 1988.

[199] B. Abi et al. Supernova neutrino burst detection with the Deep Underground Neutrino Experiment. *Eur. Phys. J. C*, 81(5):423, 2021.

[200] B. Abi et al. Prospects for beyond the Standard Model physics searches at the Deep Underground Neutrino Experiment. *Eur. Phys. J. C*, 81(4):322, 2021.

[201] B. Abi et al. The Single-Phase ProtoDUNE Technical Design Report. *arXiv*, 6 2017.

[202] B. Abi et al. First results on ProtoDUNE-SP liquid argon time projection chamber performance from a beam test at the CERN neutrino platform. *JINST*, 15(12):P12004–P12004, dec 2020.

[203] A. A. Abud et al. Design, construction and operation of the ProtoDUNE-SP Liquid Argon TPC. *JINST*, 17(01):P01005, 2022.

[204] J. Calcutt. *Measurement of π^+ – Argon Absorption and Charge Exchange Interactions Using ProtoDUNE-SP*. PhD thesis, Michigan State U., Michigan State U., 2021.

[205] A. Paudel. *A pion-argon cross section measurement in the ProtoDUNE-SP experiment with cosmogenic muon*. PhD thesis, Kansas State U., 2021.

[206] R. Diurba. *Evaluating the ProtoDUNE-SP Detector Performance to Measure a 6 GeV/c Positive Kaon Inelastic Cross Section on Argon*. PhD thesis, Minnesota U., 2021.

[207] J. S. Marshall and M. A. Thomson. The Pandora Software Development Kit for Pattern Recognition. *Eur. Phys. J. C*, 75(9):439, 2015.

[208] R. Acciarri et al. The Pandora multi-algorithm approach to automated pattern recognition of cosmic-ray muon and neutrino events in the MicroBooNE detector. *Eur. Phys. J. C*, 78(1):82, 2018.

[209] B. Aimard et al. Study of scintillation light collection, production and propagation in a 4 tonne dual-phase LArTPC. *JINST*, 16(03):P03007, 2021.

[210] A. Rubbia. Progress report on LBNO-DEMO/WA105 (2015). Technical report, CERN, Geneva, Mar 2015.

[211] D. Autiero et al. Yearly progress report on ProtoDUNE Dual Dhase (2020). Technical report, CERN, Geneva, Mar 2020.

[212] V1740 - 64 channel 12 bit 62.5 ms/s digitizer - caen. `https://www.caen.it/products/v1740/`. Accessed: 2021-10-05.

[213] Unicos wincc oa documentation. `https://unicos.web.cern.ch/unicos-wincc-oa-documentation`. Accessed: 2021-12-20.

[214] Q. Zhao, M. Guan, P. Zhang, C. Yang, J. Li, Y. Wei, L. Wang, Y. Gan, and W. Xiong. Measurement of the relative quantum efficiency of hamamatsu model r5912-20mod photomultiplier tubes at liquid argon temperature. *Journal of Instrumentation*, 16(06):T06014, jun 2021.

[215] Polyethylene naphthalate (pen) - film - material information. `http://www.goodfellow.com/E/Polyethylene-naphthalate-Film.html`. Accessed: 2021-10-05.

[216] R. Francini et al. VUV-vis optical characterization of tetraphenyl-butadiene films on glass and specular reflector substrates from room to liquid argon temperature. *JINST*, 8(09):P09006–P09006, sep 2013.

[217] B. Burak, P. Garcia, C. Jesús-Valls, T. Lux, A. Menegolli, M. C. Prata, G. L. Raselli, M. Rossella, D. Vargas, and W. Vollenberg. Comparison between photon detection efficiency and tetraphenyl-butadiene coating stability of photomultiplier tubes immersed in liquid argon. *JINST*, 15(04):C04021, 2020.

[218] J. Kapustinsky, R. DeVries, N. DiGiacomo, W. Sondheim, J. Sunier, and H. Coombes. A fast timing light pulser for scintillation detectors. *Nuclear Instruments and Methods in Physics Research Section A: Accelerators, Spectrometers, Detectors and Associated Equipment*, 241(2):612–613, 1985.

[219] D. Belver, J. Boix, E. Calvo, C. Cuesta, A. Gallego-Ros, I. Gil-Botella, S. Jiménez, C. Lastoria, T. Lux, I. Martín, J. Martínez, C. Palomares, D. Redondo, J. Soto-Oton, D. Vargas, and A. Verdugo. A light calibration system for the ProtoDUNE-DP detector. *Journal of Instrumentation*, 14(04):T04001–T04001, apr 2019.

[220] Midas (maximum integration data acquisition system). `http://midas.psi.ch`.

[221] D. Belver, J. Boix, E. Calvo, C. Cuesta, A. Gallego-Ros, I. Gil-Botella, S. Jiménez, C. Lastoria, T. Lux, I. Martín, J. Martínez, C. Palomares, J. Soto-Oton, and A. Verdugo. Protodune-dp light acquisition and calibration software. *IEEE Transactions on Nuclear Science*, pages 1–1, 2021.

[222] ROOTANA. `https://midas.triumf.ca/MidasWiki/index.php/ROOTANA`.

[223] D. Belver, E. Calvo, C. Cuesta, A. Gallego-Ros, I. Gil-Botella, S. Jiménez, C. Lastoria, I. Martín, J. Martínez, C. Palomares, J. Soto-Oton, and A. Verdugo. First testing of the hamamatsu r5912-02mod photomultiplier tube at 4-bar pressure and cryogenic temperature. *JINST*, 15(09):P09023–P09023, sep 2020.

[224] B. Abi et al. Scintillation light detection in the 6-m drift-length ProtoDUNE Dual Phase liquid argon TPC. Technical report, DUNE, 2021.

[225] E. Segreto. Evidence of delayed light emission of tetraphenyl-butadiene excited by liquid-argon scintillation light. *Phys. Rev. C*, 91:035503, 2015.

[226] S. Kubota, M. Hishida, and J. Raun. Evidence for a triplet state of the self-trapped exciton states in liquid argon, krypton and xenon. *Journal of Physics C: Solid State Physics*, 11(12):2645–2651, jun 1978.

[227] A. Gallego. *Studies on the scintillation light detection in the ProtoDUNE Dual Phase Liquid-argon TPC and its capability for the supernova trigger in DUNE*. PhD thesis, Universidad Autónoma de Madrid, 2021.

[228] P. Agnes et al. Measurement of the liquid argon energy response to nuclear and electronic recoils. *Phys. Rev. D*, 97(11):112005, 2018.

[229] X. Luo and F. Cavanna. Ion transport model for large LArTPC. *JINST*, 15(03):C03034, 2020.

[230] D. Totani. Single photon rate observation and first calorimetric energy reconstruction of beam events from lar scintillation light in protodune-sp. Presented at the LIDINE 2019, University of Manchester, UK, 2019.

[231] D. Totani. Study the spe rate comparing forward to reverse cathode polarity in microboone. Presented at the MicroBoone collaboration meeting, 2021.

[232] E. Snider and G. Petrillo. LArSoft: toolkit for simulation, reconstruction and analysis of liquid argon TPC neutrino detectors. *Journal of Physics: Conference Series*, 898:042057, oct 2017.

[233] M. A. et al. Analysis of the liquid argon scintillation light signals with the icarus t600 detector. Technical Report Technical Report ICARUS-TM/06-03, ICARUS collaboration, 2006.

[234] G. Zhu, S. W. Li, and J. F. Beacom. Developing the MeV potential of DUNE: Detailed considerations of muon-induced spallation and other backgrounds. *Phys. Rev. C*, 99(5):055810, 2019.

[235] T. T. Böhlen, F. Cerutti, M. P. W. Chin, A. Fassò, A. Ferrari, P. G. Ortega, A. Mairani, P. R. Sala, G. Smirnov, and V. Vlachoudis. The FLUKA Code: Developments and Challenges for High Energy and Medical Applications. *Nucl. Data Sheets*, 120:211–214, 2014.

[236] C. Forti, H. Bilokon, B. d'Ettore Piazzoli, T. K. Gaisser, L. Satta, and T. Stanev. Simulation of atmospheric cascades and deep underground muons. *Phys. Rev. D*, 42:3668–3689, 1990.

[237] H. Loosli. A dating method with39ar. *Earth and Planetary Science Letters*, 63(1):51–62, 1983.

[238] P. Benetti, F. Calaprice, E. Calligarich, M. Cambiaghi, F. Carbonara, F. Cavanna, A. Cocco, F. Di Pompeo, N. Ferrari, G. Fiorillo, C. Galbiati, L. Grandi, G. Mangano, C. Montanari, L. Pandola, A. Rappoldi, G. Raselli, M. Roncadelli, M. Rossella, C. Rubbia, R. Santorelli, A. Szelc, C. Vignoli, and Y. Zhao. Measurement of the specific activity of 39ar in natural argon. *Nuclear Instruments and Methods in Physics Research Section A: Accelerators, Spectrometers, Detectors and Associated Equipment*, 574(1):83–88, 2007.

[239] A. S. Barabash, R. R. Saakyan, and V. I. Umatov. On concentration of42ar in liquid argon. *Journal of Physics: Conference Series*, 718:062004, may 2016.

[240] S. Agostinelli et al. GEANT4–a simulation toolkit. *Nucl. Instrum. Meth. A*, 506:250–303, 2003.

[241] A. Abed Abud et al. Scintillation light detection in the 6-m drift-length ProtoDUNE Dual Phase liquid argon TPC. 3 2022.

[242] P. Abratenko et al. Measurement of the atmospheric muon rate with the MicroBooNE Liquid Argon TPC. *JINST*, 16(04):P04004, 2021.

[243] M. Antonello et al. Detection of Cherenkov light emission in liquid argon. *Nucl. Instrum. Meth. A*, 516:348–363, 2004.

[244] W. Maneschg, M. Laubenstein, D. Budjas, W. Hampel, G. Heusser, K. T. Knopfle, B. Schwingenheuer, and H. Simgen. Measurements of extremely low radioactivity levels in stainless steel for GERDA. *Nucl. Instrum. Meth. A*, 593:448–453, 2008.

[245] C. Benson et al. Measurements of the intrinsic quantum efficiency and absorption length of tetraphenyl butadiene thin films in the vacuum ultraviolet regime. *Eur. Phys. J. C*, 78:329, 2018.

[246] D. McKinsey, C. Brome, J. Butterworth, R. Golub, K. Habicht, P. Huffman, S. Lamoreaux, C. Mattoni, and J. Doyle. Fluorescence efficiencies of thin scintillating films in the extreme ultraviolet spectral region. *Nuclear Instruments and Methods in Physics Research Section B: Beam Interactions with Materials and Atoms*, 132(3):351–358, 1997.

[247] X.-F. Ding, L.-J. Wen, X. Zhou, Y.-Y. Ding, X.-C. Ye, L. Zhou, M.-C. Liu, H. Cai, and J. Cao. Measurement of the fluorescence quantum yield of bis-MSB. *Chin. Phys. C*, 39(12):126001, 2015.

[248] Y. Abraham, J. Asaadi, V. Basque, W. Castiglioni, R. Dorrill, M. Febbraro, B. Hackett, J. Kelsey, B. Littlejohn, I. Parmaksiz, M. Rooks, and A. Szelc. Wavelength-shifting performance of polyethylene naphthalate films in a liquid argon environment. *Journal of Instrumentation*, 16(07):P07017, jul 2021.

[249] J. Soto-Oton. Measurements of the polyethylene naphthalate performance as a wavelength shifter in protoDUNE-DP. Poster presented at Neutrino 2020, Chicago, U.S.A, 2020.

[250] V. Gehman, S. Seibert, K. Rielage, A. Hime, Y. Sun, D.-M. Mei, J. Maassen, and D. Moore. Fluorescence efficiency and visible re-emission spectrum of tetraphenyl butadiene films at extreme ultraviolet wavelengths. *Nuclear Instruments and Methods in Physics Research Section A: Accelerators, Spectrometers, Detectors and Associated Equipment*, 654(1):116–121, 2011.

[251] J. R. Graybill, C. B. Shahi, M. A. Coplan, A. K. Thompson, R. E. Vest, and C. W. Clark. Extreme ultraviolet photon conversion efficiency of tetraphenyl butadiene. *Appl. Opt.*, 59(4):1217–1224, Feb 2020.

[252] C. Lally, G. Davies, W. Jones, and N. Smith. Uv quantum efficiencies of organic fluors. *Nuclear Instruments and Methods in Physics Research Section B: Beam Interactions with Materials and Atoms*, 117(4):421–427, 1996.

[253] M. G. Boulay et al. Direct comparison of PEN and TPB wavelength shifters in a liquid argon detector. *Eur. Phys. J. C*, 81(12):1099, 2021.

[254] D. Mary, G. Teyssedre, and C. Laurent. Uv-induced degradation of poly(ethylene naphthalate) films from the standpoint of electrical and luminescence properties. In *2001 Annual Report Conference on Electrical Insulation and Dielectric Phenomena (Cat. No.01CH37225)*, pages 165–168, 2001.

[255] I. Ouchi, I. Nakai, M. Ono, and S. Kimura. Features of fluorescence spectra of polyethylene 2,6-naphthalate films. *Journal of Applied Polymer Science*, 105(1):114–121, 2007.

[256] A. Bueno, J. Lozano, A. J. Melgarejo, F. J. Muñoz, J. L. Navarro, S. Navas, and A. G. Ruiz. Characterization of large area photomultipliers and its application to dark matter search with noble liquid detectors. *Journal of Instrumentation*, 3(01):P01006–P01006, jan 2008.

[257] M. Babicz, S. Bordoni, T. Cervi, Z. Collins, A. Fava, U. Kose, M. Meli, A. Menegolli, M. Nessi, F. Pietropaolo, G. Raselli, F. Resnati, M. Rossella, P. Sala, and A. Zani. Experimental study of the propagation of scintillation light in liquid argon. *Nuclear Instruments and Methods in Physics Research Section A: Accelerators, Spectrometers, Detectors and Associated Equipment*, 2018.

[258] C. Vogl, M. Schwarz, X. Stribl, J. Grießing, P. Krause, and S. Schönert. Scintillation and optical properties of xenon-doped liquid argon. *JINST*, 17(01):C01031, 2022.

[259] M. Kuźniak and A. M. Szelc. Wavelength shifters for applications in liquid argon detectors. *Instruments*, 5(1), 2021.

[260] K. Fujii, Y. Endo, Y. Torigoe, S. Nakamura, T. Haruyama, K. Kasami, S. Mihara, K. Saito, S. Sasaki, and H. Tawara. High-accuracy measurement of the emission spectrum of liquid xenon in the vacuum ultraviolet region. *Nuclear Instruments and Methods in Physics Research Section A: Accelerators, Spectrometers, Detectors and Associated Equipment*, 795:293–297, 2015.

[261] A. Neumeier, T. Dandl, A. Himpsl, L. Oberauer, W. Potzel, S. Schönert, and A. Ulrich. Attenuation of vacuum ultraviolet light in pure and xenon-doped liquid argon —An approach to an assignment of the near-infrared emission from the mixture. *EPL*, 111(1):12001, 2015.

[262] S. Kubota, M. Hishida, S. Himi, J. Suzuki, and J. Ruan. The suppression of the slow component in xenon-doped liquid argon scintillation. *Nuclear Instruments and Methods in Physics Research Section A: Accelerators, Spectrometers, Detectors and Associated Equipment*, 327(1):71 – 74, 1993.

[263] D. Akimov, V. Belov, A. Konovalov, A. Kumpan, O. Razuvaeva, D. Rudik, and G. Simakov. Fast component re-emission in xe-doped liquid argon. *Journal of Instrumentation*, 14(09):P09022–P09022, sep 2019.

[264] A. Buzulutskov. Photon emission and atomic collision processes in two-phase argon doped with xenon and nitrogen. *EPL (Europhysics Letters)*, 117(3):39002, feb 2017.

[265] C. Galbiati, X. Li, J. Luo, D. Marlow, H. Wang, and Y. Wang. Pulse shape study of the fast scintillation light emitted from xenon-doped liquid argon using silicon photomultipliers. *Journal of Instrumentation*, 16(02):P02015–P02015, feb 2021.

[266] G. Nowak and J. Fricke. The heteronuclear excimers $ArKr*$, $ArXe*$ and $KrXe*$. *Journal of Physics B: Atomic and Molecular Physics*, 18(7):1355–1367, apr 1985.

[267] A. Neumeier, T. Dandl, T. Heindl, A. Himpsl, L. Oberauer, W. Potzel, S. Roth, S. Schönert, J. Wieser, and A. Ulrich. Intense vacuum ultraviolet and infrared scintillation of liquid ar-xe mixtures. *EPL (Europhysics Letters)*, 109(1):12001, jan 2015.

[268] E. B. Saloman. Energy levels and observed spectral lines of xenon, xe i through xe liv. *Journal of Physical and Chemical Reference Data*, 33(3):765–921, 2004.

[269] Y.-J. Wu, C. Y. R. Wu, S.-L. Chou, M.-Y. Lin, H.-C. Lu, J.-I. Lo, and B.-M. Cheng. SPECTRA AND PHOTOLYSIS OF PURE NITROGEN AND METHANE DISPERSED IN SOLID NITROGEN WITH VACUUM-ULTRAVIOLET LIGHT. *The Astrophysical Journal*, 746(2):175, feb 2012.

[270] A. Hitachi et al. Effect of ionization density on the time dependence of luminescence from liquid argon and xenon. In *Phys. Rev. B* [162], pages 5279–5285.

[271] C. G. Wahl et al. Pulse-shape discrimination and energy resolution of a liquid-argon scintillator with xenon doping. *JINST*, 9(06):P06013–P06013, jun 2014.

[272] M. Yang, A. Gatto, and N. Kaiser. Highly reflecting aluminum-protected optical coatings for the vacuum-ultraviolet spectral range. *Appl. Opt.*, 45(1):178–183, Jan 2006.

[273] J. C. Pati and A. Salam. Is baryon number conserved? *Phys. Rev. Lett.*, 31:661–664, Sep 1973.

[274] W. De Boer. Grand unified theories and supersymmetry in particle physics and cosmology. *Progress in Particle and Nuclear Physics*, 33:201–301, 1994.

[275] P. Nath and P. Fileviez Pérez. Proton stability in grand unified theories, in strings and in branes. *Physics Reports*, 441(5):191–317, 2007.

[276] K. Abe et al. Search for proton decay via $p \to e^+\pi^0$ and $p \to \mu^+\pi^0$ in 0.31 megaton·years exposure of the Super-Kamiokande water Cherenkov detector. *Phys. Rev. D*, 95(1):012004, 2017.

[277] K. Abe et al. Search for nucleon decay into charged antilepton plus meson in 0.316 megaton·years exposure of the Super-Kamiokande water Cherenkov detector. *Phys. Rev. D*, 96(1):012003, 2017.

[278] K. Abe et al. Search for proton decay via $p \to \nu K^+$ using 260 kiloton·year data of Super-Kamiokande. *Phys. Rev. D*, 90(7):072005, 2014.

[279] C. Berger et al. Lifetime limits on (B-L) violating nucleon decay and dinucleon decay modes from the Frejus experiment. *Phys. Lett. B*, 269:227–233, 1991.

[280] C. Alt, B. Radics, and A. Rubbia. Neural-network-driven proton decay sensitivity in the $p \to \bar{\nu}K^+$ channel using large liquid argon time projection chambers. *JHEP*, 04:243, 2021.

[281] C. Andreopoulos et al. The genie neutrino monte carlo generator. *Nuclear Instruments and Methods in Physics Research Section A: Accelerators, Spectrometers, Detectors and Associated Equipment*, 614(1):87–104, 2010.

[282] Hamamatsu R5912 Datasheet. `https://www.hamamatsu.com/resources/pdf/etd/LARGE_AREA_PMT_TPMH1376E.pdf`.